ISBN 978-82-326-1766-1 (printed version)
ISBN 978-82-326-1767-8 (electronic version)
ISSN 1503-8181

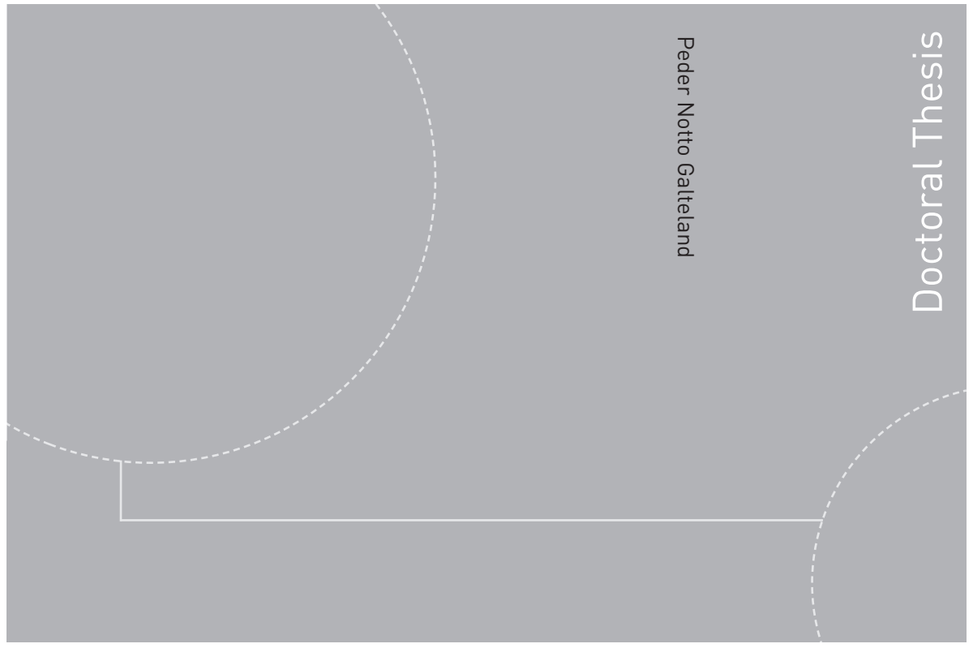

Doctoral theses at NTNU, 2016:214

Peder Notto Galteland

Monte-Carlo studies of multi-component Ginzburg-Landau theories with competing interactions

NTNU
Norwegian University of
Science and Technology
Faculty of Natural
Sciences and Technology
Department of Physics

NTNU
Norwegian University of
Science and Technology

Doctoral theses at NTNU, 2016:214

NTNU

NTNU
Norwegian University of
Science and Technology

Peder Notto Galteland

Monte-Carlo studies of multi-component Ginzburg-Landau theories with competing interactions

Thesis for the degree of Philosophiae Doctor

Trondheim, August 2016

Norwegian University of Science and Technology
Faculty of Natural Sciences and Technology
Department of Physics

NTNU
Norwegian University of
Science and Technology

NTNU
Norwegian University of Science and Technology

Thesis for the degree of Philosophiae Doctor

Faculty of Natural Sciences and Technology
Department of Physics

ISBN 978-82-326-1766-1 (printed version)
ISBN 978-82-326-1767-8 (electronic version)
ISSN 1503-8181

Doctoral theses at NTNU, 2016:214

Printed by Skipnes Kommunikasjon as

Abstract

This thesis presents four research papers in the field of condensed-matter theory. Three of the papers make use of large-scale Monte-Carlo simulations to explore various aspects of Bose-Einstein condensates with multiple superfluid components. Papers I and II relate to a two-component Bose-Einstein condensate in three spatial dimensions under rotation. They explore the phase diagram and phase transitions of the model in two regimes, where either inter- or intra-component interactions dominates, as well as at a special SU(2)-symmetric point where all density-density interactions are of equal strength. We find that this rich phase diagram, in the coexisting regime, exhibits co-centered vortex lattices with hexagonal symmetry when the inter-component interaction is attractive. These lattices evolve into intercalated hexagonal lattices as the inter-component interaction is made repulsive, and further into intercalated square lattices as the repulsive interaction is increased in strength. In the phase-separated regime, we find striped vortex lattices for intermediate inter-component coupling strengths. For sufficiently strong inter-component coupling strengths one of the condensates is completely depleted, while the other develops a hexagonal vortex line lattice, as it is effectively a single-component condensate.

Paper III investigates the phases and phase transitions of a similar model

of a two-component condensate, now in two spatial dimensions with spin-orbit coupling and zero rotation. Here we find, for low inter-component coupling strength, that the effect of the spin-orbit interaction is to modulate the condensate fields by a single $\mathbf{q}$-vector, a plane wave state. For increased inter-component couplings, but with intermediate spin-orbit coupling, we again find that one of the condensates will be depleted, making the remaining condensate effectively a single-component condensate. This completely removes the effect of the spin-orbit interaction. For both high inter-component and high spin-orbit interaction strengths, we find that the condensate forgoes the energy gained by depleting one condensate. It will rather modulate the condensate, but now with staggered condensate amplitudes. This state is a superposition of two states with modulation vectors $\mathbf{q}$ and $-\mathbf{q}$, a standing wave state. We also explore the thermal phase transitions in the absence of spin-orbit couplings, here we find Kosterlitz-Thouless transitions in all components regardless of whether or not one component has collapsed, and independent on the value of the inter-component density-density interaction strength.

The last paper explores, in a purely analytical treatment, the effect of inter-band Josephson couplings on an N-component London superconductor. It utilizes a mathematical identity to re-express the model in terms of integer-valued superconducting currents, and we show that the inclusion of inter-band couplings introduces instanton-like events in these currents. These events effectively removes the current conservation in each individual superconducting current, as is expected when introducing the Josephson coupling. However, one particular combination of current, the sum of all the currents, remains conserved even with the Josepshon coupling. We argue that this converts the phase transitions of the neutral sector into crossovers, while leaving the charged phase transition unaffected. The fluctuations of the neutral sector will weaken, but may still influence the charged fluctuations sufficiently to preempt the remaining inverted-$3DXY$ transition, making it first order. We also re-express the onset of the Higgs mass when entering the superconducting state as a blowout of loops of superconducting current.

Preface

This thesis is submitted as partial fulfillment for the requirements of the degree philosophiae doctor, at the Norwegian University of Science and Technology(NTNU), Trondheim, Norway.

It is the culmination of four years of work at NTNU, which started in May of 2012, and ended in the early summer of 2016. One year of this engagement was devoted to teaching duties at the Department of Physics at NTNU, and a half a year to completing doctorate level courses as a requirement of the degree. The research has been supervised by Prof. Asle Sudbø, with Prof. Jacob Linder as co-supervisor, and was funded by the Norwegian Research Council.

Papers I-III made use of the NOTUR supercomputing facilities in Tromsø (*Stallo*) and Trondheim (*Vilje*). Papers I and II was co-authored by Egor Babaev and Asle Sudbø, and papers III and IV was co-authored by Asle Sudbø

Peder Notto Galteland
Trondheim, June 2016

Acknowledgements

First of all I must thank my advisor, Asle Sudbø, for giving me the opportunity to take the PhD degree, for being an inspiring and knowledgable advisor, for always having time when I had a question, and for always having an idea of the way out when I was stuck with a problem. I would also like to thank Egor Babaev, my main collaborator on two of the papers included in this thesis. His knowledge and attention to detail has been a great asset to these works.

When I first started, I was warmly greeted by the other PhD-students of the group. Henrik Enoksen, with whom I shared an office for large parts of my time here quickly turned out to be a good friend and generally nice guy with excellent taste in music. Egil Vålandsmyr Herland also helped me out a lot in the beginning, showing me the ropes of Monte-Carlo algorithms, always having the time for a quick chat. Troels Arnfred Bojesen and I have had many interesting conversations about simulation algorithms, and we had the opportunity to attend a few conferences together, including a short vacation after the March Meeting in Denver. Also, Stefan Rex has been a good companion during my PhD, especially on our trips to Nordita in Stockholm, and the March Meeting in San Antonio. Last but not least of our ever-changing research group I thank Einar Stiansen and Iver Bakken

Sperstad, who I barely had the time to get to know before they finished, and Fredrik Nicolai Krohg, the newest addition to the group.

Here at the theory section, a great many other PhD-students and postdocs must be mentioned. Hans Skarsvåg, who started at the same time as me, has always been a good friend both at work and outside, and has made my time here much more enjoyable. André Kapelrud has also been a good friend, I have thoroughly enjoyed our coffee breaks and conversations. The rest of the gang also deserves a warm thank you. Camilla, Lars, Erlend, Eirik, Manu, Severin, William, Arturo, Sverre, Therese, Peter, Alireza, Dag-Vidar, Niklas, Cecilia, Sol, you have all been good friends, and I hope I can keep in touch with as many of you as possible in the future.

My family deserves a big warm thank you, my mother, father, grandmother, brothers and sister. You have all influenced me greatly throughout my life, making me into the man I am today. You are all a big part of this.

Finally, the most important person in my life, my girlfriend, Line, deserves the biggest thanks of all for supporting me through my PhD, always there with a comforting word and a warm hug. Thank you for always being there for me, and for loving me!

List of papers

Paper I:
Peder Notto Galteland, Egor Babaev, and Asle Sudbø:
Fluctuation effects in rotating Bose-Einstein condensates with broken $\mathrm{SU}(2)$ *and* $\mathrm{U}(1) \times \mathrm{U}(1)$ *symmetries in the presence of intercomponent density-density interactions*
Physical Review A **91**, 013605 (2015) [1]

Paper II:
Peder Notto Galteland, Egor Babaev, and Asle Sudbø:
Thermal remixing of phase-separated states in two-component bosonic condensates
New Journal of Physics **17**, 103040 (2015) [2]

Paper III:
Peder Notto Galteland, and Asle Sudbø:
Competing interactions in population imbalanced two-component Bose-Einstein condensates
Preprint [3]

Paper IV:
Peder Notto Galteland, and Asle Sudbø:
Current-loops, phase transitions, and the Higgs mechanism in Josephson-coupled multi-component London superconductors
Preprint (submitted to Phys. Rev. B)[4]

My contribution to the papers

I have contributed significantly to all papers where I am listed as the first author. In papers I, II and III I wrote all of the Monte-Carlo code and did all of the simulations, I did any analytical calculation present in all four papers, and I took great part in interpreting results and writing the manuscripts of all four papers. I also created all of the figures in all four papers.

Contents

1 Introduction **1**

2 Statistical Mechanics **5**
2.1 Foundations of statistical mechanics 5
2.2 Lattice models 9
2.2.1 The Ising model 9
2.2.2 The XY model 10
2.3 Spontaneous symmetry breaking and phase transitions . . . 11
2.3.1 Continuous transitions and order parameters 12
2.3.2 Symmetries and phase transitions of the zero-field Ising and XY model 13
2.3.3 First-order transitions 16
2.4 Universality and scaling laws 17
2.4.1 The exponents α, β, γ and δ 18
2.4.2 Correlation functions and the exponents ν and η . . . 21
2.5 The Ginzburg-Landau model 23
2.5.1 Lattice regularization 24
2.5.2 The London approximation 26

2.6 Topological defects . . . 27
2.7 The Kosterlitz-Thouless transition . . . 31

3 Monte-Carlo Simulations **35**
3.1 The basics of Monte-Carlo simulations . . . 35
3.1.1 Monte-Carlo integration . . . 37
3.2 Markov-chain Monte-Carlo . . . 38
3.2.1 The Metropolis-Hastings algorithm . . . 40
3.2.2 Update schemes . . . 41
3.2.3 Thermal equilibration . . . 42
3.3 Issues from finite sampling time and system size . . . 44
3.3.1 Error estimation . . . 44
3.3.2 Critical slowing down . . . 45
3.3.3 Finite size scaling . . . 46
3.3.4 Re-weighting . . . 48
3.4 Detecting a Kosterlitz-Thouless transition . . . 50

4 Bose-Einstein Condensates **53**
4.1 History . . . 53
4.2 Experimental realization of a Bose-Einstein condensate in cold atomic gases . . . 55
4.2.1 Rotation, vortices and vortex lattices . . . 56
4.2.2 Feshbach resonances . . . 57
4.2.3 Mixtures of atomic gases . . . 57
4.2.4 Optical lattices . . . 57
4.2.5 Synthetic gauge fields . . . 58
4.3 Theoretical models of Bose-Einstein condensates . . . 59
4.3.1 Rotating the condensate . . . 60
4.3.2 Spin-Orbit coupling . . . 61
4.4 Main results of papers I-III . . . 64
4.4.1 Papers I and II . . . 65
4.4.2 Paper III . . . 70
4.4.3 Outlook . . . 74

5 Multiband Superconductors **75**
5.1 History and phenomenology 75
5.2 Models of multiband superconductors 77
5.2.1 The London superconductor 80
5.2.2 Lattice London model 81
5.2.3 The Villain model 81
5.3 Vortices and duality 82
5.3.1 Charged and neutral modes 84
5.4 Character expansion 87
5.5 Main results of paper IV 89
5.5.1 Outlook 92

Bibliography **93**

Paper I **101**

Paper II **119**

Paper III **137**

Paper IV **153**

CHAPTER 1

Introduction

The goal of physics in general, and condensed matter physics in particular, has always been to describe as many phenomena of nature as possible, with as few and simple laws as possible. The *Landau-Ginzburg-Wilson* theory with its successful treatment of phase transitions in as diverse systems as liquids/solids, magnets, *superfluids* and *superconductors* is such an example. Speaking of superfluids and superconductors, these at first quite different phenomena may both be modeled by the *Ginzburg-Landau* model, another very successful theory. The prediction of macroscopic behaviour like thermodynamic phases or phase transitions from the interactions a large number of identical constituents governed by a simple set of rules is a tremendous triumph of condensed matter physics and statistical mechanics. This thesis aims to explore macroscopic behaviour stemming from the relatively simple Ginzburg-Landau description of two-component Bose-Einstein condensates, which exhibit superfluidity, and multiband London superconductors.

Bose-Einstein condensates, which have been realized experimentally

since 1995 in cold alkali atoms, are a state of matter where a macroscopic fraction of the atoms condense into the quantum ground state. Their realization in cold atomic gases, along with the subsequent development of many versatile experimental techniques like Feshbach resonances, optical lattices, and synthetic gauge fields, allows for the realization of many Hamiltonians. In addition to their versatility as a real-life model system, they are interesting in their own right. One may also create mixtures of different atomic gases, which creates a Bose-Einstein condensate with several components that may interact. This opens up the possibility of many a complex phenomenon not present in the simples condensate of a monoatomic gas. In the three first publications contained in this thesis [1–3], we have aimed to map out the phase diagram of these two-component superfluids with several interactions added, like density-density interactions of the condensate, superfluid vortex-inducing external rotation, and spin-orbit coupling. We show that these systems contain an array of interesting phases, influenced by the subtle interplay between the interactions present in the model.

A superconductor is a very different state of matter from superfluids in many ways, but they are similar in that they both exhibit dissipationless flow of currents, be it electric currents or matter currents. They are also similar in that they both may be described by the same model, the Ginzburg-Landau model, although with some alterations. The final paper of this thesis [4] examines the lattice London superconductor with multiple superconducting bands. Specifically, it aims to shed some light on the effect of introducing inter-band Josephson couplings from a slightly different angle, by re-expressing the model in terms of the actual superconducting currents rather than the phases of the London model.

The main theme of this thesis, as you may have gathered, is to explore the rather large parameter space of Ginzburg-Landau models with multiple components and various interactions. These are rather complicated beasts, and not very analytically tractable. Therefore, our main weapon will be large-scale Monte-Carlo simulations, backed up by arguments based in symmetry considerations and mean-field theory.

This thesis will first go through some of the theory needed, covering

some basic concepts of statistical mechanics in Chapter 2. Then, we will cover Monte-Carlo simulations in Chapter 3, where we present the basic requirements of a successful Monte-Carlo scheme, and some of the caveats one must be aware of. Finally we present the history and theory of the systems we wish to describe, as well as the specific theoretical models used and the main results of our four papers. Chapter 4 deals with Bose-Einstein condensates, while Chapter 5 treats the multiband superconductor.

Before we delve into the meat of this thesis, some notes on conventions and notation. We use greek indices to denote spatial coordinates, and roman indices to denote the component, or color of the order parameter fields. We will use natural units throughout this thesis, except for a few occasions where we will explicitly state otherwise, and fields and parameters will generally be defined in a dimensionless fashion.

CHAPTER 2

Statistical Mechanics

In this chapter I will give a brief introduction to the theoretical aspects which lay the groundwork of this thesis. I will address the basic statistical mechanics needed to develop the concepts used in, give an overview of the theory of phase transitions, and present the lattice and continuum models used to build up the more specialized models used in this work. The main references I have used are Refs. [5–7].

2.1 Foundations of statistical mechanics

Statistical mechanics provides the framework for our research into collective phenomena. The goal is to extract macroscopic properties, like internal energy, specific heat capacity and response to external fields, by considering only microscopic degrees of freedom. By treating these degrees of freedom, which may be constituent atoms, quasi-particles, spins, or other more abstract variables in a statistical manner one may calculate thermodynamic properties that are not defined for single elements of the system.

Given a system described by the state Ψ, where Ψ may be any set of degrees of freedom, the probability of finding the system in a specific state is

$$p[\Psi] = \frac{1}{\mathcal{Z}} e^{-\beta H[\Psi]}. \tag{2.1}$$

Here, $\beta = 1/T$ is the inverse temperature of the system, $H[\Psi]$ is the Hamiltonian which describes the system, and $\mathcal{Z}$ is a normalization factor. This distribution is the *canonical probability distribution*. The temperature can be thought of as a tuning parameter in this formulation, which is the *canonical ensemble*. This means that we consider a system of fixed particle number and volume, that may exchange energy with the surroundings. The Hamiltonian is an energy *functional* that describes the behaviour of the system. It is a function of Ψ, which in itself is typically a function of position and possibly other variables. The normalization factor $\mathcal{Z}$ is called the *partition function*, and is, as we will see in the following, a very central quantity. We may calculate it by integrating the Boltzmann weight of every possible configuration the system may be in, with a given value of β,

$$\mathcal{Z} = \int \mathcal{D}\Psi e^{-\beta H[\psi]}. \tag{2.2}$$

At first glance, this may not seem too complicated, but in fact it is. Most of the work done in the publications included in this thesis revolves around calculating or estimating this quantity. As we will see, it contains all the information about the thermodynamic quantities of the system.

The partition function is directly related to the Helmholtz free energy in the following way

$$F = -\frac{1}{\beta} \ln \mathcal{Z}. \tag{2.3}$$

This is shown through differentiation by β on both sides of the equation, resulting in

$$\begin{aligned} \frac{\partial F}{\partial \beta} &= \frac{1}{\beta^2} \ln \mathcal{Z} - \frac{1}{\beta} \frac{\partial}{\partial \beta} \ln \mathcal{Z} \\ &= -\frac{1}{\beta} F + \frac{1}{\beta} \frac{\partial}{\partial \beta} (\beta F). \end{aligned} \tag{2.4}$$

From thermodynamics, we know that the internal energy is defined as $U = \partial(\beta F)/\partial\beta$, and the entropy as $S = \beta^2 \partial F/\partial\beta$. Inserting this into the above equation leaves us with

$$F = U - TS, \tag{2.5}$$

which is the definition of the Helmholtz free energy, with $\beta = 1/T$.

Using the partition function, we may represent physical observables as expectation values of said observable using the Boltzmann factor as a probability distribution. The observables, $\mathcal{O}$, are generally functions of the degrees of freedom, $\mathcal{O} = \mathcal{O}[\Psi]$[1], and by using probability theory we may write down their expectation values as

$$\langle \mathcal{O} \rangle = \frac{1}{\mathcal{Z}} \int \mathcal{D}\Psi \mathcal{O} e^{-\beta H}, \tag{2.6}$$

which we call the *thermal average* of $\mathcal{O}$. To show the relation between thermodynamic quantities and thermal averages, let us calculate the internal energy, U, and the heat capacity at constant volume, C_V. The internal energy may be calculated by differentiating βF with respect to β, or in terms of the partition function

$$U = -\frac{\partial}{\partial\beta} \ln \mathcal{Z}. \tag{2.7}$$

The specific heat capacity at constant volume, C_V, may be calculated by two successive differentiations,

$$C_V = \beta^2 \frac{\partial^2}{\partial\beta^2} \ln \mathcal{Z}. \tag{2.8}$$

Usually, H does not have any explicit temperature dependence[2], and we may write the internal energy as the expectation value of H,

$$\begin{aligned} U &= \frac{1}{\mathcal{Z}} \int \mathcal{D}\Psi H e^{-\beta H} \\ &= \langle H \rangle, \end{aligned} \tag{2.9}$$

[1] We will suppress the functional dependence for brevity.

[2] It is implicitly temperature dependent through the fields, Ψ.

and the specific heat as the fluctuations of H,

$$C_V = \beta^2 \left(\langle H^2 \rangle - \langle H \rangle^2 \right). \tag{2.10}$$

However, if the Hamiltonian depends explicitly on temperature, we have to be careful when differentiating the partition function. In that case we have the two expressions

$$U = \left\langle H + \beta \frac{\partial H}{\partial \beta} \right\rangle, \tag{2.11}$$

and

$$C_V = \beta^2 \left(\left\langle \left(H + \beta \frac{\partial H}{\partial \beta} \right)^2 \right\rangle - \left\langle H + \beta \frac{\partial H}{\partial \beta} \right\rangle^2 - \left\langle \frac{\partial}{\partial \beta} \left(H + \beta \frac{\partial H}{\partial \beta} \right) \right\rangle \right). \tag{2.12}$$

Oftentimes, we are interested in behaviour of systems under some external field. We may use a ferromagnet in an external magnetic field as a generic example. In this case the Hamiltonian will consist of one part pertaining to the internal dynamics of the spin, and a term coupling some magnetization per unit volume, $m[\Psi]$, to an external field h. We will see a couple of examples of specific Hamiltonians in Section 2.2. In general, we may then write the Hamiltonian as

$$H = H_0 - hm, \tag{2.13}$$

which means that the system will lower its energy by aligning m along h. Now, we may calculate the magnetization by differentiating with respect to h,

$$\langle m \rangle = \frac{1}{\beta V} \frac{\partial}{\partial h} \ln \mathcal{Z}. \tag{2.14}$$

In particular, we may be interested in the zero-field magnetization,

$$\langle m \rangle \Big|_{\mathbf{h}=0} = \frac{1}{\beta V} \frac{\partial}{\partial h} \ln \mathcal{Z} \Big|_{\mathbf{h}=0}. \tag{2.15}$$

We may also calculate the magnetic susceptibility,

$$\begin{aligned}\chi &= \left(\frac{\partial m}{\partial h}\right)\Big|_{h=0} \\ &= \frac{1}{\beta V}\frac{\partial^2}{\partial h^2}\ln \mathcal{Z}\Big|_{h=0}.\end{aligned} \tag{2.16}$$

It is clear that $\mathcal{Z}$ contains all the information of the thermodynamics of the system you consider.

2.2 Lattice models

Our goal will always be to describe as much physics as possible through the use of the simplest models imaginable. In fact, quite a lot of interesting physics is described by the very simple models, or variations of them, introduced below. Before presenting the more abstract concepts, we will define these lattice models in order to have some reference point. The simplest and most used models are spin models. This is a general class of models of N unit length spins interacting on a lattice. They are described by the spin variable $\mathbf{s}_i$, where the index i denotes the lattice site. These models may be classified by the dimensionality of the vector $\mathbf{s}_i$, that is how many components the spin has, and by the dimensionality of the lattice. These quantities will be denoted by n and D, respectively. Additionally, one may consider the symmetry of the lattice, which basically decides how many nearest neighbours each spin has. We will take the lattice to be hybercubic in the following, each spin will have $2D$ nearest neighbours.

2.2.1 The Ising model

The simplest spin model is found when we take $n = 1$. As the spins must be unit length, this means that each spin takes the value $s_{\mathbf{r}} = \pm 1$. We allow each spin to interact with all its nearest neighbours on the lattice, where the interaction may be ferromagnetic or anti-ferromagnetic. A ferromagnetic interaction will lower the energy when the spins align, while an

anti-ferromagnetic interaction will lower the energy when they anti-align. We may represent this model, known as the Ising model, on the following form,

$$H = -J \sum_{\langle \mathbf{r}\mathbf{r}' \rangle} s_{\mathbf{r}} s_{\mathbf{r}'} - h \sum_{\mathbf{r}} s_{\mathbf{r}}, \tag{2.17}$$

where h is an external field, which makes it energetically favourable to have $s_{\mathbf{r}} = 1$ when $h > 0$. J is the interaction strength, which is ferromagnetic when $J > 0$, and $\langle \mathbf{r}\mathbf{r}' \rangle$ denotes summing over all nearest neighbour pairs.

2.2.2 The XY model

Next, we have the $n = 2$ spin model, the XY model. This model features interactions between two-component unit-length spins, $\mathbf{s}_{\mathbf{r}} = (s_{x,\mathbf{r}}, s_{y,\mathbf{r}})$, on a lattice. The XY model is of course similar to the Ising model in that you have spins, now with two components, which interact either ferromagnetically or anti-ferromagnetically with their nearest neighbours only. The Hamiltonian has the following form

$$H = -J \sum_{\langle \mathbf{r}\mathbf{r}' \rangle} \mathbf{s}_{\mathbf{r}} \mathbf{s}_{\mathbf{r}'} - \mathbf{h} \sum_{\mathbf{r}} \mathbf{s}_{\mathbf{r}}. \tag{2.18}$$

Here, $\mathbf{h}$ is an external field, which tends to align the spins along its direction. As the spins we consider are of unit length, a more convenient parametrization would be to use the angle of each spin relative to a reference axis. One would then have $\mathbf{s}_{\mathbf{r}} = (\cos\theta_{\mathbf{r}}, \sin\theta_{\mathbf{r}})$, and the Hamiltonian would have the form

$$H = -J \sum_{\mathbf{r}, \hat{\boldsymbol{\mu}}} \cos(\theta_{\mathbf{r}+\hat{\boldsymbol{\mu}}} - \theta_{\mathbf{r}}) - h \sum_{\mathbf{r}} \cos\theta_{\mathbf{r}}. \tag{2.19}$$

Now, we have fixed the direction of the external field along the reference axis of the spins, and introduced the alternate nearest neighbour sum over $\mathbf{r}$ and $\hat{\boldsymbol{\mu}}$, where $\hat{\boldsymbol{\mu}}$ is the unit vector in the μ direction.

One may of course have a higher value of n, which is the Heisenberg model, but it is not relevant to our discussions. Other extensions may also

be done, for instance by having longer ranged interactions beyond nearest neighbours, different couplings in different directions (anisotropies), or perhaps by combining different types of spins that couple to each other. The possibilities are really endless, and one must chose a model which properly describes the system one is interested in.

2.3 Spontaneous symmetry breaking and phase transitions

An important triumph of the statistical treatment of microscopic degrees of freedom is its ability to describe and predict macroscopic phases. The prime example here is of course taken from the Ising model, which has a ferro-magnetically ordered phase below a critical temperature.

Heuristically, phase transitions can be thought of as a competition between the internal energy of the system, and its entropy. In a ferromagnet, aligning spins will always lower the internal energy, but not always the free energy. As seen from Eq. (2.5), the free energy can also be lowered by increasing the entropy of the system, but this will increase the internal energy. This leads to a competition between order and disorder, decided by temperature[3]. At low temperature, order wins out, and spins will ferromagnetically align, while disorder reigns at high temperatures. These two phases are separated by a phase transition, over which some thermodynamical quantity changes in a non-analytical fashion.

At the heart of phase transitions lies the concepts of symmetries and spontaneous symmetry breaking. By symmetry, we mean some transformation performed on the Hamiltonian of a system, which leaves the Hamiltonian unchanged. Mathematically, if we have the Hamiltonian $H[\Psi]$, which is a functional of some set of degrees of freedom, Ψ. Then, a symmetry is some transformation

$$\Psi \to \Psi', \tag{2.20}$$

[3]Or another parameter which describes the system, like interaction strengths or external fields.

such that

$$H[\Psi'] = H[\Psi]. \tag{2.21}$$

When the transformation bringing Ψ to Ψ' is a representation of the group $\mathcal{G}$, we say that the Hamiltonian has $\mathcal{G}$ symmetry.

Spontaneous symmetry breaking is a concept which occurs in many statistical mechanics models. In general, if we have a Hamiltonian which has $\mathcal{G}$ symmetry, some specific state of the system the Hamiltonian describes may not have this symmetry (it may be symmetric under some subgroup $\mathcal{H}$ of $\mathcal{G}$). If this occurs we say that the symmetry is spontaneously broken, or that $\mathcal{G}$ has been broken down to $\mathcal{H}$. Generally, this occurs when changing some parameter of the system to bring it from the high-symmetry to the low-symmetry state, for instance by changing the temperature.

2.3.1 Continuous transitions and order parameters

With the concept of spontaneous symmetry breaking fresh in mind, let us consider a less abstract example. An uniaxial ferromagnet, a ferromagnet with an easy axis, has ferromagnetic domains which point either up or down. This kind of system has up-down symmetry, and must be described by equations that reflect this. The Ising model has this symmetry, but we will first consider a very simple, phenomenological approach, which is Landau-theory, or mean-field theory. We assume that the magnet is described by a single, space-independent order parameter, M. If $M = 0$, the system is not magnetized, and if $|M| > 0$, it has a net magnetization. Next, we construct what is known as the Landau free energy, by writing down terms in an expansion of powers in the magnetization that respects the up-down symmetry. The first few reads

$$F_L = b(T)M^2 + g(T)M^4 + \dots . \tag{2.22}$$

We may assume $g(T)$ to be temperature independent, and it must be positive for the free energy to be bounded from below. Next, we must assume that $b(T)$ changes sign from positive to negative as some critical tempera-

ture T_c is approached from above, for instance on the following form

$$b(T) = b\frac{T - T_c}{T_c}. \tag{2.23}$$

By minimizing the free energy with respect to the magnetization, we find that

$$M = \begin{cases} \pm\sqrt{\frac{-b(T)}{2g}}, & T < T_c. \\ 0, & T > T_c. \end{cases} \tag{2.24}$$

This is the prime example of spontaneous symmetry breaking. The high-temperature state has the up-down symmetry of the basic free energy describing the system, while at low temperatures the actual state the magnet picks breaks this symmetry. Fig. 2.1 shows a schematic plot of this order parameter, when it picks the positive value of M.

The magnetization, M, in this case is known as the order parameter, and it signals the entry into the ordered, low-temperature state. As the magnet is cooled below T_c, the magnetization will grow continuously from zero, which is why this type of transition has been dubbed a continuous phase transition. Now, this example is rather contrived, the Landau free energy has been constructed to have the behaviour we wish. However, as we will see, many models of statistical mechanics show exactly this behaviour of an order parameter continuously evolving from zero as temperature (or some other parameter) is varied.

2.3.2 Symmetries and phase transitions of the zero-field Ising and XY model

The Ising model, Eq. (2.17), with $h = 0$ has Z_2 symmetry, or up-down symmetry. Letting each spin $s_{\mathbf{r}} \to -s_{\mathbf{r}}$, leaves the Hamiltonian invariant. In $D \geq 2$, the breaking of this symmetry causes the model to have a continuous phase transition. The order parameter of the Ising model is the magnetization, m, defined as

$$m = \frac{1}{N}\left\langle \sum_{\mathbf{r}} s_{\mathbf{r}} \right\rangle. \tag{2.25}$$

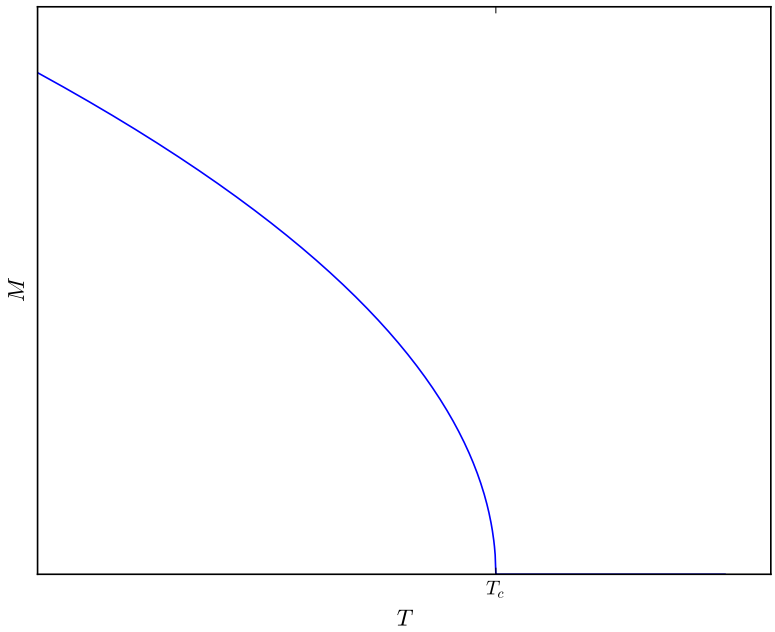

Figure 2.1: A schematic plot of the order parameter when passing through a second-order transition. As we approach the critical temperature, the order parameter evolves continuously to zero.

In two dimensions, the model has been solved exactly, while in three dimensions the phase transition has been confirmed numerically. The one dimensional model has been solved by Ising [8], and is shown to not have a phase transition. Onsager solved the two dimensional model in zero external field [9], and found the critical temperature to be $k_B T/J = 2/\ln(1+\sqrt{2})$.

The Hamiltonian of the XY-model, Eq. (2.19), with $h = 0$ is invariant under global rotations of the spin. That is, rotating each spin by a phase,

$\theta_{\mathbf{r}} \to \theta_{\mathbf{r}} + \varphi$, leaves H invariant. This is known as a U(1) symmetry. If $|h| > 0$, this symmetry is explicitly broken. With the XY model, one may also define a magnetization, $\mathbf{m}$, as

$$\mathbf{m} = \frac{1}{N} \left\langle \sum_{\mathbf{r}} (\cos\theta_{\mathbf{r}}, \sin\theta_{\mathbf{r}}) \right\rangle . \tag{2.26}$$

This measures local order. One may also define a global order parameter, the helicity modulus, Υ. This measures the response of the phases to an imposed twist through the system, and is defined as the second derivative of the free energy with respect to such an infinitesimal twist, δ_μ, where $\mu = (x, y, z, ...)$ is the direction the twist is applied.

$$\Upsilon_\mu = \frac{1}{V} \frac{\partial^2 F[\delta_\mu]}{\partial \delta_\mu^2}\bigg|_{\delta_\mu = 0} . \tag{2.27}$$

Technically, this is done by imposing the twist in the phases of the spins

$$\theta_{\mathbf{r}} \to \theta'_{\mathbf{r}} = \theta_{\mathbf{r}} - \boldsymbol{\delta} \cdot \mathbf{r}, \tag{2.28}$$

then differentiating with respect to said twist. In the zero field XY model, this calculation results in

$$\begin{aligned} \Upsilon_\mu &= \frac{1}{N} \left[\left\langle \frac{\partial^2 H}{\partial \delta_\mu^2} \right\rangle - \beta \left(\left\langle \left(\frac{\partial H}{\partial \delta_\mu} \right)^2 \right\rangle - \left\langle \frac{\partial H}{\partial \delta_\mu} \right\rangle^2 \right) \right] \\ &= \frac{J}{N} \left[\left\langle \sum_{\mathbf{r}} \cos(\theta_{\mathbf{r}+\hat{\boldsymbol{\mu}}} - \theta_{\mathbf{r}}) \right\rangle \right. \\ &\qquad \left. - J\beta \left\langle \left(\sum_{\mathbf{r}} \sin(\theta_{\mathbf{r}+\hat{\boldsymbol{\mu}}} - \theta_{\mathbf{r}}) \right)^2 \right\rangle \right], \end{aligned} \tag{2.29}$$

where one may think of the first term as energy-like, while the second is current-like. This may of course be generalized to other models, as long as there is a U(1)-phase involved, see [1, 10, 11].

The zero field model exhibits a continuous phase transition in three dimensions. In two dimensions, the situation is different, as spontaneous breaking of a continuous symmetry in $D \leq 2$ is impossible, which we will describe in a later section.

2.3.3 First-order transitions

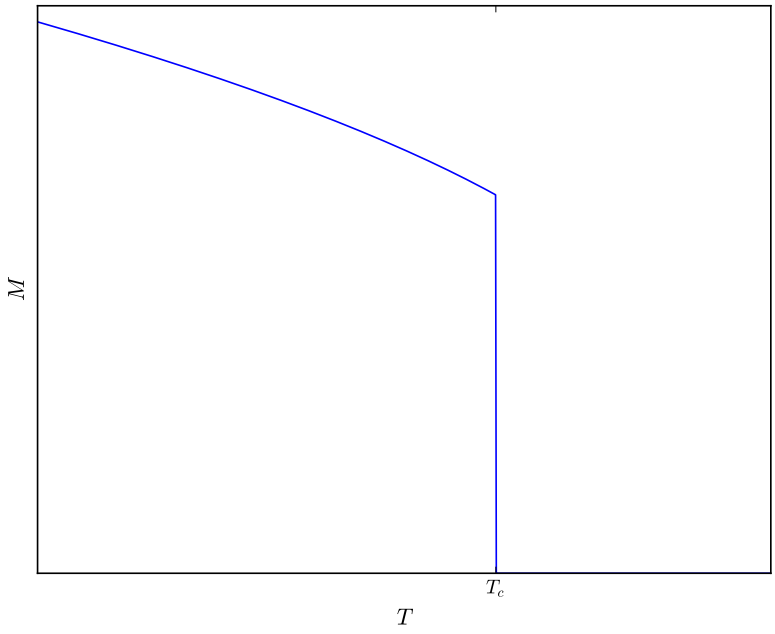

Figure 2.2: A schematic plot of the order parameter when passing through a first-order transition. At the critical temperature, the order parameter drops discontinuously to zero.

While a continuous phase transition is characterized by an order parameter which continuously approaches zero at the transition point, a first-

order transition is characterized by a discontinuous order parameter. A schematic plot of a typical order parameter in a first-order transition is shown in Fig. 2.2. Furthermore, in a first-order transition there will be a certain amount of work, or latent heat, that needs to be done in order to bring the system from one phase to the other. At the transition, there will be two coexisting phases, separated by an energy barrier[4]. This causes domains of one phase to coexist with domains of the other. This is often seen in everyday life; when water boils, bubbles of water vapor forms (domains of the high-temperature phase) in the water (domains of the low temperature phase), and more and more bubbles form as you apply more heat. In the language of Landau theory, adding a term $\propto M^3$ will make its phase transition first-order.

The term first-order transition stems from the fact that a first-order transition has a discontinuity in a first-order derivative of the free energy, for instance the magnetization. Continuous phase transitions are often called second-order transitions, as they have continuous first-order derivatives, but discontinuous second-order derivatives. For instance, the heat capacity or the magnetic susceptibility is typically discontinuous in a second order transition. This language is a remnant of Paul Ehrenfest's classification of phase transitions, where the type of transition is named after the lowest order derivative of the free energy which is discontinuous.

2.4 Universality and scaling laws

A profound concept in statistical mechanics is that of *universality classes*, the idea that widely different physical systems with phase transitions have critical properties that can be classified into a few categories. The universality classes are classified according to dimensionality of space, D, and the dimensionality of the order parameter describing the system, n. For instance, the uniaxial ferromagnet used in the example above, or in the Ising model, would have $n = 1$. A system with $n = 2$ could be a magnet

[4]This will be important to remember when looking for first-order transitions in numerical simulations.

with a hard axis, as opposed to the easy axis in the uniaxial magnet, such that the magnetization likes to point in the plane perpendicular to the hard axis. The magnetization can then be described by a two-component vector, like the XY model. A magnet without any preferred direction of magnetization, or an isotropic magnet, would have $n = 3$, which may be described by the Heisenberg model.

The beauty of universality classes is that some properties of systems which look very different at first glance, will be the same if they belong to the same universality class. For instance, the uniaxial ferromagnet and the critical point of the liquid-gas transition are both described by an order parameter with $n = 1$, belong in the same universality class, and have the same *critical exponents*. The critical exponent are the quantities that are universal within a given universality class. They describe the scaling properties of thermodynamic quantities as the critical point is approached. These scaling properties are succinctly expressed as six exponents. Four of which are related to thermodynamic quantities, α, β, γ, and δ, and two that are related to correlation functions, ν and η.

2.4.1 The exponents α, β, γ and δ

Deriving the thermodynamical exponents starts with realizing that, close to a critical point, the free energy can be written as a regular part and a singular part[5].

$$f(\tau, h) = f_R(\tau, h) + f_S(\tau, h). \tag{2.30}$$

Here, $f = F/V$ is the free energy per unit volume, $\tau = (T - T_c)/T_c$ is the reduced temperature, and h is some external field. We may assume we are discussing a magnetic system in an external magnetic field, for clarity. The critical point will then be at $(\tau, h) = (0, 0)$. Widom postulated that the singular part of the free energy obeys the relation

$$f_S(\lambda^a \tau, \lambda^b h) = \lambda f_S(\tau, h), \tag{2.31}$$

[5]This derivation loosely follows [5] and [6].

where λ is an arbitrary factor, and a and b are constants. If we choose $\lambda = |\tau|^{-1/a}$, we have

$$f_S(\tau, h) = |\tau|^{1/a} f_S\left(\frac{\tau}{|\tau|}, \frac{h}{|\tau|^{b/a}}\right). \tag{2.32}$$

The next part of the argument is to realize that $\tau/|\tau|$ may only take on two values, ± 1. Therefore, the right side may be written as two different functions of a single variable,

$$f_S(\tau, h) = |\tau|^{2-\alpha} \psi_{\pm}\left(\frac{h}{|\tau|^{\Delta}}\right). \tag{2.33}$$

Now we have defined the first critical exponent,

$$\alpha = 2 - 1/a, \tag{2.34}$$

as well as the *gap exponent*, $\Delta = b/a$. At a continuous phase transition, we know that the internal energy is well behaved, but the specific heat will have a singular behaviour. If we insert Eq. (2.33) into the definition of the specific heat, keeping in mind that we must take $h = 0$, we find the following scaling as $\tau \to 0$

$$c_V = -T\frac{\partial^2 f}{\partial T^2} \sim |\tau|^{-\alpha}. \tag{2.35}$$

Next, we may calculate the exponent related to the zero-field magnetization near T_c,

$$\begin{aligned} m\Big|_{h=0} &= -\left(\frac{\partial f}{\partial h}\right)\Big|_{h=0} \\ &= |\tau|^{2-\alpha-\Delta} \psi'_{\pm}(0). \end{aligned} \tag{2.36}$$

First of all, this tells us that $\psi'_{+}(0) = 0$, as the magnetization is zero for $\tau > 0$. Secondly, this gives us the scaling of the magnetization close to the

critical point, where one defines the exponent[6],

$$\beta = 2 - \alpha - \Delta. \tag{2.37}$$

The magnetic susceptibility defines the next exponent, it is given by

$$\begin{aligned} \chi &= \left(\frac{\partial m}{\partial h}\right)\Big|_{h=0} \\ &= |\tau|^{2-\alpha-2\Delta}\, \psi_{\pm}''(0). \end{aligned} \tag{2.38}$$

This defines γ as

$$\gamma = -2 + \alpha + 2\Delta. \tag{2.39}$$

The last thermodynamic exponent relates to the scaling of the magnetization at $\tau = 0$, but for finite h. We have

$$\begin{aligned} m\Big|_{T=T_c} &= -\left(\frac{\partial f}{\partial h}\right)\Big|_{T=T_c} \\ &= \lim_{\tau\to 0} |\tau|^{2-\alpha-\Delta}\, \psi_{\pm}'\left(\frac{h}{|\tau|^{\Delta}}\right). \end{aligned} \tag{2.40}$$

Now, the argument of $\psi_{\pm}$ tends to infinity as we approach T_c. Hence, if we assume that $\psi_{\pm} \sim (h/|\tau|^{\Delta})^{\kappa}$ in this limit, we have that

$$m\Big|_{T=T_c} = |\tau|^{2-\alpha-\Delta-\kappa\Delta}\, h^{\kappa}. \tag{2.41}$$

For m to be finite, we must have $\kappa = (2 - \alpha - \Delta)/\Delta$, and the last thermodynamic exponent, δ, is defined as

$$m\Big|_{T=T_c} = h^{1/\delta}, \tag{2.42}$$

with

$$\delta = \Delta/(2 - \alpha - \Delta). \tag{2.43}$$

[6]Not to be confused with the inverse temperature.

The observant reader has probably realized that the four exponents are not independent, as we started out with only two exponents a and b. By combining the four equations for the exponents, we find two relations between the four exponents, known as scaling laws.

$$\alpha + 2\beta + \gamma = 2, \tag{2.44}$$

$$\alpha + \beta(1 + \delta) = 2. \tag{2.45}$$

2.4.2 Correlation functions and the exponents ν and η

Correlation functions describe the correlations between the degrees of freedom of the model at a separation distance $r = \left|\mathbf{r} - \mathbf{r}'\right|$. In general we can write

$$G(\mathbf{r}, \mathbf{r}') = \langle \mathbf{s}_{\mathbf{r}} \mathbf{s}_{\mathbf{r}'} \rangle, \tag{2.46}$$

where $\mathbf{s}_i$ is for instance the Ising or XY spin of Section 2.2, or some other field variable. If we assume translational invariance, we have exponential decay of the correlation function for large r,

$$G(r) \sim \exp \frac{-r}{\xi}. \tag{2.47}$$

Here, we define ξ as the *correlation length*. The correlation function has a very different behaviour when comparing ordered and disordered phases. In the disordered phase, the field variables are completely uncorrelated, and the correlation function decays exponentially to zero. In the ordered phase, however, the correlation function will decay exponentially to a finite value. This is the manifestation of *long range order*.

At the critical point, the situation is even more interesting. Here, critical fluctuations occur across all length scales of the system. This means that the correlation length diverges, and it diverges according to a power law defined by

$$\xi \sim \tau^{-\nu}. \tag{2.48}$$

When this happens, the decay of the correlation function is reduced to a power law for large r[7],

$$G(r) \sim \frac{1}{r^{D-2+\eta}}, \tag{2.49}$$

where D is the dimensionality, and η is the final critical exponent called the *anomalous dimension*. The divergence of the correlation length means that there is no remaining relevant length scale at the critical point, aside from any lattice spacing, system size or similar scale. This means that the system is *scale invariant*, critical fluctuations occur on all length scales. Furthermore, at the critical point, all the properties of the system are determined by the universal exponents, and here lies the source of universality. It all depends on the dimensionality of space and the symmetry of the order parameter, the microscopic details of the system are irrelevant.

Finally, there are two relations between the thermodynamic exponents, and the ones defined from the correlation function. The first one follows from the fluctuation theorem, which relates the susceptibility to the correlation function at the critical point in the following way

$$\chi \sim \int \mathrm{d}^D r G(r). \tag{2.50}$$

If we insert the power law of Eq. (2.49) and assume that the only length scale present is the correlation length, we have

$$\begin{aligned} \chi \sim & \int^{\xi} \mathrm{d}r r^{D-1} \frac{1}{r^{D-2+\eta}} \\ \sim & \xi^{2-\eta} \\ \sim & \tau^{-\nu(2-\eta)}. \end{aligned} \tag{2.51}$$

Comparing this to the definition of γ, $\chi \sim \tau^{-\gamma}$, we have that

$$\gamma = \nu(2-\eta). \tag{2.52}$$

[7]But smaller than the correlation length.

The last relation, known as *hyperscaling*, is arrived at by realizing that the combination f_S/k_BT_C must have dimension $(\text{length})^{-D}$. And, the only length we know about close to the critical point is the correlation length. Therefore,

$$\begin{aligned}\frac{f_S}{k_BT_C} \sim & \xi^{-D} \\ \sim & \tau^{d\nu}.\end{aligned} \tag{2.53}$$

By using Eq. (2.33), we have our final relation[8]

$$2 - \alpha = \nu D. \tag{2.54}$$

2.5 The Ginzburg-Landau model

In all of the papers included in this thesis, the starting point is a continuum model described by a complex field, known as the *Ginzburg-Landau* model. It stems from realizing that the spatially homogeneous order parameter of Landau theory is not sufficient to accurately describe phase transitions, one must also account for spatial fluctuations. The simplest extension of Landau theory is to replace the magnetization M with a spatially varying, real valued, magnetization $m(\mathbf{r})$, and adding gradient terms to the Landau function, which now becomes a functional. In our case, however, we will always consider superfluid or superconducting order parameters with $\mathrm{U}(1)$ symmetry, and therefore need to express the model in terms of complex fields, $\psi(\mathbf{r})$.

The basic model which we will build on may be represented[9] as

$$H = \int \mathrm{d}^D r \left[\frac{1}{2m} \left| \boldsymbol{\nabla} \psi(\mathbf{r}) \right|^2 + \alpha \left| \psi(\mathbf{r}) \right|^2 + g \left| \psi(\mathbf{r}) \right|^4 + ... \right]. \tag{2.55}$$

[8] This final relation is not valid if $D > D_{\text{uc}}$, which is the *upper critical dimension* above which mean field theory is exact.

[9] I choose to use dimensionless fields and parameters here. In Paper I the model with a non-fluctuating gauge field is derived on the lattice from a dimensionful formulation.

Higher order terms are usually irrelevant, and terms of odd order are not allowed by symmetry in the cases we consider. The complex field may be written as an amplitude and a phase, both spatially varying, $\psi(\mathbf{r}) = |\psi(\mathbf{r})| \exp(i\theta(\mathbf{r}))$. Eq. (2.55) is invariant under global $\mathrm{U}(1)$ rotations of the phase θ,

$$\theta(\mathbf{r}) \to \theta(\mathbf{r}) + \varphi \ \forall \ \mathbf{r}. \tag{2.56}$$

An extension to this basic Ginzburg-Landau functional is to promote the global $\mathrm{U}(1)$ symmetry to a local symmetry. This means that the equations of motions are invariant under rotations of the phase θ, where the rotations themselves may depend on $\mathbf{r}$,

$$\theta(\mathbf{r}) \to \theta(\mathbf{r}) + \varphi(\mathbf{r}). \tag{2.57}$$

This is only possible, due to the derivative term, by adding a gauge field, $\mathbf{A}(\mathbf{r})$, which transforms in such a way that the total Hamiltonian is left invariant. If the gauge field transforms as

$$\mathbf{A}(\mathbf{r}) \to \mathbf{A}(\mathbf{r}) + \frac{1}{e}\boldsymbol{\nabla}\varphi(\mathbf{r}), \tag{2.58}$$

while θ transforms according to Eq. (2.57), the following Hamiltonian will be invariant under local $\mathrm{U}(1)$ transformations,

$$\begin{aligned} H = \int \mathrm{d}^D r \Big[\frac{1}{2m} \left|(\boldsymbol{\nabla} - ie\mathbf{A}(\mathbf{r}))\psi(\mathbf{r})\right|^2 + \alpha \left|\psi(\mathbf{r})\right|^2 + g \left|\psi(\mathbf{r})\right|^4 \\ + \frac{1}{2} \left(\boldsymbol{\nabla} \times \mathbf{A}(\mathbf{r})\right)^2 \Big]. \end{aligned} \tag{2.59}$$

Here, e is the charge, which represents the coupling strength between the matter field, $\psi(\mathbf{r})$, and the gauge field, $A(\mathbf{r})$.

2.5.1 Lattice regularization

Lattice models are very well suited for numerical simulations, as they are defined on a grid by construction. The Ginzburg-Landau model, however,

must be discretized in some way if one wants to apply numerical techniques to it. The basic scheme is to define the complex field and gauge field on a D-dimensional hypercubic lattice of sides L. That is, with $D = 3$ we take

$$\psi(\mathbf{r}) \to \psi_{\mathbf{r}}, \tag{2.60}$$

and

$$\mathbf{A}(\mathbf{r}) \to \mathbf{A}_{\mathbf{r}}, \tag{2.61}$$

where $\mathbf{r}$ now refers to the lattice vector $\mathbf{r} = \hat{\mathbf{x}} \cdot i + \hat{\mathbf{y}} \cdot j + \hat{\mathbf{z}} \cdot k + ...$ where $i, j, k, ... \in (1, ..., L)$, and $\hat{\boldsymbol{\mu}}$ is a unit vector in the $\mu = (x, y, z)$ direction. Derivatives must be replaced by lattice forward differences, $\partial_\mu \to \Delta_\mu$. If we are dealing with a covariant derivative, the forward difference must take this into account. The standard treatment is to make the replacement

$$\left(\partial_\mu - ieA_\mu(\mathbf{r})\right)\psi(\mathbf{r}) \to \frac{1}{a}\left(\psi_{\mathbf{r}+\hat{\boldsymbol{\mu}}} e^{-iea A_{\mathbf{r},\mu}} - \psi_{\mathbf{r}}\right), \tag{2.62}$$

where a is the lattice spacing. The integral must be replaced by a sum over all lattice sites

$$\int \mathrm{d}^D r \to a^D \sum_{\mathbf{r}}, \tag{2.63}$$

The Maxwell term is replaced by a lattice analogue

$$\frac{1}{2}\left(\nabla \times \mathbf{A}(\mathbf{r})\right)^2 \to \frac{1}{2a^2}\left(\boldsymbol{\Delta} \times \mathbf{A}_{\mathbf{r}}\right)^2, \tag{2.64}$$

where

$$\left[\boldsymbol{\Delta} \times \mathbf{A}_{\mathbf{r}}\right]_\mu = \sum_{\nu\lambda} \varepsilon_{\mu\nu\lambda} \Delta_\nu A_{\mathbf{r},\lambda}. \tag{2.65}$$

is the lattice analogue of the cross product

By applying the above recipes to Eq. (2.59), one may arrive at a lattice formulation of the continuum Ginzburg-Landau model. Transforming the quadratic and quartic terms is straightforward, simply replace the continuum field by the lattice analogue. The derivative term requires some massaging. If we use the covariant form of the forward difference, we may

write the term as

$$\frac{1}{2m}\int \mathrm{d}^D r\,|(\boldsymbol{\nabla}-ie\mathbf{A})\psi(\mathbf{r})|^2 \to \frac{1}{2ma^2}\sum_{\mathbf{r},\mu}\left|\psi_{\mathbf{r}+\hat{\boldsymbol{\mu}}}e^{-iea\mathbf{A}_{\mathbf{r},\mu}}-\psi_{\mathbf{r}}\right|^2. \quad (2.66)$$

Multiplying out, we have the following expression for the derivative term of the Hamiltonian, H_k,

$$H_k = \frac{1}{2ma^2}\sum_{\mathbf{r},\mu}\Big[\left|\psi_{\mathbf{r}+\hat{\boldsymbol{\mu}}}\right|^2+|\psi_{\mathbf{r}}|^2 - \psi_{\mathbf{r}+\hat{\boldsymbol{\mu}}}\psi^*_{\mathbf{r}}e^{-iea\mathbf{A}_{\mathbf{r},\mu}}-\psi^*_{\mathbf{r}+\hat{\boldsymbol{\mu}}}\psi_{\mathbf{r}}e^{iea\mathbf{A}_{\mathbf{r},\mu}}\Big]. \quad (2.67)$$

Here, we may first recognize that the two first terms in the bracket are actually the same[10]. We may also, by replacing the complex field by amplitudes and phases, identify the last term as a cosine. Hence, we have

$$H_k = \frac{1}{ma^2}\sum_{\mathbf{r},\mu}\left[|\psi_{\mathbf{r}}|^2-\left|\psi_{\mathbf{r}+\hat{\boldsymbol{\mu}}}\right||\psi_{\mathbf{r}}|\cos(\theta_{\mathbf{r}+\hat{\boldsymbol{\mu}}}-\theta_{\mathbf{r}}-eaA_{\mathbf{r},\mu})\right]. \quad (2.68)$$

Combining all this, we have the following lattice Hamiltonian

$$H = a^D\sum_{\mathbf{r}}\Big[-\frac{1}{ma^2}\sum_{\mu}\left|\psi_{\mathbf{r}+\hat{\boldsymbol{\mu}}}\right||\psi_{\mathbf{r}}|\cos(\Delta_\mu\theta_{\mathbf{r}}-eaA_{\mathbf{r},\mu}) + (b+\frac{D}{ma^2})|\psi_{\mathbf{r}}|^2+g|\psi_{\mathbf{r}}|^4+\frac{1}{2a^2}(\Delta\times\mathbf{A}_{\mathbf{r}})^2\Big], \quad (2.69)$$

where $\Delta_\mu\theta_{\mathbf{r}}=\theta_{\mathbf{r}+\hat{\boldsymbol{\mu}}}-\theta_{\mathbf{r}}$.

2.5.2 The London approximation

In many cases, the critical properties of a system described by a Ginzburg-Landau model is captured very well by phase fluctuations only (and gauge-field fluctuations, where applicable). Therefore, one often works in the

[10] Just shift the sum by one lattice constant in the first term.

London approximation, or phase-only approximation. This boils down to disallowing any fluctuation in the amplitude field, and fixing it to some value $|\psi_{\mathbf{r}}| = \rho \; \forall \; \mathbf{r}$. In this approximation, the potential becomes an unimportant constant, and we may reduce the Hamiltonian to the following simple form.

$$H = a^D \sum_{\mathbf{r}} \Big[- \frac{\rho^2}{ma^2} \sum_{\mu} \cos(\Delta_\mu \theta_{\mathbf{r}} - eaA_{\mathbf{r},\mu}) + \frac{1}{2a^2} \left(\Delta \times \mathbf{A}_{\mathbf{r}}\right)^2 \Big]. \quad (2.70)$$

In fact, this is equivalent to an XY-model, coupled to a gauge field.

2.6 Topological defects

Models that are symmetric under a group $\mathcal{G}$ also support non-perturbative objects known as topological defects[11]. In Z_2 symmetric models you find kinks (or domain points) in one dimension, domain lines in two dimensions, or domain walls in three dimensions. These are configurations where the spins point in one direction in one part of the system, and in the opposite in another part. These two domains of say up and down spins are then separated by a domain wall where the spins change direction. In Fig. 2.3, such a configuration is depicted. The domain line is emphasized with a dashed line.

Topological defects are a consequence of the field theory and its boundary conditions allowing solutions that are homotopically distinct.[12] A homotopy group in our context describes a mapping between n-dimensional spheres, S^n, and the manifold, M, of the boundary of physical space, denoted as $\Pi_n(M)$. If we take the one dimensional kink as an example, we have a mapping from the 0-dimensional sphere (simply two points $\{+1, -1\}$) onto itself (the boundary of one dimensional space is also a 0-dimensional sphere). The trivial configuration of having no kink corresponds to the trivial map, while the kink corresponds to twisting the order

[11] By non-perturbative I mean that they will never show up in perturbation theory.

[12] See [12] Chap. V.7 for a more thorough treatment and some references.

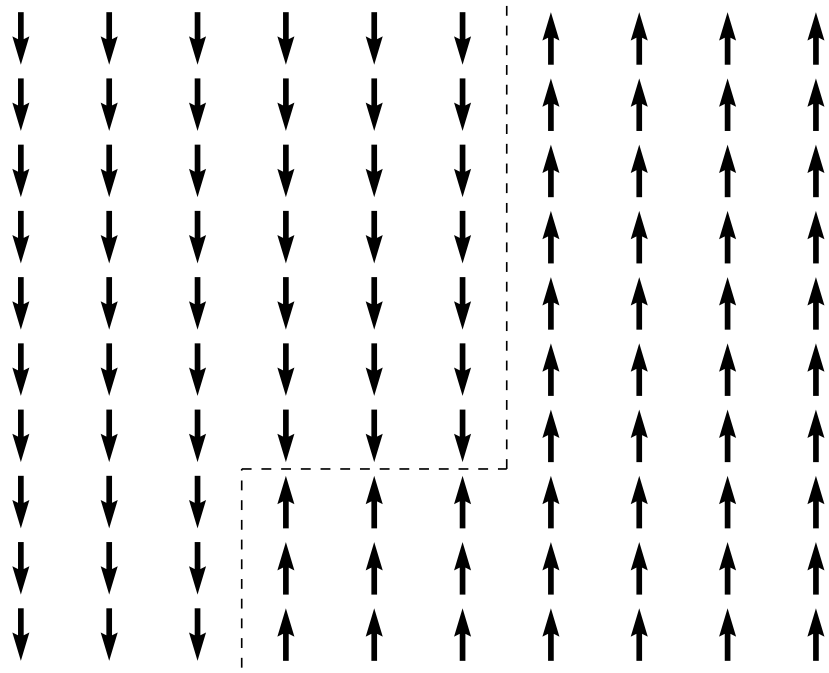

Figure 2.3: Example of a domain wall configuration in an $2D$ Ising model on a 10×10 lattice. The spins in the right part of the system point upwards, while the ones in the left point down. These two domains are separated by a wall where the spins change direction, indicated by the dashed line.

parameter from -1 to $+1$. You may also have an anti-kink with the opposite twist. The homotopy group in this case would be $\Pi_0(S^0) = \mathrm{Z}_2$, which shows that the kinks may have two different value for the topological charge (in addition to the trivial configuration of charge 0).

Now, if the order parameter has a higher symmetry, we will get other topological objects. For XY-spins in two or three dimensions the objects will be vortices or vortex lines, respectively. A single vortex configuration,

in the plane, is represented by the spins pointing radially outwards at spatial infinity, so that the spin winds around once as you trace around the vortex core. A vortex line is simply vortices stacked on top of each other. The homotopy group of these configurations are maps from S^1 to either S^1 or S^2, both of which are equal to $\mathbb{Z}$, the set of integers. Hence, vortices may have charges $\{\pm 1, \pm 2, \pm 3, ...\}$, corresponding to the number of windings of the spin as you go around the core counter-clockwise.

The energy of a single vortex may be approximated in two dimensions by the integral

$$E_V \sim \int_{r_0}^{R} \frac{\mathrm{d}r}{r} = \ln \frac{R}{r_0}, \tag{2.71}$$

where R is the system size, and r_0 is some lower cutoff, for instance the lattice spacing. It diverges logarithmically with system size, which means that a single vortex can not appear out of nowhere in the thermodynamic limit. It can not disappear either, which shows that it is a topologically protected object. If you somehow put a system into a single vortex configurations, it would cost an infinite amount of energy to unwind the vortex. There are two ways around this. First, vortices may appear in pairs of one vortex and one anti-vortex with the opposite winding. In this case the net winding at spatial infinity is zero, and the energy of the configuration will not diverge. This is relevant for the Kosterlitz-Thouless transition, which we tackle in Section 2.7. In three dimensions, similar arguments cause vortex excitations to always form closed loops rather than isolated lines.

The other 'solution' is to gauge the model: we may compensate for the energy cost of the vortex with the gauge field. If we consider a gauged two dimensional London model on the continuum (with units reinserted), we have the Hamiltonian

$$H = \frac{\hbar}{2m} \int \mathrm{d}^2 r \left(\boldsymbol{\nabla}\theta - e\mathbf{A} \right)^2 . \tag{2.72}$$

If we integrate $\boldsymbol{\nabla}\theta$ around a single vortex core in a closed contour, we find the vorticity

$$\oint_C \boldsymbol{\nabla}\theta \cdot \mathrm{d}\mathbf{l} = 2\pi n, \tag{2.73}$$

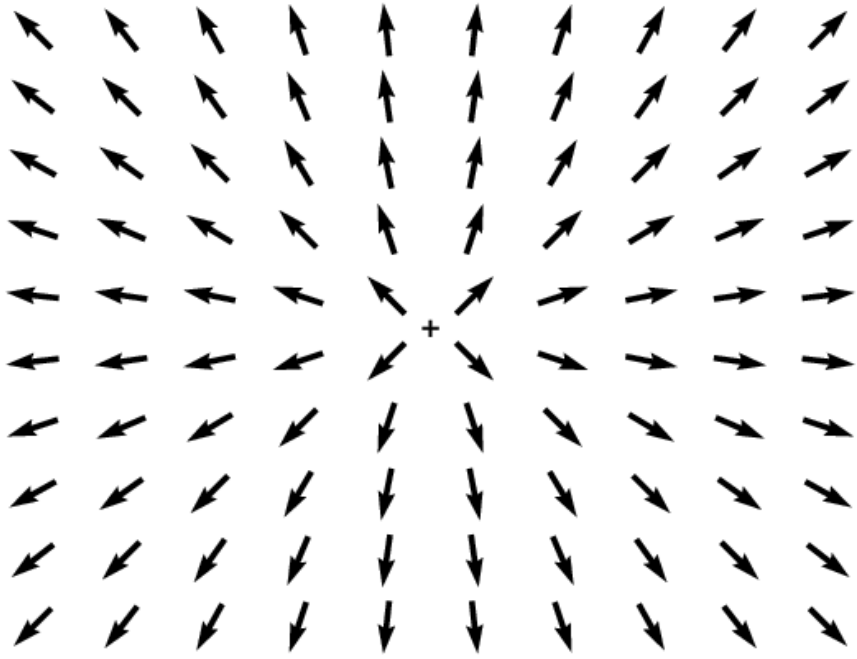

Figure 2.4: Example of a vortex configuration in an $2DXY$ model on a 10×10 lattice. The spins point radially outwards from the vortex in the center plaquette, denoted by the $+$ sign. If you move in a closed path counterclockwise around the vortex, the spins turn an angle 2π.

where n is the topological charge of the vortex. The energy of the vortex may now be cancelled out by having the gauge field in the configuration $\mathbf{A} \rightarrow \boldsymbol{\nabla}\theta/e$ at spatial infinity. This means that a vortex will carry a magnetic flux, Φ, equal to

$$\Phi = \hbar \oint_C \mathbf{A} \cdot \mathrm{d}\mathbf{l} = \frac{h}{e} n. \tag{2.74}$$

This is often written as $\Phi_0 n$, where $\Phi_0 = h/e$ is the magnetic flux quan-

tum. The interpretation of this is that vortices in models with *local* U(1) symmetry carry an integer number of magnetic flux quanta each.

The lattice model of Eq. (2.69) should also take vortices into account. With no gauge field, a vortex configuration on the lattice should have

$$\sum_{\mathbf{r},\mu\in C} \Delta_\mu \theta_{\mathbf{r}} = 2\pi n, \tag{2.75}$$

where C now is a closed contour going counter clockwise around a plaquette of the lattice. The vortices are now objects living on the plaquettes of the lattice. In order to find these vortices, we must demand that the sum of $\Delta_\mu \theta_{\mathbf{r}}$ around a plaquette is inside the primary interval of the phases, $\theta_{\mathbf{r}} \in [-\pi, \pi)$. In Eq. (2.75), n is then the number you have to add to the plaquette-sum of $\Delta_\mu \theta_{\mathbf{r}}$ to bring it back inside the primary interval. If you have a gauge field, you instead have to keep the sum of $\Delta_\mu \theta_{\mathbf{r}} - eA_{\mathbf{r},\mu}$ inside the primary interval.

2.7 The Kosterlitz-Thouless transition

A famous theorem known as the Mermin-Wagner-Hohenberg [13, 14] theorem states that a continuous symmetry can not be spontaneously broken in systems with two or fewer dimensions.

Even if no spontaneous symmetry breaking may occur, Kosterlitz and Thouless hypothesized that two-dimensional systems with continuous symmetries (like the two-dimensional XY-model) may still undergo a phase transition, dubbed a Kosterlitz-Thouless transition. They found that XY-spins in two dimensions, although they never exhibit long-range order for any finite temperature, will have what is known as quasi-long range order. This state is characterized by power-law decay of the correlations between spins, rather than exponential decay, as a disordered state would exhibit. Furthermore, they showed that the helicity modulus will have a discontinuous jump at the transition temperature [15, 16]. The mechanism behind this transition is vortex-driven. In the low-temperature phase, vortices will be confined to forming bound pairs of vortices and anti-vortices.

A single vortex will have a logarithmically diverging energy. In the high-temperature phase, these vortex anti-vortex pairs will disassociate, forming free vortices. In Fig. 2.5, two snapshots from a Monte-Carlo simulation of the $2DXY$ model is shown. The left hand panel shows the high-temperature phase, where individual vortices may move freely, while the right hand panel shows the low-temperature phase where they are bound in pairs.

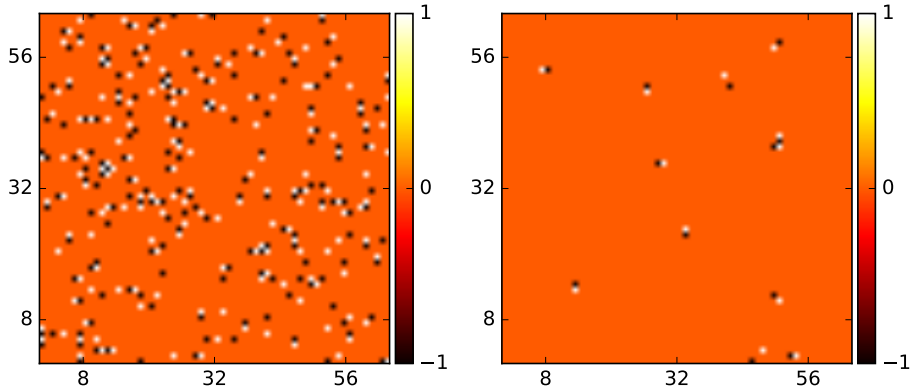

Figure 2.5: Monte-Carlo snapshots of the vorticity in a $2DXY$ model. The left panel shows a typical configuration above the KT critical temperature, where vortices are not bound in pairs, while the right panel shows that the vortices form bound pairs below the KT critical temperature.

Later, Halperin, Nelson and Young expanded on the ideas of Kosterlitz and Thouless to describe the melting transition of a two-dimensional solid [17–19]. This is known as the KTHNY-scenario, where a two-dimensional solid melts to a liquid through two KT-transitions where first quasi-long range translational order is restored, then orientational order. Like in the KT-transition of the XY-model, the two transitions of the KTHNY-scenario are driven by topological defects, known as dislocations and disclinations. Dislocations are extra rows of particles forced into a perfect periodic lattice. Disclinations are line defects that violates the orientational symmetry, basically they are single lattice points with one extra, or one fewer, nearest neighbour. In fact, an isolated dislocation is a pair of disclinations. The two KT-transitions are then driven by proliferations of first dislocations, which causes quasi-long range translational order to be lost, and then disclinations, which destroys the remaining orientational order.

In a two-dimensional solid, the particle-particle correlation function will have power law singularities, as opposed to δ-function singularities, at a set of reciprocal Bragg vectors, $\mathbf{G}$, corresponding to the periodicity of the lattice structure.

$$G(\mathbf{r}-\mathbf{r}') \sim |\mathbf{r}-\mathbf{r}'|^{\eta_{\mathbf{G}}(T)}. \tag{2.76}$$

The prediction of Halperin, Nelson and Young was that these correlations will follow a power law with a specific exponent, $\eta_{\mathbf{G}}(T)$, in the low temperature solid phase. The exponent will be dependent on temperature, and the magnitude of the Bragg vector. Specifically, as T approaches the melting temperature, T_m, from below (where quasi-long range order is lost), the exponent will approach a limiting value given by [18]

$$\begin{aligned}\eta^*_{\mathbf{G}} &= \lim_{T\to T_m^-} \eta_{\mathbf{G}}(T) \\ &= \frac{G^2a^2}{16\pi^2},\end{aligned} \tag{2.77}$$

where a is the lattice spacing. G^2a^2 will simply be a numerical factor, dependent on the lattice symmetry. For instance, for a hexagonal lattice

$\eta^*_{\mathbf{G}} = 1/3$ for the first-order peak. Hence, in order to classify a melting transition as a KTHNY-transition, one would measure the correlation function and determine the exponent, as a function of temperature. If the exponent approaches the limiting value at the melting transition, the transition may be identified as such. However, if the lattice melts before the limiting value is reached, then the transition is likely a first-order transition directly from the solid phase into the isotropic liquid phase. This would be a preemptive proliferation of *disclinations*. Several studies have been done on two-dimensional melting in various systems, and both first-order and KTHNY transitions has been found[20–27].

A third possible scenario, in the presence of a pinning potential[13], is a de-pinning transition from a commensurate solid into an isotropic liquid. This may happen, for instance, in a two-dimensional lattice superconductor in too high external fields [28–30], and would not conform to the KTHNY-scenario. If $\mathbf{M}$ is the smallest nonzero reciprocal-lattice vector common to both the pinning potential and the solid and $\mathbf{G}_0$ is the smallest reciprocal-lattice vector of the solid, one must have a sufficiently large ratio M^2/G_0^2 in order to have a KTHNY-transition in the presence of a pinning potential [18].

[13]This could be a substrate, or a numerical lattice grid,

CHAPTER 3

Monte-Carlo Simulations

This chapter will deal with Monte-Carlo simulations. What they are, why we use them, and how they work. Monte Carlo has been essential in answering questions about models in statistical mechanics (and in other fields as well) which are too complex to solve analytically. In the following we will go through the hows and whys of Monte-Carlo, in the context of spin models. Most of the material covered here may be found in [31].

3.1 The basics of Monte-Carlo simulations

As alluded to in Chapter 2, the brunt of the work in this thesis concerns calculating the partition function. Mean field theory and other approximations gets you quite a bit along the way, especially with determining ground state phase diagrams. However, phase transitions are notoriously difficult to pin down in the mean field approximation, simply because fluctuations are so important in this regime. For most models, other than the most basic like the Ising model in one or two dimensions, actually per-

forming the configuration sum of the partition function is impossible for arbitrarily large systems.

To remedy this, enter Monte-Carlo sampling techniques. The basic idea relies on the observation that, even though the configuration space is vast and exponentially increasing with system size, only a few[1] of the configurations make up the bulk of the sum in the partition function. Most configurations have a vanishingly small Boltzmann weight. Take for instance again the Ising model in zero field. At low temperatures the partition function is dominated by configurations with most of the spins aligned, while the configurations where the total magnetization is close to zero hardly contributes. By sampling mostly the configurations that "matter" one may approximate the real behaviour of the system at a given temperature with quite good accuracy.

In order to do this, one must first clearly define a scheme, or algorithm, that properly samples the configuration space. One must also carefully define the numerical error that inherently accompanies such a scheme, and properly consider the limitations and pitfalls introduced. In this chapter, we will go through the basic rules that must be fulfilled for any Monte-Carlo scheme to be valid.

Heuristically, we must construct a scheme consisting of the following steps

1. Draw a new random configuration from the space of all possible configurations.

2. Accept or reject the configuration according to some rule, which properly accepts the most important configurations.

3. Measure the physical observables relevant to the problem you want answered, this could be internal energy, specific heat, some type of order parameter (like magnetization), *etc.*

4. If sufficient statistics has been acquired, stop the simulation. If not, return to step one.

[1] A few compared to the total number of configurations, which is often enormous.

5. Calculate thermal averages of observables and properly estimate the associated numerical error.

This seemingly simple list introduces a few concepts that must be properly defined to make sure that the results of the simulation actually reflects the real behaviour of the model in question.

3.1.1 Monte-Carlo integration

The use of Monte-Carlo simulations to solve problems in statistical mechanics relies on the more general concept of Monte-Carlo integration. Say you want to integrate some terribly complicated function, $f(\mathbf{x})$, where $\mathbf{x}$ usually is a collection of a large number of degrees of freedom. Monte-Carlo integration is the process of estimating this integral by randomly sampling configurations $\mathbf{x}$ in the phase space and calculating the function value, $f(\mathbf{x})$. In mathematical terms we represent this estimate as

$$\int \mathrm{d}\Omega f(\mathbf{x}) \approx \Omega \bar{f}, \tag{3.1}$$

where Ω is the volume of phase space, and $\bar{f}$ is the mean of $f(\mathbf{x})$ evaluated at N randomly chosen points $\mathbf{x}_i$,

$$\bar{f} = \frac{1}{N} \sum_i f(\mathbf{x}_i). \tag{3.2}$$

Of course, if the integrand, $f(\mathbf{x})$, is dominated by some small area of phase space this is a terribly inefficient method of estimating the integral. And this is exactly the case when we deal with the partition function. To remedy this, we apply the concept of *importance sampling*. Instead of randomly picking the points, $\mathbf{x}_i$, we choose them according to some probability distribution, $p(\mathbf{x})$. Formally, this is equivalent to transforming the integral in the following way

$$\int \mathrm{d}\Omega f(\mathbf{x}) = \int \mathrm{d}p(\mathbf{x}) \frac{f(\mathbf{x})}{p(\mathbf{x})}, \tag{3.3}$$

where $\mathrm{d}p(\mathbf{x}) = \mathrm{d}\Omega p(\mathbf{x})$. In this case we may approximate the integral by

$$I \approx \frac{1}{N} \sum_i \frac{f(\mathbf{x}_i)}{p(\mathbf{x}_i)}. \tag{3.4}$$

The uniform sampling is then the special case of $p(\mathbf{x}) = 1/\Omega$.

To apply this to statistical mechanics we identify that the partition function is a multi-dimensional integral where $f(\mathbf{x}_i) \cong \exp(-\beta H[\Psi_i])$ and $\int \mathrm{d}\Omega \cong \int \mathcal{D}\Psi$. We also want to calculate expectation values of observables $\mathcal{O}$, in that case $f(\mathbf{x}) \cong \mathcal{O}\exp(-\beta H)/\mathcal{Z}$. If we use uniform sampling, the Monte-Carlo estimate of an expectation value would be

$$\langle \mathcal{O} \rangle \approx \frac{\sum_i \mathcal{O}[\Psi_i] e^{-\beta H[\Psi_i]}}{\sum_i e^{-\beta H[\Psi_i]}}. \tag{3.5}$$

However, a much more efficient scheme would be to use importance sampling with $p(\mathbf{x}) = p[\Psi]$, *i.e.* the canonical probability distribution, Eq. (2.1). In this case, the estimator for the expectation value of $\mathcal{O}$ simplifies to

$$\langle \mathcal{O} \rangle \approx \frac{1}{N} \sum_i \mathcal{O}[\Psi_i]. \tag{3.6}$$

The drawback is that we now have to create an algorithm that generates the values $\{\Psi_i\}$ from the canonical probability distribution, without knowing the normalization, the partition function itself. Remember, all the information about the thermodynamics of the system is contained in the normalization, $\mathcal{Z}$. Hence, if $\mathcal{Z}$ is known, one would not have to bother with Monte-Carlo simulations at all.

3.2 Markov-chain Monte-Carlo

In a Monte-Carlo simulation we want to draw random configurations from the probability distribution defined by the partition function in order to estimate the expectation value, or thermal average of some observable, $\mathcal{O}$.

Markov-chain Monte-Carlo is a scheme to stochastically generate chains of configurations according to a set of rules. The idea is to generate a chain of configurations, $X_1 \to X_2 \to ... \to X_N$ from the set of possible configurations $\{\Psi\}$, where the next configuration only depends on the previous. In fact, for it to be a proper Markov chain, the probability of moving from state Ψ_i to Ψ_j, $P(X_t = \Psi_i | X_{t+1} = \Psi_j) \equiv P(\Psi_i \to \Psi_j)$, in a step must be independent of the history of the chain. Furthermore, as these are probabilities, we require that

$$P(\Psi_i \to \Psi_j) \geq 0, \tag{3.7}$$

and

$$\sum_j P(\Psi_i \to \Psi_j) = 1. \tag{3.8}$$

The last equation simply means that we must end up somewhere in the configuration space when transitioning from state Ψ_i.

With these basic assumptions in mind, we may construct the probability, $p(X_t = \Psi_i)$, that the system is in state Ψ_i at step t in the Markov chain,

$$p(X_t = \Psi_i) = \sum_j p(X_{t-1} = \Psi_j) P(\Psi_j \to \Psi_i). \tag{3.9}$$

This may be thought of as a master equation for the Markov chain. The goal of our Markov-chain Monte-Carlo simulation of the statistical mechanics problem is for the probability of being in state Ψ_i at time t to approach an equilibrium probability. If this probability is the canonical probability distribution, $p[\Psi_i]$, we are indeed sampling the configurations from the correct distribution. That is, we must have $p(X_t = \Psi_i) = p[\Psi_i]$ for any t. Inserting this into the master equation, Eq. (3.9), and using Eq. (3.8), we have

$$\sum_j p[\Psi_j] P(\Psi_j \to \Psi_i) = \sum_j p[\Psi_i] P(\Psi_i \to \Psi_j). \tag{3.10}$$

This is known as the *balance condition*. It is common to use a more strict version of this condition, by demanding that Eq. (3.10) is satisfied term by term,

$$p[\Psi_j] P(\Psi_j \to \Psi_i) = p[\Psi_i] P(\Psi_i \to \Psi_j), \tag{3.11}$$

which is known as *detailed balance*.

In addition to detailed balance, one more condition must be fulfilled in order to properly approximate the partition function. Given a finite, but possibly very large, number of elements in your Markov chain, every point in the space of all possible configurations must be visited. This is known as *ergodicity*. This is important to fulfill, in order to avoid getting stuck in local energy minima, and to avoid improper sampling of the states in general.

3.2.1 The Metropolis-Hastings algorithm

Now we must define an algorithm which creates a Markov chain according to the canonical probability distribution. The simplest Markov-chain Monte-Carlo algorithm, the Metropolis-Hastings algorithm, relies on using the relative Boltzmann weight of the new configuration compared to the old as the probability to accept the new configuration. This automatically ensures that the configurations are picked from the actual probability distribution of the partition function, and that detailed balance is satisfied.

We may split the probability of transitioning from state Ψ_i to state Ψ_j into a product of two probabilities, one to select the new state, and one to accept it. That is,

$$P(\Psi_i \to \Psi_j) = P_S(\Psi_i \to \Psi_j) P_A(\Psi_i \to \Psi_j). \tag{3.12}$$

Generally, the selection probability is constructed to be symmetric,

$$P_S(\Psi_i \to \Psi_j) = P_S(\Psi_j \to \Psi_i). \tag{3.13}$$

In the Metropolis-Hastings algorithm, we make the choice of acceptance probability to be the ratio of the new probability weight to the old if the new weight is lower than the old, otherwise we accept the new state automatically. Mathematically, this reads

$$P_A(\Psi_i \to \Psi_j) = \min\left(1, \frac{p[\Psi_j]}{p[\Psi_i]}\right). \tag{3.14}$$

It is straightforward to realize that Eq. (3.14) satisfies detailed balance, by insertion into Eq. (3.11). If we insert Eq. (2.1) into Eq. (3.14), we have the simple expression

$$\begin{aligned} P_A(\Psi_i \to \Psi_j) &= \min\left(1, e^{-\beta(H[\Psi_j]-H[\Psi_i])}\right) \\ &\equiv \min\left(1, e^{-\beta\Delta E}\right). \end{aligned} \tag{3.15}$$

A single Monte-Carlo move following the Metropolis-Hastings algorithm is thus done in the following way:

1. From state Ψ_i, pick a new state Ψ_j.
2. Calculate ΔE.
3. Generate a random number, r, between 0 and 1.[2]
4. If $\log r \leq -\beta\Delta E$, accept the new state.

This already defines a very robust and flexible simulation scheme, but we will modify it slightly to optimize it for large-scale simulations. The Metropolis-Hastings algorithm was employed in all papers which includes results from numerical simulations.

3.2.2 Update schemes

So far, we have covered how to accept a proposed configuration, but not how to propose the new configuration. The Metropolis-Hastings algorithm relies on having a symmetric selection probability, $P_S(\Psi_i \to \Psi_j) = P_S(\Psi_j \to \Psi_i)$, but as long as this is fulfilled, we have some freedom to do this. If the model in question only includes nearest-neighbor interactions in your model, as the models considered in papers I-III, it is convenient to have a local update scheme as well. This means that you update each spin at a time, in succession[3]. One full round of attempting to update each spin

[2] To speed up the simulation, we generally generate all the random numbers needed in one go, and put it in an array.

[3] It is important to attempt to update each spin of your lattice, to fulfil ergodicity

of your lattice once, is called a single Monte-Carlo sweep. A big advantage of local updates is that ΔE only depends of the nearest neighbours of the spin you update. This makes the calculation more efficient, and it will be straightforward to make a simulation code that can run on parallel computer clusters.

The simplest way to update a single spin, just picking any random orientation of the spin, generally results in low acceptance rates. One way to avoid this is to restrict the space of possible updates (while still fulfilling ergodicity). For instance, with an XY-spin you might pick a new orientation that lies in some small interval around the initial orientation. This will greatly increase acceptance rates, as the new configuration will typically lie very close in energy to the old configuration. One caveat is that if you choose the interval too small, the configurations at different steps in your Markov chain might be highly correlated with the previously measured configuration. Hence, one must choose an interval that is small enough that acceptance rates are high, but still large enough to minimize statistical errors from correlation. We use this update scheme in all the Monte-Carlo backed papers.

3.2.3 Thermal equilibration

When a Monte-Carlo simulation is initialized, it is common to start with a completely random configuration. Chances are, this configuration will be no where near thermal equilibrium. If one were to measure observables from this point, one would essentially measure from the wrong state as the system evolves towards the true equilibrium, and statistical errors would be unnecessary large. To remedy this, one usually discards a number of initial Monte-Carlo sweeps before beginning to measure observables. This is known as thermalization, or thermal equilibration. By monitoring the internal energy of the system during thermalization as a function of Monte-Carlo time, one can make sure that the system has evolved to equilibrium if the internal energy has converged.

Fig. 3.1 shows a typical example of this, using the energy per spin, H/V at each Monte-Carlo step as a measure of convergence. Here we initialize a

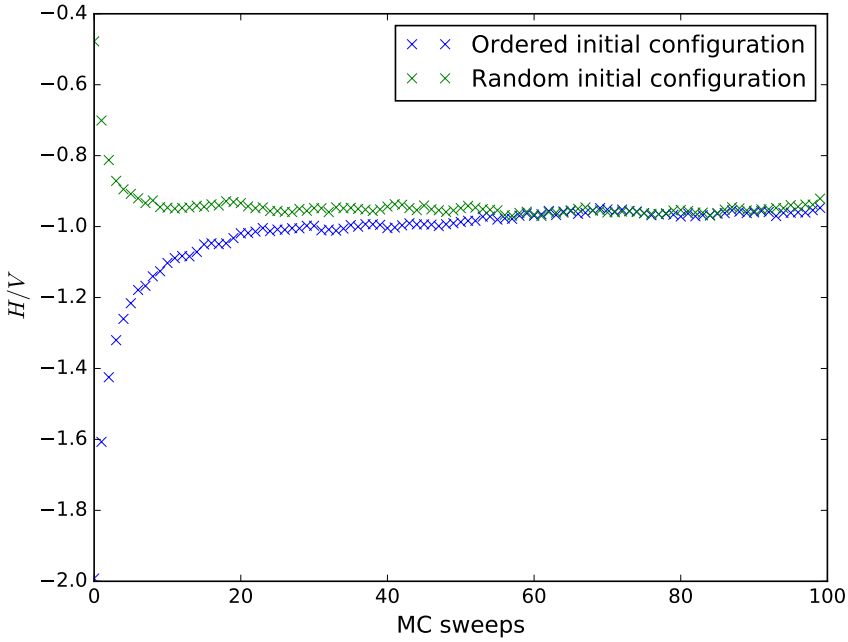

Figure 3.1: Monte Carlo time series of the configurational energy per spin for a $3D$ Ising model simulated on a 64^3 lattice, when starting from a completely ordered initial configuration and a random initial configuration. The energy quickly converges to the equilibrium value in both cases.

$3D$ Ising model at both a random configuration, and a completely ordered configuration on a lattice of $64 \times 64 \times 64$ spins. The random configuration lies at a higher energy than the equilibrium energy, while the ordered configuration lies at a lower energy, at this particular value of β. Both quickly relaxes to the equilibrium energy. The thermalization procedure evolves the system to the proper equilibrium state. It is important to thermalize long enough that the internal energy has converged, which in the case of

Fig. 3.1 occurs after roughly 60 Monte-Carlo sweeps. For more complicated models, the required number of sweeps before the system has relaxed to thermal equilibrium may be significantly higher.

3.3 Issues from finite sampling time and system size

As we perform the simulations on a computer, naturally, we are limited in some ways by finite resources. The simulation time, system size, and number of parameters we may simulate are all limited. This introduces some issues which must be dealt with, presented in the following.

3.3.1 Error estimation

During the Monte-Carlo simulations, we measure expectation values of different physical observables, $\mathcal{O}$. As shown above, one may estimate this by simply taking the arithmetic mean of the set of observables measured during the Monte-Carlo simulations. We say that one of these measurements is a measure step, and it is always performed at the end on a full Monte-Carlo sweep of the lattice. However, as we shall see below, one measure step is not necessarily taken after each Monte-Carlo sweep, we usually perform many Monte-Carlo sweeps before each measure step. Accompanying an estimate of any observables, we must have an estimate of its statistical error, otherwise it has little value. Given that the measurements, $\mathcal{O}[\Psi_i]$, are statistically independent, we may use the one standard deviation error estimate on the form

$$\sigma^2 = \frac{\langle \mathcal{O}[\Psi]^2 \rangle - \langle \mathcal{O}[\Psi] \rangle^2}{N-1}, \tag{3.16}$$

where N is the total number of measure steps.

The above estimate does not take into account that the configurations at subsequent measurements may be correlated. Say, in an extreme case, we were simulating the Ising model, and would measure the value of H after each proposed spin flip. In this case each configuration measured would

differ by a single spin, and would be highly correlated. But, even if we propose to update each spin once before measuring, the measurement could still be correlated. This is especially true if acceptance probabilities are low, for instance close to a critical point. To account for this we must estimate the *auto-correlation time*, τ_A, and modify the error estimate accordingly. In order to calculate τ_A, we define the auto-correlation function, $\varphi(t)$, which measures correlations between measurements separated by a number of measure steps, t. The auto-correlation function is defined as

$$\varphi(t) = \left(\sum_{i=1}^{N-t} \frac{\mathcal{O}[\Psi_i]\mathcal{O}[\Psi_{i+t}]}{N-t} - \langle \mathcal{O}[\Psi_i] \rangle^2 \right) \frac{1}{\langle \mathcal{O}[\Psi_i]^2 \rangle - \langle \mathcal{O}[\Psi_i] \rangle^2}. \quad (3.17)$$

If we assume that this function decays exponentially, we may define τ_A,

$$\varphi(t) \sim e^{-t/\tau_A}, \quad (3.18)$$

and we may estimate it by summing up the auto-correlation function

$$\tau_A \approx \sum_t \varphi(t). \quad (3.19)$$

Knowing τ_A, the error estimate of Eq. (3.16) is modified to

$$\sigma^2 = (1 + 2\tau_A) \frac{\langle \mathcal{O}[\Psi]^2 \rangle - \langle \mathcal{O}[\Psi] \rangle^2}{N-1}, \quad (3.20)$$

One may of course minimize the auto-correlation time by increasing the number of Monte-Carlo sweeps between each measurement step.

3.3.2 Critical slowing down

At a critical point, we have seen that the correlation length diverges. It turns out that the system will be highly correlated in time as well. This means that the auto-correlation time will diverge as well, which will worsen statistics at the critical point. In the real world this effect slows down the

dynamics of the system, hence the name critical slowing down. Close to the critical point, the auto-correlation time behaves as

$$\tau_A \sim \xi^z \sim |T - T_c|^{\nu z}, \tag{3.21}$$

where z is the model and algorithm dependent *dynamical critical exponent*. There are several algorithms that try to deal with these effects, called *cluster algorithms*, which base themselves upon updating a large number of spins at the same time. Just to name a few, some successful algorithms are the *Swendsen-Wang algorithm* [32] or the *Wolff algorithm* [33]. It is also worth mentioning the *worm algorithm* [34], while it is not considered a cluster algorithm, it still features non-local updates. All of these algorithms are useful because they have an almost zero dynamical critical exponent.

At a first order transition, a similar effect causes simulations to be increasingly difficult to handle, called exponential tunneling time. Here, we have the following behaviour at the transition point

$$\tau_A \sim e^{L^{D-1}}, \tag{3.22}$$

where L is the system size, and D is the dimensionality. The reason for this behaviour is the coexistence of phases that occurs at a first order transition. To properly sample the system at the transition, you need to sample configurations from both of the coexisting phases. The auto-correlation time may be thought of as the time the system uses to tunnel from one phase to the other. Here, we have the additional complication that the system becomes increasingly difficult to simulate as we increase the system size, which is the reason why first order transition may be hard to pin down.

3.3.3 Finite size scaling

Often, when simulating a statistical mechanics model, we want to determine what kind of phase transitions the model has. We want to find out if we are dealing with first- or second-order transitions, and what universality class they may belong to. In Chapter 2 we showed that certain quantities like the specific heat and magnetization have singularities governed by a

few critical exponents, which determine the model's universality class, as a second-order transition point is approached. We also showed that there exists a correlation length, ξ, which diverges according to $\xi \sim |T - T_c|^{-\nu}$ as we approach the critical point. In a Monte-Carlo simulation, we will be limited by the fact that we can not simulate systems in the thermodynamic limit, we have to define the model on a system of finite size. Typically, we use either a square or a cube with sides L. What this means is that, at the critical point, the correlation length will not diverge, but it will grow according to Eq. (2.48) until it reaches the limiting value of L. If we are sufficiently far away from the transition, $\xi \ll L$, and we may consider the system as if we are in the thermodynamic limit.

This may seem like a weakness of our finite system size, and will give rise to finite size effects if the system size is too small, but it may be exploited to determine the order and classification of the transition. This is known as *finite size scaling*. Quantities that would be singular at $T = T_c$, will instead be smoothed out across a critical region of size $|T - T_c| \sim L^{-1/\nu}$. This may be inserted into the definitions of the critical exponents to yield scaling laws for finite sized systems. For instance, the specific heat will scale as

$$c_v \sim L^{\alpha/\nu}, \tag{3.23}$$

and the magnetization in zero field as

$$m \sim L^{-\beta/\nu}. \tag{3.24}$$

The other scaling laws are straightforward to derive. To utilize this knowledge, one would perform simulations at a range of values for L, locate the transition point for each simulation[4], and fit this data to the appropriate scaling behaviour.

For a first-order transition, there is no true scaling in the same sense as for continuous phase transitions. However, it is still possible to verify a first-order transition by extracting the scaling exponent of the specific heat [35]. It can be shown that, in a first-order transition, the specific heat has

[4]For the specific heat this amounts to locating the peak of the curve.

the leading order behaviour

$$c_v \sim L^D. \tag{3.25}$$

That is, it has effective critical exponents $\alpha = 1$ and $\nu = 1/D$ [36, 37]. Another method is to measure the probability distribution of the internal energy per volume at the transition suspected to be first order [38, 39]. In a first-order transition, this histogram will have a bimodal distribution, where the two peaks are of equal height exactly at the transition point. The horizontal distance between the peaks relates to the latent heat released when going through the transition, and should therefore not scale with system size, so to remain finite in the thermodynamic limit. The vertical distance between the two peaks and the local minimum between them relates to the free energy barrier separating the two transitions. This barrier should increase with system size. The two peaks should grow, while the local minimum between them should be pulled downwards.

3.3.4 Re-weighting

A related issue to the above is that when performing Monte-Carlo simulations, we are necessarily restricted to simulating at a discrete set of inverse temperatures, β. This may make determining exact locations of critical points challenging, especially for strong first order transitions which will have sharp transitions. A solution to this is the concept of *re-weighting*. When we do a Monte-Carlo run, what we essentially do is measure a collection of samples of some observable, $\mathcal{O}$. These observables are drawn from the probability distribution defined in Eq. (2.1), at a given value of β. However, one would expect that this distribution changes very little if one were to change the inverse temperature by a small amount, $\beta \to \beta'$. The expectation value of $\mathcal{O}$ at β' is defined as

$$\langle \mathcal{O}(\beta') \rangle = \frac{\int \mathcal{D}\Psi \mathcal{O} e^{-\beta' H}}{\int \mathcal{D}\Psi e^{-\beta' H}}. \tag{3.26}$$

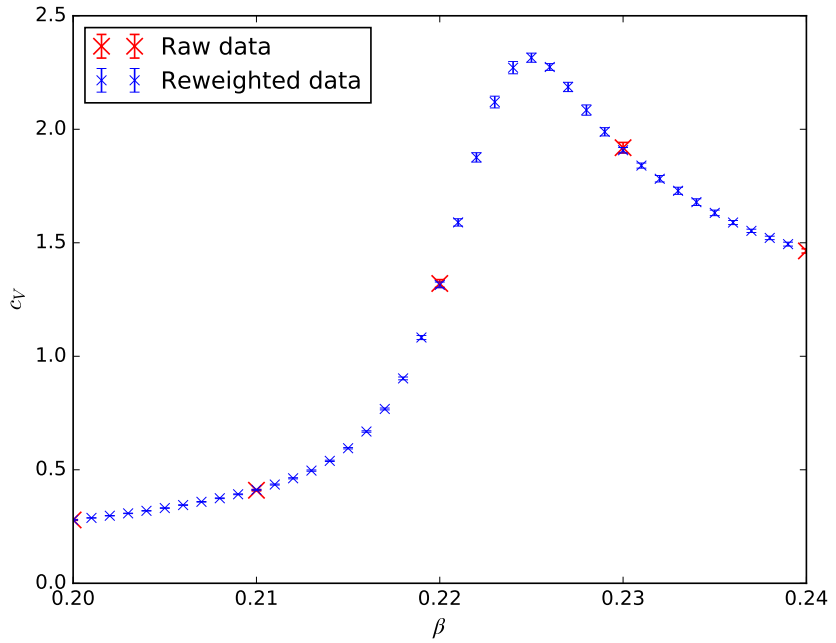

Figure 3.2: Specific heat capacity of the $3D$ Ising model on a 16^3 lattice calculated from raw and re-weighted data. The simulation was performed on the five β-values indicated by the red points, which was chosen to lie around the phase transition. Then, in post-processing, the blue points were calculated using multi-histogram re-weighting combining the data from the five simulated β-values. The re-weighted data captures the cusp of the specific heat curve nicely, even if we did not simulate exactly at these β-values. Notice how the error bars grow larger around the peak, as this is where the histogram overlap is smallest.

By multiplying each integrand by $1 = \exp -\beta H \exp \beta H$, we may re-express the expectation value as

$$\begin{aligned} \langle \mathcal{O}(\beta') \rangle &= \frac{\int \mathcal{D}\Psi \mathcal{O} e^{-(\beta'-\beta)H} e^{-\beta H}}{\int \mathcal{D} e^{-(\beta'-\beta)\Psi} e^{-\beta H}} \\ &= \frac{\left\langle \mathcal{O} e^{-(\beta'-\beta)H} \right\rangle_\beta}{\left\langle e^{-(\beta'-\beta)H} \right\rangle_\beta}. \end{aligned} \tag{3.27}$$

This means that you may calculate the expectation value of $\mathcal{O}$ at β' by calculating the expectation value of $\mathcal{O}e^{-(\beta'-\beta)H}$ and $e^{-(\beta'-\beta)H}$ in the ensemble at β. Using the Monte-Carlo estimator of Eq. (3.6) we see that this amounts to re-weighting the terms in the sum by a factor $\exp -(\beta' - \beta)H$. This simple technique is known as *Ferrenberg-Swendsen single-histogram re-weighting* [40]. There also exists a technique known as *Ferrenberg-Swendsen multi-histogram re-weighting* [41], which not surprisingly combines measurements taken from several different couplings to calculate the value of an observable at a set of new couplings. Fig. 3.2 shows an example of calculating the specific heat of the $3D$ Ising model, using multi-histogram re-weighting. A couple of caveats must be taken into consideration here. First of all, the efficiency of this method relies on the that histograms of H at β and β' overlap sufficiently, which basically amounts to having a sufficiently small separation between β' and β. Secondly, the calculation above assumes that the Hamiltonian does not depend on β explicitly.

3.4 Detecting a Kosterlitz-Thouless transition

In Section 2.7 we briefly discussed the consequences of the Mermin-Wagner-Hohenberg theorem for the XY-model. The question still remains: how do you actually detect a Kosterlitz-Thouless transition in a Monte-Carlo simulation? The defining characteristic is the behaviour of the helicity modulus, $\Upsilon = (\Upsilon_x + \Upsilon_y)/2$. At the critical inverse temperature of the KT-transition, β_{KT}, the helicity modulus has a discontinuous jump from a finite value to zero. Furthermore, the size of the jump multiplied by the critical coupling, $\beta_{\text{KT}}\Upsilon(\beta_{\text{KT}})$, has a universal value of $2/\pi$. The first method, proposed by Weber and Minnhagen [42], relies on a finite-size scaling of the helicity modulus. As the helicity modulus is a second derivative of the free energy, one must consider logarithmic corrections to it in two dimensions. Weber and Minnhagen found that these are on the form

$$\Upsilon(L) = \Upsilon(\infty)\left(1 + \frac{1}{2}\frac{1}{\ln L + C}\right), \tag{3.28}$$

as β_{KT} is approached from above. Therefore, the procedure is to calculate Υ for several system sizes, perform a fit of Υ for several values of β around the transition to the function Eq. (3.28), and determining which β provides the best fit. The value of $\Upsilon(\infty)\beta$ at the best fit may then be compared to the prediction of Kosterlitz and Thouless.

The second method, of Minnhagen and Kim [43] relies on an expansion of the free energy in the infinitesimal phase-twist defined in Eqs. (2.27) and (2.28), where Υ is the second-order derivative with respect to the twist. We expand the difference in the free energy as

$$F(\delta_\mu) - F(0) = \Upsilon_\mu \frac{\delta_\mu^2}{2!} + \Upsilon_{4,\mu} \frac{\delta_\mu^4}{4!}. \tag{3.29}$$

Where $\Upsilon_{4,\mu}$, known as the fourth-order modulus, is the fourth-order derivative of the free energy with respect to the phase twist in the μ-direction. Derivatives of odd order vanish due to symmetry. The argument is as follows. For the system is to be stable under the phase twist, Eq. (3.29) must be greater than or equal to zero. Then, if we observe that the fourth-order modulus is finite and negative at the critical point, in the thermodynamic limit, the helicity modulus *cannot* go continuously to zero at the critical point, while still keeping the free-energy difference positive. The procedure is then to measure $\Upsilon_4 = (\Upsilon_x + \Upsilon_y)/2$ around the critical point, where it will generally have a dip to a negative value, and do an extrapolation of the depth of this dip to $1/L = 0$. If this value is finite, there must be a discontinuous jump in Υ to ensure stability. In addition, one may also extrapolate the location of the lowest point of the dip to estimate the critical temperature. The convergence of the location is quite slow, however, so the first method is better suited to estimate β_{KT}. We use both the finite size scaling of Eq. (3.28) and the extrapolation of the depth of the dip in Υ_4 in Paper III.

CHAPTER 4

Bose-Einstein Condensates

This chapter will describe the motivation, and theoretical and experimental background for the largest part of this thesis. In papers I-III, we attempt to model a two-component Bose-Einstein condensate using a Ginzburg-Landau approach. I will here give a brief overview of the history of this phenomenon, describe the experimental setups in which it has been observed to motivate our theoretical and numerical work, and finally present the relevant models we have used in our simulations. Some reviews of this enormous subject can be found in Refs. [44–47]

4.1 History

The theoretical concept of Bose-Einstein condensation has existed for quite some time. Satyendra Bose developed a theory of the quantum statistics of light in 1924, which he sent to Albert Einstein. Einstein submitted the work of Bose for publication on his behalf [48], and extended the theory to matter in two later papers [49, 50]. This resulted in the concept of the

Bose gas, governed by Bose-Einstein statistics. Einstein also proposed that a non-interacting gas of bosons may, upon cooling, macroscopically occupy the lowest energy state. This was a new state of matter, now known as a Bose-Einstein condensate. It is characterized by a macroscopic fraction ρ_g/ρ where ρ_g is the density of particles in the ground state, and ρ is the total density of particles in the gas. For an ideal Bose gas[1] in three dimensions, this fraction can be shown to be

$$\frac{\rho_g}{\rho} = 1 - \left(\frac{T}{T_c}\right)^{3/2}, \tag{4.1}$$

where

$$T_c^{3/2} = \frac{\rho}{\zeta(3/2)} \left(\frac{h^2}{2\pi m k_B}\right)^{3/2}, \tag{4.2}$$

provided $T < T_c$. Here, m is the boson mass, and ζ is the Riemann zeta function. Above T_c, $\rho_g = 0$, and all particles reside in an excited state. Below T_c, a macroscopic number of particles occupy the ground state, and at $T = 0$ all particles will sit in the ground state.

In 1938, helium-4 was successfully cooled to a superfluid [51, 52], a liquid which has zero viscosity. London proposed that Bose-Einstein condensation was the mechanism for this phenomenon, as well as for superconductivity [53]. However, the theory of Einstein, and its extension by Bogoliubov only pertained to non- and weakly-interacting Bose gases, which superfluid helium is not. Because of the strong interactions in superfluid helium, the fraction of the bosons which are condensed is very low, so it was not possible to conclude that this was in fact a Bose-Einstein condensate. But, superfluidity is a property of Bose-Einstein condensates, so these phenomena are tightly related.

Experimental verification of a pure gaseous Bose-Einstein condensate came quite a bit later. In 1995, the group of Eric Cornell and Carl Wieman produced a Bose-Einstein condensate in a dilute gas of rubidium atoms [54]. In 2001, they received the Nobel Prize for this achievement, shared

[1] See for instance Ref. [7].

with Wolfgang Ketterle, who independently achieved Bose-Einstein condensation in sodium atoms [55]. Not long after the group of Hulet achieved condensation in a gas of lithium atoms [56]. Following these initial experiments, a vast amount of experimental work has been done. Gases with interactions tunable by Feshbach resonances has been achieved, mixtures of different isotopes, or of a single isotope in different hyperfine spin states has been Bose-Einstein condensed, superfluid vortices has been excited in Bose-Einstein condensates, and many schemes for producing optical lattice potentials has been developed. All of this makes cold atomic gases an incredibly exciting field, where many model systems may be realized in an experimental setup.

4.2 Experimental realization of a Bose-Einstein condensate in cold atomic gases

Since the first successful creation of a Bose-Einstein condensate in the lab there has been quite a lot of effort put into this field. As many of the results in this thesis attempt to explain previously observed phenomena in experiments, or more frequently to predict what might be observed, it is relevant to briefly discuss the different experimental setups and techniques used.

In order to create a Bose-Einstein condensate [57], one must cool down a cloud of bosonic atoms down below the transition temperature, which depending on the type and density of atoms used is on the order of a few hundred nK to a few μK. To accomplish this one first loads a magneto-optical trap with atoms. In this trap one performs an initial cooling to about 100 μK, well above the transition temperature. This first cooling procedure is done by exploiting the Doppler effect. By shining a laser on the cloud of atoms with a frequency slightly lower than the atomic transition frequency of the atom, the atoms traveling towards the laser source will have a higher chance of absorbing a photon and slowing down due to the absorbed momentum.

After the initial cooling, the gas is moved to a different magnetic trap, where it is pumped to a specific hyperfine spin state which is confined by

the trap. After pumping, it is cooled further below the critical temperature for condensation, by evaporative cooling [57, 58]. The principle here relies on using an oscillating magnetic field to transfer the most energetic atoms into a hyperfine state which is not confined by the magnetic trap, thereby removing them from the cloud and lowering the temperature of the cloud.

The versatility of atomic gases lies in the variety of ways one may tune inter-atomic interactions, add periodic lattice potentials with lasers, introduce vortices by rotating or stirring the gas, or even construct synthetic gauge fields. Combining these kinds of techniques allows you to realize a wide variety of condensed matter models in the lab. In the following we will go through some of the techniques that are relevant to the models studied in papers I-III.

4.2.1 Rotation, vortices and vortex lattices

A Bose-Einstein condensate also exhibits superfluidity, which has a few experimental manifestations. It has a critical velocity of collective excitations, below which the flow is dissipationless [59]. Furthermore, the condensate is coherent, it exhibits long-range correlations [60]. Finally, being a superfluid, it also supports topological vortex defects. By rotating the condensate, the angular momentum introduced into the gas manifests itself as quantized rotating vortices. This may be achieved either by introducing an elliptical deformation to the confinement potential and rotating the deformation [61, 62], or by 'stirring' it using a laser [63]. The former approach will allow the formation of vortex lattices with a large number of vortices, at sufficiently high rotation. The latter may be used to introduce a small number of vortices into the gas. A triangular lattice of a large number of vortices was first seen by Ketterle's group [64], but the triangular structure predicted by Abrikosov was first observed for a small number of vortices earlier [61].

4.2.2 Feshbach resonances

One of the aspects of cold atomic gases which makes them such versatile systems is the ability to manipulate interaction parameters, even during the experiment. A Feshbach resonance is a rather general phenomenon [65] that occurs in many-body systems, where a bound molecular state lies close to a scattering state. By tuning this energy difference using magnetic or optical fields, one may directly tune the s-wave scattering length, and therefore the inter-atomic interaction strength. Many of these resonances has been discovered in the alkali metals typically used in cold atom experiments[2].

4.2.3 Mixtures of atomic gases

A Bose-Einstein condensate created out of a single species is a very interesting system to study in its own right, especially when we add rotation-induced vortices. However, by mixing different species of atoms (hetero-nuclear mixtures), or mixing single-species atoms in different hyperfine states (homo-nuclear mixtures), quite a lot of new phenomena are revealed. The main reason being that you now have the opportunity to have interactions between the condensates, for instance density-density interactions which in turn influence inter-vortex dynamics or more exotic interactions like spin-orbit interactions. Another new phenomenon is phase separation, spatial segregation of the two condensates [67]. In the years since the first Bose-Einstein condensate was produced, both hetero-nuclear [68, 69] and homo-nuclear [70, 71] mixtures have been created. In the homonuclear mixtures, a rotation induced vortex lattice has also been created [72], wherein both hexagonal and square lattices were observed.

4.2.4 Optical lattices

So far we have discussed Bose-Einstein condensates that are trapped in some kind of harmonic potential, essentially making it a continuum system

[2] See [66] for a review and a comprehensive list of both optical and magnetic resonances.

where one oftentimes may describe the condensate with classical Ginzburg-Landau theories. Optical lattices [45], on the other hand, have been called quantum simulator, as they allow you to realize many quantum lattice Hamiltonians. By interfering laser beams, you may create a periodic potential for the atoms to move in. Essentially, you create an array, either 1D, 2D or 3D, depending on the setup, of many small harmonic traps. There has even been a proposal to create a synthetic four-dimensional optical lattice, by utilizing internal atomic states to create the fourth dimension [73].

4.2.5 Synthetic gauge fields

While cold atomic gases in themselves are already quite versatile in realizing a wide variety of condensed matter system, the charge neutrality of the atoms leaves more to be desired. A lot of interesting physics arises from the forces on charged particles in electromagnetic fields, for instance quantum Hall physics or the quantized vortices of a type-II superconductor. Quantized vortices may be induced in the neutral atomic gases by rotation, which may be thought of as a synthetic magnetic field in an extreme type-II superconductor, but this technique is limited by an upper critical frequency related to the trapping frequency. However, there is a tremendous amount of work done on realizing other types of synthetic gauge fields using optical lasers coupling to the internal states of the atoms in a space-dependent manner. A strong synthetic magnetic field was created using this technique [74], where quantized vortices were observed.

These techniques may also be used to create non-Abelian gauge fields, specifically spin-orbit couplings which couple a particles spin to its momentum. The same group created a synthetic spin-orbit coupling in a Rb^{87} gas [75] using lasers tuned to the internal Raman transitions of the atoms, which changes its spin. This corresponded to having equal Rashba [76] and Dresselhaus [77] spin-orbit coupling strengths. A similar technique was also used to create a synthetic spin-orbit coupling in a one-dimensional optical lattice [78]. There are also proposals to realize various spin-orbit couplings in optical lattices, by for instance driving the lattice with periodically varying magnetic fields [79], or using off-resonance lasers [80].

4.3 Theoretical models of Bose-Einstein condensates

In papers I-III, we attempt to model homo-nuclear mixtures of cold-atom Bose-Einstein condensates, by writing down a Ginzburg-Landau theory for each individual condensate. Building on Eq. (2.55), we have the base Hamiltonian given by[3]

$$H = \int \mathrm{d}\mathbf{r} \left[\frac{1}{2} \left| \boldsymbol{\nabla} \Psi \right|^2 + V(\Psi) \right]. \tag{4.3}$$

Here, Ψ is a two-component spinor of complex fields ψ_i, with $i = 1, 2$, which may be expressed further as an amplitude and a phase,

$$\psi_i = |\psi_i| \exp i\theta. \tag{4.4}$$

The index i is often referred to as a *color* index. The amplitude is associated with the density of condensate at $\mathbf{r}$, while the superfluid phase is associated with the superfluid velocity, $\mathbf{v}_i(\mathbf{r}) = \boldsymbol{\nabla}\theta_i(\mathbf{r})$. The spinor Ψ gives us a more compact notation, and gives rise to the sometimes used name of a spinor condensate. The potential V contains terms that respects the symmetries of the problem we are interested in. In general, assuming we have a U(1)-symmetry associated with rotations of the individual phases θ_i, we may write the potential as

$$V(\psi_i) = -\sum_i \alpha_i \left|\psi_i\right|^2 + \sum_{ij} g_{ij} \left|\psi_i\right|^2 \left|\psi_j\right|^2, \tag{4.5}$$

on component form. One could also add other, symmetry-breaking terms, to the potential. For instance a term $\psi_1\psi_2^* + \psi_1^*\psi_2$ would break the U(1) $\times$ U(1)-symmetry associated with rotating the individual phases down to a single U(1)-symmetry associated with rotating $\theta_1 + \theta_2$.[4]

In papers I and II we use a highly symmetric form of the potential, namely

$$V(\Psi) = \eta \left(\left|\Psi\right|^2 - 1 \right)^2 + \omega \left(\Psi^\dagger \sigma_z \Psi \right)^2, \tag{4.6}$$

[3] We suppress the $\mathbf{r}$ dependence in the fields $\psi_i(\mathbf{r})$ for brevity.

[4] This is applicable to multiband superconductors, as we will discuss in the next chapter.

or

$$V(\psi_1, \psi_2) = \eta \left(|\psi_1|^2 + |\psi_2|^2 - 1 \right)^2 + \omega \left(|\psi_1|^2 - |\psi_2|^2 \right)^2 . \tag{4.7}$$

on component form. This is simply a re-parametrization of Eq. (4.5), with $\alpha_1 = \alpha_2 = 2\eta$, $g_{11} = g_{22} = \eta + \omega$ and $g_{12} = \eta - \omega$, while also adding an unimportant constant. If we set $\omega = 0$, this Hamiltonian is symmetric under SU(2)-rotations of Ψ, while with finite ω it is symmetric under U(1)-rotations of each individual component ψ_i. In both cases, the model has an additional Z_2 symmetry corresponding to interchanging $\psi_1 \leftrightarrow \psi_2$.

In paper III, however, we use a more general form of the potential, Eq. (4.5) with the parametrization $\alpha_1 = \alpha(1 - \Delta)$, $\alpha_2 = \alpha(1 + \Delta)$, $g_{11} = g(1 - \gamma)$, $g_{22} = g(1 + \gamma)$, and $g_{12} = g\lambda$. This results in the form

$$\begin{aligned} V(\psi_i) = & -\alpha(1 - \Delta) |\psi_1|^2 - \alpha(1 + \Delta) |\psi_2|^2 \\ & + g(1 - \gamma) |\psi_1|^4 + + g(1 + \gamma) |\psi_2|^4 + 2\lambda g |\psi_1|^2 |\psi_2|^2 . \end{aligned} \tag{4.8}$$

This form is useful when you are want to describe a condensate with an imbalance in the quadratic term, parametrized by Δ, or in the quartic term, parameterized by γ. The potential of Eq. (4.8) is invariant under individual global U(1) rotations of each phase θ_i, but not under Z_2 transformations if Δ or γ is finite.

4.3.1 Rotating the condensate

In papers I and II, we want to model the effect of inter- and intra-component density-density interactions on rotation-induced vortices. The two density-density interactions present in Eq. (4.6) do not directly couple to the vortices, which are related to the phases of the condensate. However, the density-density interactions will affect the vortices indirectly through the gradient term $|\boldsymbol{\nabla}\psi_i|^2$. If we write the gradient out in terms of phases and amplitudes, we have

$$|\boldsymbol{\nabla}\psi_i|^2 = (\boldsymbol{\nabla} |\psi_i|)^2 + |\psi_i|^2 (\boldsymbol{\nabla}\theta_i)^2 . \tag{4.9}$$

The last term shows that having a lower amplitude at a point will lower the cost of having large gradients in the phase, which is exactly what occurs around a vortex. Hence, the vortices will interact through both inter- and intra-component short-range density-density interactions, as well as through long-range current-current interactions.

Now, in order to induce a net amount of vortices threading through the system, we need to apply some rotation. This is modelled by applying a gauge-field, however a non-fluctuating one[5], akin to Eq. (2.59). This modifies the gradient term of the Hamiltonian in the following way,

$$|\boldsymbol{\nabla}\psi_i|^2 \to |(\boldsymbol{\nabla} - i\mathbf{A})\,\psi_i|^2 \,. \tag{4.10}$$

$\mathbf{A}$ is related to the angular rotational velocity, $\boldsymbol{\Omega}$, through $\mathbf{A} \sim \Omega \times \mathbf{r}$. It is also important to note that when modelling a rotating condensate, one should in principle include a rotating trap potential coupling directly to the amplitudes. However, we choose to disregard this complication, as we only want to study the physics at the center of the trap.

In a Monte-Carlo simulation, you have a few options on how to implement the rotation, as you have some degree of choice stemming from gauge invariance. We choose to implement it in *Landau gauge*, which on the lattice is

$$\mathbf{A} = (0, 2\pi f x, 0), \tag{4.11}$$

where f is the number of vortices per plaquette, called the *filling fraction*, and x is the lattice coordinate in the x-direction. This introduces a constraint, $Lf \in \mathbb{N}$, due to the periodic boundary conditions. If one wants to relax this constraint, one might use *extended Landau gauge* [81].

4.3.2 Spin-Orbit coupling

Spin-orbit interactions are a generic class of interactions which couples a particle's momentum to its spin. It results in a momentum-dependent

[5] In the partition function language, this means that we do not integrate over $\mathbf{A}$.

splitting of the energy bands of particles with different spin, and it generally arises from a broken inversion symmetry of the crystal lattice in condensed matter systems. In the following we consider a two-dimensional system, as the particular type of spin-orbit coupling we consider only couples to k_x and k_y in the plane. One could of course imagine having a three-dimensional system where each layer has an internal spin-orbit coupling, but no inter-layer coupling arising from the spin-orbit coupling. One might also construct a spin-orbit coupling that is isotropic in k_x, k_y, and k_z. This is called a Weyl spin-orbit coupling [82].

In a single-particle description of a two-level system, we may express a spin-orbit operator in a general way like the following

$$\mathcal{H}_{\text{SO}} = \alpha\sigma_x k_y + \beta\sigma_y k_x. \tag{4.12}$$

More specifically, one may have a Rashba-type coupling [76] with $\alpha = -\beta$, or a Dresselhaus-type coupling [77] with $\alpha = \beta$. In addition to the spin-orbit coupling, we add a kinetic term and a Zeeman splitting, making the full operator

$$\mathcal{H} = \frac{k^2}{2m} I - \Delta\sigma_z + \mathcal{H}_{\text{SO}}, \tag{4.13}$$

where Δ is the strength of the Zeeman field, m is the particle mass and I is the identity matrix. The spectrum of Eq. (4.13) may be solved exactly, yielding

$$E_{\pm} = \frac{k^2}{2m} \pm \sqrt{\Delta^2 + \alpha^2 k_y^2 + \beta^2 k_x^2}. \tag{4.14}$$

Now we simplify to $\alpha^2 = \beta^2 \equiv \kappa^2$. In this case we have two different solutions in the lower $(-)$ band, depending on the strength of the Zeeman field. For not too high values of Δ, we have

$$k^2 = \kappa^2 m^2 - \frac{\Delta^2}{\kappa^2}. \tag{4.15}$$

However, if Δ is larger than a critical value, given by $\Delta \geq \kappa^2 m$, we have $k^2 = 0$. Fig. 4.1 shows a one dimensional cut of the lowest energy band

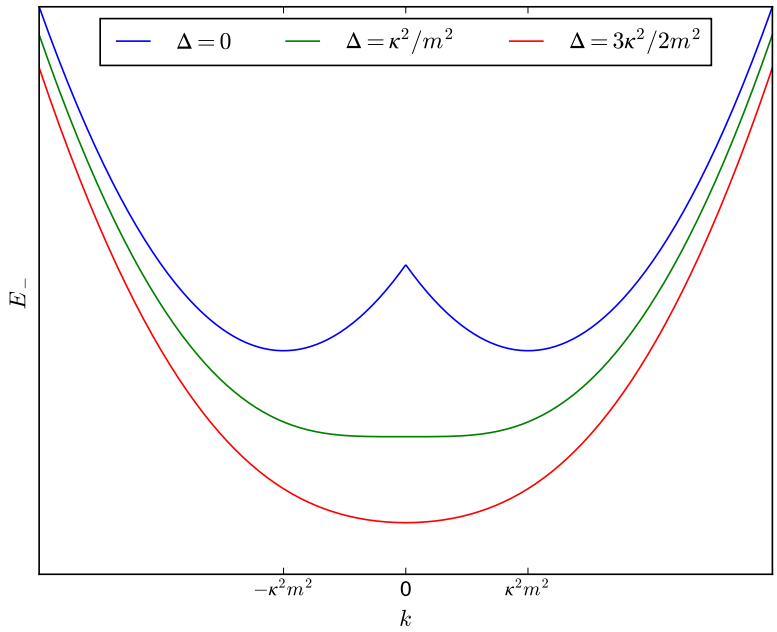

Figure 4.1: Energy of the lower band of a non-interacting two-level system with spin-orbit coupling, Eq. (4.13), for three different values of the Zeeman field, Δ. The blue curve shows $\Delta = 0$, where the band has two minima at finite momentum. The green curve shows $\Delta = \kappa^2/m$, which is the critical value of Δ where the two minima at finite momentum merge into one. Finally, the red curve shows $\Delta = 3\kappa^2/2m$, quite a bit above the critical Zeeman field.

for three different values of Δ, exemplifying the minima at finite momenta which merges into one as Δ is tuned above the critical value. Eq. (4.15) shows that the lower energy band is degenerate, the minimum can lie anywhere on the circle with radius k. However, if we were to define the non-interacting model on a lattice, and go through the same exercise as above,

one would find instead four degenerate minima at $(\pm k_0, \pm k_0)$ where

$$k_0 = \arcsin\left(\sqrt{\left[1-\left(\Delta/4\kappa^2 m\right)^2\right]/\left[1+1/2\kappa^2 m^2\right]}\right), \tag{4.16}$$

provided $\Delta < 4\kappa^2 m$ [83]. As for the continuum model, $\Delta \geq 4\kappa^2 m$ gives a single minimum at the origin.

For the Ginzburg-Landau description, we may write the general formulation of the spin-orbit coupling in the following way.

$$H_{\text{SO}} = \frac{i}{2}\int \mathbf{dr}\Psi^\dagger \left[\frac{\alpha+\beta}{2}\boldsymbol{\sigma}\cdot\boldsymbol{\nabla} + \frac{\alpha-\beta}{2}\left(\boldsymbol{\sigma}\times\boldsymbol{\nabla}\right)\cdot\hat{\mathbf{z}}\right]\Psi + \text{h.c.} \tag{4.17}$$

In paper III, we use this formulation with $\alpha = -\beta = \kappa$, resulting in

$$H_{\text{SO}} = \frac{i\kappa}{2}\int \mathbf{dr}\Psi^\dagger\left(\left(\boldsymbol{\sigma}\times\boldsymbol{\nabla}\right)\cdot\hat{\mathbf{z}}\right)\Psi + \text{h.c.}, \tag{4.18}$$

or on component form

$$H_{\text{SO}} = \frac{\kappa}{2}\int \mathbf{dr}\left[\psi_2^*\partial_x\psi_1 - \psi_1^*\partial_x\psi_2 + i\psi_2^*\partial_y\psi_1 + i\psi_1^*\partial_y\psi_2\right] + \text{h.c.}, \tag{4.19}$$

which is a pure Rashba-type spin-orbit interaction. This Hamiltonian will break the $\mathrm{U}(1)\times\mathrm{U}(1)$ symmetry arising from global rotations of each individual phase down to a single $\mathrm{U}(1)$ symmetry associated with rotating θ_1 and θ_2 the same amount. This may be viewed as a $\mathrm{U}(1)$ symmetry associated with rotating the composite phase $\theta_1+\theta_2$.

4.4 Main results of papers I-III

Here I will present the main results of papers I-III. Papers I and II deal with the same model of a two-component Bose-Einstein condensate in three dimensions, under rotation, wherein its phase diagram and phase transitions are explored. Paper I discusses the coexisting regime ($\omega \geq 0$), where both condensates are always present, while paper II discusses the regime where

phase separation is possible ($\omega < 0$). In paper III we deal with a similar model of a two-component condensate, now in two dimensions without rotation, but with spin-orbit coupling. Again we examine the phase diagram and phase transitions of the model.

4.4.1 Papers I and II

In these works [1, 2], we studied the effects of inter-component density-density interactions on the rotation-induced vortex lines in a two-component Bose-Einstein condensate in three dimensions. The full continuum Hamiltonian used was

$$H = \int \mathrm{d}^3 r \Bigg[\sum_i \frac{1}{2} \left| (\boldsymbol{\nabla} - i\mathbf{A})\, \psi_i \right|^2 + \eta \left(|\psi_1|^2 + |\psi_2|^2 - 1 \right)^2 + \omega \left(|\psi_1|^2 - |\psi_2|^2 \right)^2 \Bigg], \tag{4.20}$$

where $\mathbf{A} = (0, 2\pi f x, 0)$. As we have two condensates, and therefore two kinds of vortices, the density-mediated interactions between the two kinds of vortices allow for a much richer phase diagram than if we only had a single-component condensate. As described above, in Section 4.3.1, repulsive or attractive inter-component density-density interactions can be directly translated to repulsive or attractive inter-component vortex-vortex interactions. In the parametrization used in these papers, Eq. (4.7), the parameter ω represents the ratio between inter- and intra-component interaction strengths. A positive value of ω means the intra-component interactions dominates, while a negative ω means inter-component interactions dominates. The parameter η appears in front of the term $\left(|\Psi|^2 - 1 \right)^2$, and constrains overall fluctuations of the amplitudes, and must be positive to ensure stability. If $\omega < \eta$ the inter-component interactions are repulsive, and if $\omega > \eta$ they are attractive. Consequently, there are two types of interactions that affect the type of vortex matter we find. On the one hand, we have the inter-component density-density interactions, which are short-range and can be either attractive or repulsive. On the other hand, we have

the intra-component vortex-vortex interactions, which are always repulsive, long-ranged and isotropic.

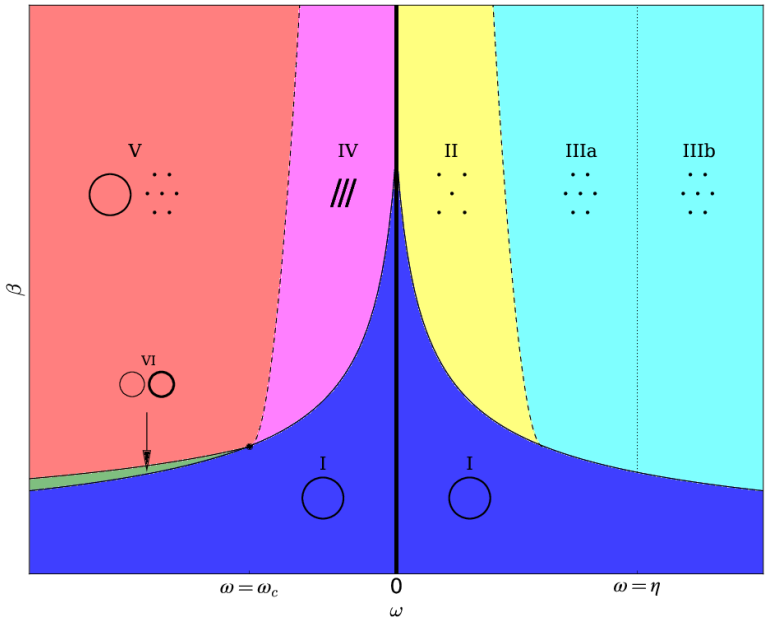

Figure 4.2: Schematic phase diagram of the two-component rotating Bose-Einstein condensate in three dimensions in the $\omega - \beta$ plane, as η and f is held fixed. We typically used $\eta = 5.0$ and $f \in 1/16, 1/32, 1/64$. Varying f or η will alter the details of the phase diagram. The x-axis then represents tuning the ratio between inter- and intra-component coupling strength from inter-component dominated on the left-hand side to intra-component dominated on the right hand side. The solid black line down the middle represent the line where they are equal, and also the line where SU(2)-symmetry is in effect. The nature of the different regions is described in the text.

These initial reflections pave the way to understand the phase diagram of the vortex matter introduced into the condensate by the rotation, shown in Fig. 4.2. Here we show the phases found in Monte-Carlo simulations, in the $\omega - \beta$ plane with η and f fixed to some generic value. Altering f or η will change the details of the phase diagram, but not the qualitative features, provided $\eta > 0$ and f is finite and not too large. Let us first discuss $\omega > 0$, the regime where intra-component interactions dominates, which corresponds to the right half of Fig. 4.2. Here, both condensates will be present for all parameter values that make physical sense. First of all, for high temperatures, both condensates will be in a vortex liquid phase, characterized by a ring-shaped vortex structure factor. This is region I in the phase diagram, colored in blue. As we cool down the condensates, the vortices will freeze into a floating solid[6], the exact nature of which depends on the value of ω. In a single-component condensate, the vortices freeze into a hexagonal vortex lattice when only influenced by the isotropic vortex-vortex interactions, now the interactions may alter that. Let us start out on the far right side of the phase diagram, where $\omega > \eta$. In this region we find a hexagonal vortex lattice in each component, where one vortex of component one is always co-centered with a vortex of component two. This is because the inter-component interaction is attractive. No energy is gained from deviating from the hexagonal lattice structure. If we lower ω slightly below η, we are in the regime with repulsive inter-component interactions. For not too low values of ω, we still find two hexagonal lattices, but they are no longer co-centered. The repulsive density-density interactions cause the vortices to avoid each other, however slightly. The states characterized by two hexagonal vortex lattices are colored cyan in the phase diagram, and are labeled IIIa and IIIb. Region IIIb refers to the co-centered vortices, while IIIa is the region where the vortices are intercalated.

For even lower values of ω, we find that the two vortex lattice assume a square symmetry, and that they are completely intercalated with each other, *i.e.* a vortex of type one will not overlap with a vortex of type two.

[6]We assume that f is low enough that we do not encounter a pinned solid for the values of β considered here.

This is because of, for this parameter range, the density-density interactions between component one and two are highly repulsive, causing the amplitudes of the individual components to be staggered with respect to each other. This staggering is most efficiently achieved in a square lattice, hence the symmetry of the vortex lattice. This in turn causes the vortices to avoid each other as they will seek the areas of low amplitude of their respective components. The square vortex lattice is less efficient than a hexagonal lattice at maximize the inter-vortex distance of each individual component, but this extra cost in energy is gained back in lowering the inter-component density-density interaction energy. The square lattice symmetry is therefore a compromise between lowering the energy from the potential, and lowering the vortex-vortex interaction energy. This region of the phase diagram is labeled II in Fig. 4.2, and is colored yellow. We find that the thermal phase transitions from region I into region II, IIIa, and IIIb show strong first order characteristics.

A final feature of the $\omega > 0$ part of the phase diagram is the shape of the demarcation line between region II and IIIa. In paper I we describe a structural transition between square vortex lattices into hexagonal lattices as the temperature is lowered. This, we argue, is because the vortex lattices become "stiffer" as the temperature is lowered, and therefore more prone to forming a hexagonal lattice. In other words, the cost of not maximizing the inter-vortex distance grows as temperature is lowered. Therefore, the vortex structure gradually evolves from a square symmetry to a hexagonal symmetry for certain values of ω.

The line $\omega = 0$ was also examined in paper I. Here, the model has a higher symmetry than when $\omega \neq 0$, namely $\mathrm{SU}(2)$ as opposed to $\mathrm{U}(1) \times \mathrm{U}(1)$. What this means, in terms of density-density interactions, is that the potential *only* contains the term proportional to $\left(|\Psi|^2 - 1\right)^2$. This is rather special, as only the total amplitude $|\Psi|^2 = |\psi_1|^2 + |\psi_2|^2$ is constrained, it costs no energy to shift amplitude from component one to component two as long as the sum of the two amplitudes is left unchanged. This in turn causes large fluctuations in the individual amplitudes. In terms of the vortices, this means that they may be unwound freely by letting the amplitude

of the associated component drop to zero. They are no longer topologically protected. However, as we force a net amount of flux through the system with the rotation, we will always have a fixed number of vortices in the system. As we describe in paper I, the main effect of this is to create a new phase where the helicity modulus is finite along the axis of rotation, without an accompanying vortex lattice. This is rather peculiar, as a finite phase coherence along the axis of rotation signals a vortex solid phase in conventional superfluids. We argue that this is directly caused by the large amplitude fluctuations, they allow for movements of entire straight vortex lines, which in turn causes the thermal averages of the vortex density to look like a vortex liquid. At a lower temperature, these collective movements of the vortex lines cease, and a number of interesting vortex structures appear.

Now we turn to the left hand side of the phase diagram shown in Fig. 4.2, which we explored in paper II. Here, the behaviour is largely described by the competition between inter-component density-density interactions wanting to deplete one of the condensates, and the isotropic vortex-vortex interactions' tendency to maximizing the inter-vortex distance. Firstly, we again find a two-component vortex liquid phase for high temperatures, labeled as region I and colored blue. For small but negative values of ω and lower temperatures, we find that the vortices form a striped lattice and are staggered between component one and two. The reason for this can be understood in light of the above-mentioned competition between density-density interactions and vortex-vortex interactions. The density-density interaction would like one amplitude to be completely suppressed, which would also put the vortices of that component in a liquid phase. However, this is at odds with the phases' wish to be ordered at this temperature, with the vortices spread out evenly, maximizing the inter-vortex distance. The response to this competition is to form stripes in the amplitudes, alternating between high and low values staggered between the two components. The vortices then arrange themselves in the low-amplitude stripes of their respective components, and maximize the inter-vortex distance within that stripe. This does not break the Z_2 symmetry that stems from swapping component one with component two. This state is labeled region IV in

Fig. 4.2, and is colored magenta. We find strong indications of a first order transition going from region I to region IV in the phase diagram. As we lower ω further, we find that one of the condensates is completely depleted as the temperature is lowered. This does break the Z_2 symmetry, and effectively reduces the model to a single component condensate. As we lower the temperature further, the vortices in the condensate that is not depleted freeze into a floating solid with hexagonal symmetry, and the minority component remains in a vortex liquid state. In this case, the energy gained from having a uniform vortex distribution is not enough to prevent one of the condensate amplitudes from depleting. We find these two transitions, the breaking of the Z_2 symmetry and the freezing of the majority component, to be separated by a small interval in β. This is reflected in Fig. 4.2, where region VI, colored green, is the phase where Z_2 is broken, but the majority condensate is still in a vortex liquid phase, making this an imbalanced vortex liquid. Region V, colored in red, represents the phase where the majority component has entered a floating solid phase. The black dot at $\omega = \omega_c$ marks the splitting of the Z_2 transition and the freezing of the lattice. We do not rigorously determine the nature of two transitions going from region I to region V via region VI, but on symmetry grounds one would expect the transition from region I to VI to be an Ising-transition, while the transition going from region VI to region V is a first-order transition associated with the freezing of the lattice.

4.4.2 Paper III

In paper III [3] we examined a two-component Bose-Einstein condensate in two-dimensions, now without rotation, but with spin-orbit coupling. We also used a different parametrization of the potential, the full Hamiltonian

we used was

$$H = \int \mathrm{d}^2 r \Bigg[\frac{1}{2} |\boldsymbol{\nabla}\psi_i|^2 - \alpha(1-\Delta)\,|\psi_1|^2 - \alpha(1+\Delta)\,|\psi_2|^2 + \frac{\kappa}{2}\left(\psi_2^*\partial_x\psi_1 - \psi_1^*\partial_x\psi_2 + i\psi_2^*\partial_y\psi_1 + i\psi_1^*\partial_y\psi_2 + \text{h.c.}\right) + g(1-\gamma)\,|\psi_1|^4 + g(1+\gamma)\,|\psi_2|^4 + 2\lambda g\,|\psi_1|^2\,|\psi_2|^2 \Bigg]. \tag{4.21}$$

Here, κ parametrizes the spin-orbit coupling strength, α and g the overall quadratic and quartic coupling strengths, Δ the deviation from equal quadratic coupling strengths, γ the deviation from equal quartic coupling strengths, and λ the deviation from having equal intra- and inter-component quadratic coupling strengths. In the paper, we fixed α and g to generic values $\alpha = 10.0$ and $g = 1.0$, Δ to a small, finite value $\Delta = 0.1$, γ to zero, and varied κ and λ. Fig. 4.3 shows the mean field phase diagram we obtained, in the λ-κ-plane.

This phase diagram was obtained by assuming that the complex fields ψ_i could be written as either a single plane wave, or by two plane waves with momentum of equal magnitude but opposite direction, both parametrized by a wave-vector $\mathbf{q}$. This was prompted by the single-particle spectrum, which shows that the ground state resides at finite momentum, and by previous works on a similar model [83, 84] which found states modulated by either one or two $\mathbf{q}$-vectors. We solved the resulting mean field equations, treating the wave-vector $\mathbf{q}$ as a variational parameter, in addition to the fields ψ_i. This resulted in three distinct phases, for finite κ, depending on the value of the interaction parameters, shown in Fig. 4.3. For small values of the inter-component coupling strength, λ, we found that modulating the condensate by a single $\mathbf{q}$-vector was favoured. This is represented by the blue region labelled I in Fig. 4.3. If we from here keep κ small, and increase λ, one of the components will deplete, and the spin-orbit coupling loses its effect. This will remove the modulation, and the

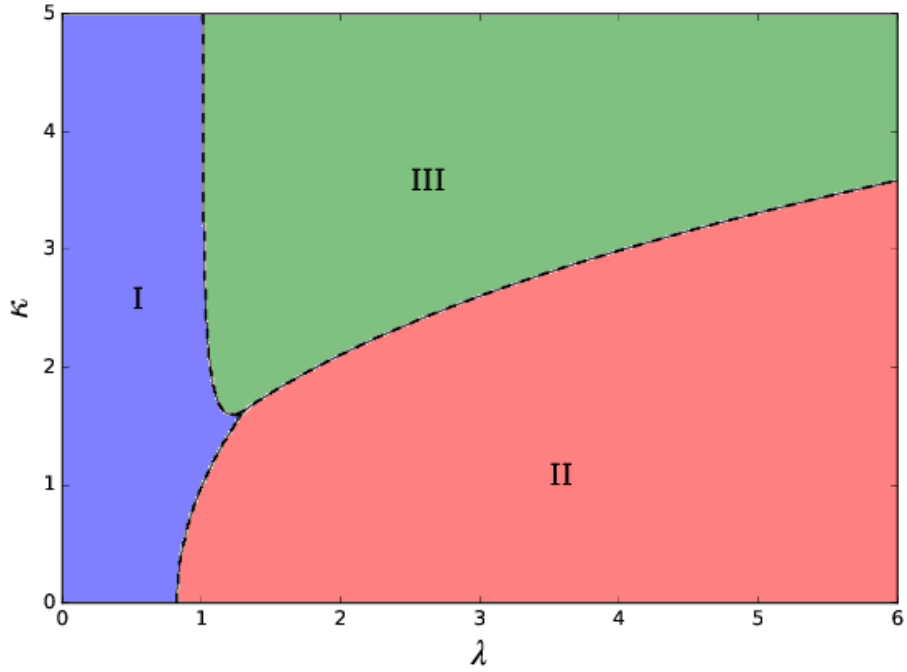

Figure 4.3: Mean field phase diagram of the two-component spin-orbit coupled Bose-Einstein condensate in two-dimensions, in the λ-κ plane. The other parameters is fixed to generic values described in the text. Region I is a state modulated by a single $\mathbf{q}$-vector, region II is a single component condensate residing at zero $\mathbf{q}$, while region III is modulated by two $\mathbf{q}$-vectors of equal magnitude but opposite direction. This figure is taken from paper III [3].

remaining condensate will reside at zero momentum. The depletion occurs because the energy gained by having a finite $\mathbf{q}$ in both of the condensates is lower than the energy gained from completely depleting one of the condensates. In Fig. 4.3 we represent this phase by the red region labelled II. However, if the spin-orbit coupling strength, κ, is sufficiently high, the

energy gained by modulating the two condensates is greater than the energy gained by simply removing one condensate altogether. This results in a compromise, where the amplitudes of both condensates are staggered with respect to each other, partially minimizing the density-density interaction energy and retaining the spin-orbit induced modulation. This phase is represented by the green region labelled III in the phase diagram.

We support and expand on these mean field results in our Monte-Carlo simulations, where we to a large extent are able to reproduce the low-temperature phase diagram quantitatively. We also find that modulation by a single $\mathbf{q}$-vector manifests itself as a striped state in the superfluid phases only, while the modulation of two $\mathbf{q}$-vectors gives a striped state in the superfluid phases, as well as a striped and staggered state in the amplitudes. For high temperatures, the model is always a two-component normal fluid state. The two states which reside at finite $\mathbf{q}$ may be though of as bosonic analogues of Fulde-Ferrell-Larkin-Ovchinnikov states in superconductors. These are states where the order parameter is paired at finite momentum, the ground states are pair-density waves. The state of region I is akin to a Fulde-Ferrel state, which is an order parameter paired at a single momentum vector, and may be thought of a plane wave state. Region III, on the other hand, is akin to a Larkin-Ovchinnikov state, which is a superposition of two order parameters paired at $\mathbf{q}$ and $-\mathbf{q}$, and is therefore like a standing wave state.

For zero κ, the model is a two-component superfluid for small values of λ, and a single-component superfluid for sufficiently large values of λ. In the Monte-Carlo simulations, we found that this model exhibited thermal phase transitions in the Kosterlitz-Thouless universality class in both components when λ is in the two-component regime, and a single Kosterlitz-Thouless transition when one component is depleted. This was found using the two techniques described in Section 3.4: fitting the helicity modulus to Eq. (3.28) and extrapolating the negative dip of the fourth order modulus to a finite value. Both techniques gave results consistent with a Kosterlitz-Thouless transition for all values of λ considered.

4.4.3 Outlook

The results contained in papers I-III predict and confirm many interesting phases present in Bose-Einstein condensed cold atomic gases. Some, like the presence of square vortex lattices in rotating two-component condensates, have already been observed [72], and others may be realized in future experiments. In particular, the curious state observed in paper I at the SU(2)-symmetric point, the striped phase observed in paper II, as well as the interplay between inter-component density-density and spin-orbit interactions observed in paper III would be interesting and feasible to observe in a experimental setup involving cold atomic gases. Furthermore, all three papers suggest several new avenues of theoretical research. It would be interesting to consider the following extensions. In paper I, the nature of the phase transition from the uniform phase into the vortex lattice phase along the SU(2)-symmetric line could be examined. Paper II presents a rather rich phase diagram, and makes a few non-rigorous remarks about the nature of the transitions between the phases contained within, which warrants further study. Finally, a number of extensions may be made regarding paper III, mainly adding a third dimension and examining the effect of the spin-orbit coupling on rotation-induced vortex matter.

CHAPTER 5

Multiband Superconductors

Up to this point in the thesis we have only discussed Bose-Einsten condensates, which exhibit superfluidity. In short, this phenomenon can be described as a fluid flowing without friction. Superconductivity is a very similar phenomenon which may occur when charged particles are involved[1], where an electric current flows without resistance. One may think of it as superfluidity of a charged condensate. A good review of the topic can be found in Ref. [85].

5.1 History and phenomenology

Superconductivity was discovered even before superfluidity, in 1911 by Heike Kammerlingh Onnes, who observed a sudden drop in resistivity to zero at a critical temperature in mercury as it was cooled to very low

[1] As opposed to the cold-atom Bose-Einstein condensates considered thus far, which are neutrally charged.

temperatures. This was the first of many *conventional* superconductors discovered over the years, others including for instance lead, niobium compounds and magnesium diboride (MgB_2). These materials are dubbed conventional superconductors, as their properties and mechanism for superconductivity may be described by the Bardeen-Cooper-Schrieffer theory [86]. In addition to the conventional superconductors, we have the *unconventional* superconductors which include copper-oxide compounds, as well as iron-based compounds. As you may have guessed, these are not described by the theory of Bardeen, Cooper and Schrieffer. Many of these superconductors have much higher critical temperatures, prompting the name *high-T_c superconductors*. Bednorz and Müller received the Nobel Prize in 1987 for their discovery of the first high-T_c superconductor, doped $La_{5-x}Ba_xCu_5O_{5(3-y)}$, in 1983 [87].

In addition to the classification into conventional and unconventional superconductors, one may classify superconductors according to their magnetic properties. We stated that the defining property of a superconductor is its zero-valued resistivity, however this is not the whole story. More interestingly, a superconductor exhibits the *Meissner effect*, complete expulsion of any magnetic field in its interior. In what is dubbed a *Type-I* superconductor, an applied magnetic field is completely expelled until the magnetic field strength reaches a critical value, H_c, where the magnetic field enters the material and destroys superconductivity. Materials that exhibit type-I superconductivity are typically pure metals like lead, mercury and aluminium. In a *Type-II* superconductor, however, there will be two critical field values, H_{c1} and H_{c2}. Below the lower critical field, H_{c1}, the material completely expels the external field. Above the lower critical field, but below the upper, H_{c2}, the magnetic field will enter the superconductor as quantized units of magnetic flux, in the form of magnetic vortices. These vortices will form an Abrikosov flux line lattice [88]. As the field is then increased further, more and more vortices enter until they completely fill the material when the upper critical field is reached, which destroys superconductivity completely. A type-II superconductor therefore exhibits an intermediate, mixed phase where it has superconductivity everywhere except inside the magnetic vortices. Type-II superconductiv-

ity is generally present in metal alloys, rather than pure metals, as well as the copper-oxides and other high-temperature superconductors. As you may have noticed, this state is very similar to a superfluid under rotation, with the magnetic vortices playing the role of the superfluid vortices.

As with the superfluid models discussed in the previous chapter, superconductors may consist of several superconducting components, here called superconducting bands. This extension will introduce non-trivial new effects, depending on the type of interactions included. On the most simple level, as all superconducting components will be charged, the electromagnetic field will mediate interactions between all bands. This will cause the vortices to couple in non-trivial ways, introducing new composite degrees of freedom, which will be discussed below. In addition, depending on the system described, one may have to include inter-band Josephson couplings which removes the current conservation of the individual condensates associated with the $\mathrm{U}(1)$ symmetry. In these Josephson-coupled multiband superconductors, with three or more bands, you may also find an additional Z_2 symmetry associated with time reversal [89–91].

5.2 Models of multiband superconductors

The basic effective model of a single component superconductor is the Ginzburg-Landau theory of a single complex order-parameter field, $\psi(\mathbf{r})$, coupled to a non-compact gauge field, $\mathbf{A}(\mathbf{r})$. This model is of course very similar to the model of a superfluid, except for one important difference. As a superconductor is a condensate of charged particles, one must also include the electromagnetic interactions of the condensate through the gauge field. Thus, the basic Hamiltonian reads[2]

$$H = \int \mathrm{d}\mathbf{r} \left[\frac{1}{2m} \left| (\boldsymbol{\nabla} - ie\mathbf{A})\, \psi \right|^2 + V(|\psi|) + \frac{1}{2} \left(\boldsymbol{\nabla} \times \mathbf{A} \right)^2 \right], \tag{5.1}$$

with

$$\mathcal{Z} = \int \mathcal{D}(\psi, \mathbf{A}) e^{-\beta H} \tag{5.2}$$

[2]We suppress the $\mathbf{r}$ dependence in the fields $\psi_i(\mathbf{r})$ and $\mathbf{A}(\mathbf{r})$ for brevity.

The important difference lies now in the fact that the gauge field $\mathbf{A}$ is a fluctuating field on its own. The potential V can be any function of ψ that respects the symmetries of the system one wishes to model. The field ψ consists of an amplitude and a phase, $\psi = |\psi| \exp i\theta$. The amplitude represents the density of the superconducting condensate, while the gradient of the phase is the superconducting current. In its most basic form, the potential will include the familiar quadratic and quartic terms,

$$V(|\psi|) = -\alpha(T) |\psi|^2 + g |\psi|^4 + \dots . \tag{5.3}$$

This allows us to define two characteristic length scale of the superconductor, which quantifies the type-I-type-II classification. The superconducting coherence length, defined as

$$\xi = \sqrt{\frac{\hbar^2}{2m |\alpha(T)|}}, \tag{5.4}$$

describes the length scale over which the condensate amplitude will vary. The second scale is the magnetic penetration depth, which describes how far into the superconductor an applied magnetic field will penetrate[3]. It is defined by

$$\lambda = \sqrt{\frac{m}{4\mu_0 e^2 |\psi_0|^2}}, \tag{5.5}$$

where $|\psi_0|$ is the equilibrium value of $|\psi|$ in the absence of a magnetic field. The ratio between these two, $\kappa \equiv \lambda/\xi$, is dubbed the Ginzburg-Landau parameter. This ratio may be directly used in the classification of a superconductor. The superconducting transition in a type-I superconductor is a first-order transition, while in a type-II superconductor it is continuous. A point separating a first-order and a continuous phase transition is called a tri-critical point, and is a general feature of such phase diagrams. Therefore, in the context of superconductors, one may define a value κ_{tri}, where the order of the superconducting phase transition, and the classification,

[3] In the definition of ξ and λ we have reinserted the proper units

changes. Landau theory predicts that a superconductor with $\kappa < 1/\sqrt{2}$ is of a type-I superconductor, while one with $\kappa > 1/\sqrt{2}$ is a type-II superconductor, and hence $\kappa_{\text{tri}} = 1/\sqrt{2}$. Monte-Carlo simulations [92] has determined the actual value of the tri-critical point to $\kappa_{\text{tri}} = 0.76(4)/\sqrt{2}$.

Eq. (5.1) describes a single-band superconductor, but we are interested in superconductors of multiple bands. This is done, not surprisingly, by adding more complex fields. By considering a field with an index, ψ_i, where i runs from 1 to N, we may describe a superconductor of N bands. The generalization is straightforward,

$$H = \int \mathrm{d}\mathbf{r} \Bigg[\sum_i \frac{1}{2m_i} \left| \left(\boldsymbol{\nabla} - ie\mathbf{A} \right) \psi_i \right|^2 + V(|\psi_1|, ..., |\psi_N|) + \frac{1}{2} \left(\boldsymbol{\nabla} \times \mathbf{A} \right)^2 \Bigg]. \tag{5.6}$$

Now, some important differences arise. First, the gauge field may now mediate interactions between the condensates. This will be discussed further once we present the specific model in question. Secondly, one may include other interactions between the condensate beyond the density-density type. One, which we do not consider in this work, is Andreev-Bashkin terms on the form $\boldsymbol{\nabla}\psi_i^* \cdot \boldsymbol{\nabla}\psi_j$. These terms, also called drag terms, induce interactions between the currents of the individual fields. Actually, this is very similar to the effect of the gauge field. A current in one component may induce a current in another component either in the same direction, or in the opposite direction, depending on the sign of the Andreev-Bashkin term. Another type of interaction, which we *do* include, is known as the Josephson interaction. This interaction *does not* conserve each individual condensate independently, which is very important in light of the phase

transitions of the system. It has the form

$$\begin{aligned} H_J = & -\int \mathbf{dr} \sum_{i<j} \eta_{ij} \left(\psi_i^* \psi_j + \psi_j^* \psi_i\right), \\ = & -\int \mathbf{dr} \sum_{i<j} \eta_{ij} \left|\psi_i\right| \left|\psi_j\right| \cos\left(\theta_i - \theta_j\right), \end{aligned} \tag{5.7}$$

Here, η_{ij} is the strength of the Josephson coupling between condensate i and j. A positive value of this coupling favours locking of the phases of the condensates to point in the same direction, while a negative value favours locking in the opposite direction. It breaks down the individual $\mathrm{U}(1)$ symmetries of each condensate into a single overall $\mathrm{U}(1)$ symmetry, if all $\eta_{ij} > 0$. This remaining symmetry corresponds to rotating the sum of all the phases.

5.2.1 The London superconductor

It turns out that, as far as the phase transitions is concerned, it suffices to consider only fluctuations in the phases of the complex field (as well as the gauge field) when describing a single component type-II superconductor [81] with a sufficiently large value of the Ginzburg-Landau parameter, κ. To this end, one may write the complex field as a constant amplitude (called the bare stiffness of the phase) times the fluctuating phase factor, $\psi_i = \rho_i \exp i\theta_i$. When one has multiple bands, it suffices that the band with the largest bare stiffness has a sufficiently large associated ratio λ/ξ [93]. In this case, the Hamiltonian reads

$$\begin{aligned} H = \int \mathbf{dr} \Bigg[& \sum_i \frac{\rho_i^2}{2} \left(\nabla\theta_i - e\mathbf{A}\right)^2 - \sum_{i<j} \rho_i \rho_j \eta_{ij} \cos(\theta_i - \theta_j) \\ & + \frac{1}{2} \left(\boldsymbol{\nabla} \times \mathbf{A}\right)^2 \Bigg]. \end{aligned} \tag{5.8}$$

The potential is now an unimportant constant, and the condensate amplitudes, ρ_i, are parameters. The parameter m_i may be absorbed into ρ_i.

5.2.2 Lattice London model

In paper IV, the specific model we consider is that of a multiband lattice London superconductor. The most straightforward way to arrive at this particular model is to discretize the complex field and the gauge field on a cubic grid, then replace the derivatives with a lattice derivative. At this point one has a lattice model with amplitude fluctuations included, similar to the models considered in papers I-III, Eqs. (4.20) and (4.21), but with a fluctuating gauge field. Taking the London limit at this point results in the following model

$$H = \sum_{\mathbf{r}} \Bigg[-\sum_{i,\mu} \rho_i^2 \cos(\Delta_\mu \theta_{\mathbf{r},i} - eA_{\mathbf{r},\mu}) - \sum_{i<j} \rho_i \rho_j \eta_{ij} \cos(\theta_{\mathbf{r},i} - \theta_{\mathbf{r},j}) + \frac{1}{2} \left(\boldsymbol{\Delta} \times \mathbf{A}_{\mathbf{r}}\right)^2 \Bigg]. \tag{5.9}$$

5.2.3 The Villain model

Preserving the periodic structure of the phase degrees of freedom is of great importance when constructing a proper lattice model. The lattice London model, which uses trigonometric functions, accomplishes this immediately. Another option is to use what is known as the Villain approximation [94]. It amounts to replacing the cosine function with the square of its argument, while also inserting a new integer valued field to preserve the periodic structure. If we take a N-component lattice London model, with $\eta_{ij} = 0$, the initial Hamiltonian of Eq. (5.9) will transform into

$$H = \frac{1}{2} \sum_{\mathbf{r}} \rho_i^2 (\boldsymbol{\Delta}\theta_{\mathbf{r},i} + 2\pi \mathbf{n}_{\mathbf{r},i} - e\mathbf{A}_{\mathbf{r}})^2 + \frac{1}{2} \sum_{\mathbf{r}} \left(\boldsymbol{\Delta} \times \mathbf{A}_{\mathbf{r}}\right)^2, \tag{5.10}$$

now with

$$\mathcal{Z} = \int \mathcal{D}(\psi, \mathbf{A}) \sum_{\{\mathbf{n}\}} e^{-\beta H} \tag{5.11}$$

Here, $\mathbf{n}_{\mathbf{r},i}$ is an integer-valued vector field running from $-\infty$ to ∞, introduced to account for the periodicity of each phase $\theta_{\mathbf{r},i}$. Eq. (5.10) is known as the Villain model, and it may be generalized to include Josephson couplings as well [93]. In brief words, this is done by introducing an additional integer-valued *scalar* field for each phase combination which is Josephson coupled. It has the same symmetries as the lattice London model, and the same qualitative phase diagram. However, the approximation will renormalize the couplings, which leads to a quantitatively different phase diagram.

5.3 Vortices and duality

In all of the above models of superconductors, topological defects of the order field drives the phase transition. These defects, vortices, are analogous to the vortices of BECs and superfluids introduced in the previous chapter. In this case, however, they represent holes in the superconducting states, carrying quantized magnetic flux. In a single-component superconductor, in the extreme type-II limit where the London approximation is valid, the superconducting phase transition is entirely driven by a proliferation of vortex loops [81, 95, 96], in zero external magnetic field. These vortex loops will fill the system, and therefore completely suppress superconductivity, making the system behave as a normal metal. This transition is analogous to the superfluid to normal fluid transition of He^4, first suggested by Onsager [97, 98]

With the Villain model, Eq. (5.10), as a starting point, one may derive a model which has the vortices as the basic degrees of freedom, not the phases. This dual model will more directly represent the relevant topological defects of the superconductor. This derivation is rather lengthy, and has already been presented quite elegantly in Ref. [93]. Therefore, I will only quote the final result here, as it provides an enlightening and alternate

viewpoint to both the lattice London model, as well as the integer current model we derive in paper IV and below. The partition function in the dual picture is

$$\mathcal{Z} = \prod_i \sum_{\{\mathbf{v}_i\}} \delta_{\mathbf{\Delta}\cdot\mathbf{v}_i,0} e^{-\beta H}, \tag{5.12}$$

where H is

$$H = 2\pi^2 \sum_{\mathbf{r},\mathbf{r}'} \sum_{ij} \rho_i^2 \mathbf{v}_{\mathbf{r},i} V_{ij}(\mathbf{r}-\mathbf{r}') \mathbf{v}_{\mathbf{r},j}. \tag{5.13}$$

This is a model of integer-valued vortex-fields, $\mathbf{v}_{\mathbf{r},i}$, defined on the dual lattice to the original lattice. They represent the vorticity passing through the plaquettes of the original lattice, and are constrained to form closed loops. $V_{ij}(\mathbf{r}-\mathbf{r}')$ is the vortex-vortex interaction potential in real space. It is more conveniently represented in Fourier space, as

$$V_{ij}(\mathbf{q}) = \frac{\varrho_i^2}{\left|\mathbf{Q}_\mathbf{q}\right|^2 + e^2 \sum \rho_i^2} + \frac{\delta_{ij} - \varrho_i^2}{\left|\mathbf{Q}_\mathbf{q}\right|^2}, \tag{5.14}$$

where we have defined $\varrho_i^2 \equiv \rho_i^2 / \sum_i \rho_i^2$, for brevity. It contains both the screened intra- and inter-vortex interactions mediated by the gauge field in the first term, and the unscreened intra-vortex interactions which are the Coulomb interaction of the vortices themselves in the second term. The momentum appearing in the potential, $\mathbf{Q}_\mathbf{q}$ is the lattice momentum, $Q_{\mathbf{q},\mu} = 2\sin(q_\mu/2)$[4]. The term $e^2 \sum_i \rho_i^2$ in the first denominator is the reason for the screening, and in may be thought of as the bare mass of the gauge field[5]. If $e = 0$, there is no coupling to the gauge field, and the potential reduces to

$$V_{ij}(\mathbf{q}) = \frac{\delta_{ij}}{\left|\mathbf{Q}_\mathbf{q}\right|^2}. \tag{5.15}$$

This leaves us with only the unscreened intra-component Coulomb repulsion between the vortices.

[4]Essentially, it is the Fourier representation of the Δ_μ operator.

[5]The gauge field is massive in the superconducting state, due to the Meissner effect.

This dual model shows that there are inter- and intra-component vortex-vortex interaction mediated by the gauge field, as well as intra-component vortex-vortex interactions, mediated by phase fluctuations. This makes the N-component London superconductor a very rich model, as the gauge-field will mediate interactions between vortices of all types. In short, it will lead to an interesting phase diagram, with different scenarios occurring depending on the values of the charge, e, and the individual phase stiffnesses, ρ_i. It will also lead to formation of new composite objects made up of individual vortices, which will further influence the phase diagram and transitions. This will be discussed in the following.

5.3.1 Charged and neutral modes

With multiple condensates, the elementary degrees of freedom may combine into new composite degrees of freedom. The continuum London superconductor may be rewritten in such a way, starting from Eq. (5.8), we may represent the gradient term as

$$H = \frac{1}{2\sum_i \rho_i^2} \int \mathbf{dr} \Bigg[\left(\sum_i \rho_i^2 \boldsymbol{\nabla}\theta_i - e \sum_i \rho_i^2 \mathbf{A} \right)^2 + \sum_{i<j} \rho_i^2 \rho_j^2 \left[\boldsymbol{\nabla}(\theta_i - \theta_j) \right]^2 \Bigg] + \dots \,. \tag{5.16}$$

At first glance, this tells us that we may define one mode, the sum of all the phases, which will interact with the gauge field, and many other modes which does not interact with the gauge field. The sum of all the phases, dubbed the charged mode, $\sum_i \rho_i \theta_i \equiv \Theta$, will have a charge $e\sum_i \rho_i^2$. The phase differences, $\theta_i - \theta_j \equiv \vartheta_{ij}$, of which there will be $N(N-1)/2$, are dubbed neutral modes. It is important to note that this representation has too many degrees of freedom, if we interpret all ϑ_{ij} as such. In Eq. (5.8), there are N phases, while Eq. (5.16) has $N(N-1)/2 + 1 > N$. In other words, if one were to define a partition function from Eq. (5.16) directly, and integrate over $\int \mathcal{D}(\Theta, \vartheta_{ij})$, the resulting partition function would be

incorrect. The reason for this is that each individual phase is a constituent in $N-1$ phase differences, as well as the phase sum. If one individual phase is excited, $N-1$ composite neutral modes are excited as a consequence. Hence, they are not all independent, and may not be integrated over as such.

It is also possible to separate the dual model of Eq. (5.13) in terms of charged and neutral vortices [93], which leads to the following Hamiltonian.

$$H = \frac{2\pi^2}{\left(\sum_i \rho_i^2\right)} \left[\frac{\left(\sum_i \rho_i^2 \mathbf{v}_{\mathbf{q},i}\right) \cdot \left(\sum_j \rho_j^2 \mathbf{v}_{-\mathbf{q},j}\right)}{\left|\mathbf{Q}_{\mathbf{q}}\right|^2 + e^2 \sum \rho_i^2} + \sum_{ij} \frac{\rho_i^2 \rho_j^2 \left(\mathbf{v}_{\mathbf{q},i} - \mathbf{v}_{\mathbf{q},j}\right)\left(\mathbf{v}_{-\mathbf{q},i} - \mathbf{v}_{-\mathbf{q},j}\right)}{\left|\mathbf{Q}_{\mathbf{q}}\right|^2} \right]. \quad (5.17)$$

Here, $\mathbf{v}_{\mathbf{q},i}$ is simply $\mathbf{v}_{\mathbf{r},i}$ in reciprocal space. Again, it is clear that there is a single mode which interacts through the gauge field, and is therefore screened, while there are $N(N-1)/2$ vortex modes which only interact through the unscreened vortex-vortex Coulomb interactions.

In spite of the redundant degrees of freedom, Eqs. (5.16) and (5.17) provide a very interesting viewpoint regarding the phase transitions in the model. Several papers [11, 93] have explored the phase transitions in models with multiple U(1) symmetries and zero Josephson coupling, and show that the classification into charged and neutral modes is vital to understanding their phase transitions. In addition to, as described above, proliferating individual vortices, one may have phase transitions associated with proliferation of composite vortices. These composite vortices will correspond to 2π phase windings of several individual phases at the same point in space. Using the same terms as above, a charged vortex is a 2π winding of *all* phases θ_i simultaneously at the same point, $\mathbf{r}$. This may also be called a superconducting vortex. In addition to this one superconducting vortex mode, there will be $N(N-1)/2$ neutral vortex modes, corresponding to a 2π winding in one phase and a -2π winding in another. These may also be called superfluid vortices, as they do not interact through the gauge field.

Depending on the values of the bare phase stiffnesses and the charge, one may observe several scenarios. First, let us assume we have N components with equal stiffnesses, and a charge e relatively large. The low temperature phase in this case will be a superconducting superfluid, where one mode is superconducting, and $N-1$ modes are superfluid. As we increase temperature, the superconducting mode corresponding to the phase sum will lose coherence first, provided the charge is sufficiently large [11]. Lowering temperature further will cause the neutral modes to proliferate, presumably in a superposition of $N-1$ phase transitions in the $3DXY$-universality class.

Next, we describe the situation if one lowers the electric charge, e. This will cause the critical temperature of the charged sector to increase, while not altering the critical temperatures of the neutral sector(s) much at all. When they merge, the proliferation of the neutral vortices will trigger proliferation of the charged vortices as well. This interplay between the sectors causes the transition to become first order, which has been shown in Monte-Carlo simulations with $N = 2$ [11], both with equal and unequal bare stiffnesses of the two phases. This has been dubbed a preemptive vortex-loop proliferation, and was first observed in Monte-Carlo simulations of a two-component superfluid with Andreev-Bashkin current-current interactions [99].

Finally, for unequal bare phase stiffnesses, $N = 2$, and a sufficiently low charge, one may have the following scenario. As the temperature is lowered, individual vortices of one of the components will cause the system to lose superfluidity, entering a phase with only superconductivity in the remaining component. Then, as temperature is lowered further, the second type of vortices proliferate, and superconductivity is lost in an inverted $3DXY$ transition[11]. If $N > 2$ in this scenario, one will find a succession of $N-1$ superfluid transitions, corresponding to the $N-1$ superfluid modes losing coherence, and then a final superconducting phase transition [93].

5.4 Character expansion

The main idea behind paper IV is to utilize what is known as a character expansion [100] on the action of Eq. (5.9). To this end we apply the identity

$$e^{a\cos x} = \sum_{b=-\infty}^{\infty} I_b(a) e^{ibx}. \tag{5.18}$$

to all cosine terms in the action of a lattice London superconductor. Here, $I_b(a)$ is the modified Bessel function of the first kind. This introduces new, integer-valued fields, b, which may be have one or more components depending on the nature of x. This kind of expansion is an expansion in the traces of the irreducible representations of the underlying symmetry group. For degrees of freedom invariant under the U(1) group, x, these traces are simply $\exp ibx$.

As a simple example, let us apply this identity to a single-band lattice-London superconductor, defined by the Hamiltonian

$$H = -\sum_{\mathbf{r},\mu} \cos\left(\Delta_\mu \theta_{\mathbf{r}} - e\mathbf{A}_{\mathbf{r},\mu}\right) + \frac{1}{2}\sum_{\mathbf{r}} \left(\mathbf{\Delta} \times \mathbf{A}_{\mathbf{r}}\right)^2. \tag{5.19}$$

We may now apply Eq. (5.18) to the cosine term, yielding a partition function

$$\mathcal{Z} = \int \mathcal{D}(\theta, \mathbf{A}) \prod_{\mathbf{r}} \left(\prod_{\mu} \sum_{b_{\mathbf{r},\mu}=-\infty}^{\infty} I_{b_{\mathbf{r},\mu}}(\beta) e^{i b_{\mathbf{r},\mu}(\Delta_\mu \theta_{\mathbf{r}} - e A_{\mathbf{r},\mu})} \right) \prod_{\mathbf{r}} \times e^{-\frac{\beta}{2}(\mathbf{\Delta}\times\mathbf{A}_{\mathbf{r}})^2}. \tag{5.20}$$

As we mentioned above, this introduces a new integer-vector field, $\mathbf{b}_{\mathbf{r}}$, which will represent the actual superconducting currents. These supercurrents will be dual objects to the integer-valued vortex fields, $\mathbf{v}_{\mathbf{r}}$, introduced in Eq. (5.13), and they are defined on the dual lattice to that of the vortex fields. A vortex will have a loop of supercurrent flowing around it, and a supercurrent will have a loop of vorticity flowing around it. After

performing a lattice integration of parts, moving the lattice difference from θ to b, we may integrate out the phase-degrees of freedom, which leaves a constraint on the $\mathbf{b}$-field.

$$\mathbf{\Delta} \cdot \mathbf{b}_{\mathbf{r}} = 0 \, \forall \, \mathbf{r}, \tag{5.21}$$

it is divergenceless. Now we may also integrate out the gauge fields, the details of which may be found in paper IV, which introduces long-range current-current interactions between the $\mathbf{b}$-fields. The resulting partition function reads

$$\mathcal{Z} = \sum_{\mathbf{b}} \left(\prod_{\mathbf{r}} \delta_{\mathbf{\Delta} \cdot \mathbf{b}_{\mathbf{r}}, 0} \right) \left(\prod_{\mathbf{r}, \mu} I_{b_{\mathbf{r}, \mu}}(\beta) \right) e^{-S_G}, \tag{5.22}$$

where

$$S_G = \sum_{\mathbf{r}, \mathbf{r}'} \frac{e^2}{2\beta} D(\mathbf{r} - \mathbf{r}') \mathbf{b}_{\mathbf{r}} \cdot \mathbf{b}_{\mathbf{r}'}, \tag{5.23}$$

is the part of the action containing the gauge-mediated interaction. $D(\mathbf{r}, \mathbf{r}')$ is the current-current interaction potential in real space. The current-current interaction may be represented in reciprocal space as $D_{\mathbf{q}} = 1/\left|\mathbf{Q}_{\mathbf{q}}\right|^2$, where $\mathbf{Q}_{\mathbf{q}}$ again is the lattice momentum.

What this calculation shows us is that the lattice London superconductor may be re-expressed as an integer valued vector-current field, $\mathbf{b}_{\mathbf{r}}$, which is divergence-free and interacts with itself in two ways. One way being the on-site repulsion set in effect by the Bessel functions, the other being the long range interaction mediated by the gauge field. The phase transition in the current language will occur in the opposite way as in the vortex language. At low temperatures, in the superconducting state, the supercurrents proliferate and fill the system completely. The vortices, however, only form small closed loops. As temperature is increased towards the critical temperature, the supercurrents will collapse[6] and superconductivity is lost. You may view this dual description as occurring in exactly the same way as in the vortex picture, but with an inverted temperature axis.

[6] At the same temperature the vortices proliferate.

5.5 Main results of paper IV

The main result of paper IV is the interpretation of a multiband London superconductor, after transforming it using Eq. (5.18) and integrating out the original phase-degrees of freedom. The specific form of the partition function we use, may be written as

$$\mathcal{Z} = \sum_{\{\theta,\mathbf{A}\}} \prod_{\mathbf{r}} \left(\prod_{i,\mu} e^{\beta \cos(\Delta_\mu \theta_{\mathbf{r},i} - e A_{\mathbf{r},\mu})} \right) \left(\prod_{i<j} e^{\beta\eta \cos(\theta_{\mathbf{r},i} - \theta_{\mathbf{r},j})} \right) \times e^{\frac{-\beta}{2}(\Delta \times \mathbf{A}_{\mathbf{r}})^2}. \tag{5.24}$$

Here, we simplified the Hamiltonian of Eq. (5.9) by choosing all stiffnesses equal to unity, and all $\eta_{ij} = \eta > 0$. Having $\eta > 0$ ensures that there are no frustrated phases. After using the identity Eq. (5.18) on the cosine terms stemming both from the gradients and from the Josephson interaction, we arrive at the following partition function.

$$\mathcal{Z} = \sum_{\{\mathbf{b},m\}} \prod_{\mathbf{r},i} \delta_{\mathbf{\Delta}\cdot\mathbf{b}_{\mathbf{r},i}, \sum_{j\neq i} m_{\mathbf{r},i,j}} \prod_{\mathbf{r},\mu,i} I_{b_{\mathbf{r},i,\mu}}(\beta) \prod_{\mathbf{r},i<j} I_{m_{\mathbf{r},i,j}}(\beta\eta) e^{-S_G}. \tag{5.25}$$

The details of the derivation may be found in paper IV. Now, the gauge action, S_G, is

$$S_G = \frac{e^2}{2\beta} \sum_{\mathbf{r},\mathbf{r}'} \sum_{ij} \mathbf{b}_{\mathbf{r},i} \cdot \mathbf{b}_{\mathbf{r}',j} D(\mathbf{r} - \mathbf{r}'), \tag{5.26}$$

where the current-interaction potential, $D(\mathbf{r} - \mathbf{r}')$, has the same Fourier representation as before, $D_{\mathbf{q}} = 1/\left|\mathbf{Q}_{\mathbf{q}}\right|^2$. Eq. (5.25) is a direct generalization of Eq. (5.22). The integer-valued vector field, $\mathbf{b}_{\mathbf{r},i}$ has the same interpretation as before as the supercurrents, but now with an added index, i, as we have N supercurrents. The gauge-mediated interaction has the same basic form, but it now mediates interactions between all currents, both inter- and intra-component. Contrary to the vortex-vortex interaction

of Eq. (5.13), $D(\mathbf{r}-\mathbf{r}')$ only represents gauge-mediated interactions. The analogue of the Coulomb intra-vortex interactions is in this case the contact interactions contained in the Bessel function $I_{b_{\mathbf{r},i,\mu}}(\beta)$. The effect of the Josephson interaction is seen mainly by the inclusion of a new integer-valued scalar field, $m_{\mathbf{r},i,j} = -m_{\mathbf{r},j,i}$. They appear in the δ-function constraint, where they give the supercurrents a finite divergence. They also interact with each other through a contact Bessel-function term. If we set $\eta = 0$, we must have $m_{\mathbf{r},i,j} = 0 \; \forall \; \mathbf{r}, i, j$, and we revert to N divergence-free supercurrents, as $I_n(0)$ is unity for $n = 0$, and zero for all $n > 0$.

The effect of the scalar fields, $m_{\mathbf{r},i,j}$, is as follows. Instead of only having closed loops of supercurrents of a single component, it is now possible to end a supercurrent of one component, i, on a site, *if* there is a supercurrent of any other component, j, coming out of the site. This changing of color from i to j is then an excitation of ± 1 in $m_{\mathbf{r},i,j}$, which may be thought of as an instanton-like event. As each instanton event must consist of one supercurrent component entering the site and one exiting, we will still have closed loops of supercurrent, but the current may change color an arbitrary amount of times before coming full circle again. The effect of the Josephson coupling is to snip the closed currents of the individual superconducting components into pieces, then gluing them back together into closed loops consisting of all combinations of the different components. The net effect of this is to convert the phase transitions in the individual components into crossovers, for any value of η. However, something survives. If one sums δ-function constraint over all components, one finds

$$\begin{aligned} \sum_i \mathbf{\Delta} \cdot \mathbf{b}_{\mathbf{r},i} &= -\sum_i \sum_{j \neq i} m_{\mathbf{r},i,j} \\ &= 0 \; \forall \; \mathbf{r}. \end{aligned} \tag{5.27}$$

That is, one particular combination of the supercurrents is still divergence-free. Interestingly, and perhaps not surprisingly, it is the sum of all the components. Remember, that in the vortex and phase language, it was the sum of all the components which coupled to the gauge field, and here it is no different. From Eq. (5.26) one sees that the sum of all the superconduct-

ing components interact through the gauge field. As this particular combination, $\sum_i \mathbf{b}_{\mathbf{r},i}$ is divergence-free, it should have a phase transition. And this phase transition is expected to be in the inverted $3DXY$-universality class, if it is not influenced by the neutral modes. We also calculated the gauge-field correlator in terms of the integer-valued current fields, and show that the onset of the Meissner effect is driven by a blowout of current-loops in the charged sector of the model. This is a complement to previous work, which has shown that the vortex-loop proliferation in the charged sector drives the transition from the Meissner state into the normal metal state [93]. The two descriptions are therefore dual to each other.

In paper IV we also use the identity of Eq. (5.18) to transform the model where the phases are separated into charged and neutral modes, with explicit expressions provided for $N = 2$ and $N = 3$, taking care to integrate out the redundant degrees of freedom properly. This allows us to explicitly show that one must introduce a single integer-valued vector field which is divergence-free and coupled to the gauge field, and $N(N-1)/2$ integer-valued vector fields which have a finite divergence due to the instanton events, and not coupled to the gauge field. The field with zero divergence may be associated with the superconducting vortices of Eq. (5.17), while the remaining fields with nonzero divergence are associated with the superfluid vortices. The phase transitions present in the neutral sector without the Josephson coupling present will be converted into crossovers, while the phase transition in the charged sector is unaffected. What then remains, for any value of e or $\eta \neq 0$, is a single superconducting phase transition associated with the collapse (proliferation) of the composite superconducting currents (vortices). This transition may be either first or second order, depending on whether or not the remaining fluctuations in the neutral sector are strong enough to influence the fluctuations of the charged sector. This will depend on the strength of the Josephson coupling, but also on the location of the crossovers in neutral sector relative to the phase transition of the charged sector.

5.5.1 Outlook

Paper IV presents a new formulation, Eq. (5.25), a schematic phase diagram, as well as an entirely new way of probing the Higgs mechanism in multi-band superconductors. These results suggest further research, in particular a Monte-Carlo study of the action of Eq. (5.25) in order to confirm the predictions of paper IV, and to further confirm the predictions of previous Monte-Carlo studies of the London model [101]. The action of Eq. (5.25) more directly expresses the relevant degrees of freedom, and is particularly suited for worm-type algorithms because of its link-current nature. However, the long-range interactions introduced by integrating out the gauge field make the model more challenging to simulate on parallel computers.

Bibliography

[1] P. N. Galteland, E. Babaev, and A. Sudbø, Phys. Rev. A **91**, 013605 (2015).

[2] P. N. Galteland, E. Babaev, and A. Sudbø, New Journal of Physics **17**, 103040 (2015).

[3] P. N. Galteland and A. Sudbø, Preprint (2016).

[4] P. N. Galteland and A. Sudbø, Preprint (2016).

[5] J. Binney, *The Theory of Critical Phenomena: An Introduction to the Renormalization Group*, Oxford Science Publ (Clarendon Press, 1992).

[6] E. Hauge, *Go critical!* (NTNU Lecture notes, 2001).

[7] J. O. Andersen, *Introduction to Statistical Mechanics* (Akademica Publishing, 2009).

[8] E. Ising, Zeitschrift für Physik **31**, 253.

[9] L. Onsager, Phys. Rev. **65**, 117 (1944).

[10] E. K. Dahl, E. Babaev, and A. Sudbø, Phys. Rev. Lett. **101**, 255301 (2008).

[11] E. V. Herland, E. Babaev, and A. Sudbø, Phys. Rev. B **82**, 134511 (2010).

[12] A. Zee, *Quantum Field Theory in a Nutshell*, Nutshell handbook (Princeton Univ. Press, Princeton, NJ, 2003).

[13] N. D. Mermin and H. Wagner, Phys. Rev. Lett. **17**, 1133 (1966).

[14] P. C. Hohenberg, Phys. Rev. **158**, 383 (1967).

[15] J. M. Kosterlitz and D. J. Thouless, Journal of Physics C: Solid State Physics **6**, 1181 (1973).

[16] J. M. Kosterlitz, Journal of Physics C: Solid State Physics **7**, 1046 (1974).

[17] B. I. Halperin and D. R. Nelson, Phys. Rev. Lett. **41**, 121 (1978).

[18] D. R. Nelson and B. I. Halperin, Phys. Rev. B **19**, 2457 (1979).

[19] A. P. Young, Phys. Rev. B **19**, 1855 (1979).

[20] K. J. Strandburg, Rev. Mod. Phys. **60**, 161 (1988).

[21] K. Chen, T. Kaplan, and M. Mostoller, Phys. Rev. Lett. **74**, 4019 (1995).

[22] J. G. Dash, Rev. Mod. Phys. **71**, 1737 (1999).

[23] K. Zahn, R. Lenke, and G. Maret, Phys. Rev. Lett. **82**, 2721 (1999).

[24] M. A. Bates and D. Frenkel, Phys. Rev. E **61**, 5223 (2000).

[25] J. Dietel and H. Kleinert, Phys. Rev. B **73**, 024113 (2006).

[26] S. I. Lee and S. J. Lee, Phys. Rev. E **78**, 041504 (2008).

[27] I. Guillamon, H. Suderow, A. Fernandez-Pacheco, J. Sese, R. Cordoba, J. M. De Teresa, M. R. Ibarra, and S. Vieira, Nat Phys **5**, 651 (2009).

[28] S. Hattel and J. Wheatley, Phys. Rev. B **50**, 16590 (1994).

[29] S. A. Hattel and J. M. Wheatley, Phys. Rev. B **51**, 11951 (1995).

[30] M. Franz and S. Teitel, Phys. Rev. Lett. **73**, 480 (1994).

[31] D. Landau and K. Binder, *A Guide to Monte Carlo Simulations in Statistical Physics* (Cambridge University Press, 2009).

[32] R. H. Swendsen and J.-S. Wang, Phys. Rev. Lett. **58**, 86 (1987).

[33] U. Wolff, Phys. Rev. Lett. **62**, 361 (1989).

[34] N. Prokof'ev and B. Svistunov, Phys. Rev. Lett. **87**, 160601 (2001).

[35] M. S. S. Challa, D. P. Landau, and K. Binder, Phys. Rev. B **34**, 1841 (1986).

[36] M. E. Fisher and A. N. Berker, Phys. Rev. B **26**, 2507 (1982).

[37] J. L. Cardy and P. Nightingale, Phys. Rev. B **27**, 4256 (1983).

[38] J. Lee and J. M. Kosterlitz, Phys. Rev. Lett. **65**, 137 (1990).

[39] J. Lee and J. M. Kosterlitz, Phys. Rev. B **43**, 3265 (1991).

[40] A. M. Ferrenberg and R. H. Swendsen, Phys. Rev. Lett. **61**, 2635 (1988).

[41] A. M. Ferrenberg and R. H. Swendsen, Phys. Rev. Lett. **63**, 1195 (1989).

[42] H. Weber and P. Minnhagen, Phys. Rev. B **37**, 5986 (1988).

[43] P. Minnhagen and B. J. Kim, Phys. Rev. B **67**, 172509 (2003).

[44] A. J. Leggett, Rev. Mod. Phys. **73**, 307 (2001).

[45] I. Bloch, Nat Phys **1**, 23 (2005).

[46] I. Bloch, J. Dalibard, and W. Zwerger, Rev. Mod. Phys. **80**, 885 (2008).

[47] V. Galitski and I. B. Spielman, Nature **494**, 49 (2013).

[48] Bose, Zeitschrift für Physik **26**, 178 (1924).

[49] A. Einstein, Sitzungsber. Kgl. Preuss. Akad. Wiss. **1924**, 261 (1924).

[50] A. Einstein, Sitzungsber. Kgl. Preuss. Akad. Wiss. **1925**, 3 (1924).

[51] P. Kapitza, Nature **141**, 74 (1938).

[52] J. F. Allen and A. D. Misener, Nature **141**, 75 (1938).

[53] F. London, Nature **141**, 643 (1938).

[54] M. H. Anderson, J. R. Ensher, M. R. Matthews, C. E. Wieman, and E. A. Cornell, Science **269**, 198 (1995).

[55] K. B. Davis, M. O. Mewes, M. R. Andrews, N. J. van Druten, D. S. Durfee, D. M. Kurn, and K. W., Phys Rev Lett **75**, 3969 (1995).

[56] C. C. Bradley, C. A. Sackett, J. J. Tollett, and R. G. Hulet, Phys. Rev. Lett. **75**, 1687 (1995).

[57] H. J. Lewandowski, D. M. Harber, D. L. Whitaker, and E. A. Cornell, Journal of Low Temperature Physics **132**, 309.

[58] O. J. Luiten, M. W. Reynolds, and J. T. M. Walraven, Phys. Rev. A **53**, 381 (1996).

[59] C. Raman, M. Köhl, R. Onofrio, D. S. Durfee, C. E. Kuklewicz, Z. Hadzibabic, and W. Ketterle, Phys. Rev. Lett. **83**, 2502 (1999).

[60] M. R. Andrews, C. G. Townsend, H.-J. Miesner, D. S. Durfee, D. M. Kurn, and W. Ketterle, Science **275**, 637 (1997).

[61] K. W. Madison, F. Chevy, W. Wohlleben, and J. Dalibard, Phys. Rev. Lett. **84**, 806 (2000).

[62] P. C. Haljan, I. Coddington, P. Engels, and E. A. Cornell, Phys. Rev. Lett. **87**, 210403 (2001).

[63] M. R. Matthews, B. P. Anderson, P. C. Haljan, D. S. Hall, C. E. Wieman, and E. A. Cornell, Phys. Rev. Lett. **83**, 2498 (1999).

[64] J. R. Abo-Shaeer, C. Raman, J. M. Vogels, and W. Ketterle, Science **292**, 476 (2001).

[65] H. Feshbach, Annals of Physics **19**, 287 (1962).

[66] C. Chin, R. Grimm, P. Julienne, and E. Tiesinga, Rev. Mod. Phys. **82**, 1225 (2010).

[67] S. B. Papp, J. M. Pino, and C. E. Wieman, Phys. Rev. Lett. **101**, 040402 (2008).

[68] G. Modugno, M. Modugno, F. Riboli, G. Roati, and M. Inguscio, Phys. Rev. Lett. **89**, 190404 (2002).

[69] D. J. McCarron, H. W. Cho, D. L. Jenkin, M. P. Köppinger, and S. L. Cornish, Phys. Rev. A **84**, 011603 (2011).

[70] C. J. Myatt, E. A. Burt, R. W. Ghrist, E. A. Cornell, and C. E. Wieman, Phys. Rev. Lett. **78**, 586 (1997).

[71] D. S. Hall, M. R. Matthews, J. R. Ensher, C. E. Wieman, and E. A. Cornell, Phys. Rev. Lett. **81**, 1539 (1998).

[72] V. Schweikhard, I. Coddington, P. Engels, S. Tung, and E. A. Cornell, Phys. Rev. Lett. **93**, 210403 (2004).

[73] H. M. Price, O. Zilberberg, T. Ozawa, I. Carusotto, and N. Goldman, Phys. Rev. Lett. **115**, 195303 (2015).

[74] Y.-J. Lin, R. L. Compton, K. Jimenez-Garcia, J. V. Porto, and I. B. Spielman, Nature **462**, 628 (2009).

[75] Y.-J. Lin, K. Jimenez-Garcia, and I. B. Spielman, Nature **471**, 83 (2011).

[76] Y. A. Bychkov and E. I. Rashba, J. Phys. C **17**, 6039 (1984).

[77] G. Dresselhaus, Phys. Rev. **100**, 580 (1955).

[78] C. Hamner, Y. Zhang, M. A. Khamehchi, M. J. Davis, and P. Engels, Phys. Rev. Lett. **114**, 070401 (2015).

[79] J. Struck, J. Simonet, and K. Sengstock, Phys. Rev. A **90**, 031601 (2014).

[80] C. J. Kennedy, G. A. Siviloglou, H. Miyake, W. C. Burton, and W. Ketterle, Phys. Rev. Lett. **111**, 225301 (2013).

[81] A. K. Nguyen and A. Sudbø, Phys. Rev. B **60**, 15307 (1999).

[82] B. M. Anderson, G. Juzeliūnas, V. M. Galitski, and I. B. Spielman, Phys. Rev. Lett. **108**, 235301 (2012).

[83] D. Toniolo and J. Linder, Phys. Rev. A **89**, 061605 (2014).

[84] W. S. Cole, S. Zhang, A. Paramekanti, and N. Trivedi, Phys. Rev. Lett. **109**, 085302 (2012).

[85] K. Fossheim and A. Sudbø, *Superconductivity: Physics and Applications* (Wiley, 2005).

[86] J. Bardeen, L. N. Cooper, and J. R. Schrieffer, Phys. Rev. **106**, 162 (1957).

[87] J. G. Bednorz and K. A. Müller, Zeitschrift für Physik B Condensed Matter **64**, 189.

[88] A. Abrikosov, J. Phys. Chem. Solids **2**, 199 (1957).

[89] T. A. Bojesen, E. Babaev, and A. Sudbø, Phys. Rev. B **88**, 220511 (2013).

[90] T. A. Bojesen, E. Babaev, and A. Sudbø, Phys. Rev. B **89**, 104509 (2014).

[91] T. Bojesen and A. Sudbø, Journal of Superconductivity and Novel Magnetism **28**, 3193 (2015).

[92] S. Mo, J. Hove, and A. Sudbø, Phys. Rev. B **65**, 104501 (2002).

[93] J. Smiseth, E. Smørgrav, E. Babaev, and A. Sudbø, Phys. Rev. B **71**, 214509 (2005).

[94] Villain, J., J. Phys. France **36**, 581 (1975).

[95] C. Dasgupta and B. I. Halperin, Phys. Rev. Lett. **47**, 1556 (1981).

[96] A. K. Nguyen and A. Sudbø, Phys. Rev. B **58**, 2802 (1998).

[97] L. Onsager, Nuovo Cimento **6**, Suppl. No. 2, 249 (1949).

[98] R. P. Feynman, Progress in Low Temperature Physics **1** (1955).

[99] E. K. Dahl, E. Babaev, S. Kragset, and A. Sudbø, Phys. Rev. B **77**, 144519 (2008).

[100] H. Kleinert, *Gauge Fields in Condensed Matter* (World Scientific, 1989).

[101] K. A. H. Sellin and E. Babaev, Phys. Rev. B **93**, 054524 (2016).

Paper I

Fluctuation effects in rotating Bose-Einstein condensates with broken $\mathrm{SU}(2)$*and* $\mathrm{U}(1) \times \mathrm{U}(1)$ *symmetries in the presence of intercomponent density-density interactions*

Physical Review A **91**, 013605 (2015)

Fluctuation effects in rotating Bose-Einstein condensates with broken SU(2) and U(1) × U(1) symmetries in the presence of intercomponent density-density interactions

Peder Notto Galteland,[1] Egor Babaev,[2] and Asle Sudbø[1]
[1]*Department of Physics, Norwegian University of Science and Technology, N-7491 Trondheim, Norway*
[2]*Department of Theoretical Physics, The Royal Institute of Technology, 10691 Stockholm, Sweden*
(Received 16 October 2014; published 6 January 2015)

Thermal fluctuations and melting transitions for rotating single-component superfluids have been intensively studied and are well understood. In contrast, the thermal effects on vortex states for two-component superfluids with density-density interaction, which have a much richer variety of vortex ground states, have been much less studied. Here, we investigate the thermal effects on vortex matter in superfluids with U(1) × U(1) broken symmetries and intercomponent density-density interactions, as well as the case with a larger SU(2) broken symmetry obtainable from the [U(1) × U(1)]-symmetric case by tuning scattering lengths. In the former case we find that, in addition to first-order melting transitions, the system exhibits thermally driven phase transitions between square and hexagonal lattices. Our main result, however, concerns the case where the condensate exhibits SU(2) symmetry, and where vortices are not topological. At finite temperature, the system exhibits effects which do not have a counterpart in single-component systems. Namely, it has a state where thermally averaged quantities show no regular vortex lattice, yet the system retains superfluid coherence along the axis of rotation. In such a state, the thermal fluctuations result in transitions between different (nearly) degenerate vortex states without undergoing a melting transition. Our results apply to multicomponent Bose-Einstein condensates, and we suggest how to detect some of these unusual effects experimentally in such systems.

DOI: 10.1103/PhysRevA.91.013605 PACS number(s): 67.85.Fg, 67.25.dk, 67.60.Bc, 67.85.Jk

I. INTRODUCTION

Bose-Einstein condensates (BECs) with a multicomponent order parameter, and the topological defects such systems support, represent a topic of great current interest in condensed matter physics [1–15]. Such multicomponent condensates may be realized as mixtures of different atoms, mixtures of different isotopes of an atom, or mixtures of different hyperfine spin states of an atom. The interest in such condensates from a fundamental physics point of view is mainly attributed to the fact that one may tune various interaction parameters over a wide range in a BEC. This enables the study of a variety of physical effects which are not easily observed in other superfluid systems such as ^{3}He and ^{4}He.

The behavior of a single-component BEC under rotation is well known. The ground state is a hexagonal lattice of vortex defects which melts to a vortex liquid via a first-order phase transition. This is well described by the London model, where amplitude fluctuations may be ignored. Over the years, in the context of studying vortex lattice melting in high-T_c superconductors, many works have confirmed this through numerical Monte Carlo simulations for systems in the frozen gauge, three-dimensional (3D) *XY*, and Villain approximations [16–25], as well as in the lowest-Landau-level approximation [26], and by mapping it to a model of 2D bosons [27]. Single-component condensates have been available experimentally for quite some time [28,29], and the hexagonal lattice ground state has been verified [30].

Condensates with two components of the order parameter have also been studied extensively. Analytical works focusing on determining the $T = 0$ ground states have demonstrated a range of interesting possible lattice structures [5,6,10,13,14,31]. By varying the ratio between inter- and intracomponent couplings, the ground-state lattice undergoes a structural change from hexagonal symmetry through square symmetry to double-core lattices and interwoven sheets of vortices. Similar systems with three components have also been studied [15]. Experimentally, spinor condensates have been realized in two general classes of systems. The first option is to use one species of atoms, usually rubidium, and prepare it in two separate hyperfine spin states [1,2]. Vortices [3] and vortex lattices [7] have been realized in these binary mixtures, where both hexagonal and square vortex lattice states were observed. The other option is to mix condensates of two different species of atoms [4,12]. The use of Feshbach resonances [32,33] allows direct tuning of the scattering lengths, and by extension the inter- and intracomponent interactions of multicomponent condensates [8,9,11].

In this paper, we consider a specific model of a two-component BEC, which has the full range of fluctuations of the order-parameter field included, as well as intercomponent density-density interactions. We consider the model with U(1) × U(1) and as SU(2) symmetries. For the U(1) × U(1) case, we find a succession of square and hexagonal vortex ground-state patterns as the intercomponent interaction strength is varied, along with the possibility of thermal reconstruction from a square to a hexagonal vortex lattice as temperature is reduced.

The SU(2)-symmetric case is interesting and experimentally realizable. In this case U(1) vortices are no longer topological, in contrast to the [U(1) × U(1)]-symmetric case. In this case, when fluctuation effects are included we find a highly unusual vortex state where there is no sign of any vortex lattice. Nonetheless, global phase coherence persists. This state of vortex matter is a direct consequence of massless amplitude fluctuations in the order parameter, when the broken symmetry of the system is SU(2). At the SU(2) point, but at lower temperatures, we also observe dimerized vortex ground-state patterns.

The paper is organized as follows. The model and definitions of relevant quantities are presented in Sec. II. The technical details of the Monte Carlo simulations are briefly considered in Sec. III. In Sec. IV, the results are presented and discussed. In Sec. V, we discuss how to experimentally verify the results we find. Some technical details and the investigation of the order of the melting transitions with full amplitude distributions included, for the cases $N = 1$ and $N = 2$, are relegated to Appendixes.

II. MODEL AND DEFINITIONS

In this section we present the model used in the paper, first in a continuum description and then on a three-dimensional cubic lattice appropriate for Monte Carlo simulations. The relevant quantities for the discussion are also defined.

A. Continuum model

We consider a general Ginzburg-Landau (GL) model of an N-component Bose-Einstein condensate, coupled to a uniform external field, which in the thermodynamical limit is defined as

$$\mathcal{Z} = \int \prod_{i}^{N} \mathcal{D}\psi_i' e^{-\beta H}, \tag{1}$$

where

$$H = \int d^3r \left[\sum_{i=1}^{N} \sum_{\mu=1}^{3} \frac{\hbar^2}{2m_i} \left| \left(\partial_\mu - i \frac{2\pi}{\Phi_0} A_\mu' \right) \psi_i' \right|^2 + \sum_{i}^{N} \alpha_i' |\psi_i'|^2 + \sum_{i,j=1}^{N} g_{ij}' |\psi_i'|^2 |\psi_j'|^2 \right] \tag{2}$$

is the Hamiltonian. Here, the field A_μ' formally appears as a nonfluctuating gauge field and parametrizes the angular velocity of the system. The fields ψ_i' are dimensionful complex fields, i and j are indices running from 1 to N denoting the component of the order parameter (a "color" index), α_i' and g_{ij}' are Ginzburg-Landau parameters, Φ_0 is the coupling constant to the rotation induced vector potential, and m_i is the particle mass of species i. For mixtures consisting of different atoms or different isotopes of one atom, the masses will depend on the index i, while for mixtures consisting of atoms in different hyperfine spin states, the masses are independent of i. The inter- and intracomponent coupling parameters g_{ij}' are related to real inter- and intracomponent scattering lengths a_{ij} in the following way:

$$g_{ii}' = \frac{4\pi\hbar^2 a_{ii}}{m_i}, \tag{3}$$

$$g_{ij}' = \frac{8\pi\hbar^2 a_{ij}}{m_{ij}} \quad (i \neq j), \tag{4}$$

where $m_{ij} = m_i m_j/(m_i + m_j)$ is the reduced mass. In this paper we focus on using BECs of homonuclear gases with several components in different hyperfine states; hence $m_i = m \; \forall \; i$. Intercomponent drag in BEC mixtures has been considered in previous works using Monte Carlo simulation (ignoring amplitude fluctuations), but we will not consider this case here [34–38].

We find it convenient for our purposes to rewrite (2) in the following form, the details of which are relegated to Appendix A:

$$H = \int d^3r \left[\frac{1}{2} (D_\mu \Psi)^\dagger (D_\mu \Psi) + V(\Psi) \right]. \tag{5}$$

Here, Ψ is an N-component spinor of dimensionless complex fields, which consists of an amplitude and a phase, $\psi_i = |\psi_i| \exp(i\theta_i)$, $D_\mu = \partial_\mu - i\frac{2\pi}{\Phi_0} A_\mu'$ is the covariant derivative, and summation over repeated spatial indices is implied. We neglect, for simplicity, the presence of a trap and the centrifugal part of the potential. We consider only the case where the vector potential is applied to each component of Ψ, as follows from the fact that the masses are independent of species index i.

We have studied this model in detail with $N = 2$, where we write the potential in the form

$$V(\Psi) = \eta(|\Psi|^2 - 1)^2 + \omega(\Psi^\dagger \sigma_z \Psi)^2. \tag{6}$$

This formulation is more relevant for our discussion, as it immediately highlights the symmetry of Ψ, as well as the soft constraints applied to it. The details of the reparametrization are shown in Appendix A.

Note that Eq. (6) may also be rewritten in the form (correct up to an additive constant term)

$$V = (\eta + \omega)(|\psi_1|^4 + |\psi_2|^4) + 2(\eta - \omega)|\psi_1|^2|\psi_2|^2. \tag{7}$$

Comparing with Eq. (2), we have $g_{11} = g_{22} \equiv g = \eta + \omega$ and $g_{12} = \eta - \omega$. The model features repulsive intercomponent interactions provided $\eta - \omega > 0$, and this is the case we will mainly focus on. We will however briefly touch upon the case $\eta - \omega < 0$ corresponding to an attractive intercomponent density-density interaction, which leads to ground states with overlapping vortices in components 1 and 2. Normalizability of the individual order-parameter components, or equivalently boundedness from below of the free energy, requires that $\eta + \omega > 0$. Thus, while $\omega > \eta$ makes physical sense, $\omega < -\eta$ does not. In this paper, we assume $\eta > 0$ and $\omega \geqslant 0$.

Two-component BECs feature considerably richer physics than a single-component BEC. Since the gauge field parametrizing the rotation of the system is nonfluctuating, there is no gauge-field-induced current-current interaction between the two condensates (unlike in multicomponent superconductors). The only manner in which the two superfluid condensates interact is via the intercomponent density-density interaction $2(\eta - \omega)|\psi_1|^2|\psi_2|^2$. In the limit where the amplitudes of each individual component are completely frozen and uniform throughout the system, one recovers the physics of two decoupled 3D XY models, with a global U(1) × U(1) symmetry. The density-density interaction between ψ_1 and ψ_2 leads to interactions between the topological defects excited in each component. As a result, a first-order melting of two decoupled hexagonal lattices is not the only possible phenomenon that could take place. Previous experiments and numerical studies have reported a structural change of the ground state from a hexagonal to a square lattice of vortices as the effective intercomponent coupling is increased [5–7]. This corresponds

to increasing the ratio η/ω in our case. As we will see below, other unusual phenomena can also occur, notably when thermal fluctuations are included.

One special case of the model deserves some extra attention. If one takes the limit $\omega \to 0$ in Eq. (6) the symmetry of the model is expanded to a global SU(2) symmetry. One may then shift densities from one component to the other with impunity, as long as $|\psi_1|^2 + |\psi_2|^2$ is left unchanged. This effectively leads to massless amplitude fluctuations in the components of the order parameter. Therefore, it is possible to unwind a 2π phase winding in one component by letting the amplitude of the same component vanish. The introduction of this higher symmetry leads to very different vortex ground states than what are found in the [U(1) × U(1)]-symmetric case with $\omega \neq 0$.

B. Separation of variables

In multicomponent GL models complex objects, such as combinations of vortices of different colors, are often of interest. In general, it is possible to rewrite an N-component model coupled to a gauge field, fluctuating or not, in terms of one mode coupled to the field and $N-1$ neutral modes [39,40]. For a more general discussion of charged and neutral modes in the presence of amplitude fluctuations see Refs. [41] and [42]. Considering only the kinetic part of the two-component Hamiltonian H_k, we have the following expression:

$$H_k = \frac{1}{2|\Psi|^2}|\psi_1^*\partial_\mu\psi_1 + \psi_2^*\partial_\mu\psi_2 - iA_\mu|\Psi|^2|^2 + \frac{1}{2|\Psi|^2}|\psi_1\partial_\mu\psi_2 - \psi_2\partial_\mu\psi_1|^2. \quad (8)$$

Hence, the first mode couples to the applied rotation, while the second does not. This corresponds to the phase combinations $\theta_1 + \theta_2$ and $\theta_1 - \theta_2$, respectively.

C. Lattice regularization

In order to perform simulations of the continuum model, we define the field Ψ on a discrete set of coordinates, i.e., $\Psi(\mathbf{r}) \to \Psi_{\mathbf{r}}$, where $\mathbf{r} \in (i\hat{\mathbf{x}} + j\hat{\mathbf{y}} + k\hat{\mathbf{z}}|\ i,j,k = 1,\ldots,L)$. Here, L is the linear size in all dimensions; the system size is $V = L^3$. We use periodic boundary conditions in all directions. By replacing the differential operator by a gauge-invariant forward difference

$$\left(\frac{\partial}{\partial r_\mu} - iA_\mu(\mathbf{r})\right)\Psi(\mathbf{r}) \to \frac{1}{a}(\Psi_{\mathbf{r}+a\hat{\boldsymbol{\mu}}}e^{-i(2\pi/\Phi_0)aA'_{\mu,\mathbf{r}}} - \Psi_{\mathbf{r}}), \quad (9)$$

and introducing real phases and amplitudes $\psi_{\mathbf{r},i} = |\psi_{\mathbf{r},i}|e^{i\theta_{\mathbf{r},i}}$ we can rewrite the Hamiltonian:

$$H = \sum_{\substack{\mathbf{r},\hat{\boldsymbol{\mu}}\\ i}} |\psi_{\mathbf{r}+\hat{\boldsymbol{\mu}},i}||\psi_{\mathbf{r},i}|\cos(\theta_{\mathbf{r}+\hat{\boldsymbol{\mu}},i} - \theta_{\mathbf{r},i} - A_{\mu,\mathbf{r}}) + \sum_{\mathbf{r}} V(\Psi_{\mathbf{r}}). \quad (10)$$

The lattice spacing is chosen so that it is smaller than the relevant length scale of variations of the amplitudes. A dimensionless vector potential A_μ has also been introduced. See Appendix A for details. We denote the argument of the cosine as $\chi^\mu_{\mathbf{r},i}$, as a shorthand.

D. Observables

An important and accessible quantity when exploring phase transitions is the specific heat of the system,

$$c_V = \beta^2\frac{\langle H^2\rangle - \langle H\rangle^2}{L^3}. \quad (11)$$

While crossing a first-order transition there is some amount of latent heat in the system, manifesting itself as a δ-function peak of the specific heat in the thermodynamic limit. On the lattice one expects to see a sharp peak, or anomaly, at the transition. This is used to characterize the transition as first order.

A useful measure of the global phase coherence of the system is the helicity modulus, which is proportional to the superfluid density. It serves as a probe of the transition from a superfluid to a normal fluid. In the disordered phase, the moduli in all directions are zero, characterizing an isotropic normal-fluid phase. The cause of this is a vortex loop blowout. Moving to the ordered phase, all moduli evolve to a finite value. If we turn on the external field we still have zero coherence in all directions in the disordered phase. In the ordered phase, however, the helicity modulus along the direction of the applied rotation jumps to the finite value through a first-order transition. The value of the transverse moduli will remain zero. Formally, the helicity modulus is defined as a derivative of the free energy with respect to a general, infinitesimal phase twist along r_μ [43]. That is, we perform the replacement

$$\theta_{\mathbf{r},i} \to \theta'_{\mathbf{r},i} = \theta_{\mathbf{r},i} - b_i\delta_\mu r_\mu \quad (12)$$

in the free energy, and calculate

$$\Upsilon_{\mu,(b_1,b_2)} = \left.\frac{\partial^2 F[\theta']}{\partial\delta_\mu^2}\right|_{\delta_\mu=0}. \quad (13)$$

Here, $b = (b_1,b_2)$ represents some combination of the phases θ_1 and θ_2, $b_1\theta_1 + b_2\theta_2$. To probe the individual moduli, b_i is chosen as $b_i = (1,0)$ or $b_i = (0,1)$. The composite phase-sum variable is represented by the choice $b_i = (1,1)$, while $b_i = (1,-1)$ is the phase difference. Generally, for a two-component model, the helicity modulus can be written as the sum of two indivudual moduli and a cross term [36,40],

$$\Upsilon_{\mu,(b_1,b_2)} = b_1^2\Upsilon_{\mu,(1,0)} + b_2^2\Upsilon_{\mu,(0,1)} + 2b_1b_2\Upsilon_{\mu,12}. \quad (14)$$

For the model considered in this paper, the individual helicity moduli can be written as

$$\langle\Upsilon_{\mu,i}\rangle = \frac{1}{V}\left[\left\langle\sum_{\mathbf{r}}\psi_{\mathbf{r}_i}\psi_{\mathbf{r}+\hat{\boldsymbol{\mu}},i}\cos\left(\chi^\mu_{\mathbf{r},i}\right)\right\rangle - \beta\left\langle\left(\sum_{\mathbf{r}}\psi_{\mathbf{r},i}\psi_{\mathbf{r}+\hat{\boldsymbol{\mu}},i}\sin\left(\chi^\mu_{\mathbf{r},i}\right)\right)^2\right\rangle\right], \quad (15)$$

while the mixed term has the form

$$\langle \Upsilon_{\mu,12} \rangle = -\beta \left\langle \left(\sum_{\mathbf{r}} |\psi_{\mathbf{r},1}||\psi_{\mathbf{r}+\hat{\boldsymbol{\mu}},1}| \sin\left(\chi^{\mu}_{\mathbf{r},1}\right) \right) \times \left(\sum_{\mathbf{r}} |\psi_{\mathbf{r},2}||\psi_{\mathbf{r}+\hat{\boldsymbol{\mu}},2}| \sin\left(\chi^{\mu}_{\mathbf{r},2}\right) \right) \right\rangle. \quad (16)$$

We denote the helicity modulus of the phase sum $\Upsilon_{\mu,(1,1)}$ as Υ^{+}_{μ} as a shorthand.

The structure factor $S_i(\mathbf{q}_\perp)$ can be used to determine the underlying symmetry of the vortex lattice. Square and hexagonal vortex structures will manifest themselves as four or six sharp Bragg peaks in reciprocal space. In a vortex liquid phase one expects a completely isotropic structure factor. The structure factor is defined as the Fourier transform of the longitudinally averaged vortex density $\langle n_i(\mathbf{r}_\perp)\rangle$, which is subsequently thermally averaged,

$$S_i(\mathbf{q}_\perp) = \frac{1}{L_x L_y f} \left\langle \left| \sum_{\mathbf{r}_\perp} n_i(\mathbf{r}_\perp) e^{-i\mathbf{r}_\perp \cdot \mathbf{q}_\perp} \right| \right\rangle. \quad (17)$$

Here $n_i(\mathbf{r}_\perp)$ is the density of vortices of color i averaged over the z direction,

$$n_i(\mathbf{r}_\perp) = \frac{1}{L_z} \sum_{z} n_i(\mathbf{r}_\perp, z), \quad (18)$$

and $\mathbf{r}_\perp$ is $\mathbf{r}$ projected onto a layer of the system with a given z coordinate. The vortex density is calculated by traversing each plaquette of the lattice, adding the factor $\chi^{\mu}_{i,\mathbf{r}}$ of each link. Each time we have to add (or subtract) a factor of 2π in order to bring this sum back into the primary interval of $(-\pi,\pi]$ a vortex of color i and charge $+1$ (-1) is added to this plaquette.

In addition to the structure factor, we look at thermally averaged vortex densities $\langle n_i(\mathbf{r}_\perp)\rangle$ as well as thermally and longitudinally averaged amplitude densities $\langle |\psi_i|^2(\mathbf{r}_\perp)\rangle$, defined similarly to Eq. (18),

$$|\psi_i|^2(\mathbf{r}_\perp) = \frac{1}{L_z} \sum_{z} |\psi_i|^2(\mathbf{r}_\perp, z). \quad (19)$$

This provides an overview of the real-space configuration of the system.

When including amplitude fluctuations, which, when the potential term is disregarded, are unbounded from above, it is of great importance to make sure all energetically allowed configurations are included. To this end, we measured the probability distribution of $|\psi_i|^2$, $P(|\psi_i|^2)$ during the simulations by making a histogram of all field configurations at each measure step, and normalizing its underlying area to unity in postprocessing.

The uniform rotation applied to the condensates is implemented in the Landau gauge:

$$\mathbf{A} = (0, 2\pi f x, 0), \quad (20)$$

where f is the density of vortices in a single layer. Note that this implies a constraint $Lf \in (1,2,3,\ldots)$ due to the periodic boundary conditions. When probing a first-order melting transition, it is important to choose a filling fraction large enough that an anomaly in the specific heat is detectable. However, if the filling fraction is too large, one may transition directly from a vortex liquid into a pinned solid, completely missing the *floating solid* phase of interest. This scenario is characterized by a sharp jump in not only the longitudinal, but also the transverse helicity modulus [44,45]. One must therefore chose f small enough to assure that the vortex line lattice is in a floating solid phase when it melts.

III. DETAILS OF THE MONTE CARLO SIMULATIONS

The simulations were performed using the Metropolis-Hastings algorithm [46,47]. Phase angles were defined as $\theta \in (-\pi,\pi]$, and amplitudes as $|\psi|^2 \in (0, 1+\delta\psi]$. The choice of $\delta\psi$ will be discussed further, as it is important to ensure inclusion of the full spectrum of fluctuations. Both the phases and the amplitudes were discretized to allow the use of tables for trigonometric and square root functions in order to speed up computations. We typically simulated systems of size $L^3 = 64^3$, with sizes up to $L^3 = 128^3$ used to resolve anomalies in the specific heat. We used 10^6 Monte Carlo sweeps per inverse temperature step, and up to 10^7 close to the transition. 10^5 additional sweeps were typically used to thermalize the system. In the simulations, we examined time series of the internal energies taken during both the thermalization runs and the measurement runs to make sure the simulation converged. One sweep consists of picking a new random configuration for each of the four field variables separately in succession, at each lattice site. Measurements were usually performed with a period of 100 sweeps, in order to avoid correlations. Ferrenberg-Swendsen multihistogram reweighting was used to improve statistics around simulated data points, and jackknife estimates of the errors are used.

Figure 1 shows the probability distribution of the amplitudes, $\mathcal{P}(|\psi_i|^2)$. We get a peaked distribution for finite ω. On the other hand, when $\omega = 0$, this is no longer the case. The distribution now approaches a uniform distribution on the interval $(0,1]$. In this case the parameter η serves to control

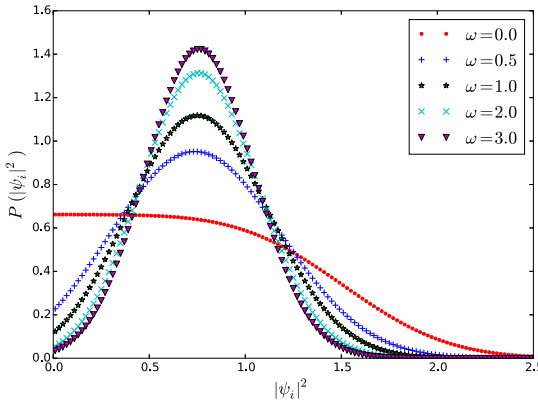

FIG. 1. (Color online) The probability distribution of the amplitudes, $\mathcal{P}(|\psi_i|^2)$, for $N = 2$, at inverse temperature $\beta = 1.20$, $f = 1/32$, and $\eta = 2$, with ω values from 0 to 3. The distribution is completely symmetric in i.

the approach to uniformity, $\eta \to \infty$ corresponding to the CP^1 limit.

With these initial simulation runs as a basis, we choose $\delta\psi$ appropriately in order to capture the entire spectrum of fluctuations.

IV. RESULTS OF THE MONTE CARLO SIMULATIONS

In this section, the η-ω phase diagram of ground states is explored by slow cooling and examination of vortex and amplitude densities, as well as structure factors. In addition to the expected hexagonal and square vortex ground states, several interesting regions of the parameter space are investigated further. A special case between the square and the hexagonal regions of the phase diagram is discovered, where the lattice first forms a square structure, but thermally reconstructs into a hexagonal lattice as the temperature is decreased further. Furthermore, we consider in detail the $\omega = 0$ line in the phase diagram, where we discover additional vortex fluctuation effects. For $\omega = 0$, the system features an SU(2) symmetry. An unusual feature is an interesting state with global phase coherence, but without a regular vortex lattice. In this case ordinary vortices do not have topological character due to SU(2) symmetry. Additionally, we obtain several interesting vortex structures characterized by dimerlike configurations at lower temperatures. Here, we observe honeycomb lattices, or double-core lattices, and stripe configurations, consistent with previous $T = 0$ results [6].

We also examine the melting transitions of the square and hexagonal lattices with the full amplitude distribution included, as well as the melting of the hexagonal lattice in a model with $N = 1$ as a benchmark of the method. To classify the transition, we look at thermal averages of the specific heat, helicity moduli, and vortex structure factors. These results are presented in Appendixes B and C.

A. The η-ω phase diagram

Adding a second matter field and intercomponent density-density interactions results in a considerably richer set of ground states than in the single-component case. In the absence of a fluctuating part of the rotational "gauge field" there will be no gauge-field-mediated intercomponent current-current interactions. For $\eta - \omega < 0$ (η,$\omega > 0$) the effective intercomponent density-density coupling $\eta - \omega$ is negative and the ground state of each color of condensate has a hexagonal symmetry, as shown in Fig. 2(a). If, on the other hand $\eta - \omega > 0$, the intercomponent coupling becomes positive. Now, for sufficiently large ratios η/ω, the vortices arrange themselves into two interpenetrating square lattices, shown in Fig. 2(b). The value of the ratio η/ω for which the lattice reconstructs depends on the strength of the rotation f. If we neglect fluctuations, $\eta - \omega < 0$ is expected to result in a hexagonal lattice, while $\eta - \omega > 0$ leads to a square lattice for sufficiently large η/ω.

The physics of the reconstruction of the lattice can be explained by modulations of the amplitude fields. The existence of static periodic amplitude modulations (density variations) is due to the presence of vortices. Without vortices ($f = 0$) and $\omega > 0$, the ground state is one where both amplitudes are

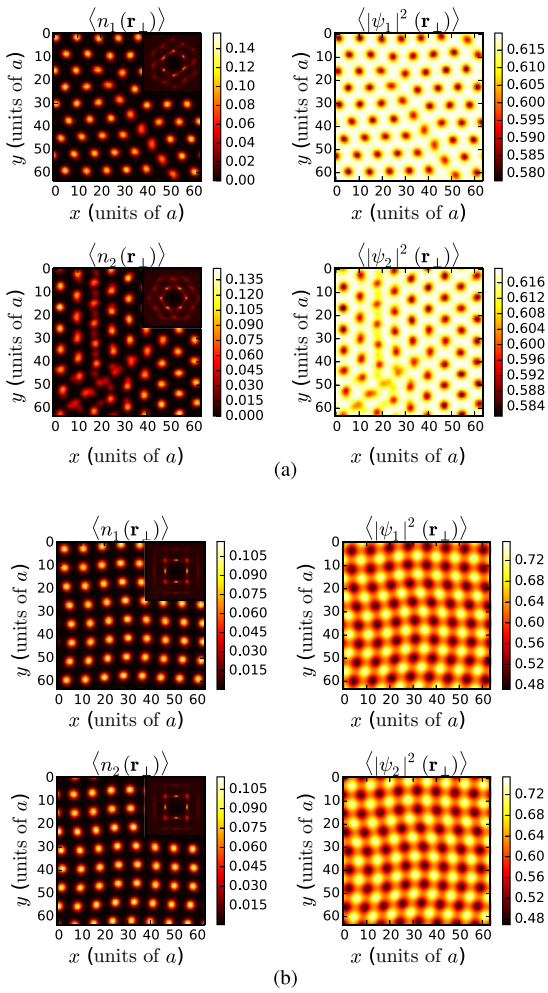

FIG. 2. (Color online) Representative configurations of the two main ordered phases in the U(1) × U(1) region. (a) shows a square structure at (η,ω) = (5.0,0.5), while (b) illustrates the hexagonal structure at (η,ω) = (5.0,5.0). Each subfigure shows vortex densities $\langle n_i(\mathbf{r}_\perp)\rangle$ in the left column, amplitude densities $\langle|\psi_i|^2(\mathbf{r}_\perp)$ in the right column, and structure factors (insets) of each component as indicated. The induced vortex density and inverse temperature are fixed to $f = 1/64$ and $\beta = 1.5$ in both subfigures.

equal and smooth. Vortices in one component tend to suppress locally the corresponding amplitude, which in turn means that the term $\eta(|\psi_1|^2 + |\psi_2|^2 - 1)^2$ enhances the amplitude of the other component. At small ω, i.e., large $\eta - \omega$, there is a strong tendency to form a square density lattice due to this intercomponent density-density interaction. Conversely, if ω is large enough compared to η, the density-density interaction is not strong enough to overcome the isotropic current-current interactions between same-species vortices. In other words if the current-current interactions dominate the interspecies density-density interactions, a hexagonal lattice is

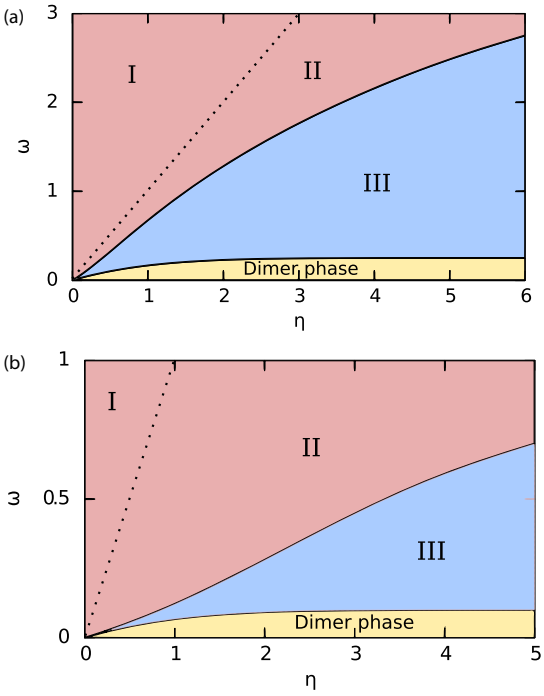

FIG. 3. (Color online) The η-ω phase diagram of the ground states for $f = 1/32$ (a) and $f = 1/64$ (b). The simulations were performed for a range of (η,ω) pairs to determine the zero-temperature ground state. Approximate demarcation lines for the phase boundaries separating hexagonal lattices, square lattices, and dimerized phases, were drawn from these results (solid lines). I denotes the phase where the hexagonal vortex lattices in the two components are cocentric, II denotes the case where the hexagonal lattices are intercalated, while III denotes the square lattice phase. The dotted line is the line $\omega = \eta$ at which the intercomponent density-density interaction $2(\eta - \omega)|\psi_1|^2|\psi_2|^2$ changes sign. See also Figs. 11 and 12 in Appendix D.

energetically favored over a square lattice, and vice versa. Note that similarly a square vortex lattice forms in two-component London models with dissipationless drag when there are competing inter- and intraspecies current-current vortex interactions [34,35].

Figures 3(a) and 3(b) show the phase diagrams for filling fractions $f = 1/32$ and $f = 1/64$, respectively. The separation line is approximate and drawn from several separate simulations.

To clarify what is going in Figs. 3(a) and 3(b), we refer to Figs. 11 and 12 in Appendix D. Here, we show tableaus to illustrate in more detail how the density and vortex lattices reconstruct at a temperature well below any melting temperatures of the vortex (and density) lattices, as the density-density interaction $2(\eta - \omega)|\psi_1|^2|\psi_2|^2$ is varied. Specifically, we fix the interaction parameter η, as well as the inverse temperature β and filling fraction f, while increasing the parameter ω. This reduces the effective intercomponent density-density interaction which favors a square lattice, until the lattice reconstructs from square to hexagonal symmetry.

When $\eta = \omega$, it is seen from Eq. (7) that the two components of the order parameter decouple. For $\omega < \eta$ the intercomponent density-density interaction is repulsive, while it is attractive for $\omega > \eta$. For $\omega < \eta$, the vortex lattices (and the density lattices) are intercalated, while for $\omega > \eta$ they are cocentric. In Figs. 3(a) and 3(b) we illustrate the demarcation line between the two situations as a dotted line in the hexagonal phase.

Beyond the square and hexagonal lattices we also observe dimer configurations of vortices for $\omega = 0$, which will be discussed further below. The calculations are consistent with the ground states obtained in Refs. [6] and [10].

B. Thermally induced reconstruction of vortex lattices

Now we move to discussion of the effects of thermal fluctuations in these systems. Figure 4 shows the vortex densities in component 1 in reciprocal space, as β is increased, i.e., as temperature is reduced, in a temperature range below where the lattice melts. The actual melting of the two-component lattice is discussed in Sec. IV C. We fix the filling fraction $f = 1/64$, as well as the interaction parameters $\eta = 2$ and $\omega = 0.5$.

For the highest temperatures shown in Fig. 4 the vortex lattice is square. Upon cooling the system, the vortex lattice reconstructs into a hexagonal lattice, consistent with the ground-state phase diagram of Fig. 3(b). The density-density interaction term $2(\eta - \omega)|\psi_1|^2|\psi_2|^2$ aids formation of a square lattice at higher temperatures, while the current-current interactions drive the lattice towards a hexagonal configuration when it is cooled further. This means that the free energy per vortex of the square lattice, which is lower than that of the hexagonal lattice at $\beta = 0.90$, has become larger than that of the hexagonal lattice when $\beta = 1.50$. This is essentially the combination of an energetic and an entropic effect. We observe this reconstruction not too far away from the demarcation line separating a square and a hexagonal vortex lattice. Deep inside the hexagonal phase in Fig. 3(b), we observe direct vortex lattice melting from a hexagonal lattice to a vortex liquid. We note that intermediate entropically stabilized vortex lattice phases were a subject of interesting investigation in the different system of U(1) × U(1) superconductors [48]; however, the vortex interaction form is different in our case.

C. SU(2) vortex states

The limit $\omega \to 0$ is quite different from the [U(1) × U(1)]-symmetric case $\omega \neq 0$. From Eq. (6), it is seen that the Hamiltonian is invariant under SU(2) transformations of Ψ. Vortices, which are topological in a U(1) × U(1) model, are no longer topological in the SU(2) case. One may unwind a 2π phase winding by entirely transferring density of one component to the other, which may be done at zero energy cost.

Figure 5 shows one of the main results of this paper. These are simulations with SU(2) symmetry, i.e., $\omega = 0$, as well as $\eta = 5.0$ and $f = 1/64$. The top panel show the phase stiffness associated with the phase sum, Υ_μ^+. This is the physically relevant phase variable in this case, as it couples to the rotation.

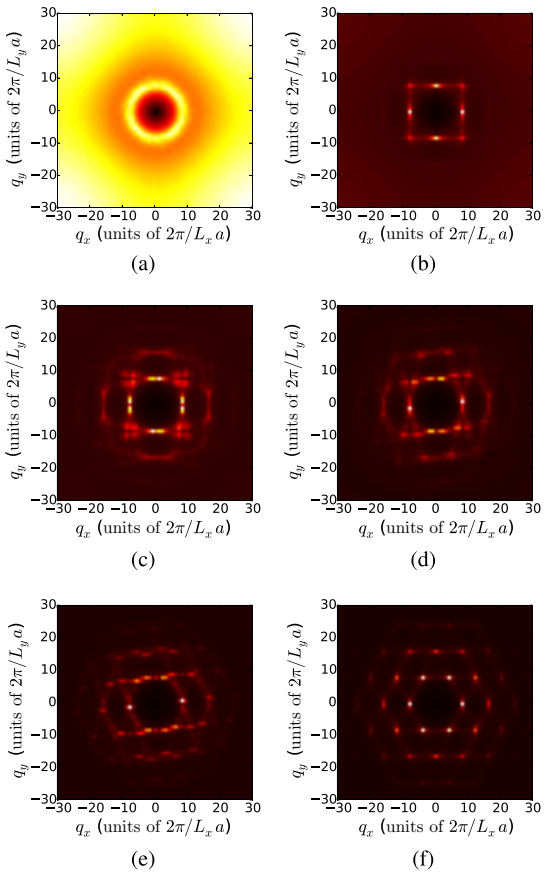

FIG. 4. (Color online) Thermally induced reconstruction from a square vortex lattice in either of the components at $\eta = 2, \omega = 0.5$, to a hexagonal vortex lattice, as β is increased. Here, $f = 1/64$. (a)–(f) show inverse temperatures $\beta = \{0.80, 0.90, 1.20, 1.30, 1.34, 1.38\}$, respectively. Each subfigure shows $S_1(\mathbf{q}_\perp)$ only; $S_2(\mathbf{q}_\perp)$ is identical. The physical reason for the reconstruction originates with the inter-component density-density interaction term $2(\eta - \omega)|\psi_1|^2|\psi_2|^2$), and is explained in detail in the text.

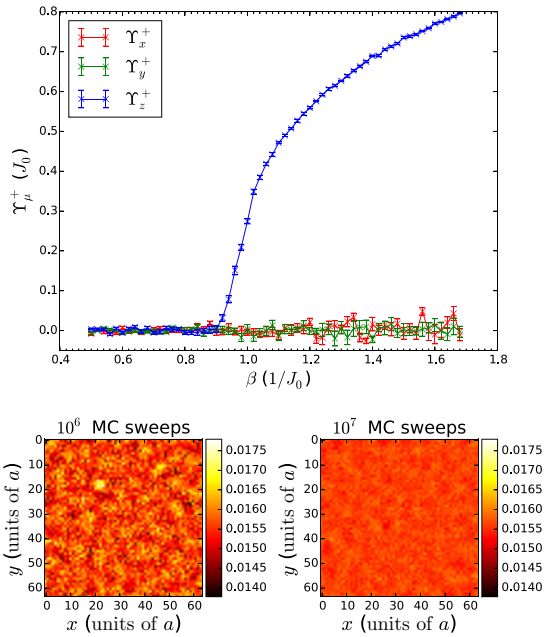

FIG. 5. (Color online) Illustration of the observed state with coherence along the direction of the rotation axis without a regular vortex lattice, seen only with SU(2) symmetry. The parameters used are $\omega = 0.0$, $\lambda = 5$, and $f = 1/64$. The top panel shows the helicity modulus of the phase sum, Υ_μ^+. The two bottom panels show the vortex densities $n_1(\mathbf{r}_\perp)$ at $\beta = 0.94$, where the z-directed modulus is clearly finite. The bottom left and bottom right panels are taken from simulations using 10^6 and 10^7 Monte Carlo sweeps, respectively. No apparent vortex line structure is seen here, and by increasing the number of Monte Carlo sweeps the variations of the vortex density are smoothed out further. Note how the value of the average vortex density seems to converge towards $1/64$.

We observe that the stiffness along the z direction becomes finite at an inverse temperature $\beta \sim 0.9$. This is what one would expect when a vortex lattice forms. However, the bottom panels, which show the vortex density of component 1 at $\beta = 0.94$, show no apparent signs of vortex ordering. Hence, we have an unusual situation. There is a relatively large β range where we have a finite z-directed helicity modulus of the phase sum, but no apparent ordering of induced vortices. A finite helicity modulus generally means that there are straight vortex lines with very little transverse fluctuations threading the entire system along the direction in question. In the U(1) picture this corresponds to a regular vortex lattice. For an SU(2) condensate, this is no longer the case. Large relative amplitude fluctuations can occur since they have zero energy cost in the ground state as the energy is no longer minimized by a preferential value of $|\psi_1|^2 - |\psi_2|^2$. This results in many (nearly) degenerate vortex states between which the system can fluctuate, thus greatly simplifying the effort of moving an entire, almost straight, vortex line. We are left with a phase where we have coherence along the z direction, but no regular vortex lattice appears in thermal averages. Nearly straight vortex lines will shift between a large number of degenerate, or nearly degenerate, states at a time scale shorter than a typical Monte Carlo run.

The bottom panels of Fig. 5 show some inhomogeneities of the vortex densities, exemplifying that this is not an ordinary vortex liquid with segments of vortex lines executing transverse meanderings along their direction, which would yield zero helicity modulus along the direction of the field-induced vortices. Rather, what we have is a superposition of many latticelike states of nearly straight vortex lines, where the fluctuations are largely collective excitations of entire nearly straight lines, rather than fluctuations of smaller segments of lines.

We emphasize again that these collective excitations originate with large amplitude fluctuations due to the SU(2) softness of the amplitudes of the components of the superfluid order parameter, rather than with phase fluctuations. Increasing the

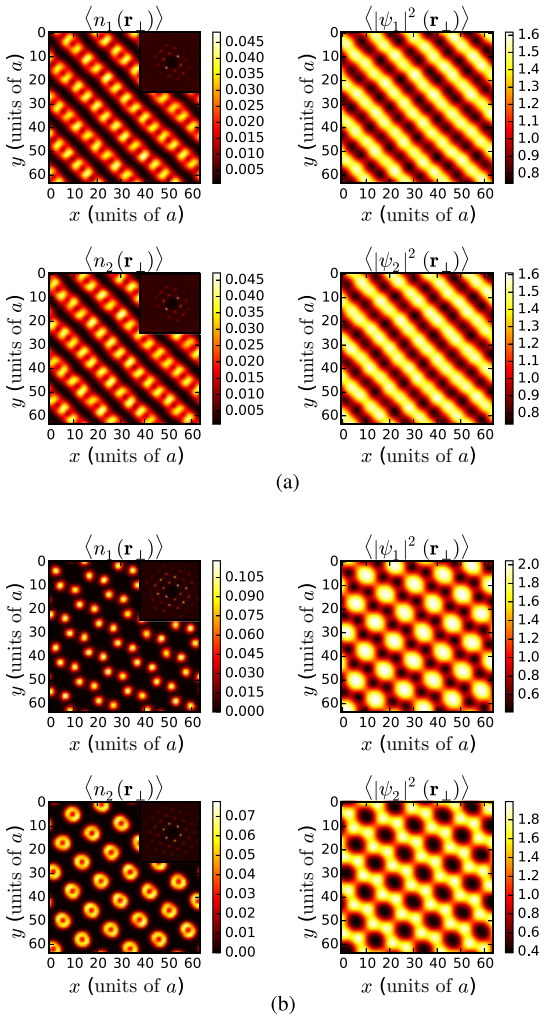

FIG. 6. (Color online) Two examples of SU(2) vortex configurations from a single simulation, for two different inverse temperatures. The parameters η, f, and ω are fixed in each subfigure, at $\eta = 1.0$, $\omega = 0.0$, and $f = 1/64$. (a) shows $\beta = 0.84$, while (b) shows $\beta = 1.50$. Each subfigure shows vortex densities $\langle n_i(\mathbf{r}_\perp)\rangle$ in the left column, amplitude densities $\langle|\psi_i|^2(\mathbf{r}_\perp)\rangle$ in the right column, and structure factors (insets) of each component as indicated. This illustrates the degeneracy of the vortex line lattice in the isotropic limit, as the configurations evolve when β is varied. See Appendix D for more details.

number of Monte Carlo sweeps by an order of magnitude smooths these variations out (without noticably altering the value of Υ_z^+), as seen in the bottom right panel of Fig. 5. Note how the average value of the vortex density seems to converge towards $1/64$. This is what we expect for a vortex lattice or liquid in a [U(1) × U(1)]-symmetric model, as the density of thermal vortices will average to zero, and f is the average flux density per plaquette.

As the system is cooled further, the movements of large vortex lines cease, and a regular vortex lattice appears. However, degeneracy must still be present, as the exact pattern formed by the lattice is distinctively different between simulations (keeping all parameters equal). The lattice also has a tendency to shift between configurations as the temperature is varied, below the temperature of initial vortex-lattice formation. We observe two distinct classes of vortex states, illustrated in Fig. 6. The two are stripes [Fig. 6(a)] and honeycomb lattices [Fig. 6(b)], both of which are seen in Ref. [6]. Note that these vortex densities are taken from a single simulation, after the lattice has formed. Within the accuracy of our simulations the obtained states are not metastable. The evidence of this is obtained by performing several independent runs from different initial configurations. Again, we refer to Appendix D, where Fig. 13 illustrates the degeneracy in the vortex line lattices obtained in the isotropic limit in further detail.

V. EXPERIMENTAL CONSIDERATIONS

Hexagonal and square lattices have already been observed in binary condensates of rubidium [7]. However, an SU(2) condensate has not been realized experimentally. In this section, we briefly outline under what circumstances an observation of an SU(2) vortex state may be feasible.

In order to experimentally realize SU(2) conditions, one requires a two-component BEC, where both intra- and intercomponent interactions are equal. As we have seen, the SU(2) physics crucially depends on this, since even minor deviations from this condition immediately yield U(1) × U(1) physics. This corresponds to $\omega = 0$ in our parametrization. Intra- and intercomponent density-density interactions are given in terms of scattering lengths. While tuning of these in an experiment is possible with Feshbach resonances, it may still be a challenge to tune two scattering lengths independently to be equal to a third, to arrive at the SU(2) point. From what is known for scattering lengths of real systems, it appears that a mixture of two species of the same atom, but in different hyperfine states, lends itself more readily to a realization of an SU(2) condensate than a mixture of different atoms or a mixture of different isotopes of the same atom. This is so, since in the former case, the relevant scattering lengths typically *a priori* are much more similar to each other than they are in more heterogeneous mixtures.

One promising candidate therefore appears to be a condensate of ^{87}Rb prepared in the two hyperfine states $|F = 1, m_f = 1\rangle \equiv |1\rangle$ and $|F = 2, m_f = -1\rangle \equiv |2\rangle$. In this system, the three relevant s-wave scattering lengths already have values close to the point of interest, $a_{11} = 100.4a_B$, $a_{22} = 95.00a_B$, and $a_{12} = 97.66a_B$, where a_B is the Bohr radius [2,49]. Reference [11] reports on a *magnetic* Feshbach resonance at a field of approximately 9.1 G, where control of a_{12} of the order of $10a_B$ is possible. Additionally, Ref. [50] reports on an *optical* Feshbach resonance of the state $|F = 1, m_F = -1\rangle$, able to tune the intracomponent scattering length, using two Raman lasers, with detuning parameters approximately given by $\Delta_1 = 2\pi \times 75$ MHz and $\Delta_2 = 2\pi \times 20$ MHz. Here, varying Δ_2 tunes the value of the scattering length around the Feshbach resonance, while varying Δ_1 changes the width. Hence, greater control of the resonance is possible with an

optical Feshbach resonance compared to a magnetic one. Presumably, there should exist optical Feshbach resonances able to tune the scattering length of either the $|1\rangle$ or the $|2\rangle$ state, for instance the one reported to exist at 1007 G for the $|1\rangle$ state [51]. This resonance should be far enough away from the intercomponent resonance at 9.1 G to not cause any interference.

This suggests one possible setup. Namely, prepare a two-component condensate of ^{87}Rb in the $|1\rangle$ and $|2\rangle$ states under rotation, and tune a_{12} to a_{22} using a magnetic field. Then, tune a_{11} to the same value using optical techniques, while taking time-of-flight images of the condensate. The prediction is that as the system is tuned through the optical Feshbach resonance, one should observe a hexagonal composite vortex lattice at subresonance frequencies, the nonunique vortex ordering pattern, discussed above, at a frequency where all scattering lengths are equal, close to the optical Feshbach resonance, and finally the reappearance of a hexagonal vortex lattice at frequencies above the frequency where all lengths are equal (Fig. 6). The observation of a featureless rotating condensate would be a direct manifestation of the loss of topological character of U(1) vortices in the SU(2)-symmetric case. It would be interesting to study the dynamics of the vortex lattice in this case with methods like those used in [52]. For other discussions of SU(N) models in cold atoms see Refs. [53] and [54].

In actual experiments, a magnetic trap is used to confine the condensate in a given lateral region. The effect of this on thermal fluctuations in vortex matter has been studied in detail in previous theoretical works for the one-component case, without amplitude fluctuations [55,56]. The effect of the trap is to yield a maximum overall condensate density at the center of the trap, while depleting it towards the edge of the trap. As a result, the lattice melts more easily near the edge of the trap. As can be inferred from the work on single-component melting [55,56], the results of the present paper, where no inhomogeneity due to a magnetic trap has been accounted for, is therefore most relevant to the region close to the center of the trap.

VI. CONCLUSIONS

In this paper, we have investigated a two-component U(1) × U(1) and SU(2) Bose-Einstein condensate with density-density interaction under rotation at finite temperature, thereby extending previous works which calculated the zero-temperature ground state numerically. In the U(1) × U(1) case we report that thermal fluctuations can lead to a phase transition between hexagonal and square vortex lattices with increased temperature.

In the isotropic, SU(2), limit, we have observed an intermediate state of global phase coherence without an accompanying vortex lattice in the thermally averaged measurements. In addition, we observe a variety of dimerized vortex states, such as dimerized stripes and honeycomblike lattices, which exist for a wide range of temperature. These lattices could be observed in binary Bose-Einstein condensates in two separate hyperfine states, by precisely tuning the inter- and intracomponent scattering lengths to the SU(2) point through the use of Feshbach resonances.

ACKNOWLEDGMENTS

We thank Erich Mueller for useful discussions. P.N.G. thanks NTNU and the Norwegian Research Council for financial support. E.B. was supported by by the Knut and Alice Wallenberg Foundation through a Royal Swedish Academy of Sciences Fellowship, by the Swedish Research Council Grants No. 642-2013-7837 and No. 325-2009-7664, and by the National Science Foundation under the CAREER Award No. DMR-0955902, A.S. was supported by the Research Council of Norway, through Grants No. 205591/V20 and No. 216700/F20. This work was also supported through the Norwegian consortium for high-performance computing (NOTUR).

APPENDIX A: REWRITING THE GENERAL HAMILTIONIAN

Here we present the details of rewriting Eq. (2) into Eq. (5), which is more suited for our purposes. We repeat the starting point here for convenience.

$$H = \int d^3r \left[\sum_{i=1}^{N} \sum_{\mu=1}^{3} \frac{\hbar^2}{2m_i} \left| \left(\partial_\mu - i \frac{2\pi}{\Phi_0} A'_\mu \right) \psi'_i \right|^2 + \sum_{i}^{N} \alpha'_i |\psi'_i|^2 + \sum_{i,j=1}^{N} g'_{ij} |\psi'_i|^2 |\psi'_j|^2 \right]. \tag{A1}$$

First, we scale the field variables and Ginzburg-Landau parameters, to obtain some dimensionless quantities:

$$\alpha'_i = \alpha_0 \alpha_i, \tag{A2}$$

$$g'_{ij} = g_0 g_{ij}, \tag{A3}$$

$$|\psi'_i| = \sqrt{\frac{\alpha_0}{g_0}} |\psi_i|. \tag{A4}$$

This gives us the Hamiltonian,

$$H = \frac{\alpha_0^2}{g_0} \int d^3r \left[\sum_{i=1}^{N} \sum_{\mu=1}^{3} \frac{\hbar^2}{2m_i \alpha_0} \left| \left(\partial_\mu - i \frac{\Phi_0}{2\pi} A'_\mu \right) \psi_i \right|^2 + \sum_{i}^{N} \alpha_i |\psi_i|^2 + \sum_{i,j=1}^{N} g_{ij} |\psi_i|^2 |\psi_j|^2 \right], \tag{A5}$$

which on the lattice reads

$$H = \frac{\alpha_0^2 a^3}{g_0} \sum_{\mathbf{r}} \left[\sum_{i=1}^{N} \sum_{\mu=1}^{3} \frac{\hbar^2}{m_i \alpha_0 a^2} \times [|\psi_{\mathbf{r},i}|^2 - |\psi_{\mathbf{r}+\hat{\boldsymbol{\mu}},i}||\psi_{\mathbf{r},i}| \cos(\theta_{\mathbf{r}+\hat{\boldsymbol{\mu}},i} - \theta_{\mathbf{r},i} - A_{\mu,\mathbf{r}})] + \sum_{i}^{N} \alpha_i |\psi_{\mathbf{r},i}|^2 + \sum_{i,j=1}^{N} g_{ij} |\psi_{\mathbf{r},i}|^2 |\psi_{\mathbf{r},j}|^2 \right], \tag{A6}$$

where a is the lattice constant, and we have introduced

$$A_\mu = \frac{2\pi}{\Phi_0} a A'_\mu. \tag{A7}$$

Next, we specialize to the case $N = 2$, $\alpha_1 = \alpha_2$, $g_{11} = g_{22} \equiv g$, and $m_1 = m_2$, and define a^2 to be equal to $\hbar^2/m\alpha_0$, which sets our length scale. Note that it should not be confused with the coherence length in the multicomponent case without intercomponent density-density interaction. For the definition of coherence lengths in the presence of multiple components and intercomponent density-density interactions, see Refs. [57] and [58]. The energy scale is defined as J_0 as follows:

$$J_0 = \frac{\alpha_0^2 a^3}{g_0}. \tag{A8}$$

The coupling parameters η and ω used in this paper are defined by comparing the potential term of Eq. (A6) to the form where the soft constraints $|\psi_1|^2 + |\psi_2|^2 = 1$ and $|\psi_1|^2 - |\psi_2|^2 = 0$ are implemented. Thus, we have

$$V(\Psi) = \eta(|\psi_1|^2 + |\psi_2|^2 - 1)^2 + \omega(|\psi_1|^2 - |\psi_2|^2)^2, \tag{A9}$$

with

$$\eta = -\frac{\alpha}{2} - \frac{3}{2}, \tag{A10}$$

$$\omega = \frac{g - g_{12}}{2}. \tag{A11}$$

The lattice version of the Hamiltonian reads

$$\begin{aligned} H = &\sum_{\substack{\mathbf{r},\hat{\boldsymbol{\mu}} \\ i}} |\psi_{\mathbf{r}+\hat{\boldsymbol{\mu}},i}||\psi_{\mathbf{r},i}|[\cos(\theta_{\mathbf{r}+\hat{\boldsymbol{\mu}},i} - \theta_{\mathbf{r},i} - A_{\mu,\mathbf{r}})] \\ &+ \sum_{\mathbf{r}} \eta(|\psi_1|^2 + |\psi_2|^2 - 1)^2 \\ &+ \sum_{\mathbf{r}} \omega(|\psi_1|^2 - |\psi_2|^2)^2. \end{aligned} \tag{A12}$$

This model will then have the following continuum form:

$$H = \int d^3r \left[\sum_i^N \frac{1}{2} \left| (\partial_\mu - iA_\mu)\psi_i \right|^2 + V(\Psi) \right]. \tag{A13}$$

APPENDIX B: FIRST-ORDER LATTICE MELTING FOR $N = 1$ RECONSIDERED

As a benchmark on simulations with amplitude fluctuations included, we verify the well-established first-order melting transition on this model with only a single component of the order-parameter field, in the presence of amplitude fluctuations. The added feature of the computation is that the complete amplitude-distribution function was utilized, through the methods described in Sec. III. In this case, the term in the potential proportional to ω in Eq. (6) is absent, and the potential reduces to

$$V(\Psi) = \eta(|\Psi|^2 - 1)^2. \tag{B1}$$

With amplitude fluctuations neglected, this model reduces to the much studied uniformly frustrated 3D XY model, with well-known results as mentioned in the Introduction of the paper. The model features a first-order phase transition manifested as a melting of the frustration-induced hexagonal lattice of vortices [16,18–25]. The fluctuations responsible for driving this transition are massless transverse phase fluctuations of the order parameter.

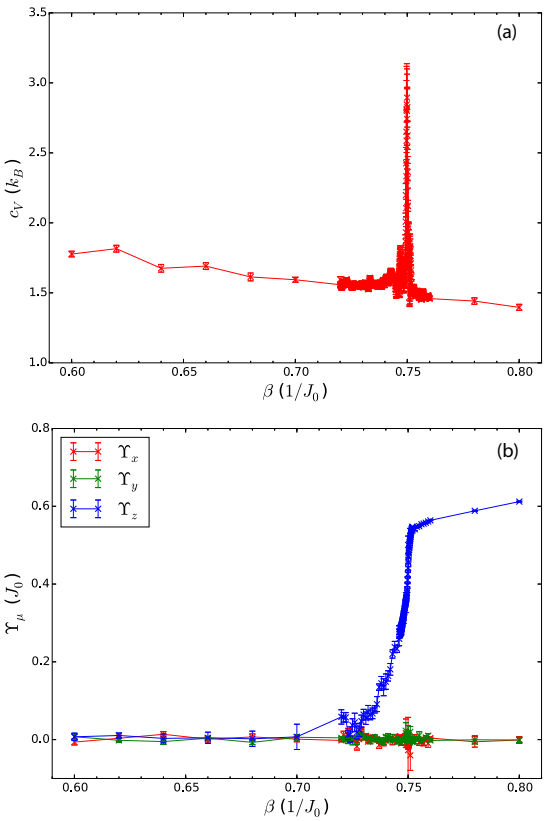

FIG. 7. (Color online) Specific heat (a) and helicity moduli (b) for $N = 1$, $f = 1/16$, and $\eta = 10$. At $\beta = 0.751$ we see a clear anomaly in the specific heat accompanied by a sharp jump in the longitudinal helicity modulus. The transverse moduli remain zero throughout the transition.

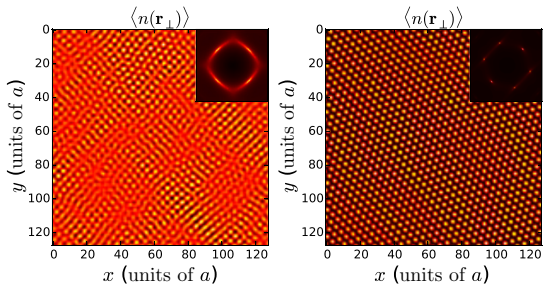

FIG. 8. (Color online) Vortex density $n(\mathbf{r}_\perp)$ and structure factor $S(\mathbf{q}_\perp)$ (inset) for $N = 1$, $f = 1/16$, and $\eta = 10$, at inverse temperatures $\beta = 0.749$ (left) and $\beta = 0.752$ (right). This corresponds to temperatures slightly higher and lower, respectively, than the transition point $\beta = 0.751$.

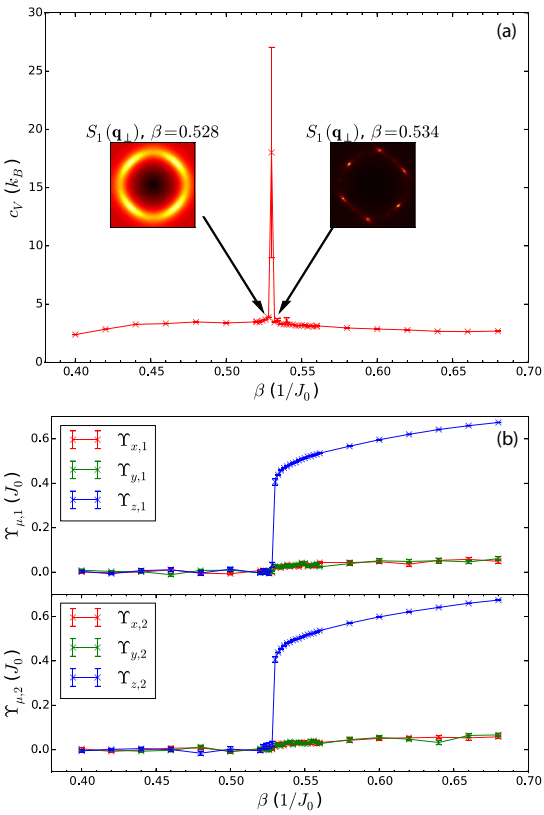

FIG. 9. (Color online) Specific heat (a) and helicity moduli of both components (b), for $N = 2$, $f = 1/16$, $\omega = 1.0$, and $\eta = 0.5$. At $\beta \approx 0.53$ we see a clear anomaly in the specific heat accompanied by a sharp jump in the longitudinal helicity moduli of both components. The transverse helicity moduli remain at zero throughout the transition. The insets in (a) show the structure factors at the high- and low-temperature sides of the transition, respectively, $\beta = 0.528$ and $\beta = 0.534$. This clearly shows that the sharp anomaly in the specific heat separates an isotropic phase from a phase with hexagonal order.

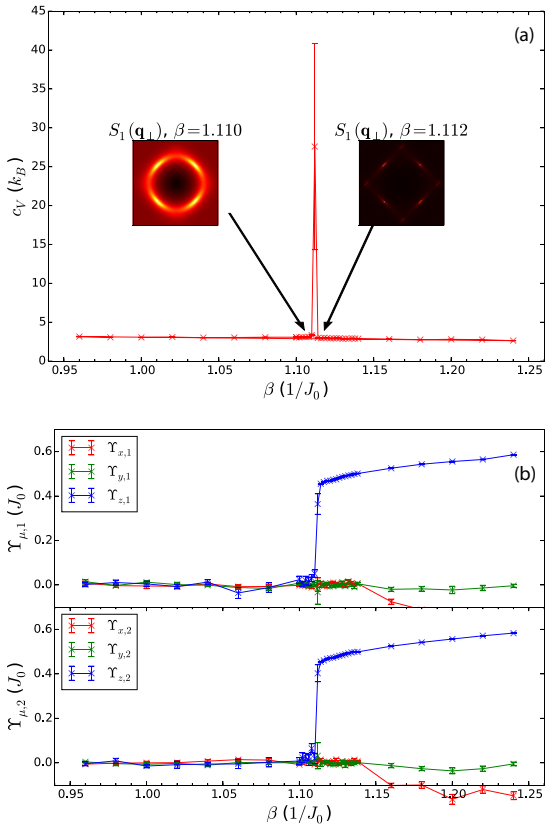

FIG. 10. (Color online) Specific heat (a) and helicity moduli of both components (b), for $N = 2$, $f = 1/16$, $\omega = 1.0$, and $\eta = 2.0$. At $\beta \approx 1.11$ we see a clear anomaly in the specific heat accompanied by a sharp jump in the longitudinal helicity moduli of both components. The transverse helicity moduli remain at zero throughout the transition, except for the x-directed modulus which drops to a negative value at a point well separated from the transition. The insets in (a) show the structure factors at the high- and low-temperature sides of the transition, respectively, $\beta = 1.110$ and $\beta = 1.112$. This clearly shows that the sharp anomaly in the specific heat separates an isotropic phase from a phase with square order.

The simulations were performed with $\eta = 10$. Figure 7(a) shows the specific heat, which has strong signs of an anomaly at $\beta = 0.751$. Figure 7(b) shows that the anomaly in the specific heat is accompanied by a relatively sharp jump in the helicity modulus in the z direction. It is also important to note that the helicity moduli in the transverse directions remain zero throughout the transition. This indicates that the vortex lattice melts in a genuine phase transition, and not as a result of thermal depinning from the underlying numerical lattice. This is therefore a strong indication of a first-order melting transition. Figure 8 shows the vortex density and structure factor immediately before and after the transition. The high-temperature side shows an incoherent vortex liquid, characterized by a circular structure factor. The low-temperature side shows that a clear hexagonal structure is established as soon as the liquid freezes.

We emphasize that these results are not unexpected. The purpose of including them here is to demonstrate that the method of including amplitude fluctuations into the computation of the vortex lattice melting reproduces the known result for $N = 1$, previously obtained in the absence of amplitude fluctuations [16,18–25], but generally believed to be correct also when amplitude fluctuations are included.

APPENDIX C: FIRST-ORDER LATTICE MELTING FOR $N = 2$

We next consider the melting transition for $N = 2$, where the intercomponent density-density interaction $2(\eta - \omega)|\psi_1|^2|\psi_2|^2$ term in the potential energy in Eq. (7) comes into play. We consider the $[U(1) \times U(1)]$-symmetric case, i.e.,

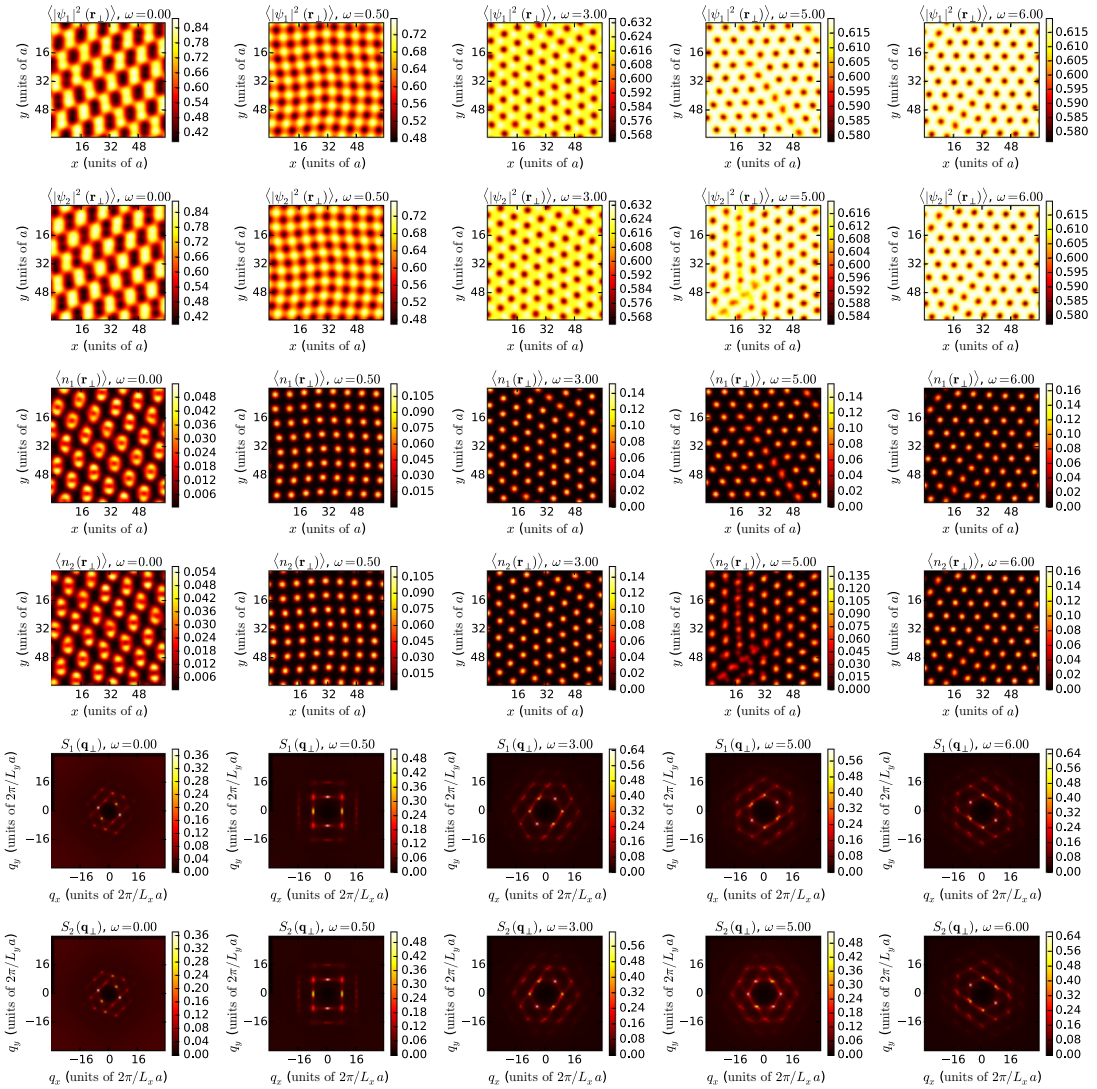

FIG. 11. (Color online) Tableau illustrating the different density and vortex lattices in real space, as the parameter ω increases, i.e., as the intercomponent density-density interaction $2(\eta-\omega)|\psi_1|^2|\psi_2|^2$ decreases. This interaction promotes a square density and vortex lattice. The parameters f, β, and η are fixed to $f = 1/64$, $\beta = 1.5$, and $\eta = 5$ while ω is increased from 0.0 to 6.0 horizontally. The six rows show, from top to bottom the amplitude densities of components 1 and 2, the vortex densities of components 1 and 2, and the structure factors of components 1 and 2. For $\omega = 0$, which is the SU(2)-symmetric case, the system exhibits a dimerized phase in component 1, which is complementary to a dimerized phase in component 2, shifted with respect to that of component 1 by an amount corresponding to the lattice constant of the density lattice. The ground state, where the roles of components 1 and 2 are interswitched, is degenerate with the illustrated phase. Note that an area of the system with a high vortex density always corresponds to an area with a low amplitude density. For the SU(2)-symmetric case, U(1) vortices are not topological. When $\omega \neq 0$, the SU(2) symmetry is broken down to U(1) $\times$ U(1), and U(1) vortices are topological. The reduction of the interaction $2(\eta-\omega)|\psi_1|^2|\psi_2|^2$ reduces the tendency towards formation of square density and vortex lattices, leading to an eventual reconstruction to a standard hexagonal vortex lattice, and hence a hexagonal density lattice.

$\omega \neq 0$. Again, the full spectrum of amplitude fluctuations is included, using the methods described in Sec. III.

For parameters $(\eta,\omega,f) = (0.5,1.0,1/16)$ and $(\eta,\omega,f) = (2.0,1.0,1/16)$ the lattices are clearly hexagonal and square, respectively. The hexagonal lattice obtained for $\eta = 0.5$ and $\omega = 1.0$ was found to have a melting transition at $\beta \approx 0.53$. Figure 9(a) shows the specific heat with a δ-function-like anomaly at this temperature. Around this point, we have

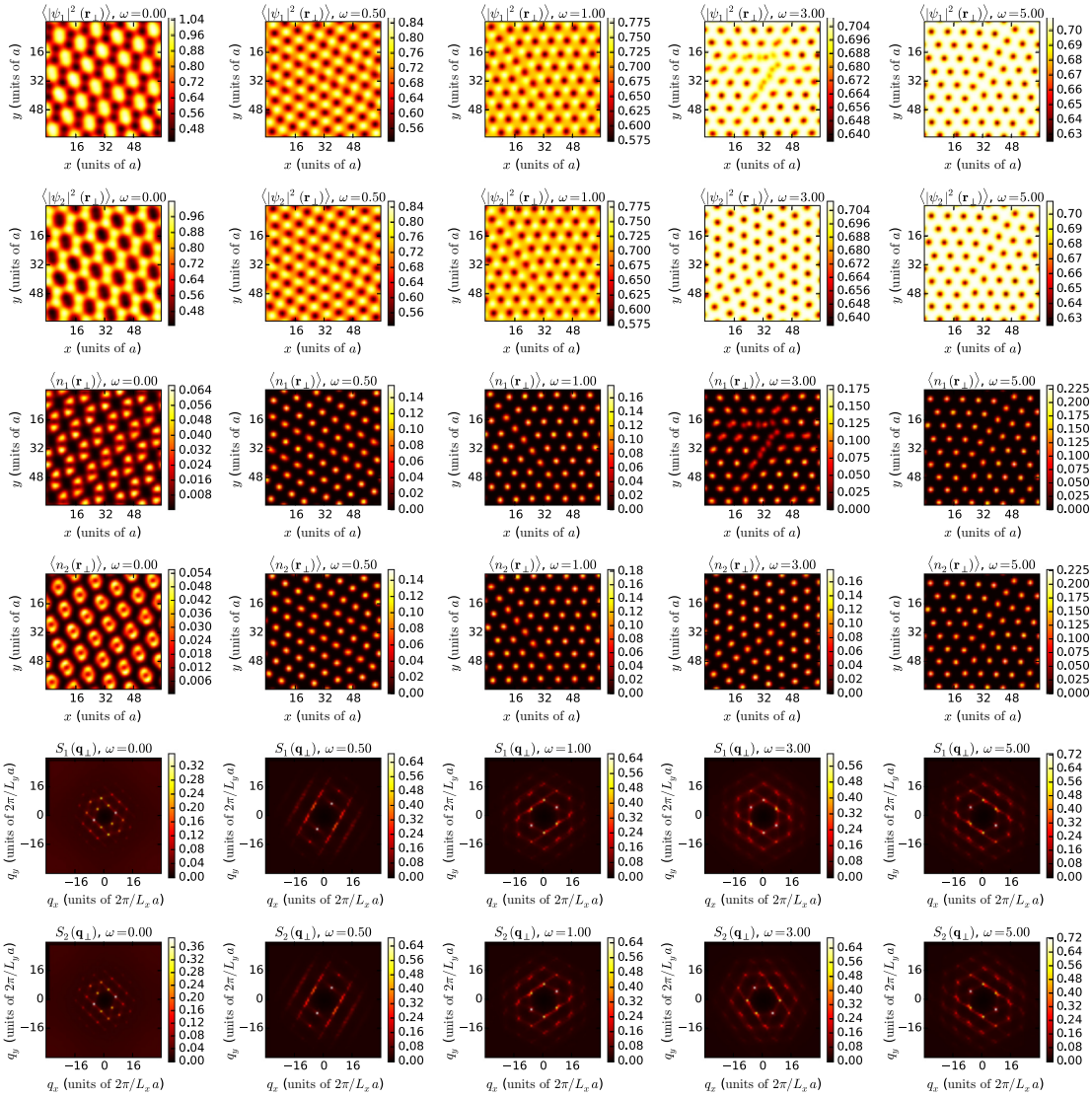

FIG. 12. (Color online) Tableau illustrating the different density and vortex lattices in real space, as the parameter ω increases, i.e., as the intercomponent density-density interaction $2(\eta-\omega)|\psi_1|^2|\psi_2|^2$ decreases. This interaction promotes a square density and vortex lattice. The parameters f, β, and η are fixed to $f = 1/64$, $\beta = 1.5$, and $\eta = 3$ while ω is increased from 0.0 to 5 horizontally. The six rows show, from top to bottom, the amplitude densities of components 1 and 2, the vortex densities of components 1 and 2, and the structure factors of components 1 and 2.

used a closely spaced set of temperatures, in order to get a proper resolution of the anomaly. Figure 9(b) shows the helicity moduli of both components. Both of the z-directed stiffnesses have a zero expectation value in the disordered phase, indicating no phase coherence. In the ordered phase, both of $\langle\Upsilon_{z,i}\rangle$ develop finite expectation values which means that the system has superfluidic properties along the direction of rotation. The two phases are divided by a sharp jump in the longitudinal phase stiffness, a characteristic of a first-order transition. The drop is even sharper than was obtained for the $N = 1$ case, indicating an even larger latent heat associated with the transition. The x- and y-directed stiffnesses remain zero in the ordered state, which rules out any possibility of numerical pinning effects [44,45]. Looking further at the insets of Fig. 9(a), which show the structure factors in the disordered and ordered phases, we see clear evidence of an incoherent vortex liquid at $\beta < 0.53$ in the left inset, while the right inset shows an ordered hexagonal vortex liquid lattice at $\beta > 0.53$.

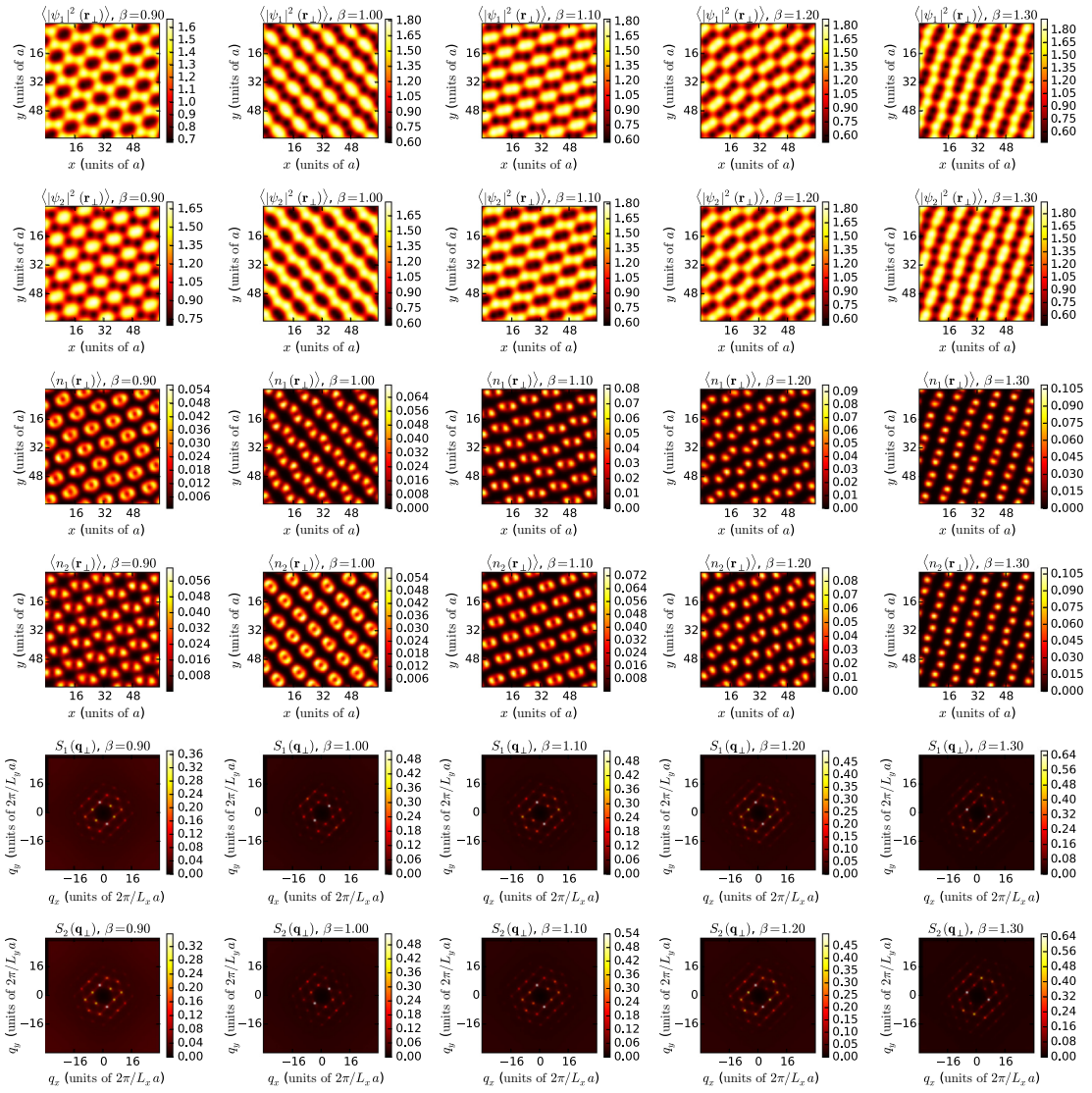

FIG. 13. (Color online) Tableau illustrating the different SU(2) density and vortex lattices in real space, as the parameter β increases. The parameters f, η, and ω are fixed to $f = 1/64$, $\eta = 1.0$, and $\omega = 0.0$ while β is increased from 0.9 to 1.3 horizontally. The six rows show, from top to bottom, the amplitude densities of components 1 and 2, the vortex densities of components 1 and 2, and the structure factors of components 1 and 2. Note how the vortex structures and the density structures always track, that is, an area of the system with a high vortex density always corresponds to an area with a low amplitude density.

Turning to the square lattice, now the parameters in question are $\eta = 2.0$ and $\omega = 1.0$. The transition point is located at $\beta \approx 1.11$. Figure 10(a) shows the specific heat. Again, an anomaly is located at the transition point. The helicity moduli, shown in Fig. 10(b), also show first-order behavior. Both z-directed components are zero on the high-temperature side, and develop a finite value through a sharp jump at the low-temperature side. It is important to also consider the transverse components. Both $\langle \Upsilon_{x,i} \rangle$ and $\langle \Upsilon_{y,i} \rangle$ are zero throughout the area of interest. Here we note that the x-directed modulus drops to a tiny negative value at a point after the transition. This is a nonphysical effect, most likely caused by a metastable state. We believe this is simply a numerical artifact, as we used a lower amount of Monte Carlo time away from the transition. Turning our attention to the structure factors, shown in the insets of Fig. 10(b), we again see the isotropic vortex liquid in

the disordered side of the transition; the ordered side shows a square fourfold symmetry.

Thus, both the square and the hexagonal lattices undergo first-order melting transitions from their respective ordered phases, into an isotropic vortex line liquid.

APPENDIX D: INTERCOMPONENT INTERACTION, AND ITS EFFECT ON DENSITY AND VORTEX LATTICES

In this Appendix, we include more detailed figures of the vortex and density structures in real and reciprocal space, as the intercomponent interaction $2(\eta - \omega)|\psi_1|^2|\psi_2|^2$ is varied, to supplement the points made in Secs. IV A and IV C.

Figures 11 and 12 illustrate how the vortex lattice and the component densities reconstruct as the intercomponent density-density interaction $(\eta - \omega)|\psi_1|^2|\psi_2|^2$ changes. We do this by fixing η at 5.0 and 3.0, respectively, and tuning ω. The inverse temperature β is also fixed in both tableaus. Common in both figures is that the vortices first form two interlaced square lattices for sufficiently small ω, and, by extension, large intercomponent coupling. Then the lattices reconstruct into a hexagonal structure. Note that the hexagonal lattices of the two components start out slightly shifted with respect to each other, but become completely cocentered when $\omega > \eta$. This final state corresponds to an attractive intercomponent coupling.

The behavior of the amplitude densities is explained in Sec. IV A, and we can compare the reasoning to the top two rows of Figs. 11 and 12. First of all, the presence of a vortex locally suppresses the amplitude, which again may affect the immediate neighborhood, depending on the value of the intercomponent coupling. For strong repulsive couplings a suppression of the amplitude of one color in an area leads to an enhancement of the amplitude of the other color in the same area. The absence of vortices in the neighborhood then leads to the opposite effect. This causes staggering of the amplitude densities and formation of distinct vortex sublattices. Considering carefully the range of variation in the amplitudes, it is seen that there are rather large gradients for the square structures. When the coupling is only weakly repulsive or even attractive there is a much less dramatic effect. The variations in the amplitudes are much smaller; there is little to no staggering.

The first column of Figs. 11 and 12 is in a different class from the rest. Here $\omega = 0$, and we are in the SU(2) regime. Figure 13 further illustrates the wide variety of ground states obtainable here. This tableau, in contrast to the two previous ones, has a fixed η and ω, while we vary the inverse temperature β from column to column. These pictures are all taken from a single simulation, evolved through Monte Carlo sampling from a single randomized initial state as β is increased. The vortex lattice initially forms at around $\beta = 0.7$ and evolves continuously. It continues to evolve even at the lowest temperatures ($\beta = 1.5$) used in the simulation. This pattern is common in all simulations done with similar parameter sets.

The common features in the SU(2) lattices are clearly seen in Fig. 13. The vortices tend to form dimers, which usually have some global alignment. The alignment is evident in the Bragg peaks, as we in most cases have two opposing peaks of higher intensity than the rest. The vortex dimer complexes always arrange themselves in a hexagonal structure, which is also seen in the structure factors.

[1] C. J. Myatt, E. A. Burt, R. W. Ghrist, E. A. Cornell, and C. E. Wieman, Phys. Rev. Lett. **78**, 586 (1997).

[2] D. S. Hall, M. R. Matthews, J. R. Ensher, C. E. Wieman, and E. A. Cornell, Phys. Rev. Lett. **81**, 1539 (1998).

[3] M. R. Matthews, B. P. Anderson, P. C. Haljan, D. S. Hall, C. E. Wieman, and E. A. Cornell, Phys. Rev. Lett. **83**, 2498 (1999).

[4] G. Modugno, M. Modugno, F. Riboli, G. Roati, and M. Inguscio, Phys. Rev. Lett. **89**, 190404 (2002).

[5] E. J. Mueller and T.-L. Ho, Phys. Rev. Lett. **88**, 180403 (2002).

[6] K. Kasamatsu, M. Tsubota, and M. Ueda, Phys. Rev. Lett. **91**, 150406 (2003).

[7] V. Schweikhard, I. Coddington, P. Engels, S. Tung, and E. A. Cornell, Phys. Rev. Lett. **93**, 210403 (2004).

[8] S. B. Papp, J. M. Pino, and C. E. Wieman, Phys. Rev. Lett. **101**, 040402 (2008).

[9] G. Thalhammer, G. Barontini, L. De Sarlo, J. Catani, F. Minardi, and M. Inguscio, Phys. Rev. Lett. **100**, 210402 (2008).

[10] K. Kasamatsu and M. Tsubota, Phys. Rev. A **79**, 023606 (2009).

[11] S. Tojo, Y. Taguchi, Y. Masuyama, T. Hayashi, H. Saito, and T. Hirano, Phys. Rev. A **82**, 033609 (2010).

[12] D. J. McCarron, H. W. Cho, D. L. Jenkin, M. P. Köppinger, and S. L. Cornish, Phys. Rev. A **84**, 011603 (2011).

[13] P. Kuopanportti, J. A. M. Huhtamäki, and M. Möttönen, Phys. Rev. A **85**, 043613 (2012).

[14] K. Kasamatsu, H. Takeuchi, M. Tsubota, and M. Nitta, Phys. Rev. A **88**, 013620 (2013).

[15] M. Cipriani and M. Nitta, Phys. Rev. A **88**, 013634 (2013).

[16] Y.-H. Li and S. Teitel, Phys. Rev. Lett. **66**, 3301 (1991).

[17] R. E. Hetzel, A. Sudbø, and D. A. Huse, Phys. Rev. Lett. **69**, 518 (1992).

[18] T. Chen and S. Teitel, Phys. Rev. B **55**, 11766 (1997).

[19] X. Hu, S. Miyashita, and M. Tachiki, Phys. Rev. Lett. **79**, 3498 (1997).

[20] A. K. Nguyen and A. Sudbø, Phys. Rev. B **58**, 2802 (1998).

[21] A. K. Nguyen and A. Sudbø, Phys. Rev. B **57**, 3123 (1998).

[22] S. Ryu and D. Stroud, Phys. Rev. B **57**, 14476 (1998).

[23] A. K. Nguyen and A. Sudbø, Phys. Rev. B **60**, 15307 (1999).

[24] S.-K. Chin, A. K. Nguyen, and A. Sudbø, Phys. Rev. B **59**, 14017 (1999).

[25] A. K. Nguyen and A. Sudbø, Europhys. Lett. **46**, 780 (1999).

[26] H. Nordborg and G. Blatter, Phys. Rev. Lett. **79**, 1925 (1997).

[27] J. Hu and A. H. MacDonald, Phys. Rev. B **56**, 2788 (1997).

[28] M. H. Anderson, J. R. Ensher, M. R. Matthews, C. E. Wieman, and E. A. Cornell, Science **269**, 198 (1995).

[29] K. B. Davis, M.-O. Mewes, M. R. Andrews, N. J. van Druten, D. S. Durfee, D. M. Kurn, and W. Ketterle, Phys. Rev. Lett. **75**, 3969 (1995).
[30] J. R. Abo-Shaeer, C. Raman, J. M. Vogels, and W. Ketterle, Science **292**, 476 (2001).
[31] M. Kobayashi and M. Nitta, J. Low Temp. Phys. **175**, 208 (2014).
[32] H. Feshbach, Ann. Phys. (NY) **19**, 287 (1962).
[33] S. Inouye, M. R. Andrews, J. Stenger, H.-J. Miesner, D. M. Stamper-Kurn, and W. Ketterle, Nature (London) **392**, 151 (1998).
[34] E. K. Dahl, E. Babaev, and A. Sudbø, Phys. Rev. B **78**, 144510 (2008).
[35] E. K. Dahl, E. Babaev, and A. Sudbø, Phys. Rev. Lett. **101**, 255301 (2008).
[36] E. K. Dahl, E. Babaev, S. Kragset, and A. Sudbø, Phys. Rev. B **77**, 144519 (2008).
[37] A. Kuklov, N. Prokof'ev, and B. Svistunov, Phys. Rev. Lett. **92**, 030403 (2004).
[38] A. Kuklov, N. Prokof'ev, and B. Svistunov, Phys. Rev. Lett. **93**, 230402 (2004).
[39] J. Smiseth, E. Smørgrav, E. Babaev, and A. Sudbø, Phys. Rev. B **71**, 214509 (2005).
[40] E. V. Herland, E. Babaev, and A. Sudbø, Phys. Rev. B **82**, 134511 (2010).
[41] E. Babaev, L. D. Faddeev, and A. J. Niemi, Phys. Rev. B **65**, 100512 (2002).
[42] J. Garaud, J. Carlström, E. Babaev, and M. Speight, Phys. Rev. B **87**, 014507 (2013).
[43] M. E. Fisher, M. N. Barber, and D. Jasnow, Phys. Rev. A **8**, 1111 (1973).
[44] M. Franz and S. Teitel, Phys. Rev. Lett. **73**, 480 (1994).
[45] S. Hattel and J. Wheatley, Phys. Rev. B **50**, 16590 (1994).
[46] N. Metropolis, A. W. Rosenbluth, M. N. Rosenbluth, A. H. Teller, and E. Teller, J. Chem. Phys. **21**, 1087 (1953).
[47] W. K. Hastings, Biometrika **57**, 97 (1970).
[48] S. B. Chung and S. A. Kivelson, Phys. Rev. B **82**, 214512 (2010).
[49] K. M. Mertes, J. W. Merrill, R. Carretero-González, D. J. Frantzeskakis, P. G. Kevrekidis, and D. S. Hall, Phys. Rev. Lett. **99**, 190402 (2007).
[50] G. Thalhammer, M. Theis, K. Winkler, R. Grimm, and J. H. Denschlag, Phys. Rev. A **71**, 033403 (2005).
[51] T. Volz, S. Dürr, S. Ernst, A. Marte, and G. Rempe, Phys. Rev. A **68**, 010702 (2003).
[52] D. V. Freilich, D. M. Bianchi, A. M. Kaufman, T. K. Langin, and D. S. Hall, Science **329**, 1182 (2010.
[53] M. A. Cazalilla and A. M. Rey, Rep. Prog. Phys. **77**, 124401 (2014).
[54] A. V. Gorshkov, M. Hermele, V. Gurarie, C. Xu, P. S. Julienne, J. Ye, P. Zoller, E. Demler, M. D. Lukin, and A. M. Rey, Nat. Phys. **6**, 289 (2010).
[55] S. Kragset, E. Babaev, and A. Sudbø, Phys. Rev. Lett. **97**, 170403 (2006).
[56] S. Kragset, E. Babaev, and A. Sudbø, Phys. Rev. A **77**, 043605 (2008).
[57] J. Carlström, E. Babaev, and M. Speight, Phys. Rev. B **83**, 174509 (2011).
[58] D. F. Agterberg, E. Babaev, and J. Garaud, Phys. Rev. B **90**, 064509 (2014).

Paper II

Thermal remixing of phase-separated states in two-component bosonic condensates

New Journal of Physics **17**, 103040 (2015)

New Journal of Physics
The open access journal at the forefront of physics

Deutsche Physikalische Gesellschaft DPG
IOP Institute of Physics

Published in partnership with: Deutsche Physikalische Gesellschaft and the Institute of Physics

OPEN ACCESS

RECEIVED
25 June 2015

REVISED
10 September 2015

ACCEPTED FOR PUBLICATION
14 September 2015

PUBLISHED
19 October 2015

PAPER

Thermal remixing of phase-separated states in two-component bosonic condensates

Peder Notto Galteland[1], **Egor Babaev**[2] **and Asle Sudbø**[1,3]

[1] Department of Physics, Norwegian University of Science and Technology, N-7491 Trondheim, Norway
[2] Department of Theoretical Physics, The Royal Institute of Technology, 10691 Stockholm, Sweden
[3] Author to whom any correspondence should be addressed.

E-mail: asle.sudbo@ntnu.no

Keywords: Bose–Einstein condensates, phase separation, thermal remixing, phase transitions, competing orders

Abstract

We consider a two-component interacting bosonic condensate with dominating intra-species repulsive density–density interactions. We study the phase diagram of the system at finite temperature with rotation, using large-scale Monte Carlo simulations of a two-component Ginzburg–Landau model of the system. In the presence of rotation, the system features a competition between long-range vortex–vortex interactions and short-range density–density interactions. This leads to a rotation-driven 'mixing' phase transition in a spatially inhomogeneous state with a broken U(1) symmetry. Thermal fluctuations in this state lead to nematic two-component sheets of vortex liquids. At sufficiently strong inter-component interaction, we find that the superfluid and $\mathbb{Z}_2$ phase transitions split. This results in the formation of an intermediate state which breaks only $\mathbb{Z}_2$ symmetry. It represents two phase separated normal fluids with a difference in their densities.

1. Introduction

Multi-component phase-coherent condensates, such as multi-component superconductors and Bose–Einstein condensates (BECs), have proven to be a rich ground for exploring quantum phenomena in condensed matter physics. In particular, BECs serve as a highly useful synthetic model systems for a wide variety of real condensed matter systems, due to their tunable interactions using magnetic and optical Feshbach-resonances. By creating mixtures of the same boson in different hyperfine states, one effectively creates multicomponent condensates [1–4]. Furthermore, by using crossed lasers, one may set up lattice model systems with a vast combinations of intersite hopping matrix elements, as well as intrasite interactions, both intra- and interspecies [5–10]. This means that these model systems, apart from being interesting in their own right, emulate various aspects of a plethora of condensed matter systems of great current interest, such as multicomponent superconductors, Mott-insulators, and even topologically nontrivial band insulators. The latter follows from the recent realization of synthetic spin-orbit couplings in such condensates [11–13]. Of particular interest is the physics of these systems in the strong coupling regime.

BECs with two components of the order parameter (two species of particles) represent a first step away from ordinary single-component condensates. This extension opens up a whole vista of physics which has no counterpart compared to single-component condensates, due to the wide variety of interspecies couplings that may be generated. Thus, these systems display physics which is beyond what is ordinarily seen in condensed matter systems, but may nevertheless serve as useful model systems for future artificially engineered condensed matter systems. As such, it is of interest to chart their physical properties to the maximum extent over a wide range of parameters.

The parameter range where inter-component density–density interactions exceed intra-component density–density interactions signals the onset of immiscibility, or phase separation, of the two components. Numerical works solving the Gross–Pitaevskii ground-state equations have also found interesting vortex lattices in this regime [14–16, 19–24]. The effect of the repulsive inter-component density–density interactions

overpowering the intra-component interactions causes the condensate to form intertwined sheets of vortices when the condensate is subject to rotation [25]. The condition for immiscibility is readily realized experimentally, using magnetic and optical Feschbach resonances [16, 26]. Several works have also focused on the critical properties of the rotation-free model using RG, mean-field and quantum Monte Carlo simulations [17, 18].

In the present paper, we focus on the regime of density–density interactions where the inter-component interactions are larger than the intra-component interactions. This regime is qualitatively different from the case in which the intra-component interactions dominate, in that immiscibility (phase-separation) of the condensate components sets in. This leads to density-modulated non-uniform ground states. Previous works have studied the effect of an inter-component density–density interaction on the rotation-induced non-homogeneous ground states. These works were mostly limited to two spatial dimensions solving the Gross–Pitaevskii ground-state equations [14–16, 19–25], although certain aspects of the three-dimensional case were also studied at the mean-field level [15, 24]. Here, we consider the case of three dimensions, taking fully into account the thermal density- and phase-fluctuation of the condensate ordering fields.

2. Definitions

2.1. Model

We consider a general Ginzburg–Landau (GL) model of an N-component BECs, which in the thermodynamic limit is defined as

$$\mathcal{Z} = \int \prod_{i}^{N} \mathcal{D}\psi_i \mathrm{e}^{-\beta H}, \tag{1}$$

where

$$H = \int \mathrm{d}^3 r \left[\sum_{i=1}^{N} \sum_{\mu=1}^{3} \frac{\hbar^2}{2m_i} \left| \left(\partial_\mu - \mathrm{i} \frac{2\pi}{\Phi_0} A_\mu \right) \psi_i \right|^2 + \sum_{i}^{N} \alpha_i \left| \psi_i \right|^2 + \sum_{i,j=1}^{N} g_{ij} \left| \psi_i \right|^2 \left| \psi_j \right|^2 \right] \tag{2}$$

is the Hamiltonian. This model is a description of the condensate while the particle content of the system outside the condensate is not captured by equation (2). Here, the field A_μ formally appears as a non-fluctuating gauge-field and parametrizes the angular velocity of the system under rotation. The condensate fields ψ_i are dimensionful complex fields which are allowed to fluctuate both in phase and amplitude. Importantly, the phases are defined with compact support $-\pi < \theta_i \leq \pi$, leading to the appearance of topological defects in the form of vortices (two dimensions) and vortex loops (three dimensions) in the condensate. The model is thus capable of capturing all thermal fluctuations of the condensate, including vortex-fluctuations destroying long-range phase coherence in the condensate. Moreover, i and j are indices running from 1 to N denoting the component of the order parameter (a 'color' index). The parameters α_i and g_{ij} are chemical potentials and interaction parameters of the model, respectively. Φ_0 is the coupling constant to the rotation-induced vector potential, and m_i is the particle mass of species i. For mixtures consisting of different atoms or different isotopes of one atom, the masses will depend on the index i, while for mixtures consisting of same atoms in different hyperfine states, the masses are equal among the components i. The inter- and intra-component coupling parameters g_{ij} are related to real inter- and intra-component scattering lengths a_{ij}, in the following way

$$g_{ii} = \frac{4\pi\hbar^2 a_{ii}}{m_i}, \tag{3}$$

$$g_{ij} = \frac{2\pi\hbar^2 a_{ij}}{m_{ij}}; \ (i \neq j). \tag{4}$$

Here, $m_{ij} = m_i\, m_j/(m_i + m_j)$ is the reduced mass. In this work, we focus on homonuclear condensates with several components in different hyperfine states, i.e. $m_i = m \forall\ i$. Note that when $g_{12} = g_{21} \equiv \lambda g > g_{11} = g_{22} \equiv g$, i.e. $\lambda > 1$, there is a strong tendency in the system to phase separate, leading to two immiscible quantum fluids. For a homonuclear binary mixture, we have $m_{ij} = m_i/2$. Then, it suffices that $a_{ij} > a_{ii}$ for the inter-component density–density interactions to dominate the intra-component density–density interactions.

It is convenient to rewrite the potential (repeated indices are summed over) as follows [27]

$$V \equiv \alpha_i \left| \psi_i \right|^2 + g_{ij} \left| \psi_i \right|^2 \left| \psi_j \right|^2, \tag{5}$$

by introducing interaction parameters η, ω, such that $g = \eta + \omega$, and $\lambda g = \eta - \omega$, i.e. $\eta = g(1 + \lambda)/2$, $\omega = g(1 - \lambda)/2$. Here, λ denotes the ratio between the inter- and intra-component interactions. Then, equation (5) takes the form (up to an additive constant)

$$V = \left(\alpha_1 + 2\eta\right)\left|\psi_1\right|^2 + \left(\alpha_2 + 2\eta\right)\left|\psi_2\right|^2 + \eta\left(\left|\psi_1\right|^2 + \left|\psi_2\right|^2 - 1\right)^2 + \omega\left(\left|\psi_1\right|^2 - \left|\psi_2\right|^2\right)^2. \tag{6}$$

For $\lambda > 1$, $\omega < 0$, with the proviso that $\eta + \omega = \eta - |\omega| > 0$ for stability. Furthermore, we will assume that $\alpha_1 = \alpha_2$, $\alpha_1 \neq \alpha_2$ acts as an external field conjugate to the pseudo-magnetization of the system.

We discretize the model on a cubic lattice with sides L by defining the order parameter field on a discrete set of coordinates $\psi_i(\mathbf{r}) \to \psi_{\mathbf{r},i}$, $\mathbf{r} \in (i\hat{\mathbf{x}} + j\hat{\mathbf{y}} + k\hat{\mathbf{z}}|\ i, j, k = 1, \ldots, L)$. The covariant derivative is replaced by a forward difference

$$D_\mu \psi_i(\mathbf{r}) \to \frac{1}{a}\left(\psi_{\mathbf{r}+a\hat{\boldsymbol{\mu}},i} e^{-iaA_{\mu,\mathbf{r}}} - \psi_{\mathbf{r},i}\right). \tag{7}$$

Here, the lattice version of the non-fluctuating gauge field is parametrized in Landau gauge, $A_{\mu,\mathbf{r}} = (0,\ 2\pi fx,\ 0)$, where f is the number of vortices per plaquette, or filling fraction. The lattice spacing, a, is fixed to be smaller than the characteristic length scale of the variations of the order parameter, and $\hat{\boldsymbol{\mu}} \in (\hat{\mathbf{x}},\ \hat{\mathbf{y}},\ \hat{\mathbf{z}})$ is a unit vector.

Thus, the lattice version of the Hamiltonian we consider is given by

$$\begin{aligned} H = &- \sum_{\substack{\mathbf{r},\hat{\boldsymbol{\mu}} \\ i}} \left|\psi_{\mathbf{r}+\hat{\mu},i}\right|\left|\psi_{\mathbf{r},i}\right| \cos\left(\theta_{\mathbf{r}+\hat{\mu},i} - \theta_{\mathbf{r},i} - A_{\mu,\mathbf{r}}\right) \\ &+ \sum_{\mathbf{r},i}\left(\alpha_i + 2\eta\right)\left|\psi_{\mathbf{r},i}\right|^2 \\ &+ \sum_{\mathbf{r}} \eta\left(\left|\psi_{\mathbf{r},1}\right|^2 + \left|\psi_{\mathbf{r},2}\right|^2 - 1\right)^2 \\ &+ \sum_{\mathbf{r}} \omega\left(\left|\psi_{\mathbf{r},1}\right|^2 - \left|\psi_{\mathbf{r},2}\right|^2\right)^2. \end{aligned} \tag{8}$$

Here, we have written the order parameter fields as real amplitudes and phases, $\psi_{\mathbf{r},i} = |\psi_{\mathbf{r},i}|\ e^{i\theta_{\mathbf{r},i}}$. In addition, we have defined an energy scale, $J_0 = \alpha_0^2 a^3 / g_0^3$, where α_0 and g_0 are the parameters of the GL theory at $T = 0$. Throughout, we fix $\eta = 5.0$ and $\alpha_1 + 2\eta = \alpha_2 + 2\eta = 0$. This guarantees a non-zero ground state condensate density for all values of ω.

2.2. Ground state symmetry

Equation (8) defines two superfluids coupled by density–density interactions. When there is no phase separation, we have a U(1) × U(1) symmetry broken in the ground state. When the inter-component interaction is equal to the intra-component interaction the system breaks $SU(2)$ symmetry. Here, we are interested in the phase separated case. In this case, the system breaks an additional $\mathbb{Z}_2$ symmetry, corresponding to interchanging $\psi_1 \leftrightarrow \psi_2$. That is, when $\omega > 0$, $|\psi_1|^2 = |\psi_2|^2$ is favored. This represents a $\mathbb{Z}_2$ -symmetric state. On the other hand, when $\omega < 0$, $|\psi_1|^2 \neq |\psi_2|^2$ is favored, such that $|\psi_1|^2 - |\psi_2|^2$ may acquire a nonzero expectation value, with equal probabilities that the expectation value is either positive or negative. This corresponds to breaking an Ising-like $\mathbb{Z}_2$ symmetry. Thus, the ground state breaks a composite $U(1) \times Z_2$ symmetry.

2.3. Observables

The equilibrium phases of the model are characterized by several order parameters. To identify the Ising-like, phase separated order of the system we define

$$\Delta = \left|\left\langle\left|\psi_1\right|^2\right\rangle - \left\langle\left|\psi_2\right|^2\right\rangle\right|, \tag{9}$$

where $\langle|\psi_i|^2\rangle$ is the thermal and spatial average of $|\psi_i(\mathbf{r})|^2$

$$\left\langle\left|\psi_i\right|^2\right\rangle = \left\langle\frac{1}{L^3}\sum_{\mathbf{r}}\left|\psi_{i,\mathbf{r}}\right|^2\right\rangle. \tag{10}$$

A finite value of Δ signals relative density depletion in either of the condensates. In addition to $\mathbb{Z}_2$ order, it is important to monitor the U(1) ordering of the system. The helicity modulus measures phase coherence along a given direction of the system. It is defined as

$$\Upsilon_{\mu,i} = \frac{1}{L^3}\frac{\partial^2 F\left[\theta'\right]}{\partial \delta_\mu^2}\bigg|_{\delta_\mu = 0}. \tag{11}$$

Here, $F[\theta']$ is the free energy with an infinitesimal phase twist, δ_μ, applied along the μ-direction, *i.e.*, we make the replacement

$$\theta_{\mathbf{r},i} \to \theta'_{\mathbf{r},i} = \theta_{\mathbf{r},i} - \boldsymbol{\delta} \cdot \mathbf{r} \tag{12}$$

in F.

We also identify the nature of the phases by computing thermal averages of real-space configurations of densities $\langle |\psi_i(\mathbf{r}_\perp)|^2 \rangle$ and vortices $\langle |n_i(\mathbf{r}_\perp)|^2 \rangle$ in the system. These are computed by averaging the quantity along the z-direction of the system, with subsequent thermal averaging. That is

$$\left\langle n_i\left(\mathbf{r}_\perp\right)\right\rangle = \left\langle \frac{1}{L_z}\sum_z n_{i,\mathbf{r}} \right\rangle. \tag{13}$$

and

$$\left\langle \left|\psi_i\left(\mathbf{r}_\perp\right)\right|^2 \right\rangle = \left\langle \frac{1}{L_z}\sum_z \left|\psi_{i,\mathbf{r}}\right|^2 \right\rangle. \tag{14}$$

The vorticity, $n_{i,\mathbf{r}}$ is calculated by traversing a plaquette with surface normal in the z-direction, adding the phase difference $\theta_{\mathbf{r}+\hat{\mu},i} - \theta_{\mathbf{r},i} - A_{\mu,\mathbf{r}}$ on each link. If this plaquette sum turns out to have a value outside the primary interval, $(-\pi, \pi]$, $2n\pi$ $(-2n\pi)$ is added to the sum, which inserts a vortex of charge $+n(-n)$ on the plaquette.

To further characterize vortex structures, we examine the structure factor of the vortices, defined as

$$S_i\left(\mathbf{q}_\perp\right) = \left\langle \left| \frac{1}{L^3 f}\sum_{\mathbf{r}_\perp, z} n_{i,\mathbf{r}} e^{i\mathbf{q}_\perp \cdot \mathbf{r}_\perp} \right|^2 \right\rangle. \tag{15}$$

This is simply the Fourier-transform of the z-averaged vorticity. To improve the resolution of the interesting q-vectors, we remove the $\mathbf{q}_\perp = 0$ point from the figures. We also calculate

$$\max\left(S_i\left(\mathbf{q}_\perp\right)\right) = \left\langle \max\left(\left| \frac{1}{L^3 f}\sum_{\mathbf{r}_\perp, z} n_{i,\mathbf{r}} e^{i\mathbf{q}_\perp \cdot \mathbf{r}_\perp} \right|^2 \right) \right\rangle, \tag{16}$$

in order to monitor the development of peaks in the structure factor across transition points.

We also compute the specific heat capacity

$$\frac{C_V L^3}{\beta^2} = \langle (H - \langle H \rangle)^2 \rangle. \tag{17}$$

as a means of precisely locating the various transition points.

2.4. Details of the Monte-Carlo simulations

We consider the model on a lattice of size $L_x \times L_y \times L_z$, using the Monte-Carlo algorithm, with a simple restricted update scheme of each physical variable, and Metropolis–Hastings [28, 29] tests for acceptance. Here, L_i is the linear extent of the system in the Cartesian direction $i \in (x, y, z)$. In all our simulation, we have used cubic systems $L_x = L_y = L_z = L$, with $L \in \{32, 64, 96\}$. At each inverse temperature, 10^6 Monte-Carlo steps are typically used, while 10^5 additional sweeps are used for equilibration. Each Monte-Carlo step consists of an attempt to update each amplitude and phase separately in succession, at each lattice site. To improve acceptance rates, we only allow each update to change a variable within a limited interval around the previous value, the size of which is chosen by approximately maximizing acceptance rates and minimizing autocorrelations. The Mersenne–Twister algorithm is used to generate the pseudo-random numbers needed [30]. To ensure that the state is properly equilibrated, time series of the internal energy measured during equilibration are examined for convergence. To avoid metastable states, we make sure that several simulations with identical parameters and different initial seeds of the random number generator anneals to the same state. Measurements are post-processed with multiple histogram reweighting [31]. Error estimates are determined by the jackknife method [32].

3. Mixing and superfluid phase transitions in the presence of rotation

In this section we consider the effect of imposing a finite rotation on the condensate. Our main results are presented for a system size of $L = 64$ and $f = 1/32$, but we have considered system sizes $L \in \{32, 64, 96\}$.

Introducing a finite amount of (rotation-induced) vortices in the ground state significantly alters the simple arguments regarding the expected ground state symmetry presented above. The effect of the vortices is to suppress the parameter regime where a broken $\mathbb{Z}_2$ symmetry is found, $\Delta \neq 0$. Recall that for $f = 0$, the ground state the broken $\mathbb{Z}_2$ symmetry will reduce the condensate to a single component condensate with a single broken U(1) symmetry in the ground state. A finite amount of vortices alters this. Vortices interact via long range current–current interactions. It is energetically favorable to maximize the distance between vortices, subject to

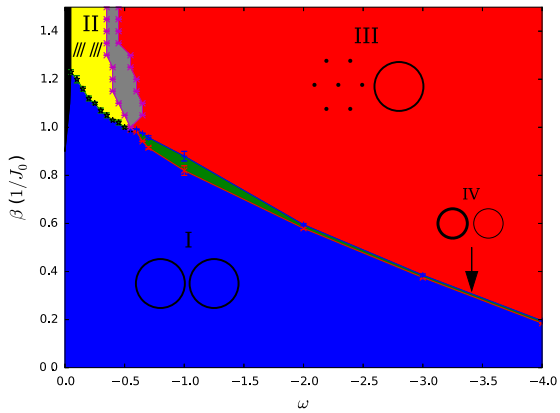

Figure 1. The phase diagram of the two-component Bose–Einstein condensate at finite rotation, $f \neq 0$, $\eta = 5$, and $\omega < 0$. Negative ω may lead to the breaking of the $\mathbb{Z}_2$ -symmetry in the problem, in addition to the usual breaking of the obvious $\mathrm{U}(1) \times \mathrm{U}(1)$ -symmetry. Region I is a $\mathbb{Z}_2$ - as well as $\mathrm{U}(1) \times \mathrm{U}(1)$ -symmetric two-component vortex-liquid phase. Region II is a $\mathbb{Z}_2$ -symmetric striped (nematic) phase consisting of a two-component vortex liquid with broken translational symmetry in a direction perpendicular to the stripes, but not in the direction parallel to the stripes. Region III is a phase with broken $\mathbb{Z}_2$ -symmetry, and with broken translational symmetry in one condensate component, but not the other. Region IV is similar to Region III, except that no translational symmetry is broken in either condensate component. The gray region represents upper and lower bounds of the transition line between Region II and III. Details are explained in the main body of the paper.

the constraint that a specific number of them has to be contained within a given area perpendicular to the direction of rotation. This effect leads to a uniform distribution of minima (equivalently maxima) in the condensate densities. On the other hand, density suppression by vortices in one component in general allows the densities in the second component to nucleate. The short-range repulsive inter-component density–density interaction $(\eta - \omega)(|\psi_1|^2|\psi_2|^2 + |\psi_2|^2|\psi_1|^2)$ (which exceeds the intra-component density–density interaction $(\eta + \omega)(|\psi_1|^2|\psi_1|^2 + |\psi_2|^2|\psi_2|^2)$ for $\omega < 0$), tends to produce regions where the density one component is large while the other is small, and vice versa. Below a critical value of $-\omega = -\omega_c \approx +0.6$, we do not see any onset of $\Delta \neq 0$ at any value of β as the system is cooled from a uniform state. That is, the interface tension between the phases is sufficiently low and the overall free energy, which includes long range inter vortex interaction, is minimized by the state with $\Delta = 0$.

For the subsequent discussion, it helps to consider a schematic phase diagram of the system with $f \neq 0$, which we have obtained through large-scale Monte-Carlo simulations. The phase diagram is shown in figure 1. Region I denotes the simple translationally invariant high-temperature $\mathbb{Z}_2$ - and $\mathrm{U}(1) \times \mathrm{U}(1)$ -symmetric two-component phase with equal densities of both condensate components. Region II shows the $\mathbb{Z}_2$ -symmetric striped phase. Region III is a region with broken $\mathbb{Z}_2$ -symmetry, with one high-density condensate component in a uniform hexagonal vortex lattice phase, and one low-density component in a uniform vortex liquid phase. The gray region separating Region II and III represents upper and lower bounds of the transition between Region II and III. Region IV is a region with broken $\mathbb{Z}_2$ -symmetry, but with the two condensates both in a vortex-liquid phase. Thus, the phase transition separating Region I from Region II is a phase-transition line separating a two-component isotropic vortex liquid from a two-component striped (nematic) vortex liquid. The line separating Region I from Region IV is one where a $\mathbb{Z}_2$ -symmetry is broken, and the line separating Region II from Region IV is one where a translational symmetry is broken and the system acquires non-zero helicity modulus

3.1. Transition from Region I to Region II

We first consider the thermally driven transition from the high-temperature symmetric two-component vortex liquid phase, Region I, to the low-temperature two-component striped (nematic) phase, Region II, for fixed negative ω, but where $|\omega| < |\omega_c|$, i.e. to the left of the splitting point where Region IV opens up.

In figure 2 we show the specific heat c_V, helicity moduli in the z-direction $\Upsilon_{z,i}$ as the inverse temperature β is varied, for $f = 1/32$ and $\omega = -0.50$. This corresponds to a value of $-\omega$ to the left of the splitting point where Region IV opens up (see figure 1). The longitudinal helicity moduli $\Upsilon_{z,i}$ of both components develop a finite expectation value. The onset of this finite value is accompanied by an anomaly in the specific heat.

We note the sharp, δ-function anomaly in the specific heat and the discontinuous behavior of the helicity moduli in both components. These features are all straightforwardly interpreted as signals of a first-order phase transition. This is furthermore borne out by performing a computation of the histogram of the free energy

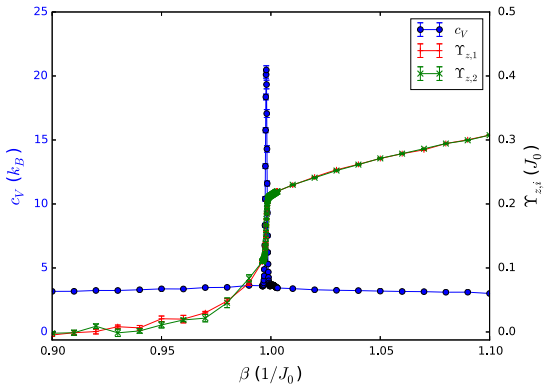

Figure 2. Specific heat, c_V, and helicity moduli along the z-axis , $\Upsilon_{z,i}$, with $f = 1/32$ and $\omega = -0.50$, i.e as the system transitions from Region I to Region II in figure 1.

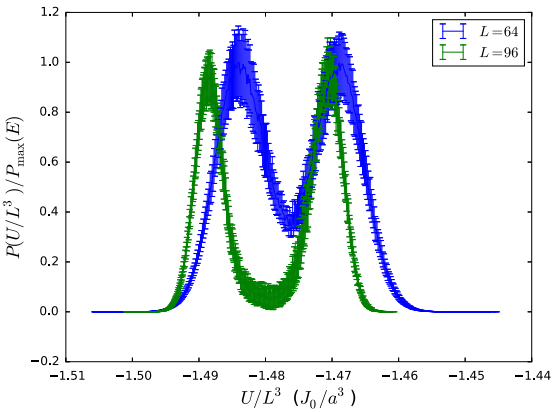

Figure 3. Histograms of the probability distribution of the internal energy per site, U/L^3, at the transition point $\omega = -0.5$, $\beta \approx 0.9995$, separating Region I from Region II in figure 1, for $L = \{64, 96\}$. Multi-histogram reweighting was used to obtain histograms with approximately equal peak heights.

versus internal energy of the system at precisely at the transition, see figure 3. This shows a double-dip structure with a peak in between, the standard hallmark of two degenerate coexisting states separated by a surface whose energy is given by the height of the peak between the minima. This surface energy clearly scales up with system size (more precisely it scales with the cross-sectional area of the system), while the difference between the energies separating the two degenerate states approaches a finite value as the system size increases. The histograms develop into two separate δ-function peaks as the system size increases, while the difference in the internal energy between the two degenerate states of equal probability (equivalently of equal free energy) is the latent heat of the system. The latter clearly approaches a finite value per degree of freedom as the system size increases, demonstrating the first-order character of the transition.

To further characterize the transition I $\rightarrow$ II, figure 4, shows the $\mathbb{Z}_2$ order parameter Δ and the structure functions $S_i(\mathbf{q}_\perp)$, $i \in (1, 2)$ in a narrow range around the transition point. From the top panel, it is seen that $\Delta = 0$ for all β considered. Moreover, we see that as β is increased, the maximum value of the structure function, corresponding to the developing Bragg peaks in the low temperature phase are significantly increased at the transition temperature. The maximum is measured by averaging the maximum of the structure function at each measurement, regardless of location, hence the actual value may differ from what is seen in the bottom panel of figure 4. The onset of the latter marks the transition from a uniform two-component vortex liquid to a two-component nematic vortex liquid, a striped phase. The mechanism for producing the striped phase is described above. In the striped phase, it is difficult to equilibrate the system at each new temperature step with only local MC-updates, as is evident from the noise in the structure functions seen on the low temperature side

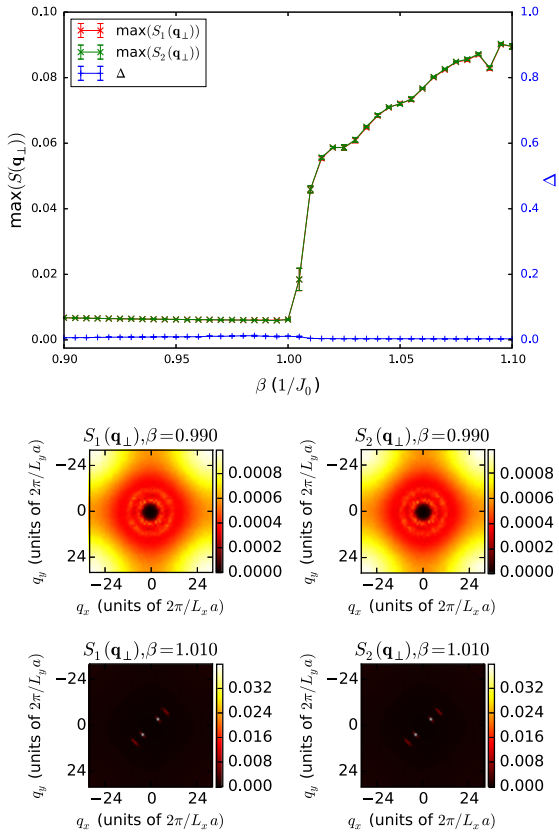

Figure 4. $\mathbb{Z}_2$ order parameter Δ and vortex structure functions $S_i(\mathbf{q}_\perp)$, $i \in (1,\ 2)$ in the vicinity of the transition from Region I to Region II, figure 1, with $f = 1/32$, $\omega = -0.50$. The top panel shows Δ as a function of β, as well as maxima of the structure functions $\max\left(S_i(\mathbf{q}_\perp)\right)$. The four bottom panels show the structure functions $S_1(\mathbf{q}_\perp)$ and $S_2(\mathbf{q}_\perp)$ for the two values $\beta = 0.990$ and $\beta = 1.010$.

of the top panel of figure 4. This noise would most likely be improved by using different approaches, for instance cluster algorithms. However, the noise does not alter our conclusions regarding the transition, or the nature of the striped phase. Note that in the thermodynamic limit, isolated vortex sheets can be expected to be in the state of one-dimensional (1D) liquid at any finite temperature in analogy with the absence of crystalline order in 1D systems.

We thus conclude that the transition from Region I to Region II is a first order phase-transition involving the breaking of a composite $\mathrm{U}(1) \times \mathrm{U}(1)$ symmetry, from an isotropic two-component vortex liquid in Region I to a two-component nematic phase of intercalated lattices of stripes of 1D vortex liquids in Region II. We next go on to consider in some more detail the structure functions, primarily to gain more insight into the character of the striped phase of Region II.

The four bottom panels of figure 4 show the structure functions $S_i(\mathbf{q}_\perp)$, $i \in (1,\ 2)$ at two values of β, $\beta = 0.990$ and $\beta = 1.010$. At $\beta = 0.990$, both structure functions show ring-like structures characteristic of an isotropic liquid. Notice also that the intensity of the rings are equal, which is a consequence of the fact that $\Delta = 0$. At $\beta = 1.010$, both structure functions have developed Bragg peaks in one direction bot no Bragg peaks in the corresponding perpendicular direction. This is indicative of a striped phase.

This may be further corroborated by correlating the structure functions with real-space vortex structures for various values of β. This is shown in figure 5.

One aspect of the structure functions shown in the two bottom rows of figure 5, is particularly important. Consider first the case $\beta = 0.900$, well within Region 1 for $\omega < \omega_c$. This is shown in the leftmost column of figure 5. The real-space vortex configurations in both components are disordered. Moreover, $S_i(\mathbf{q}_\perp)$, $i \in (1,\ 2)$ both components feature ring-structures characteristic of an isotropic liquid phase. The value of $|\mathbf{q}|$ at which the rings appear is a measure of the average inverse separation between the vortices in the isotropic liquids. The intensities of both structure functions is the same. Consider next the case $\beta = 0.995$, shown in the middle

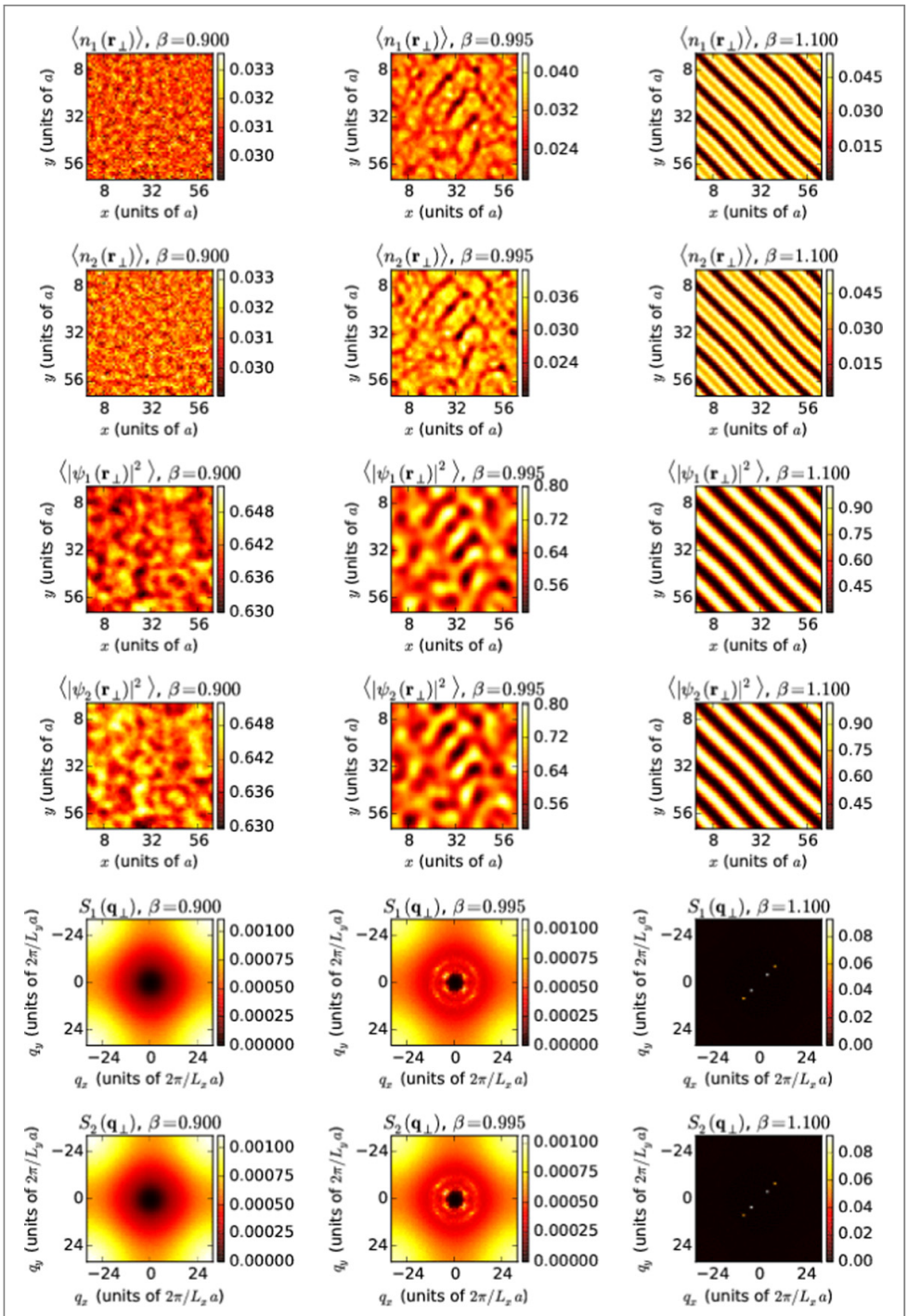

Figure 5. Tableaux showing detailed real space and reciprocal space pictures of the transition from Region I to Region II. The inverse temperature is varied between each column, $\beta \in \{0.900,\ 0.995,\ 1.100\}$. Each row shows averaged vortex densities of each component, $\langle n_i(\mathbf{r}_\perp)\rangle$, averaged amplitude densities of each component, $\langle|\psi_i(\mathbf{r}_\perp)|\rangle$, and vortex structure functions of each component, $S_i(\mathbf{q}_\perp)$. The leftmost column corresponds to an inverse temperature well within Region I, the middle column is at an inverse temperature just below the transition into Region II, while the rightmost column is well within Region II.

column of figure 5. From the real-space pictures, one discerns a tendency towards stripe-formation. This is reflected in $S_i(\mathbf{q}_\perp)$, $i \in (1, 2)$, where the ring-like structures now instead are anisotropic, developing peaks in the direction perpendicular to the direction of the incipient stripes. At even lower temperatures $\beta = 1.100$, well within Region II where stripes are fully developed, the tendency towards anisotropies in $S_i(\mathbf{q}_\perp)$, $i \in (1, 2)$ is even more obvious. This is shown in the rightmost column of figure 5. In this case, Bragg-peaks have fully developed in the directions perpendicular to the stripes. There are, however, no Bragg peaks in the direction parallel to the stripes. If the stripes were perfectly straight, there would be two weak Bragg peaks in these directions. This would be the 1D analog of the ring-like liquid structures of the isotropic liquid. The value of $|\mathbf{q}|$ at which this single weak peak occurs corresponds to the inverse average separation between vortices within the stripes. The reason they are not observed in our calculations, is due to the slight fluctuations in the shape of the stripes, which wash the Bragg peaks out.

We thus conclude that Region II is a striped phase where the stripes form 1D vortex liquids. Vortices in quasi-1D systems have finite energy and cannot form a 1D solid at any finite temperature. This is consistent with the structure factor we observe. On the other hand, the interaction between stripes may not be negligible, so the details of the phase diagram in Region II warrant further investigation. A notable feature of this state is the finite helicity modulus in z-direction, even if the structure factors show absence of vortex ordering within stripes. This highly unusual situation originates with the positive interface energy between the two condensates. That is, consider a stripe-liquid in x-direction. A vortex line in the z-direction is free to execute transverse meanderings in the x-direction. A superflow in the z-direction would produce a y-component of the Magnus-force on the x-components of the fluctuating vortex lines. However, vortex segments are restrained from moving in y-direction due to the stripe interface tension. This results in the observed finite helicity modulus in z-direction. Similar results are found for a number of other ω-values we have considered, for[4] $-\omega < 0.6$.

3.2. Transition from Region I to Region III, via Region IV

Increasing $-\omega$ further, such that the inter-species density–density interaction increases, eventually favors a different pattern of phase-separation of the two components, despite the effect of long-range current–current interactions between rotation-induced vortices promoting uniform density distributions. This leads to a broken $\mathbb{Z}_2$ -symmetry. The condensate component with a globally suppressed density will therefore be in a vortex-liquid phase while the condensate component with globally enhanced density will be in a vortex lattice phase. Thus, the broken symmetries of the ordered phase are $\mathrm{U}(1) \times \mathbb{Z}_2$, and the breaking of these symmetries are split into two separate transitions. The splitting occurs because the $\mathrm{U}(1)$ -sector directly couples to the rotation, while the $\mathbb{Z}_2$ -sector does not. The phase-transition in the stiff $\mathrm{U}(1)$ -sector, which is a vortex-lattice melting, is therefore separated from the $\mathbb{Z}_2$ -transition by an amount which depends on f.

This is illustrated in figure 6, showing Δ, specific heat C_V, and $\Upsilon_{z,1}$, $\Upsilon_{z,2}$ as functions of β. The $\mathbb{Z}_2$ order parameter Δ has an onset at $\beta_{\mathbb{Z}_2}$, at which the specific heat has an anomaly. This transition is a transition where an Ising like order parameter is broken, and can be continuous. There is no onset of $\Upsilon_{z,2}$, showing that component 2 remains in a vortex liquid phase. Component 1 forms a vortex solid at lower temperature, as evidenced by the onset of $\Upsilon_{z,1}$. This happens at a $\beta_{\mathrm{U}(1)}$ which is separated from $\beta_{\mathbb{Z}_2}$, as explained above. The freezing of component one is effectively a freezing transition of a single component, and is therefore expected to be a first-order transition. Accompanying this one would expect to see a second, smaller anomaly in the specific heat, at a lower temperature. This is not observed in the simulations performed, as the small anomaly is completely overshadowed by the large specific heat peak from the $\mathbb{Z}_2$ transition.

Figure 7 shows the structure functions $S_1(\mathbf{q}_\perp)$ and $S_2(\mathbf{q}_\perp)$ at $\omega = -4.0$ at three different values of β, namely $\beta = (0.184, 0.190, 0.195)$. These values correspond to Regions I, IV, and III in figure 1, respectively. Here again, we see the freezing of one component across the transition, while the other component remains in the liquid phase. The additional information we get out of these panels is that one component remains an *isotropic* vortex liquid, while the other component freezes into a hexagonal vortex liquid. This sets the low-temperature Region III (see figure 1) at $\omega = -4.0$ drastically apart from the low-temperature Region II (see figure 1) at $\omega = -0.50$. The latter features a low-temperature two-component nematic vortex liquid phase with broken rotational invariance, the former case features a low-temperature mixed isotropic vortex liquid/hexagonal vortex lattice phase.

Taking figure 1 and figure 6 at face value, suggests that two separate transitions exist. However, one cannot entirely rule out finite-size artifacts associated with a single transition where the onset of $\Upsilon_{z,1}$ would coincide with the onset of Δ in figure 6. By examining the structure factors, examples of which are shown in the middle panel of figure 7 it is evident that a relatively large intermediate regime corresponding to Region IV is observed. From the sharp onset of Δ, accompanied by the specific heat peak, we determine the transition temperature for

[4] We also observed much smaller but finite helicity modulus in the direction perpendicular to stripes, which we interpret as a consequence of weak standard geometric pinning of domain walls.

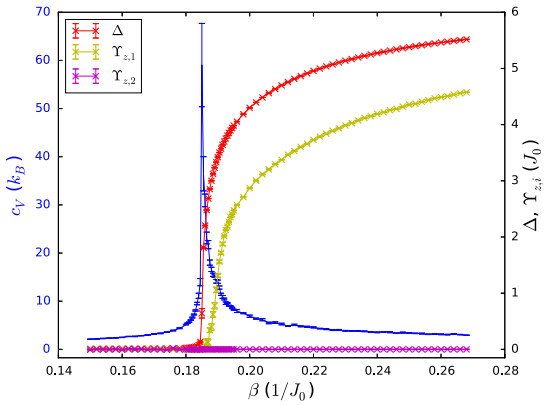

Figure 6. The phase transitions between Region I and Region IV, and between Region IV and Region III, for $f = 1/32$, $\omega = -4.0$, and $L = 64$. Note the separation between the onset of Δ and $\Upsilon_{z,i}$. The onset of Δ signals the breaking of a $\mathbb{Z}_2$ -symmetry, along with the associated anomaly in specific heat C_V. This marks the transition from Region I to Region IV in figure 1. In Region IV, we have $\Delta \neq 0$, while both components remain in isotropic vortex liquid states. In passing from Region IV to Region III in figure 1, the onset of one of the helicity moduli, $\Upsilon_{z,1}$ say, signals the freezing of the vortex liquid in the corresponding component, while the absence of an onset of the helicity modulus, $\Upsilon_{z,2}$ say, in the other component shows that this component remains in a vortex liquid phase. The onset of $\Upsilon_{z,1}$ signals the breaking of a U(1) -symmetry associated with vortex-liquid freezing.

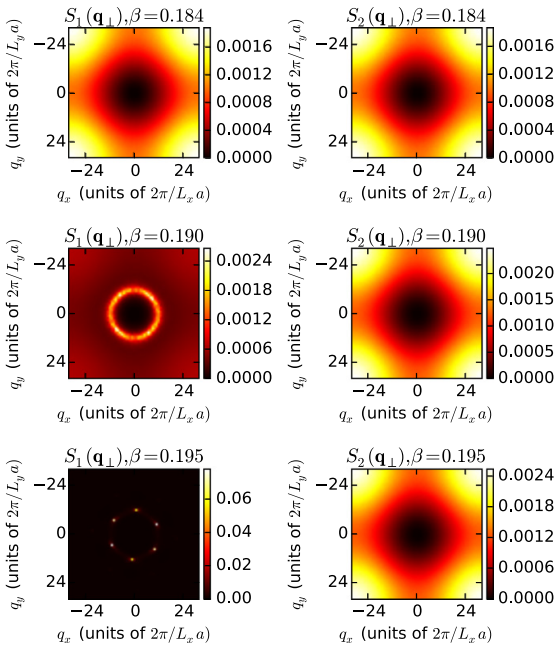

Figure 7. The phase transitions of the system for $f = 1/32$, $\omega = -4.0$. Structure functions $S_1(\mathbf{q}_\perp)$ and $S_2(\mathbf{q}_\perp)$ at three different values of β, namely $\beta = (0.184,\ 0.190,\ 0.195)$, corresponding to Regions I, IV, and III in figure 1, respectively.

the $\mathbb{Z}_2$ symmetry breaking to be $\beta_{\mathbb{Z}_2} = 0.1850(5)$. The appearance of six sharply defined Bragg peaks in the structure factor, appear at a lower temperature $\beta = 0.195(1)$. The onset of $\Upsilon_{z,1}$ prior to the appearence of the Bragg peaks may be a finite size effect. That being said, simulating larger system sizes may also alter the details of the transition temperatures.

On general grounds one may expect that phase IV should exist. The simulations unambiguously identify a state where one component has a vortex lattice while the other component with a suppressed density is in a state of tensionless vortex matter. Since a vortex liquid can form due to positional disorder of tension-full vortex lines,

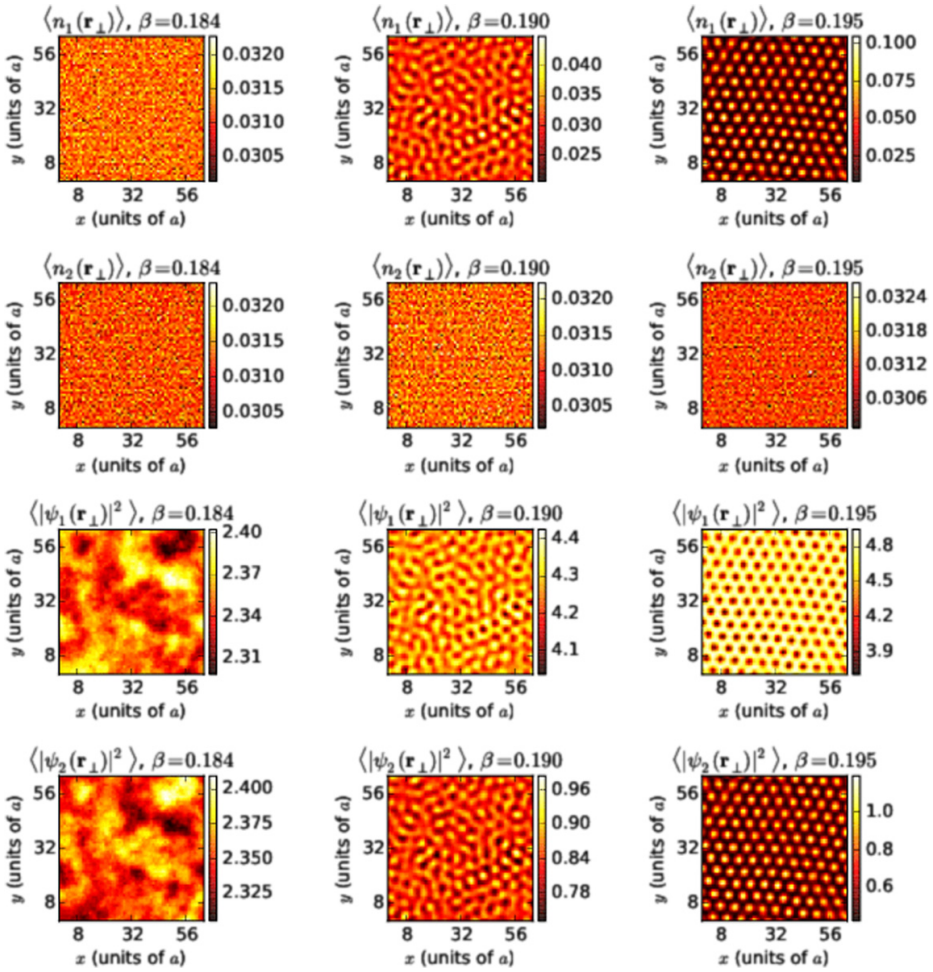

Figure 8. Tableaux showing detailed real space pictures of the transition from Region I to Region III, via Region IV. The inverse temperature is varied between each column, $\beta \in \{0.184,\ 0.190,\ 0.195\}$, and $\omega = -4$. Each row shows, from top to bottom, averaged vortex densities of each component, $\langle n_i(\mathbf{r}_\perp)\rangle$, and averaged amplitude densities of each component, $\langle|\psi_i(\mathbf{r}_\perp)|\rangle$. Note the vortex-ordering in one of the components, and the lack of vortex-ordering in the other component, as the system transitions from the symmetric phase Region I ($\beta = 0.184$) to the low-temperature phase Region III ($\beta = 0.195$). Note also the disparity in density-amplitudes in the two components in the intermediate regime Region IV ($\beta = 0.190$), due to the $\mathbb{Z}_2$ -symmetry breaking.

it can be expected that the tension-full vortex liquid in the dominant component still suppresses the density of subdominant component leading to the appearance of the state IV. Alternatively, suppose that one starts out from a low-temperature phase-separated state where one components is in a vortex lattice state and the other component effectively has a much lower density. The vortex lattice of the dominant component may melt without affecting the density in this component, since vortex-lattice melting is driven by phase-fluctuations of the superfluid order parameter, not density fluctuations. Further investigation of this part of the phase diagram is warranted.

For a more detailed overview of the transition, figure 8 shows the evolution of $\langle n_i(\mathbf{r}_\perp)\rangle$, $\langle|\psi_i(\mathbf{r}_\perp)|\rangle$, and $S_i(\mathbf{q}_\perp)$ across the three Regions, I, IV, and III. If one follows the evolution of the vortex densities in each component, it is seen that the component which acquires a low stiffness in Region IV and III is virtually unchanged, i.e. it remains in a completely uniform state. The other component, on the other hand, evolves from a uniform state in Region I, through being close to freezing into a hexagonal lattice in Region IV, and finally into a hexagonal structure in Region III. The amplitude densities corroborate this picture. In Region I they are on average equal and uniform, while in Region IV the difference in stiffness is clearly seen. Here some inhomogeneities arise in the stiff component as the vortices are close to entering a hexagonal phase, which is also reflected in the soft component simply because of the local intercomponent repulsion. In Region III, the

amplitude density of the stiff component is high and uniform with small dips corresponding to each vortex. The soft component is low and uniform with small peaks, again due to intercomponent interactions.

3.3. Transition from Region II to Region III

Finally, we consider the transition from Region II to Region III. In Region II, we have $\Delta = 0$, while in Region III, $\Delta \neq 0$. Therefore the Regions II and III are separated by a $\mathbb{Z}_2$ -symmetry breaking. Stripe-forming systems in general have complicated structural transitions. We find an intermediate regime where the lattice of stripes has disordered, but where the hexagonal lattice/isotropic liquid-mixture has not yet fully developed. This results in multiple metastable, but robust coexisting phases of vortices in components 1 and 2 residing in different parts of the condensate. These two coexisting phases are separated by a surface of positive surface energy. This surface constrains the motion of vortex systems. As a result, in the finite systems which we simulate, the helicity modulus $\Upsilon_{z,i}$ acquire nonzero values in both components in this intermediate regime.

As $-\omega$ is increased further, such that one component becomes dominant and the other is suppressed, the minor component becomes normal. Note that when the inclusions of the normal component become isolated, they represent quasi-1D subsystems. Quasi-1D systems are superfluid only at zero temperature. However, simulations on finite systems may still display finite helicity modulus. As the density of the component increases, the corresponding intra-component current–current interaction between the rotation-induced vortices in this component increases. Hence, the intra-component long-range interaction for this component dominates, and a hexagonal vortex-lattice results. Consequently, the helicity-moduli in the two components have quite different behavior as $-\omega$ increases. In the component that eventually takes up a vortex lattice state, it increases monotonically with $-\omega$. In the other component, it is non-monotonic as a function of ω, eventually approaching 0 deep into Region III.

Typical examples of the vortex structures that appear between Region II and Region III in figure 1 are shown in figure 9. These are all metastable, long-lived states which prevent equilibration of the system. We have been unable to locate the sharp separatrix between these two regions, and whether there are other stable intermediate phases due to the lack of equilibration. Note that this problem is known in other stripe-forming systems where phases are separated by metastable and glassy states [41, 42]. The gray area in figure 1 represents upper and lower bounds for the transition. The bounds were determined by determining the parameter range where the simulation equilibrates to either striped or hexagonal/liquid separated configurations, exclusively.

4. Conclusions

In this paper, we have considered the states of a two-component BEC in the situation where inter-component density–density interactions dominate the intra-component density–density interactions. The two components of the condensate are assumed to be comprised of homonuclear atoms in two different hyperfine states. The problem features an Ising-like symmetry. This Ising (or $\mathbb{Z}_2$) symmetry emerges from the dominance of the inter-component interactions over the intra-component ones. The spontaneous breaking of this Ising-symmetry corresponds to a spontaneously generated, interaction-driven, imbalance between condensates in different hyperfine states.

At finite rotation, we find four regions, denoted Regions I, II, III, and IV, of thermodynamically stable states, see figure 1. Region I is a high-temperature regime where the system remains in a two-component isotropic vortex liquid phase with equal densities of both components. Region II is a nematic phase (broken rotational symmetry) with ordered stripes of 1D vortex liquids, and with equal densities in different components. This state features a spontaneously broken composite $\mathrm{U}(1) \times \mathrm{U}(1)$ -symmetry, but is $\mathbb{Z}_2$ -symmetric. In addition it spontaneously breaks translation symmetry in one direction due to formation of periodic modulation of condensate densities. Region III is a mixed state with one component in a $\mathrm{U}(1)$ -symmetric isotropic vortex liquid phase while the other component resides in a hexagonal vortex lattice phase with broken $\mathrm{U}(1)$ -symmetry. The origin of the different behaviors of the two components is that Region III also features a spontaneously broken $\mathbb{Z}_2$ -symmetry, i.e. a difference in the densities of the two components. The component with a large density has higher phase stiffness than the component with the lower density, hence the discrepancy in their vortex states. Finally, Region IV is a region intermediate between Region I and Region III, in which $\mathrm{U}(1)$ -symmetry is not broken in either of the components, but where a spontaneously generated imbalance between densities of hyperfine states exists. Both components are in an isotropic and disordered vortex state.

The phase transition from Region I to Region II in figure 1 is a first-order composite $\mathrm{U}(1) \times \mathrm{U}(1)$ transition. The phase transition between Region I and Region IV is associated with a spontaneous $\mathbb{Z}_2$ symmetry breaking where a difference in densities of the two condensates sets in. The phase-transition between Region IV and Region III is a first order $\mathrm{U}(1)$ transition associated with the freezing of an isotropic vortex liquid in one component into a hexagonal vortex lattice in the same component, while the other component (the one with

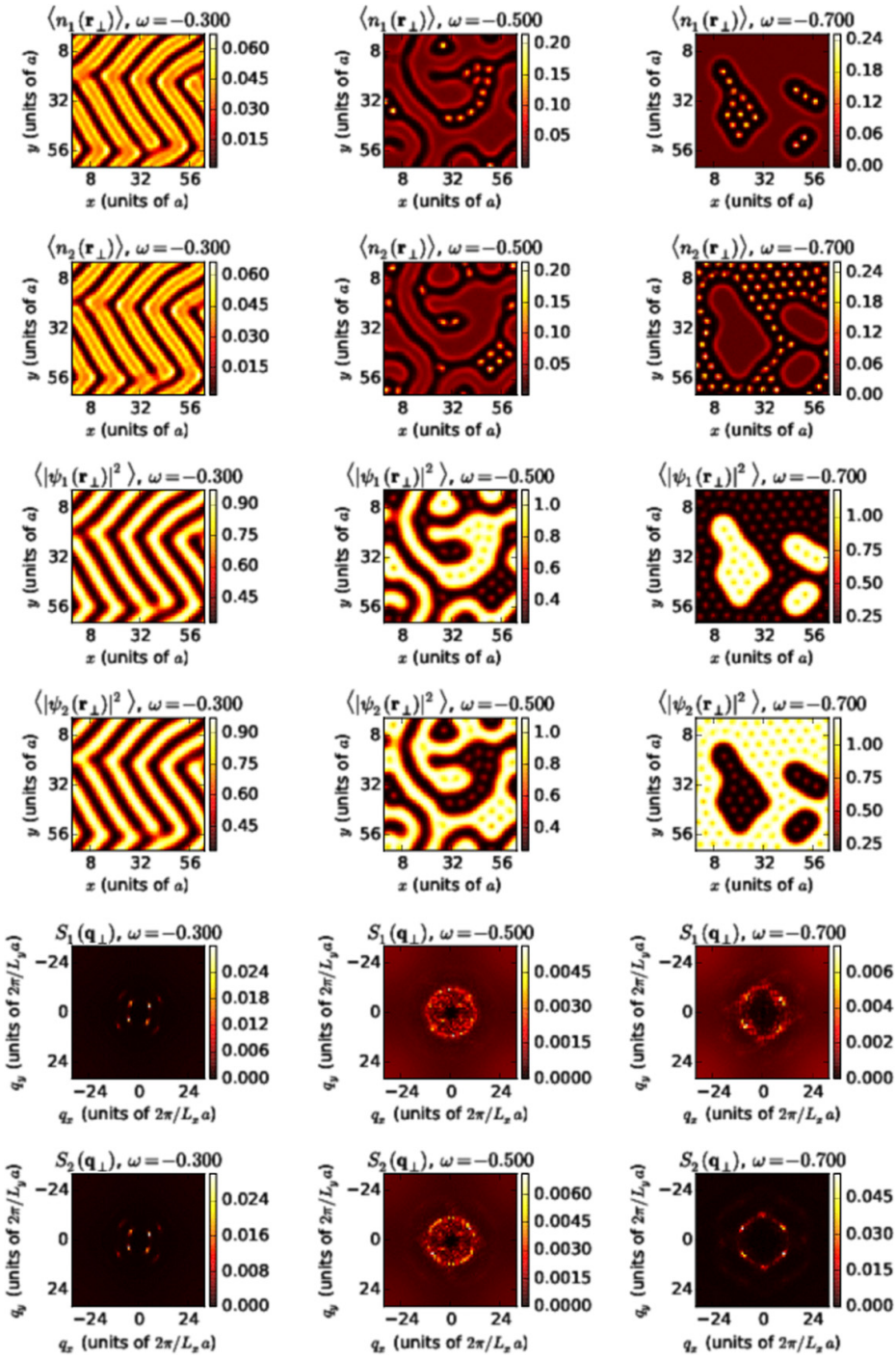

Figure 9. Tableaux showing detailed real space and reciprocal space pictures of the transition from Region II to Region III. The parameter ω is varied between each column, $\omega \in \{-0.300,\ -0.500,\ -0.700\}$, while the inverse temperature is fixed, $\beta = 1.2$. Each row shows, from top to bottom, averaged vortex densities of each component, $\langle n_i(\mathbf{r}_\perp)\rangle$, averaged amplitude densities of each component, $\langle|\psi_i(\mathbf{r}_\perp)|\rangle$, and vortex structure functions of each component, $S_i(\mathbf{q}_\perp)$. The first column shows a configuration close to a pure Region II configuration, the second column is a configuration from the highly metastable crossover region, while the last column shows a configuration close to a pure Region III configuration. Note that we consider both the first and the last column to be in Region II and III, respectively, as they consist of purely of domains with configurations from either region, not a mixture of the two.

depleted density due to the $\mathbb{Z}_2$ -symmetry breaking) remains in the isotropic vortex liquid phase. The phase transition from Region II to Region III, driven by increasing the dominance of inter-component density–density interactions over intra-component density–density interactions, involves at the very least a spontaneous breaking of a $\mathbb{Z}_2$ -symmetry as the two condensate components pass from a nematic state of intercalated lattices of 1D vortex liquids into a mixed state of an isotropic vortex liquid in one component and a hexagonal vortex lattice in the other component. This transition is characterized by a broad regime of metastable states with inhomogeneous phase separation.

Figure 8 suggests that the rotation frequency is much smaller than the second critical frequency Ω_{c2}. A crude estimate for the rotation frequency may be obtained as follows. If the rotation frequency were to be set at upper critical rotation frequency Ω_{c2}, the vortex cores would start overlapping, thus covering the plane perpendicular to the rotation. The actual rotation frequency Ω may thus be estimated in terms of the upper critical rotation as $\Omega/\Omega_{c2} = c$, where c is a numerical factor given by the fraction of the area of the plane perpendicular to the rotation which is covered by vortex cores. Thus, an estimate, based on core size, gives $\Omega \propto 0.1\ \Omega_{c2}$. This puts the system well outside the regime of lowest-Landau level physics. The system is therefore indeed in a regime where it makes sense to talk about vortex-degrees of freedom rather than zeroes of the order parameter as the relevant degrees of freedom. For this rotation frequency, we have found the critical value of ω (one of our interaction parameters) to observe phase IV to be $\omega_c \approx -0.6$. This requires scattering lengths $a_{12}/a_{11} > 1.3$. Since these scattering lengths *a priori* are similar, and can be manipulated with Feshbach resonances, it seems feasible to be able to observe phase IV. In order to see the striped ground states phase II, the requirement is only that $a_{12}/a_{11} > 1$, which certainly seems to be within the realms of possibility.

In this paper we have studied the system in the thermodynamic limit. Nonetheless, the results also yield insights into certain aspects of the physics of finite systems with phase separation of species in which the total numbers of particles are finite and independently conserved. For instance, for conserved total number of particles and in the absence of rotation, a finite two-component system can form a bi-domain in the low temperature state in the parameter regime we have considered in this paper. In our case, the ground state is a mono-domain. In both cases, however, the system evolves into similar mixed states at increased temperature. Thus, although the thermodynamic limit calculations provide insights into the phases and phase transitions in the systems, it also calls for further investigation of finite systems of this kind in the presence of a trap.

Acknowledgments

PNG was supported by NTNU and the Research Council of Norway. EB was supported by the Knut and Alice Wallenberg Foundation through a Royal Swedish Academy of Sciences Fellowship, by the Swedish Research Council grants 642-2013-7837, 325-2009-7664, and by the National Science Foundation under the CAREER Award DMR-0955902, AS was supported by the Research Council of Norway, through Grants 205591/V20 and 216700/F20, as well as European Science Foundation COST Action MPI1201. This work was also supported through the Norwegian consortium for high-performance computing (NOTUR).

References

[1] Myatt C J, Burt E A, Ghrist R W, Cornell E A and Wieman C E 1997 *Phys. Rev. Lett.* **78** 586
[2] Modugno G, Modugno M, Riboli F, Roati G and Inguscio M 2002 *Phys. Rev. Lett.* **89** 190404
[3] Thalhammer G, Barontini G, de Sarlo L, Catani J, Minardi F and Inguscio M 2008 *Phys. Rev. Lett.* **100** 210402
[4] McCarron D J, Cho H W, Jenkin D L, Köppinger M P and Cornish S L 2011 *Phys. Rev.* A **84** 011603
[5] Raithel G, Birkl G, Kastberg A, Phillips W D and Rolston S L 1997 *Phys. Rev. Lett.* **78** 630
[6] Müller-Seydlitz T, Hartl M, Brezger B, Hänsel H, Keller C, Schnetz A, Spreeuw R J C, Pfau T and Mlynek J 1997 *Phys. Rev. Lett.* **78** 1038
[7] Hamann S E, Haycock D L, Klose G, Pax P H, Deutsch I H and Jessen P S 1998 *Phys. Rev. Lett.* **80** 4149
[8] Friebel S, D'Andrea C, Walz J, Weitz M and Hänsch T W 1998 *Phys. Rev.* A **57** R20
[9] Guidoni L and Verkerk P 1998 *Phys. Rev.* A **57** R1501
[10] Catani J, de Sarlo L, Barontini G, Minardi F and Inguscio M 2008 *Phys. Rev.* A **77** 011603
[11] Lin Y-J, Compton R L, Jimnez-Garca K, Porto J V and Spielman I B 2009 *Nature* **482** 628
[12] Lin Y-J, Compton R L, Perry A R, Phillips W D, Porto J V and Spielman I B 2009 *Phys. Rev. Lett.* **102** 130401
[13] Galitski V and Spielman I B 2013 *Nature* **494** 49
[14] Kasamatsu K, Tsubota M and Ueda M 2003 *Phys. Rev. Lett.* **91** 150406
[15] Kasamatsu K, Takeuchi H, Tsubota M and Nitta M 2013 *Phys. Rev.* A **88** 013620
[16] Tojo S, Taguchi Y, Masuyama Y, Hayashi T, Saito H and Hirano T 2010 *Phys. Rev.* A **82** 033609
[17] Celabrese P, Pelissetto A and Vicari E 2002 *Phys. Rev.* B **67** 054505
[18] Ceccarelli G, Nespolo J, Pelissetto A and Vicari E 2015 arXiv:cond-mat/1506.04895
[19] Cipriani M and Nitta M 2013 *Phys. Rev.* A **88** 013634
[20] Catelani G and Yuzbashyan E A 2010 *Phys. Rev.* A **81** 033629
[21] Mueller E J and Ho T-L 2002 *Phys. Rev. Lett.* **88** 180403
[22] Filatrella G, Malomed B A and Salerno M 2014 *Phys. Rev.* A **90** 043629
[23] Kuopanportti P, Huhtamäki J A M and Möttönen M 2012 *Phys. Rev.* A **85** 043613

[24] Battye R A, Cooper N and Sutcliffe P M 2002 *Phys. Rev. Lett.* **88** 080401
[25] Kasamatsu K and Tsubota M 2009 *Phys. Rev.* A **79** 023606
[26] Papp S B, Pino J M and Wieman C E 2008 *Phys. Rev. Lett.* **101** 040402
[27] Galteland P N, Babaev E and Sudbø A 2015 *Phys. Rev.* A **91** 013605
[28] Metropolis N, Rosenbluth A W, Rosenbluth M N, Teller A H and Teller E 1953 *J. Chem. Phys.* **21** 1087
[29] Hastings W K 1970 *Biometrika* **57** 97
[30] Matsumoto M and Nishimura T 1998 *ACM Trans. Model. Comput. Simul.* **8** 3
[31] Ferrenberg A M and Swendsen R H 1989 *Phys. Rev. Lett.* **63** 1195
[32] Berg B A 1992 *Comput. Phys. Commun.* **69** 7
[33] Bojesen T A, Babaev E and Sudbø A 2014 *Phys. Rev.* B **89** 104509
[34] Bojesen T A, Babaev E and Sudbø A 2013 *Phys. Rev.* B **88** 220511
[35] Dahl E K, Babaev E, Kragset S and Sudbø A 2008 *Phys. Rev.* B **77** 144519
[36] Herland E V, Babaev E and Sudbø A 2010 *Phys. Rev.* B **82** 134511
[37] Kuklov A, Prokofev N, Svistunov B and Troyer M 2006 *Ann. Phys., NY* **321** 1602
[38] Kragset S, Smørgrav E, Hove J, Nogueira F S and Sudbø A 2006 *Phys. Rev. Lett.* **97** 247201
[39] Kuklov A, Prokof'ev N and Svistunov B 2005 arXiv:cond-mat/0501052
[40] Kuklov A, Prokof'ev N and Svistunov B 2004 *Phys. Rev. Lett.* **92** 030403
[41] Sellin K A H and Babaev E 2013 *Phys. Rev.* E **88** 042305
[42] Garaud J and Babaev E 2015 *Phys. Rev.* B **91** 014510

Paper III

Competing interactions in population imbalanced two-component Bose-Einstein condensates

Preprint

Competing interactions in population-imbalanced two-component Bose-Einstein condensates

Peder Notto Galteland[1] and Asle Sudbø[1]

[1]*Department of Physics, NTNU, Norwegian University of Science and Technology, N-7491 Trondheim, Norway*

(Dated: June 22, 2016)

We consider a two-component Bose-Einstein condensate with and without synthetic "spin-orbit" interactions in two dimensions. Density- and phase-fluctuations of the condensate are included, allowing us to study the impact of thermal fluctuations and density-density interactions on the physics originating with spin-orbit interactions. In the absence of spin-orbit interactions, we find that inter-component density interactions deplete the minority condensate. The thermally driven phase transition is driven by coupled density and phase-fluctuations, but is nevertheless shown to be a phase-transition in the Kosterlitz-Thouless universality class with close to universal amplitude ratios irrespective of whether both the minority- and majority condensates exist in the ground state, or only one condensate exists. In the presence of spin-orbit interactions we observe three separate phases, depending on the strength of the spin-orbit coupling and inter-component density-density interactions: a phase-modulated phase with uniform amplitudes for small intercomponent interactions, a completely imbalanced, effectively single-component, condensate for intermediate spin-orbit coupling strength and sufficciently large inter-component interactions, and a phase-modulated *and* amplitude-modulated phase for sufficiently large values of both the spin-orbit coupling and the inter-component density-density interactions. The phase which is modulated by a single $\boldsymbol{q}$-vector only is observed to transition into an isoptropic liquid through a strong depinning transition with periodic boundary conditions, which weakens with open boundaries.

I. INTRODUCTION

Spin-orbit coupling (SOC) underpins many fascinating phenomena in condensed matter physics, including the spin-Hall[1,2] effects and the existence of topological insulators[3–6]. SOC is also important for determining the physical properties of such important functional materials as GaAS[7]. Due to the fundamental magneto-electric character of SOC in charged systems, it also has important ramification for the manipulation of spin-degrees of freedom using electric fields, currently a research topic of intense focus. While these examples represent systems where a real physical spin is coupled to the orbital motion of electrons, similar phenomena may also be investigated in bosonic systems. Here, the SOC does not originate with a relativistic correction to the equations of motion, as they do in the electronic systems mentioned above. Rather, they are synthetic in the sense of being engineered[8,9] Rashba[10]- and Dresselhaus[11] couplings in multi-component Bose-Einstein condensates. Such multi-component condensates could be either homo-nuclear with different species occupying different hyperfine spin states[12,13], or they could be mixtures of different types of bosons[14,15]. In either case, one may associate an index with each species of the condensate, serving as an internal "'spin"-degree of freedom. A great advantage of studying the physics of competing interactions and couplings in Bose-Einstein condensates or other ultracold atomic systems is that the interaction parameters, namely density-density interactions and "spin-orbit" couplings, are highly tunable. This facilitates the study of a wide range of phenomena otherwise not accessible in standard condensed matter systems.

SOC in a confined bosonic gas of cold atoms has been achieved using an optical Raman-dressing scheme[8]. A similar scheme has also been used in cold fermionic gases[16]. In optical lattices[17] a synthetic SOC has been realized in a one-dimensional lattice using a similar Raman-dressing scheme[18]. Other proposals for realizing SOC in an optical lattice include periodically driving the lattice with an oscillating magnetic field gradient[19], or by using off-resonance laser beams[20]. The two latter schemes avoids the problem of heating caused by spontaneous emission of photons as they do not rely on near-resonant laser fields.

In the case of topological insulators, the classification scheme and the physical properties of these systems are largely worked out and predicted at zero temperature and ignoring many-body interactions[6,21–23]. It seems worthwhile to examine the effects of both temperature and many-body interactions on the effect of SOC. In this respect, looking at "pseudo-spin" Bose-Einstein condensates offers an attractive alternative for studying many-body effects, since one can, among other things, perform large-scale Monte-Carlo simulations without the complicating factors arising from Fermi-statistics in the problem. Bosonic systems also have the attractive property of featuring a condensate at low enough temperatures, such that one has a mean-field starting point to compare with, at least provided the system is placed far enough away in parameter space from critical point arising either from interaction effects or thermal fluctuations.

Previous works on bosonic spin-orbit coupled condensates have shown that their ground state has a periodically modulated striped spin structure both in a lattice model[24,25] and by numerically solving the continuum Gross-Pitaevskii equations[26]. Including SOC splits the energy bands of spin-up and spin-down particles into bands of definite helicity, where the lower band will have minima at finite momentum, provided that any additional Zeeman-splitting (i.e imbalance in the condensate density) of the bands is not too large. A continuum model will have a degenerate ring of minima in momentum space, with fixed length of the momentum-vector in two dimensions, while a square lattice will break the degeneracy down to four points along the diagonals of the lattice. It has also been shown that, in the weak coupling limit, the bosons will condense either into one or two minima in the ground state, depending on the strength of the intra-component inter-

actions. However, thermal fluctuations have not been considered before in such systems.

In this paper, we therefore consider a two-dimensional two-component Bose-Einstein condensate with a Rashba synthetic SOC. The condensates are also assumed to be population-imbalanced with different densities among the components in the ground state. Fluctuation effects are strong in two-dimensional system such that no local order parameters exist for systems with continuous symmetries. Even so, one may get some rough insights into the effects of varying interactions and temperature at the mean-field level. For a spin-orbit coupled system featuring a non-uniform ground state, this differs from the case where one expects a uniform ground state, in that the gradient terms of the theory need to be included even at the mean-field level. We will perform such a mean-field analysis in this paper, and compare the results to what we obtain in large-scale Monte-Carlo simulations. At low temperatures, we find that that a mean-field analysis yields results for critical values of interaction parameters that destroy the minority-condensate in good agreement with Monte-Carlo simulations. At elevated temperatures, we find that the amplitude-fluctuating two-component condensate undergoes Kosterlitz-Thouless phase transitions for two qualitatively different parameter regimes. *i)* In the absence of SOC, we find that the condensate loses phase-coherence via proliferation of vortex-antivortex pairs in an amplitude-fluctuating background, and that this phase transition is a Kosterlitz-Thouless phase transition with a universal amplitude ratio of the jump in superfluid density to critical temperature given by $2/\pi$. *ii)* In a parameter regime where SOC plays a role, and gives a non-uniform ground state in the form of stripes of modulated *phases* (but not amplitudes) of the condensate ordering fields, we find via finite-size scaling of the structure functions at the pseudo-Bragg vectors that the stripes melt through thermal depinning from the lattice, and not in a Kosterlitz-Thouless-Halperin-Nelson-Young phase transition. When the condensate we study features a non-uniform ground state, it may be thought of as a bosonic analogue to either a two-dimensional two-component superconductor in a Larkin-Ovchinnikov state, or to a one-component superconductor in a Fulde-Ferrell state. The former features topological order at finite temperature, the latter is topologically disordered at any finite temperature[27].

The paper is structured as follows. Section II presents the model and observables we use to classify the states and transitions observed. Section III contains the mean-field calculations. Section IV describes the Monte-Carlo scheme we use. In Section V all our Monte-Carlo results as well as discussions of their significance is included. We present our conclusions in Section VI.

II. MODEL

In this section, we present the lattice model used in the Monte-Carlo simulations, discuss some of its basic properties and present the observables measured in simulations to classify the phases and phase transitions we observe.

A. Ginzburg-Landau model

The starting point of our formulation is the standard two-component Ginzburg-Landau model with an added SOC, given by

$$H = \int d^2r \left[\frac{1}{2} \left| \nabla \Psi \right|^2 + V(\Psi) \right] + H_{\mathrm{SO}} \tag{1}$$

Here, $\Psi^\dagger = (\psi_1^*, \psi_2^*)$ is a spinor of two complex fields, where the individual components may be though of as a pseudospin degree of freedom, and V is the potential. We allow the potential to contain inter- and intra-component density-density interactions, as well as a chemical potential. The chemical potential is chosen to have different strengths for each component, which may be viewed as a Zeeman-like field acting on the pseudospins.

$$V(\Psi) = \sum_i \alpha_i |\psi_i|^2 + \sum_{ij} g_{ij} |\psi_i|^2 |\psi_j|^2 \tag{2}$$

The term containing the spin-orbit interaction, H_{SO}, is of the Rashba type, on the form

$$H_{\mathrm{SO}} = \frac{i\kappa}{2} \int d^2r \Psi^\dagger \left((\boldsymbol{\sigma} \times \nabla) \cdot \hat{\boldsymbol{z}} \right) \Psi + \mathrm{h.c.} \tag{3}$$

We may write the SOC on component form

$$H_{\mathrm{SO}} = \frac{\kappa}{2} \int d^2r \Big[\psi_2^* \partial_x \psi_1 - \psi_1^* \partial_x \psi_2 + i\psi_2^* \partial_y \psi_1 + i\psi_1^* \partial_y \psi_2 \Big] + \mathrm{h.c.} \tag{4}$$

To simplify the representation of the potential term, we introduce the following parametrization $\alpha_1 = \alpha(1-\Delta)$, $\alpha_2 = \alpha(1+\Delta)$, $g_{11} = g(1-\gamma)$, $g_{22} = g(1+\gamma)$, $g_{12} = \lambda g$. Δ thus tunes the imbalance of the components, γ tunes the relative strengths of the intra-component density-density interations, while λ tunes the strength of the inter-component density-density interaction. The latter is responsible for producing a phase-separated state.

B. Lattice formulation

To arrive at a lattice model suitable for Monte-Carlo simulations, we discretize the continuous fields ψ_i on a square grid, that is we let $\psi_i \to \psi_{\boldsymbol{r},i}$, where $\boldsymbol{r} = (r_x, r_y)$, $r_\mu \in (1, \ldots, L)$ and $\mu \in (x, y)$. The derivatives are converted to forward finite differences through the replacement

$$\partial_\mu \psi_i \to \frac{1}{a} \left(\psi_{\boldsymbol{r}+\hat{\boldsymbol{\mu}},i} - \psi_{\boldsymbol{r},i} \right), \tag{5}$$

where $\hat{\boldsymbol{\mu}}$ is a unit vector in the μ-direction, and a is the lattice spacing. We suppress the lattice spacing in the following expressions, real space distances are plotted in units of a, while

reciprocal space is plotted in units of $2\pi/La$. By introducing real amplitudes and phases, $\psi_{\boldsymbol{r},i} = |\psi_{\boldsymbol{r},i}| \exp(i\theta_{\boldsymbol{r},i})$ we may write the derivatives of the Hamiltonian in terms of trigonometric functions.

We write the Hamiltonian as a sum of three terms as follows

$$H = H_K + H_{\rm SO} + H_V. \tag{6}$$

H_K contains the kinetic terms, which are written in the standard cosine formulation

$$H_K = \sum_{\mathbf{r},\hat{\boldsymbol{\mu}},i} \left(|\psi_{\mathbf{r}}|^2 - |\psi_{\mathbf{r}+\hat{\boldsymbol{\mu}},i}|\,|\psi_{\mathbf{r},i}| \cos \Delta_\mu \theta_{\mathbf{r},i} \right). \tag{7}$$

The potential term, with the new parametrization, is now written as

$$\begin{aligned} H_V = \sum_{\mathbf{r}} \Big[& -\alpha(1-\Delta)\,|\psi_{\boldsymbol{r},1}|^2 - \alpha(1+\Delta)\,|\psi_{\boldsymbol{r},2}|^2 \\ & + g(1-\gamma)\,|\psi_{\boldsymbol{r},1}|^4 + g(1+\gamma)\,|\psi_{\boldsymbol{r},2}|^4 \\ & + 2g\lambda\,|\psi_{\boldsymbol{r},1}|^2\,|\psi_{\boldsymbol{r},2}|^2 \Big] \end{aligned} \tag{8}$$

The SOC term on the lattice may also be described in terms of trigonometric functions. By replacing the differential operators of Eq. (4) by the forward difference representation of Eq. (5), and then replacing the complex fields with the amplitude and phase representation, we may write this particular term of the Hamiltonian as

$$\begin{aligned} H_{\rm SO} = -\kappa \sum_{\mathbf{r}} \Big[& |\psi_{\boldsymbol{r},1}|\,|\psi_{\boldsymbol{r}+\hat{\boldsymbol{x}},2}| \cos(\theta_{\boldsymbol{r}+\hat{\boldsymbol{x}},2} - \theta_{\boldsymbol{r},1}) \\ & - |\psi_{\boldsymbol{r},2}|\,|\psi_{\boldsymbol{r}+\hat{\boldsymbol{x}},1}| \cos(\theta_{\boldsymbol{r}+\hat{\boldsymbol{x}},1} - \theta_{\boldsymbol{r},2}) \\ & + |\psi_{\boldsymbol{r},1}|\,|\psi_{\boldsymbol{r}+\hat{\boldsymbol{y}},2}| \sin(\theta_{\boldsymbol{r}+\hat{\boldsymbol{y}},2} - \theta_{\boldsymbol{r},1}) \\ & + |\psi_{\boldsymbol{r},2}|\,|\psi_{\boldsymbol{r}+\hat{\boldsymbol{y}},1}| \sin(\theta_{\boldsymbol{r}+\hat{\boldsymbol{y}},1} - \theta_{\boldsymbol{r},2}) \Big]. \end{aligned} \tag{9}$$

C. London model

Thermal fluctuations of the phases of the complex order parameter component are the most relevant fluctuations. Hence, it is useful first to neglect the amplitude fluctuations and consider a London-model of the problem. To this end, we write the complex fields as $\psi_i = \rho_i \exp i\theta_i$, where only the phase θ_i is allowed to fluctuate. Note that this also implies that we assume the amplitudes to be uniform. To arrive at a London formulation we write the Ginzburg-Landau Hamiltonian of Eq. (1) on component form, and replace the complex fields with a constant amplitude and a fluctuating phase, as described above. This gives

$$\begin{aligned} H = \int d^2 r \Big[& \sum_i \frac{\rho_i^2}{2} (\nabla\theta_i)^2 \\ & - \kappa\rho_1\rho_2 \Big[\sin(\theta_1 - \theta_2)\partial_x(\theta_1 + \theta_2) \\ & + \cos(\theta_1 - \theta_2)\partial_y(\theta_1 + \theta_2) \Big] \Big], \end{aligned} \tag{10}$$

such that two composite variables with very different behaviors emerge. On the one hand, $\theta_- \equiv \theta_1 - \theta_2$ has a preferential value: in the presence of the gradients of the phase sum the second term in the above equations has phase-locking effects. On the other hand, $\theta_+ \equiv \theta_1 + \theta_2$ has first order gradient terms, which may make it energetically favorable to modulate this phase. As the SOC-term couples the two variables, there may be subtle interplay between them influencing the phase transitions of the model.

The scaling dimension of the SOC-term will be one less than a Josephson coupling, which is a singular perturbation that is relevant at any strength of the coupling.

Below, we will perform a mean-field analysis, where we assume that the phases and amplitudes of the boson condensate are modulated by some wave vector, which is included as a variational parameter when the free energy is minimized. This result may be compared to the previous work done on SOC bosons. We also compare the mean-field analysis to Monte-Carlo simulations of the interacting lattice model.

D. Observables

The phase transition observed at $\kappa = 0$ is classified by examining the helicity modulus, defined by

$$\langle \Upsilon_{i,\mu} \rangle \equiv \frac{1}{V} \frac{\partial^2 F(\Delta_{i,\mu})}{\partial \Delta_{i,\mu}^2}, \tag{11}$$

along with the fourth order modulus

$$\langle \Upsilon_{4,i,\mu} \rangle \equiv \frac{1}{V^2} \frac{\partial^4 F(\Delta_{i,\mu})}{\partial \Delta_{i,\mu}^4}. \tag{12}$$

where $\Delta_{i,\mu}$ is an infinitesimal twist applied to the phase $\theta_{r,i}$ in the μ-direction. The transition manifests itself as a discontinuity in the helicity modulus in the thermodynamic limit. This translates to a dip in the fourth order modulus that does not vanish in the thermodynamic limit. See Appendix A for more details. As the x- and y-directions are equivalent, we will consider the average of $\Upsilon_{i,x}$ and $\Upsilon_{i,y}$ denoted by $\Upsilon_{i,\perp}$, as well as the average of $\Upsilon_{4,i,x}$ and $\Upsilon_{4,i,y}$ denoted by $\Upsilon_{4,i,\perp}$.

To examine the thermal melting of the spin-orbit induced ground-state modulation, we calculate the specific heat, C_v. It is given as fluctuations of the Hamiltonian

$$C_V = \beta^2 \left(\langle H^2 \rangle - \langle H \rangle^2 \right) \tag{13}$$

To compare the Monte-Carlo results to mean-field calculations, we measure the average amplitude u_i, defined as

$$u_i = \left\langle \sum_{\boldsymbol{r}} |\psi_{i,r}|^2 \right\rangle. \tag{14}$$

Note that we use the same notation for both the mean field value and the thermal average of $|\psi_i|^2$. It should be clear from the context which one is discussed. We also measure the thermal average of the density as a function of position, $\langle |\psi_i(\boldsymbol{r})|^2 \rangle$ to examine possible modulations in the density substrate. To monitor the thermal fluctuations in the condensate densities, we compute their probability distribution, $\mathcal{P}(|\psi_i|^2)$ by making a histogram of the field configurations at each measuring step of the Monte-Carlo simulations.

In order to monitor the formation of the modulated ground state, we compute the phase correlation function, defined by

$$G_X(\boldsymbol{r}, \boldsymbol{r}') = \langle e^{i\theta_{\boldsymbol{r},X}} e^{-i\theta_{\boldsymbol{r}',X}} \rangle \tag{15}$$

Here, X may represent either component 1, 2, as well as the sum or difference of the two, $\theta_1 + \theta_2$ and $\theta_1 - \theta_2$. We also calculate its fourier transform, the phase structure function, defined by

$$G_X(\boldsymbol{q}) = \frac{1}{V} \sum_{\boldsymbol{r},\boldsymbol{r}'} e^{i\boldsymbol{q}\cdot(\boldsymbol{r}-\boldsymbol{r}')} G_X(\boldsymbol{r}, \boldsymbol{r}'). \tag{16}$$

At large distances, r, the correlation function is expected to scale as $G_X(r) \sim r^{-\eta}$. We measure this exponent by extracting the value of $G_X(\boldsymbol{q})$ at a particular value, $\boldsymbol{Q}$, which in turn defines the exponent $\eta_{\boldsymbol{Q}}$ as

$$G_X(\boldsymbol{Q}) \sim L^{2-\eta}. \tag{17}$$

III. MEAN-FIELD THEORY

Inter-component density interactions suppress the minority condensate at sufficiently strong values of the coupling value. To get crude estimates for the interaction parameters needed for this to occur, we start out by considering the model in the mean-field approximation. The full fluctuation spectrum of the bosonic ordering fields will be considered in subsequent sections. Here, we give the mean-field theory in a continuum model.

In order to account for the fact that the ground state generically is modulated in the presence of SOC, we assume that the complex fields ψ_i are given in terms of a mean field value plus fluctuations, multiplied by a spatial plane wave modulation with momentum $\boldsymbol{q}$. In general, we may use the ansatz[28,29]

$$\psi_{1,\boldsymbol{q}} = \sqrt{u_1 + \delta u_1} \exp i(\phi_1 + \delta\phi_1 - \arg \boldsymbol{q} + \boldsymbol{q}\cdot\boldsymbol{r}) \tag{18}$$

$$\psi_{2,\boldsymbol{q}} = \sqrt{u_2 + \delta u_2} \exp i(\phi_2 + \delta\phi_2 + \boldsymbol{q}\cdot\boldsymbol{r}), \tag{19}$$

where $\arg \boldsymbol{q}$ is the orientation of $\boldsymbol{q}$ with respect to some reference axis. Specifically, we follow previous work and assume that the ground state is either modulated by a single wave vector (denoted Ψ_0), or by two oppositely aligned wave vectors (denoted Ψ_π). That is

$$\Psi_0 = \begin{pmatrix} \psi_{1,\boldsymbol{q}} \\ \psi_{2,\boldsymbol{q}} \end{pmatrix}, \tag{20}$$

and

$$\begin{aligned} \Psi_\pi &= \frac{1}{2} \begin{pmatrix} \psi_{1,\boldsymbol{q}} + \psi_{1,-\boldsymbol{q}} \\ \psi_{2,\boldsymbol{q}} + \psi_{2,-\boldsymbol{q}} \end{pmatrix} \\ &= \begin{pmatrix} -\sqrt{u_1 + \delta u_1} e^{i\phi_1 + i\delta\phi_1 - i\bar{\theta}} \sin \boldsymbol{q}\cdot\boldsymbol{r} \\ \sqrt{u_2 + \delta u_2} e^{i\phi_2 + i\delta\phi_2} \cos \boldsymbol{q}\cdot\boldsymbol{r} \end{pmatrix}, \end{aligned} \tag{21}$$

where $\bar{\theta}$ is the average angle of $\boldsymbol{q}$ and $-\boldsymbol{q}$ with respect to the x-axis. Here, the amplitudes, phases, and the wave-vectors are to be regarded as variational parameters in the mean-field free energy of the modulated state.

Inserting these expression into Eq. (1) and using the mean-field values only, we obtain the two free energy densities f_0 and f_π.

$$f_0 = \frac{|\boldsymbol{q}|^2}{2}(u_1 + u_2) - 2|\boldsymbol{q}|\,\kappa\sqrt{u_1 u_2}\sin(\phi_1 - \phi_2) + V_0. \tag{22}$$

$$f_\pi = \frac{|\boldsymbol{q}|^2}{4}(u_1 + u_2) - |\boldsymbol{q}|\,\kappa\sqrt{u_1 u_2}\cos(\phi_1 - \phi_2) + V_\pi. \tag{23}$$

Here, the potentials V_0 and V_π differ slightly due to numerical factors obtained when integrating over space. They have the forms

$$\begin{aligned} V_0 = &-\alpha\Big[(1-\Delta)u_1 + (1+\Delta)u_2\Big] \\ &+ g\Big[(1-\gamma)u_1^2 + (1+\gamma)u_2^2 + 2\lambda u_1 u_2\Big] \end{aligned} \tag{24}$$

and

$$\begin{aligned} V_\pi = &-\frac{\alpha}{2}\Big((1-\Delta) + u_1(1+\Delta)u_2\Big) \\ &+ \frac{g}{8}\Big[3(1-\gamma)u_1^2 + 3(1+\gamma)u_2^2 + 2\lambda u_1 u_2\Big] \end{aligned} \tag{25}$$

Note from Eqs. (22) and (23), that in a modulated ground state the SOC essentially acts as a phase locking on $\phi_1 - \phi_2$ in a system with a uniform ground state. We may minimize Eqs. (22) and (23) with respect to this phase difference, assuming that $|q| \neq 0$ and $u_i \neq 0\ \forall\ i$, which yields a phase locking of $\phi_1 - \phi_2 = \pi/2$ for f_0 and $\phi_1 - \phi_2 = 0$ for f_π. The angle $\arg \boldsymbol{q}$ in the single q-vector case and the average angle $\bar{\theta}$ drops out of the equations, which reflects the degeneracy of the single particle spectrum.

Considering the modulation vector present in Eqs. (22) and (23) as a variational parameter and assuming $u_i \neq 0\ \forall\ i$, we find

$$|\boldsymbol{q}| = \frac{2\kappa\sqrt{u_1 u_2}}{u_1 + u_2} \tag{26}$$

in both cases. With this solution inserted into the free energy densities, they become

$$f_0 = -\frac{2\kappa^2 u_1 u_2}{u_1 + u_2} + V_0, \tag{27}$$

and

$$f_\pi = -\frac{\kappa^2 u_1 u_2}{u_1 + u_2} + V_\pi. \tag{28}$$

Eqs. (27) and (28) may in principle be solved for u_1 and u_2, but as they are cubic the expressions for the solutions are unwieldy and not particularly illuminating. Instead, we numerically minimize both free energy densities, and then determine the ground state for a given parameter range by finding $\min(f_0, f_\pi)$. This gives the regions of the phase diagram where the ground state is modulated by either one or two wave vectors. For the SOC to be effective, it is also required that $u_1 u_2 \neq 0$. For $u_1 u_2 = 0$, the model reverts to a single component condensate, i.e. a "spinless" model where SOC cannot be operative.

In Fig. 1, we plot a few representative values of f_0 and f_π as a function of λ, for two values of κ. For the lowest value of κ, it is seen that $f_0 < f_\pi$ for all values of λ. Hence, a ground state modulated by two q-vectors is not found. For a larger value of κ, $f_0 < f_\pi$ for low and high values of λ, while for intermediate values of λ, $f_\pi < f_0$. Thus, for large enough κ and intermediate values of λ, there is the possibility of finding ground states modulated by two q-vectors.

Moreover, it is seen that for both values of κ, f_0 is independent of λ when λ reaches some value $\lambda = \lambda^*$. This happens at the value for which the minority condensate (u_1 in this case) is completely suppressed. Furthermore, the second crossing of f_0 and f_π always occurs at values of $\lambda > \lambda^*$. Therefore, for given κ and with increasing λ, the ground state modulated by two q-vectors always transitions into a uniform ground state with one condensate completely suppressed.

Note also that f_0 increases more rapidly with λ than f_π. This is due to difference in the potentials V_0 and V_π, Eqs. (24) and (25). Therefore, having two crossings of f_0 and f_π as a function of λ means that one of the crossing points must always be to the right of the point where f_0 becomes λ-independent. Thus, f_0 being minimal always transitions into f_π being minimal II as λ increases. There will never be a transition from f_π being minimal back to f_0 being minimal with increasing λ.

This may be summarized as follows. In Fig. 2, we show the results of numerically solving Eqs. (27) and (28) in the $\lambda - \kappa$ plane. Region I represents the area where the single-q modulated ground state is preferred, region III where the two-q modulated ground state is preferred, and region II is the area where $u_1 u_2 = 0$ minimizes the free energy, making this state a uniform, single-component state. The two lines separating I and II, and II and III are located by the crossings of the free energies f_0 and f_π, and they therefore represent first-order phase transitions at the mean-field level. The line separating region I and II is a direct transition between a ground state modulated by one q-vector and a uniform ground state, without an intermediate ground state modulated by two q-vectors. The location of this line is therefore determined by the value of λ where f_0 ceases to the dependent on λ, while f_π represents a higher-energy state which is irrelevant. The order of this phase-transition is determined by whether $\partial f_0/\partial\lambda$ is continuous or discontinuous at λ_c. We have $\partial f_0/\partial\lambda \approx (\partial f_0/\partial u_1)(\partial u_1/\partial\lambda)$. Using Eq. 27, we see that this is determined by $\partial u_1/\partial\lambda$. Since u_1 vanishes in a finite interval in λ, $\partial u_1/\partial\lambda$ has to be discontinuous at λ^*, and hence so does f_0. The transition line separating I and II is therefore also first order.

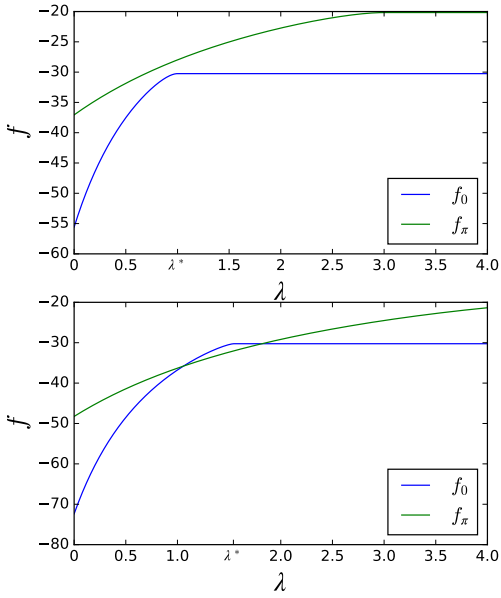

FIG. 1. Results for minimum values of f_0 and f_π as a function of λ for two values of κ. Top panel: $\kappa = 1$. Bottom panel: $\kappa = 2$. Note how f_0 ceases to be dependent on λ for large λ, at some value λ^*. Note also the discontinuity in the derivative of f_0 at $\lambda = \lambda^*$.

IV. DETAILS OF THE MONTE-CARLO SIMULATIONS

The model is simulated using the Monte-Carlo algorithm with a simple restricted update scheme of each physical variable, using Metropolis-Hastings[30,31] tests for acceptance. The model is discretized on a rectangular lattice of size $L_x \times L_y$, with periodic boundary conditions. Typically, $5 \cdot 10^6$ Monte-Carlo sweeps is used at each temperature step, with an additional $5 \cdot 10^5$ sweeps discarded for equilibration. One sweep consist of attempting to update each physical variable on each lattice site once in succession. The proposed new value for each variable is picked within a restricted region around the

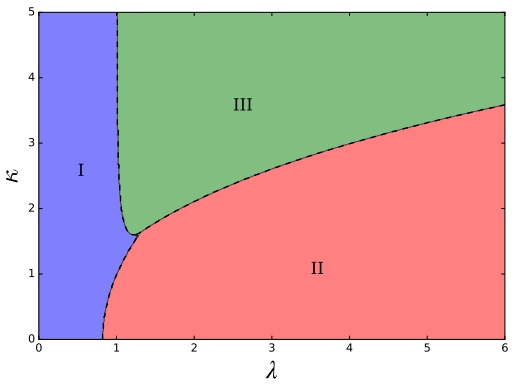

FIG. 2. Mean field phase diagram in the λ-κ plane, with other parameters $\alpha = 10.0$, $g = 1.0$, $\Delta = 0.1$, $\gamma = 0.0$, $m = 1.0$. Region I and III are the regions where both components exist and the effect of SOC is present, resulting in a ground state at finite momentum. In region I the ground state is modulated by a single wave-vector. In region III, the ground state is modulated by two oppositely directed wave vectors. Region II is the region where the inter-component interactions suppress the minority condensate, which results in a single-component condensate at zero momentum.

old value, where the size of the region is chosen to allow for both high acceptance rates, and low autocorrelation times. To further minimize auto-correlation times and increase simulation efficiency, we measure observables with a period of 100 Monte-Carlo sweeps. Pseudo-random numbers are generated with the Mersenne-Twister algorithm[32]. During equilibration, time series of the internal energy is examined for convergence, this ensures proper equilibration. To avoid metastable states, several simulations with identical parameters, but differing initial seeds of the pseudo-random number generator are performed to make sure they anneal to the same state. Measurements are post-processed using multiple-histogram re-weighting[33], and error estimates are determined with the Jackknife method[34].

The allowed range of amplitude fluctuations is determined during the equilibration procedure, by first allowing it to fluctuate to a very large value ($|\psi_i|^2 \sim 10$ was typically used) and then reducing the value to include all values that had a non-zero probabilty of being picked according to the measured probability distribution, $\mathcal{P}(|\psi_i|^2)$.

Unless otherwise stated, we fix $\alpha_0 = 10.0$, $g = 1.0$, and $\gamma = 0.0$. The large value of $\alpha_0 = 10.0$ is chosen to have sharp probability distributions of the amplitudes. Generally, a square lattice of $L_x = L_y \equiv L = 64$ is used in simulations, but system sizes of $L \in (16, 24, 32, 40, 48, 56, 64, 96, 128, 160, 192, 224, 256)$ are used for performing a finite size scaling (FSS) analysis.

V. RESULTS OF THE MONTE-CARLO SIMULATIONS

In this section, we present Monte-Carlo simulations to corroborate and expand on the arguments given in the previous sections. The model exhibits three different classes of BECs for different parameter regimes. For strong inter-component interactions and zero to intermediate SOC, there will be only one superfluid condensate present. With no SOC, but for intermediate inter-component interactions, the model is a two-component coupled superfluid. Finally, for intermediate interactions and SOC, the model is a two-component superfluid with a finite q-vector. This schematic picture shown in Fig. 2 is captured by a simple mean field argument, but we find it to be essentially correct also when thermal fluctuations are taken into account in Monte-Carlo simulations. We also examine the thermal phase transitions present in the cases of zero SOC and when the condensate is modulated by a single q-vector.

A. Kosterlitz-Thouless transition in the absence of spin-orbit coupling

When $\kappa = 0$, the model represents a two-component BEC coupled by density-density interactions, which may collapse to a single-component condensate for strong inter-component interactions. When neglecting amplitude fluctuations (which of course decouples the condensates), the model reduces to the XY-model. Here, the low-temperature phase is characterized by quasi long-range order of the superfluid order parameter, where vortices and anti-vortices form bound pairs. As the temperature is increased, the bound vortex-antivortex pairs unbind at a Kosterlitz-Thouless (KT) transition[35,36]. As a check of simulations we indeed obtain that the two-component model with amplitude fluctuations included belongs in the KT universality class by establishing that the helicity modulus undergoes a discontinuous jump to zero as the system is heated from the low-temperature state, with the value of the jump close to the predicted universal value. We examine various values for the inter-component coupling λ, and find that the above remains true for all the values of λ we have considered.

Fig. 3 shows the helicity modulus and fourth order modulus of component 2 for system sizes $L \in (16, 24, 32, 40, 48, 56, 64)$ with inter-component coupling strength $\lambda = 2.0$. The inset shows the depth of the dip in the fourth order modulus as a function of inverse linear system size. By fitting the helicity modulus to Eq. (A8) we determine the discontinuous jump to be $\Upsilon(\infty)\beta_c = 0.650(1)$ at $\beta_c = 0.282$. Extrapolation of the value of the negative dip to $1/L = 0$ gives a finite value of $0.49(1)$. This is clear evidence for a discontinuous jump in the helicity modulus, placing the transition in the Kosterlitz-Thouless universality class.

Similar results are obtained for values of $\lambda \in (0.0, 0.25, 0.5, 0.75, 1.25, 1.5, 1.75, 2.0)$ as shown in Table I. For the values of λ where both condensates persist, transitions of KT type is observed in both components, at different critical couplings. In all cases considered, the value of the minimum in Υ_4 converges to a nonzero value. This demon-

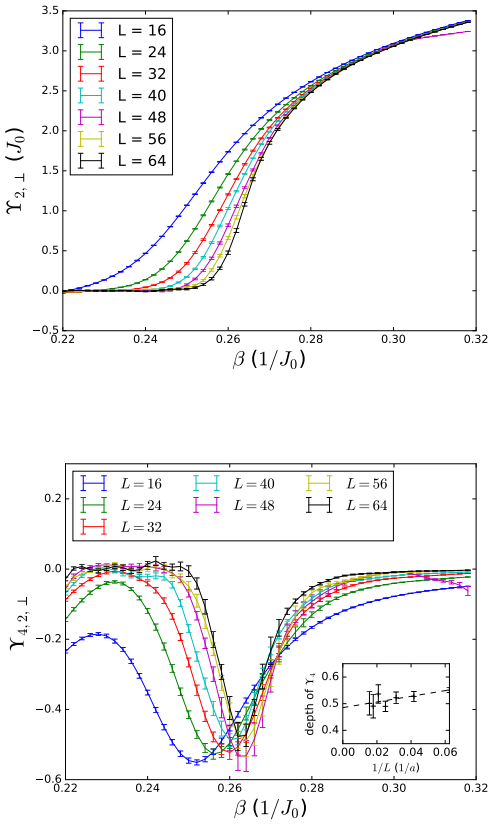

FIG. 3. Helicity modulus (top panel) and fourth order modulus (bottom panel) of component 2 as a function of β for several system sizes, with $\lambda = 2.0$ and $\kappa = 0.0$. The inset of the bottom figure shows the value of the dip in the fourth order modulus as a function of inverse system size. The dashed line is a linear extrapolation to the thermodynamic limit. At this value of the inter-component coupling strength, the condensate density of component 1 is extinguished, and hence exhibits no KT-transition.

strates that there is a discontinuous jump in the helicity modulus, regardless of the value of the inter-component interaction strength, and whether or not the minority condensate is depleted. Additionally, the value of the discontinuous jump varies weakly with λ, and is close to the universal value of $2/\pi$. This indicates that fluctuations in the condensate amplitude only have a minor effect on the details of the transition. None of the obtained jumps are within the prediction $2/\pi$, with error estimates, but most are close. Moreover, the fitting routine was sensitive to the system sizes that were included. Both effects may have been caused by the inclusion of amplitude fluctuations. Also note that the critical temperature and depth of the dip varies very weakly with λ, as long as $\lambda \geq 1.0$. This is very reasonable, as the model is effectively a single component condensate in this regime, so varying the intercomponent interaction strength should have little to no effect.

Finally, we remark that the fit of the discontinuous jump and the determination of the depth of the dip in the fourth order modulus are two independent methods for detecting a KT-transition. As both methods give good results consistent with the KT-prediction, we are confident in claiming that the two-component imbalanced BEC without SOC has one or two transitions, depending on the value of the intercomponent coupling strength, in the KT universality class.

B. Spin-orbit induced modulated ground states

Preliminary arguments based on the non-interacting energy spectrum and mean field calculations suggest that the ground state of the spin-orbit coupled BEC resides at either one or two finite q-vectors. In order to confirm this, Monte-Carlo simulations of the full lattice model, Eqs. (6) to (9), were performed in parameter regions corresponding to region I and III in the phase diagram of Fig. 2.

1. *Single q-vector*

To observe the predicted modulated state where a single q-vector is present, we perform simulations of the lattice model at $\kappa = 1.0$ and $\lambda = 0.0$. Fig. 4 shows the real parts of the phase correlation function, Eq. (15), and the structure factors of the phase sum and phase difference variable in the low temperature phase, when the inverse temperature is $\beta = 1.5$. The phase correlation function Eq. (15) for the phase sum composite variable is modulated with a single q-vector along the diagonal. The phase difference composite variable shows no modulation. It is, however, highly correlated, which is a result of the effective Josephson locking. This is in accord with expectations based on the London-approximation, where amplitudes are frozen, see Eq. (10). The London case, with non-modulated amplitudes, suffices to describe the situation with relatively small values of intercomponent density-density interactions, where amplitudes are constant throughout the system. The SOC-term tends to lock $\theta_1 - \theta_2$ at constant value, since the strength of the SOC-term effectively is constant due to the constant values of the amplitudes, while SOC induces a gradient in $\theta_1 + \theta_2$. The $\theta_1 + \theta_2$-modulations therefore originate with SOC-coupling.

In these simulations, the amplitudes are also allowed to fluctuate. The real-space amplitude plots shown in Fig. 5, show that the spatial amplitude fluctuations are small. In this regime the potential does not favor large density differences between the two components, and there is no phase separation. The state we observe is the same as was found in Refs. 24 and 25, where a single minimum in the non-interacting spectrum is populated for $\lambda < 1$.

TABLE I. Summary of the results obtained when searching for the KT-transition. Each row shows, for both components, the critical inverse temperature at which the best fit to Eq. (A8), β_c, the size of the jump at this inverse temperature, $\Upsilon_\infty\beta_c$, as well as the extrapolation of the value of the minimum in the fourth order modulus to $1/L = 0$. When $\lambda \geq 1.0$, the density of component 1 has been completely depleted, and there is no phase transition in this sector, as signified by the entries marked N/A.

	Component 1			Component 2		
λ	β_c	$\Upsilon_\infty\beta_c$	value of minimum in Υ_4	β_c	$\Upsilon_\infty\beta_c$	value of minimum in Υ_4
0.00	0.280	0.617(1)	0.56(3)	0.226	0.642(2)	0.58(7)
0.25	0.391	0.609(1)	0.367(8)	0.249	0.5(3)	0.67(3)
0.50	0.605	0.595(1)	0.239(9)	0.284	0.625(1)	0.49(3)
0.75	2.24	0.58(1)	0.068(4)	0.290	0.627(1)	0.50(2)
1.00	N/A	N/A	N/A	0.292	0.662(1)	0.48(2)
1.25	N/A	N/A	N/A	0.290	0.667(1)	0.46(3)
1.50	N/A	N/A	N/A	0.290	0.703(1)	0.50(1)
1.75	N/A	N/A	N/A	0.284	0.653(1)	0.61(5)
2.00	N/A	N/A	N/A	0.282	0.650(1)	0.49(1)

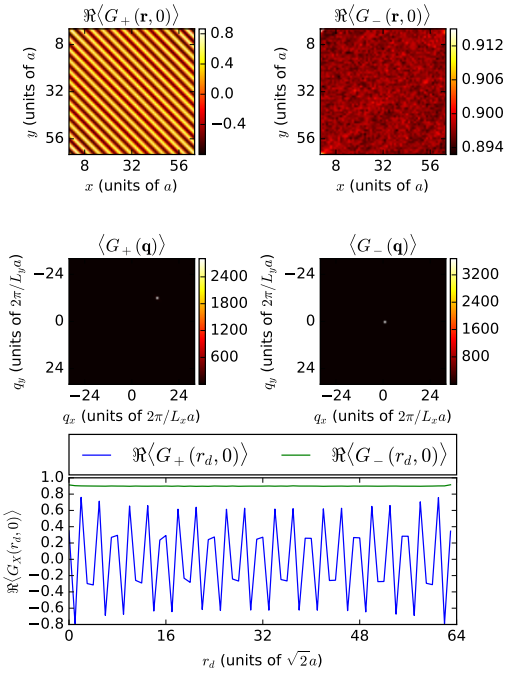

FIG. 4. The real part of the phase correlation function Eq. (15) in real (top row) and reciprocal (middle row) space of the phase sum (left column) and phase difference (right column), at parameters $\kappa = 1.0$, $\lambda = 0.0$ and $\beta = 1.0$. The bottom panel shows a real-space cut along the diagonal perpendicular to the stripes, r_d, of both the phase sum and phase difference correlation functions. The effect of the SOC is manifest in the phase sum, which is modulated by a wave-vector, $\boldsymbol{Q}$. The phase difference, exhibits no modulations in the spatial correlation. We have removed the reference point $\boldsymbol{r} = 0$ from the real space plots to improve visibility of the correlations.

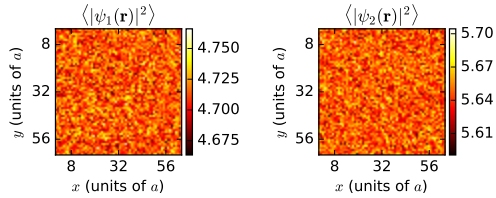

FIG. 5. Thermal amplitude averages in real space for component 1 (left panel) and 2 (right panel), at parameters $\kappa = 1.0$, $\lambda = 0.0$ and $\beta = 1.0$. As seen on the scale of the color map, there is very little spatial fluctuations around the average, u_i, in each individual component.

2. *Double q-vector*

The ground state modulated by two oppositely directed q-vectors only occurs, in mean field, at sufficiently high values of both κ and λ. In order to observe this state, we perform simulations at $\kappa = 1.7$ and $\lambda = 1.2$, with $\beta = 1.0$, inside region III of Fig. 2. In Fig. 6 we show Monte-Carlo calculations of the correlation function of the phase sum and difference, in both real and reciprocal space. As in the single-q vector case, the phase-sum correlation is modulated, although now with a larger $|\boldsymbol{q}|$. The increase of the length of the q-vector directly reflects the larger value of the SOC strength.

Another important difference between the double-q vector state compared to the single-q vector state is shown in Fig. 7, which shows the thermal averages of the amplitudes. In this case, the amplitudes are also modulated. Furthermore, the amplitudes of the two components are staggered, when component 1 has a large amplitude, component 2 has a low amplitude, and vice versa. This is further exemplified in the bottom panel of Fig. 7, where we show a cut along the diagonal perpendicular to the stripes in the amplitude densities. Here it is clearly seen that the two amplitude variations are mirror images of each other, only shifted relative to each other by the difference in the average amplitudes due to the component imbalance.

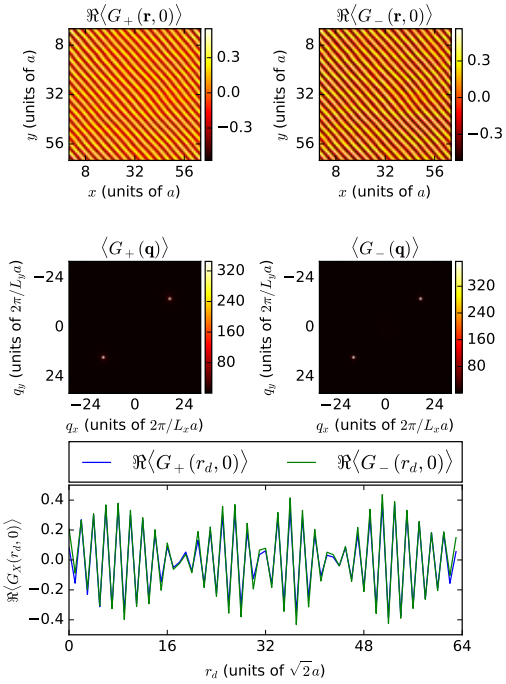

FIG. 6. Real part of phase correlation function Eq. (15) in real (top row) and reciprocal (middle row) space of the phase sum (left column) and phase difference (right column), at parameters $\beta = 1.0$, $\lambda = 1.2$ and $\kappa = 1.7$. In the bottom panel, we also show a real-space cut along the diagonal perpendicular to the stripes, r_d, of both correlation functions. It is shown that both the phase sum and the phase difference are modulated by two oppositely aligned wave-vectors, $\pm\boldsymbol{Q}$, with equal magnitude. We have removed the reference point $\boldsymbol{r} = 0$ from the real space plots to improve visibility of the correlations.

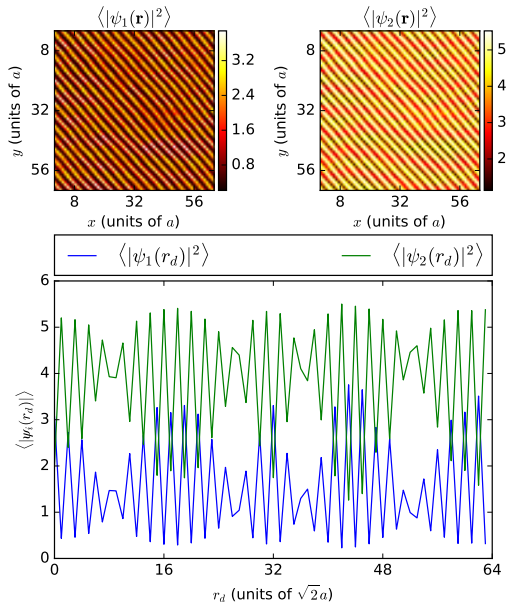

FIG. 7. Thermal amplitude averages in real space for component 1 (top row, left panel) and 2 (top, row, right panel), at parameters $\beta = 1.0$, $\lambda = 1.2$ and $\kappa = 1.7$. The bottom panel shows a cut of the amplitude averages along the diagonal perpendicular to the stripe modulations, r_d. Both amplitudes are modulated in this region of parameter space, but around different mean values because of the density imbalance. Furthermore, the amplitude of component 1 is staggered compared to component 2. This minimizes the potential energy from the inter-component density-density interaction, while still minimizing the SOC interaction energy.

Unlike the single-q vector case, the phase-difference correlation is also modulated. This may now be understood as follows. The system is in a parameter-regime where λ is large enough to induce staggering of the amplitudes of the condensates, in order to minimize energy. The London-approximation, Eq. (10), therefore no longer suffices to describe the system, and we revert to Eq. (9). It is the term with the minus-sign in H_{SO} that leads to the frustration of $\theta_1 - \theta_1$. Were this sign to be reversed, we would have had $\theta_1 - \theta_2 = 0$. Since the amplitudes are modulated, so are the gradients of the amplitudes, and so is therefore the strength of the frustration in the phase-difference. This difference is therefore itself modulated. The modulation of $\theta_1 - \theta_1$ therefore originates with the modulation of amplitudes, which is a consequence of strong inter-component density-density interactions. Recall from above that the modulation of $\theta_1 + \theta_1$ originates with SOC.

C. Interaction-induced destruction of modulated ground states

The mean field calculations presented in Section III predict a breakdown of the modulated ground state shown in Fig. 4 when the inter-component interaction parameter, λ, reaches the threshold shown in Fig. 2, provided $\kappa \lesssim 1.5$. Above this threshold, the condensate transitions from a single-q condensate into a condensate modulated by two opposite wave vectors. For $\gamma = 0$, and $\Delta > 0$, which we consider here, component 1 is the minority component that collapses. The mechanism for the collapse is that inter-component interactions drive the minority component to zero to eliminate the interaction energy. When the model collapses to an effective one component model there will no effects of the SOC, as the q-vectors of the modulation induced by it are proportional to $u_1 u_2$, at the mean field level.

To show this suppression, we compute the thermal amplitude averages of both components in the low temperature phase, shown in Fig. 8, when $\beta = 1.0$, $\kappa = 1.0$ and $\lambda = 2.0$.

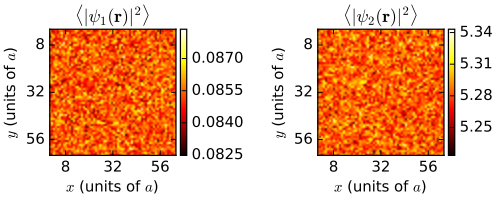

FIG. 8. Thermal amplitude averages in real space for component 1 (top row, left panel) and 2 (top, row, right panel), at parameters $\kappa = 1.0$, $\lambda = 2.0$ and $\beta = 1.0$.

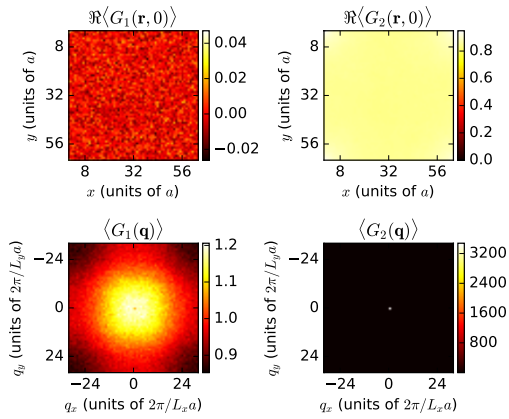

FIG. 9. Real part of the phase correlation function Eq. (15) in real space (top row) and reciprocal space(bottom row) for the phase of component 1(left column) and component 2(right column), at parameters $\kappa = 1.0$, $\lambda = 2.0$ and $\beta = 1.0$. We have removed the reference point $\boldsymbol{r} = 0$ from the real space plots to improve visibility of the correlations.

That is, every parameter is identical to what is shown in Figs. 4 and 5, except the inter-component interaction is increased above the critical value given by the mean field calculations. It is evident that both amplitudes are now again unmodulated, but the amplitude of component 1 has been almost completely depleted. Its small finite value is only a remnant of the thermal fluctuations included in the simulations.

To further explore the effect of the depletion, we compute the phase correlation function Eq. (15) and its Fourier transform, Eq. (15) and Eq. (16). Fig. 9 shows the real parts of both the phase correlation function Eq. (15), and structure factor of both individual componentsThere are no modulations in the either of the phase correlation function Eq. (15), and both structure factors are isotropic. However, while the phase of component 1 is completely uncorrelated, the phase of component 2 is strongly correlated. The reasons for this is that: *i)* the condensate amplitude of component 1 has been completely depleted, leaving the phase of this component completely uncorrelated at all temperatures, and *ii)* the non-suppressed condensate has entered a low-temperature superfluid state, akin to what we observe for $\kappa = 0$, even though we still have a finite SOC, however ineffective.

Fig. 10 summarizes the results obtained in the Monte-Carlo simulations, showing an overview of the different ground states obtained at slow annealing from a random initial state at high temperature down to $\beta = 6.0$, for different values of (κ, λ). The size of region I was largely unaffected. For intermediate values of κ and sufficiently large values of λ, we observe that the spin-orbit induced modulations of both the amplitudes and the phases are pinned to the crystal axes of the numerical lattice. This is represented by the large error bars of the red points denoting the transition from region II to region III obtained from the Monte-Carlo simulations. We determine these particular error bars by finding the upper and lower limits in κ where we can confidently observe a pure double q-vector condensate, or a pure single component condensate. That aside, the mean-field and MC calculations correspond remarkably well, even close to the area where the three transition lines meet.

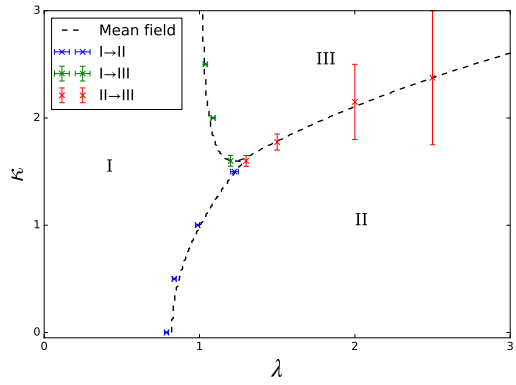

FIG. 10. Phase diagram obtained from numerical Monte-Carlo simulations compared to mean field predictions. The points with error bars correspond to observed transition points, blue points correspond to the transition from region I to region II, green points the transition from region I to region III, and red points the transition from region II to region III. The dashed lines are the corresponding transition lines obtained from mean field calculations, shown in Fig. 2

D. Thermal disordering of single-q modulated state

Thermal fluctuations of the superfluid phases are also expected to disorder the modulated ground state pattern induced by the SOC. The modulation which appears in region I at low temperatures is characterized by modulated superfluid order, or superfluid order with a texture. The temperature driven dis-

ordering of this modulated superfluid state is expected to lie in the KT-universality class. In order to examine the thermal phase transition from the low temperature phase of region I into the high temperature phase, we perform simulations of the full Hamiltonian as written in Eq. (6) and in the London limit. The London limit is employed here as it is the minimal model which captures the effect of the SOC. As discussed in section Section V B, in region I where the condensate is only modulated by a single $\boldsymbol{q}$-vector, we find that the amplitudes are essentially uniform. Hence, the amplitude fluctuations are largely irrelevant for this phase, and we may therefore employ the London limit. The London limit is taken by fixing $|\psi_{\boldsymbol{r},i}| = 1 \; \forall \; \boldsymbol{r}, i$, which simplifies the Hamiltonian greatly.

In order to determine the nature of the thermal phase transition which disorders the modulated superfluid we measure the helicity modulus of the phase sum variable, the exponent $\eta_{\boldsymbol{Q}}$, and the specific heat. The helicity modulus is modified compared to the case with no SOC, due to the extra terms in the Hamiltonian. The value of the exponent $\eta_{\boldsymbol{q}}$ is expected to approach the limit $1/4$ from below as the critical inverse temperature is approached from above[37] In Figs. 11 and 12 we show the results of the simulations with and without amplitude fluctuations included, respectively. The top panels show the specific heat on the left axis, and the value of the exponent $\eta_{\boldsymbol{Q}}$ on the right axis. We also show the scaling of the specific heat peak in the insets of the top panels, and we find its exponent to be $0.8(2)$ with amplitude fluctuations included, and $0.66(9)$ in the London limit. In the bottom panels we show the helicity modulus of the phase sum variable, both of which exhibit a sharp jump which coincides with the drop in the scaling exponent and the specific heat peak. In both cases, The sharp peak of the specific heat with its large scaling exponent, the abrupt drop of the exponent $\eta_{\boldsymbol{Q}}$, and the sharp jump and large error bars of the helicity modulus all point towards a strong de-pinning transition separating the modulated superfluid phase and the normal fluid phase. The similar behaviours between the two cases of Fig. 11 and Fig. 12 suggests that the London model is in fact a good effective model for this particular transition. We believe the main reason for the pinning is the periodic boundary conditions applied to the model. This biases the stripes to connect with themselves at the boundaries of the system, which in turn causes very slow equilibration at the critical point, as evident in the large error bars of especially the helicity modulus. In particular, fluctuations associated with shifting or rotating the stripe configurations is particularly hard to resolve in the Monte Carlo simulations, as these are large scale movements, which in turn are made even more difficult to resolve with periodic boundary conditions applied.

In an attempt to reduce the pinning effects present in Figs. 11 and 12 and confirm their origin, we slightly alter the model. Instead of taking the London limit with $|\psi_{\boldsymbol{r},i}| = 1 \; \forall \; \boldsymbol{r}, i$, we define a Thomas-Fermi trap which decouples the stripes from the boundaries of the system. Specifically, we fix

$$|\psi_{\boldsymbol{r},i}| = \begin{cases} 1 - \left(\frac{r}{R}\right)^4, & r < R. \\ 0, & r > R. \end{cases} \tag{29}$$

However, this comes at the cost of not having a well defined helicity modulus. This is the case for this particular model, as the decoupling of the stripes from the system boundary is the same as applying open boundary conditions. The helicity modulus relies on calculating the free energy difference between the system with periodic boundary conditions, and the system where an infinitesimal twist is applied to the phases at the boundary[38,39] The simulation results of the London model in a Thomas-Fermi potential are shown in Fig. 13. Here we show only the scaling of the first order peak in the phase sum structure function and the specific heat. Fig. 13 shows that the signs of pinning which we are able to examine, namely the sharp peak of the specific heat and the sharp drop of $\eta_{\boldsymbol{Q}}$ is

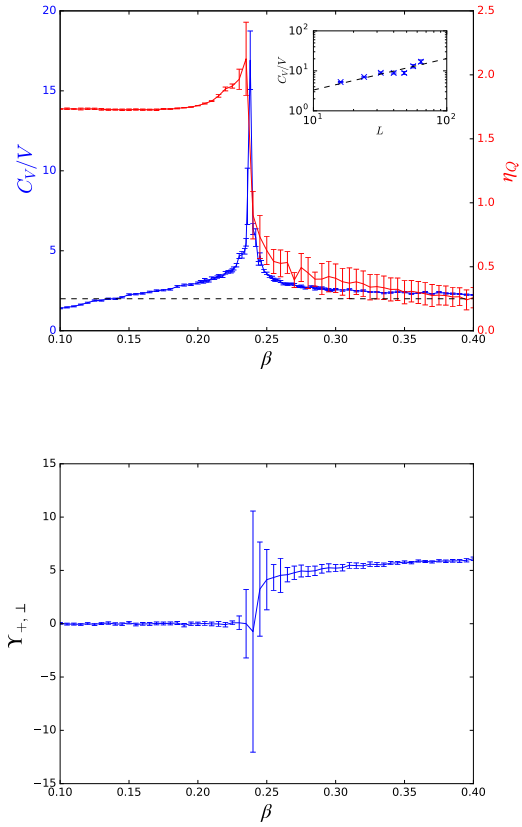

FIG. 11. Phase-sum structure function at the first Bragg peak, $\boldsymbol{Q}$, as a function of β for system sizes $L \in (16, 24, 32, 40, 48, 56, 64)$ as well as specific heat C_V/V for $L = 64$ (top), and helicity modulus of the phase-sum variable, $\Upsilon_{+,\perp}$ (bottom), at $\kappa = 1.0$ in the London limit. The inset of the top panel show the scaling of the peak of the specific heat curves for the same system sizes used in the structure function scaling. Note how the drop in the exponent $\eta_{\boldsymbol{Q}}$ as well as the jump in the helicity modulus both coincide with the sharp peak in the specific heat.

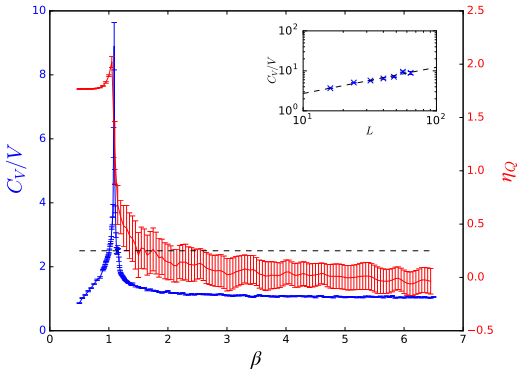

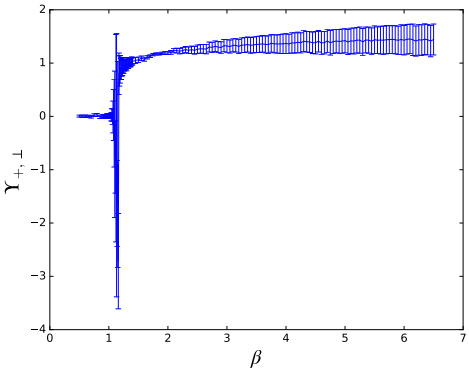

FIG. 12. Phase-sum structure function at the first Bragg peak, $\boldsymbol{Q}$, as a function of β for system sizes $L \in (16, 24, 32, 40, 48, 56, 64)$ as well as specific heat C_V/V for $L = 64$ (top), and helicity modulus of the phase-sum variable, $\Upsilon_{+,\perp}$ (bottom), at $\kappa = 1.0$ in the London limit. The inset of the top panel show the scaling of the peak of the specific heat curves for the same system sizes used in the structure function scaling. Note how the drop in the exponent $\eta_{\boldsymbol{Q}}$ as well as the jump in the helicity modulus both coincide with the sharp peak in the specific heat.

greatly reduced when the Thomas-Fermi potential is present. The specific heat curve still shows a peak which coincides with the onset of scaling in the structure function, but the height and sharpness of the peak is reduced. We also find the peak to still exhibit scaling, with an exponent $0.17(4)$, as shown in the inset of Fig. 13. Without the helicity modulus we are unable to confidently determine the nature of the phase transition, but it is evident that the signs of pinning is almost removed. In all likelihood, the remaining pinning signatures are associated with the aforementioned difficulty of moving or rotating entire stripe configurations, and will disappear in the continuum limit.

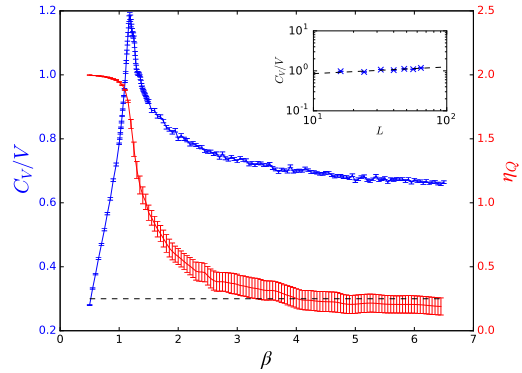

FIG. 13. Specific heat , C_V/V, (left axis) and the exponent $\eta_{\boldsymbol{Q}}$ (right axis). The inset shows a finite size scaling of the peak of the specific heat for system sizes $L \in (16, 24, 32, 40, 48, 56, 64)$ at $\kappa = 1.0$ in the London limit with a Thomas-Fermi potential applied. The full specific heat curve shown in the main panel is for the largest system sizes simulated, $L = 64$ Note how the peak of the specific heat curves coincides with the jump in the exponent $\eta_{\boldsymbol{Q}}$.

As a comparison, we show results for the specific heat and the exponent $\eta_{\boldsymbol{Q}}$ taken from a simulation of the $2DXY$-model in Fig. 14. Here the exponent is measured by performing a finite size scaling of the height of the $\boldsymbol{q} = 0$ peak in the phase structure function. The defining characteristic which shows that this is a KT-transition is the fact that the exponent $\eta_{\boldsymbol{Q}}$ reaches the limiting value of $1/4$ exactly at the KT-transition temperature, $\beta_{\mathrm{KT}} \approx 1.12$. We also show the scaling of the specific heat peak, which has an exponent of 0 within the errors of our simulation.

Comparing the three different models of Figs. 11 to 13, we may conclude that the thermal transition from region I of the phase diagram shown in Fig. 10 into the disordered phase is a transition from a modulated two-dimensional superfluid phase into a normal fluid state. The transition has strong de-pinning characteristics when we apply periodic boundary conditions. These characteristics weakens and we approach a transition consistent with a KT-transition when we remove the periodic boundary conditions, but we are not able to rigorously characterize the transition as such due to the lack of a well defined helicity modulus.

VI. CONCLUSIONS

We have studied a model of an imbalanced two-component Bose-Einstein condensate, with and without spin-orbit coupling in two spatial dimensions, including density-density interactions among the components. Specifically, we have examined the modulations in the phase-texture of the complex order parameter components induced by the spin-orbit coupling, its disordering and suppression by thermal fluctuations and interaction effects, as well as the modulations of the

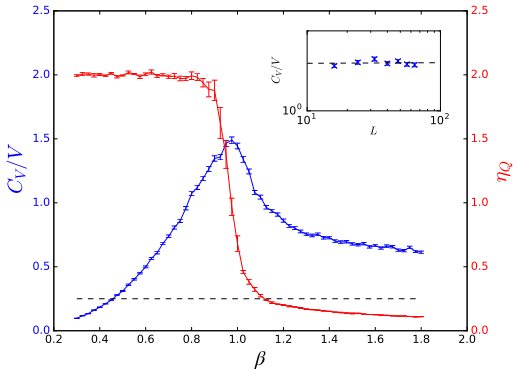

FIG. 14. Finite size scaling of the height of the $\boldsymbol{q} = 0$ peak in of the structure function calculated in an XY-model. System sizes $L \in (16, 24, 32, 40, 48, 56, 64)$ have been used. The exponent grows linearly with temperature to the predicted value of $1/4$ (represented by the dotted line) at the critical temperature of KT-transition, $\beta_{\mathrm{KT}} \approx 1.12$.

amplitude-texture induced by a subtle interplay between spin-orbit and inter-component interactions. We also examined the phase transitions of the model in the parameter regime where SOC is absent.

In the absence of SOC, we found that the phase transition of the model is in the KT universality class for all values of the inter-component interaction strength we have considered. Here we observed a KT-transition in the non-suppressed superfluid condensate. These conclusions are made based on finite size scaling of the helicity modulus at the transition point, as well as extrapolation of the negative dip of the fourth order modulus to a non-zero value in the thermodynamic limit. Both methods strongly indicate a discontinuous jump in the superfluid density at the critical temperature.

In the presence of SOC, we observed a phase-modulated ground state at finite momenta in Monte-Carlo simulations. When the inter-component interactions are weaker than the intra-component interactions, we find that the condensates occupies a single minimum at finite momentum, in agreement with previous works. This manifests itself as a modulation of the phases of the condensate ordering fields. For sufficiently strong inter-component interactions and intermediate spin-orbit interactions, we observed that the spin-orbit induced modulation is completely supressed in favour of a completely imbalanced condensate. For strong spin-orbit coupling and sufficiently strong inter-component interactions, however, the total interaction energy is minimized by keeping the phase-modulation and introducing an additional, staggered modulation of the amplitudes with the same period. In this phase we observe that the condensate occupies two q-vectors of equal magnitude but opposite alignment.

Finally, we examined the thermal phase transition of the spin-orbit induced plane-wave modulated superfluid ground state into the normal fluid state in the London approximation. We show that the inclusion of periodic boundary conditions introduce a strong pinning effect, which weakens as we decouple the stripes from the edges of the system by applying a Thomas-Fermi potential. In the presence of the potential, we see signs of a Kosterlitz-Thouless transition, but we are not able to confirm this.

ACKNOWLEDGMENTS

We thank Egor Babaev for useful discussions. P. N. G. was supported by NTNU and the Research Council of Norway. A. S. was supported by the Research Council of Norway, through Grants 205591/V20 and 216700/F20, as well as European Science Foundation COST Action MPI1201. This work was also supported through the Norwegian consortium for high-performance computing (NOTUR).

Appendix A: Classification of the KT-transition

The defining characteristic of a Kosterlitz-Thouless transition is the universal jump of $2/(\pi\beta_c)$ of the superfluid density at the critical temperature, in the thermodynamic limit. Consider the free energy, where the phase of component i is twisted by an infinitesimal factor along the μ-direction, $F(\Delta_{i,\mu})$. Technically, this amounts to replacing the phase of component i by a twisted phase,

$$\theta_{i,\mathbf{r}} \to \theta_{i,\mathbf{r}} - r_\mu \Delta_{i,\mu} \tag{A1}$$

The superfluid density, or helicity modulus, is the second derivative of the free energy with respect to the twist,

$$\langle \Upsilon_{i,\mu} \rangle \equiv \frac{1}{V} \frac{\partial^2 F(\Delta_{i,\mu})}{\partial \Delta_{i,\mu}^2}. \tag{A2}$$

Similarly, the fourth order modulus is the fourth derivative of the free energy with respect to the twist,

$$\langle \Upsilon_{4,i,\mu} \rangle \equiv \frac{1}{V^2} \frac{\partial^4 F(\Delta_{i,\mu})}{\partial \Delta_{i,\mu}^4}. \tag{A3}$$

Derivatives of odd order vanish due to symmetry.

In terms of amplitudes and phases of the Ginzburg-Landau theory for a two-component condensate, the helicity modulus is

$$V\langle \Upsilon_{i,\mu} \rangle = \langle c_{i,\mu} \rangle - \beta \langle s_{i,\mu}^2 \rangle, \tag{A4}$$

while the fourth order modulus is

$$\begin{aligned} V^2\langle \Upsilon_{4,i,\mu} \rangle = &-3V^2\beta\langle (\Upsilon_{i,\mu} - \langle \Upsilon_{i,\mu} \rangle)^2 \rangle \\ &-4V\langle \Upsilon_{i,\mu} \rangle + 3\langle c_{i,\mu} \rangle + 2\beta^3 \langle s_{i,\mu}^4 \rangle, \end{aligned} \tag{A5}$$

where we have defined

$$c_{i,\mu} \equiv \sum_{\mathbf{r}} |\psi_{i,\mathbf{r}+\boldsymbol{\mu}}| \, |\psi_{i,\mathbf{r}}| \cos\left(\theta_{i,\mathbf{r}+\boldsymbol{\mu}} - \theta_{i,\mathbf{r}}\right), \tag{A6}$$

$$s_{i,\mu} \equiv \sum_{\mathbf{r}} |\psi_{i,\mathbf{r}+\boldsymbol{\mu}}| \, |\psi_{i,\mathbf{r}}| \sin\left(\theta_{i,\mathbf{r}+\boldsymbol{\mu}} - \theta_{i,\mathbf{r}}\right). \tag{A7}$$

This similar to the expressions obtained when considering a 2DXY model. The amplitude fluctuations only influence the moduli indirectly by weighting the terms in the sums. Hence, the moduli of each component are coupled indirectly through the potential.

At the critical temperature, the helicity modulus is expected to scale as

$$\Upsilon_{i,\mu}(L) = \Upsilon(\infty)\left(1 + \frac{1}{2}\frac{1}{\log L + C}\right) \tag{A8}$$

with system size[35]. We fit the data at finite size for different values of β, and determining at which β the best fit is obtained by using the Anderson-Darling test statistic. This allows an extrapolation of the value of the jump, $\Upsilon(\infty)$, which may be compared to the KT-prediction. This will also result in an estimate of the critical temperature.

By considering an expansion of the free energy in terms of the phase twist,

$$F(\Delta_{i,\mu}) - F(0) = \langle \Upsilon_{i,\mu} \rangle \frac{\Delta_{i,\mu}^2}{2} + \langle \Upsilon_{4,i,\mu} \rangle \frac{\Delta_{i,\mu}^4}{4!}. \tag{A9}$$

For the system to be stable, the change in the free energy has to greater or equal to zero. If $\Upsilon_{4,i,\mu}$ is finite and negative in the thermodynamic limit at the critical temperature, $\Upsilon_{i,\mu}$ cannot go continuously to zero at the critical temperature[36]. Therefore, by calculating the negative dip in the fourth order modulus for increasing system size, a finite value as $L \to \infty$ signals a discontinuous jump in the helicity modulus. Furthermore, the temperature at which the dip is located should converge to the critical temperature. Extrapolation of the location of the dip may therefore be compared to the above estimate of the critical temperature, as an additional consistency check. However, this convergence is generally quite slow.

[1] Y. K. Kato, R. C. Myers, A. C. Gossard, and D. D. Awschalom, Science **306**, 1910 (2004).
[2] M. Konig, Science **318**, 766 (2007).
[3] C. L. Kane and E. J. Mele, Phys. Rev. Lett. **95**, 146802 (2005).
[4] B. A. Bernevig, T. L. Hughes, and S.-C. Zhang, Science **314**, 1757 (2006).
[5] D. Hsieh, Nature **452**, 970 (2008).
[6] M. Z. Hasan and C. L. Kane, Rev. Mod. Phys. **82**, 3045 (2010).
[7] J. D. Koralek, Nature **458**, 610 (2009).
[8] Y.-J. Lin, K. Jimenez-Garcia, and I. B. Spielman, Nature **471**, 83 (2011).
[9] V. Galitski and I. B. Spielman, Nature **494**, 49 (2013).
[10] Y. A. Bychkov and E. I. Rashba, J. Phys. C **17**, 6039 (1984).
[11] G. Dresselhaus, Phys. Rev. **100**, 580 (1955).
[12] C. J. Myatt, E. A. Burt, R. W. Ghrist, E. A. Cornell, and C. E. Wieman, Phys. Rev. Lett. **78**, 586 (1997).
[13] D. S. Hall, M. R. Matthews, J. R. Ensher, C. E. Wieman, and E. A. Cornell, Phys. Rev. Lett. **81**, 1539 (1998).
[14] G. Modugno, M. Modugno, F. Riboli, G. Roati, and M. Inguscio, Phys. Rev. Lett. **89**, 190404 (2002).
[15] D. J. McCarron, H. W. Cho, D. L. Jenkin, M. P. Köppinger, and S. L. Cornish, Phys. Rev. A **84**, 011603 (2011).
[16] P. Wang, Z.-Q. Yu, Z. Fu, J. Miao, L. Huang, S. Chai, H. Zhai, and J. Zhang, Phys. Rev. Lett. **109**, 095301 (2012).
[17] I. Bloch, Nat Phys **1**, 23 (2005).
[18] C. Hamner, Y. Zhang, M. A. Khamehchi, M. J. Davis, and P. Engels, Phys. Rev. Lett. **114**, 070401 (2015).
[19] J. Struck, J. Simonet, and K. Sengstock, Phys. Rev. A **90**, 031601 (2014).
[20] C. J. Kennedy, G. A. Siviloglou, H. Miyake, W. C. Burton, and W. Ketterle, Phys. Rev. Lett. **111**, 225301 (2013).
[21] A. P. Schnyder, S. Ryu, A. Furusaki, and A. W. W. Ludwig, Phys. Rev. B **78**, 195125 (2008).
[22] A. Kitaev, AIP Conference Proceedings **1134**, 22 (2009).
[23] X.-L. Qi, T. L. Hughes, S. Raghu, and S.-C. Zhang, Phys. Rev. Lett. **102**, 187001 (2009).
[24] W. S. Cole, S. Zhang, A. Paramekanti, and N. Trivedi, Phys. Rev. Lett. **109**, 085302 (2012).
[25] D. Toniolo and J. Linder, Phys. Rev. A **89**, 061605 (2014).
[26] K. Kasamatsu, Phys. Rev. A **92**, 063608 (2015).
[27] L. Radzihovsky, Phys. Rev. A **84**, 023611 (2011).
[28] C. Wang, C. Gao, C.-M. Jian, and H. Zhai, Phys. Rev. Lett. **105**, 160403 (2010).
[29] T. A. Sedrakyan, A. Kamenev, and L. I. Glazman, Phys. Rev. A **86**, 063639 (2012).
[30] N. Metropolis, A. W. Rosenbluth, M. N. Rosenbluth, A. H. Teller, and E. Teller, J. Chem. Phys. **21**, 1087 (1953).
[31] W. K. Hastings, Biometrika **57**, 97 (1970).
[32] M. Matsumoto and T. Nishimura, ACM Trans. Model. Comput. Simul. **8**, 3 (1998).
[33] A. M. Ferrenberg and R. H. Swendsen, Phys. Rev. Lett. **63**, 1195 (1989).
[34] B. A. Berg, Computer Physics Communications **69**, 7 (1992).
[35] H. Weber and P. Minnhagen, Phys. Rev. B **37**, 5986 (1988).
[36] P. Minnhagen and B. J. Kim, Phys. Rev. B **67**, 172509 (2003).
[37] J. M. Kosterlitz, Journal of Physics C: Solid State Physics **7**, 1046 (1974).
[38] M. E. Fisher, M. N. Barber, and D. Jasnow, Phys. Rev. A **8**, 1111 (1973).
[39] Y.-H. Li and S. Teitel, Phys. Rev. B **47**, 359 (1993).

Paper IV

Current-loops, phase transitions, and the Higgs mechanism in Josephson-coupled multi-component London superconductors

Preprint (submitted to Phys. Rev. B)

Current-loops, phase transitions, and the Higgs mechanism in Josephson-coupled multi-component superconductors

Peder Notto Galteland[1] and Asle Sudbø[1]

[1]*Department of Physics, NTNU, Norwegian University of Science and Technology, N-7491 Trondheim, Norway*

(Dated: May 31, 2016)

The N-component London $\mathrm{U}(1)$ superconductor is expressed in terms of integer-valued supercurrents. We show that the inclusion of inter-band Josephson couplings introduces instantons in the current fields, which convert the phase transitions of the charge-neutral sector to crossovers. The instantons only couple to the neutral sector, and leave the phase transition of the charged sector intact. The remnant non-critical fluctuations in the neutral sector influence the one remaining phase transition in the charged sector, and may alter this phase transition from a $3DXY$ inverted phase transition into a first-order phase transition depending on what the values of the gauge-charge and the inter-component Josephson coupling are. This preemptive effect becomes more pronounced with increasing number of components N, since the number of charge-neutral fluctuating modes that can influence the charged sector increases with N. We also calculate the gauge-field correlator, and by extension the Higgs mass, in terms of current-current correlators. We show that the onset of the Higgs-mass of the photon (Meissner-effect) is given in terms of a current-loop blowout associated with going into the superconducting state as the temperature of the system is lowered.

PACS numbers:

I. INTRODUCTION

Models with multiple $\mathrm{U}(1)$ condensates coupled by a vector potential are relevant to a variety of condensed matter systems. The number of possible interactions between the individual condensates make the models much more complex than single-band systems. Multiple, individually conserved condensates are applicable to systems of low temperature atoms, such as hydrogen under extreme pressures[1–6] and as effective models of easy-plane quantum anti-ferromagnets[7,8]. Superconductors with multiple superconducting bands, such as MgB_2[9–11] and iron pnictides[12] may also be described by a model of multiple $\mathrm{U}(1)$ condensates, but in these systems the individual condensates are not conserved. Inter-band Josephson couplings must always be included, as they cannot *a priori* be excluded on symmetry grounds.

Ginzburg-Landau models of N-component superconductors in the London limit host a rich variety of interesting phenomena[13–16]. Each condensate supports topological vortex line defects, which represent disorder in the condensate ordering field. When the condensates are coupled through a gauge field, the vortices carry magnetic flux quanta, and may be bound into composite vortices with $\pm 2\pi$ phase windings in multiple condensates[17]. It turns out that this gives rise to composite superfluid modes that do not couple to the gauge field, even though their constituent vortices interact via the gauge field. In addition to the superfluid modes, there will be a single charged mode which is coupled by the gauge field. This causes the N-component model without Josephson interactions to have $N-1$ superfluid phase transitions and a single superconducting phase transition[17]. For certain values of the gauge charge these transitions will interfere in a non-trivial way, causing the transitions to merge in a single first-order transition[18,19].

The question of the nature of the phase transitions present in Josephson-coupled multiband superconductors is of considerable interest. Symmetry arguments dictate that the inclusion of the Josephson coupling breaks the $[\mathrm{U}(1)]^n$ symmetry down to $\mathrm{U}(1)$, at any strength. The Josephson term locks the superfluid modes so that the phase transition in the neutral sector is replaced by a crossover[17], while the phase transition in the gauge-coupled sector is expected to remain. If this transition remains continuous, it is expected to be in the inverted $3\mathrm{D}XY$ universality class[17]. A recent study has observed a first order transition in this model for weak Josephson coupling[20], suggesting a subtle interplay between the two length scales dictated by the Josephson length and the magnetic field penetration depth. Also of note is multiband superconductors with frustrated inter-band couplings, which is $\mathrm{U}(1) \times \mathrm{Z}_2$ symmetric. These systems have been shown to have a single first-order transition in three dimensions from a symmetric state into a state that breaks both $\mathrm{U}(1)$ and Z_2 symmetry for weak values of the gauge field coupling. For stronger values of the charge, the transitions split[21,22].

In this paper we present an alternate approach to the multiband superconductor which has certain advantages over standard formulations, and which allows further analytical insights to be made. In particular, we are able reconcile the different results for the character of the phase transition in the charged sector found in Refs. 17 and 20 in the presence of interband Josephson-couplings. By applying a character expansion[23,24] to the action, we replace the phases of the order parameter with integer-current fields. These currents are the actual supercurrents of the model. Section II presents the details and basic properties of the multiband superconductor in the London limit. In Section III A we present the character expansion, apply it to the model with no Josephson coupling, and compare the resulting representation to the original model. We apply the character expansion to the multiband superconductor with Josephson couplings in Section III B and discuss it in the light of the current representation. In Section IV we present the calculation of the Higgs mass in terms of current-correlators. We present our conclusions in Section V.

II. STANDARD REPRESENTATION OF THE MODEL

We consider a model of N bosonic complex matter fields in three dimensions. The matter fields are given by $\psi_\alpha(\boldsymbol{r}) = |\psi_\alpha(\boldsymbol{r})| \exp i\theta_\alpha(\boldsymbol{r})$, interacting through a single non-compact U(1) gauge field, $\boldsymbol{A}(\boldsymbol{r})$. We also allow inter-band Josephson couplings of the matter fields. In the general case, this is described by a partition function

$$\mathcal{Z} = \int \mathcal{D}\boldsymbol{A} \left(\prod_\alpha \int \mathcal{D}\psi_\alpha \right) e^{-S}, \tag{1}$$

where the action is

$$S = \beta \int d^3r \Bigg\{ \frac{1}{2} \sum_\alpha \left(|\nabla - ie\boldsymbol{A}(\boldsymbol{r})) \, \psi_\alpha(\boldsymbol{r})|^2 + V\left(\{ |\psi_\alpha(\boldsymbol{r})| \} \right) + \frac{1}{2} (\nabla \times \boldsymbol{A}(\boldsymbol{r}))^2 - \sum_{\alpha<\beta} \lambda_{\alpha,\beta} \, |\psi_\alpha(\boldsymbol{r})| \, |\psi_\beta(\boldsymbol{r})| \cos\left(\theta_\alpha(\boldsymbol{r}) - \theta_\beta(\boldsymbol{r}) \right) \Bigg\}. \tag{2}$$

The potential V contains terms that are powers of $|\psi_\alpha|$. At this point we employ the phase-only, or London, approximation and choose all bare stiffnesses, $|\psi_\alpha|$, equal to unity. Hence, V is an unimportant constant. We will also focus on equal couplings between all bands, *i.e.* $\lambda_{\alpha,\beta} = \lambda \; \forall \; \alpha, \beta$. The action is then given by

$$S = \beta \int d^3r \Bigg\{ \frac{1}{2} \sum_\alpha \left(\nabla\theta_\alpha(\boldsymbol{r}) - e\boldsymbol{A}(\boldsymbol{r}) \right)^2 + \frac{1}{2} (\nabla \times \boldsymbol{A}(\boldsymbol{r}))^2 - \lambda \sum_{\alpha<\beta} \cos\left(\theta_\alpha(\boldsymbol{r}) - \theta_\beta(\boldsymbol{r}) \right) \Bigg\} \tag{3}$$

We regularize this action on a cubic lattice of size L^3 by defining the fields on a discrete set of coordinates $r_\mu \in (1, \ldots, L)$, that is $\theta_\alpha(\boldsymbol{r}) \to \theta_{\boldsymbol{r},\alpha}$ and $\boldsymbol{A}(\boldsymbol{r}) \to \boldsymbol{A}_{\boldsymbol{r}}$. On the lattice, the action reads

$$S = \beta \sum_{\boldsymbol{r}} \Bigg\{ - \sum_{\mu,\alpha} \cos\left(\Delta_\mu \theta_{\boldsymbol{r},\alpha} - eA_{\boldsymbol{r},\mu} \right) + \frac{1}{2} (\Delta \times \boldsymbol{A}_{\boldsymbol{r}})^2 - \lambda \sum_{\alpha<\beta} \cos\left(\theta_{\boldsymbol{r},\alpha} - \theta_{\boldsymbol{r},\beta} \right) \Bigg\}. \tag{4}$$

Here, we use the cosine function to represent the kinetic term of the continuum Hamiltonian in a way that preserves the periodic nature of the phases. Alternatively, one may arrive at Eq. (4) by directly replacing the derivatives in Eq. (2) with the gauge invariant forward difference,

$$(\nabla - ie\boldsymbol{A}(\boldsymbol{r}))\psi_\alpha(\boldsymbol{r}) \to \psi_{\boldsymbol{r}+\hat{\boldsymbol{\mu}},\alpha} e^{-ie\boldsymbol{A}_{\boldsymbol{r}}} - \psi_{\boldsymbol{r},\alpha}, \tag{5}$$

and then taking the London limit as described above. We discuss the two-dimensional case in Appendix B.

In the formulation of Eq. (4) with $\lambda = 0$, the model is known[17,19] to have one phase transition from a normal state to a superconducting state in one composite degree of freedom, and $N-1$ phase transitions from a normal fluid to a superfluid in the remaining degrees of freedom. The reason for this division into one superconducting and $N-1$ superfluid degrees of freedom becomes apparent when one correctly identifies the relevant combinations of the phase fields. The part of the continuum action describing the coupling between the phases and the gauge field is

$$S' = \beta \int d\boldsymbol{r} \left\{ \frac{1}{2} \sum_\alpha \left(\nabla\theta_\alpha(\boldsymbol{r}) - e\boldsymbol{A}(\boldsymbol{r}) \right)^2 \right\}. \tag{6}$$

This can be rewritten into[17]

$$S' = \beta \int d\boldsymbol{r} \Bigg\{ \frac{1}{2N} \left(\sum_\alpha \nabla\theta_\alpha(\boldsymbol{r}) - Ne\boldsymbol{A}(\boldsymbol{r}) \right)^2 + \frac{1}{2N} \sum_{\alpha<\beta} \left[\nabla \left(\theta_\alpha - \theta_\beta \right) \right]^2 \Bigg\}. \tag{7}$$

Hence, the phase combination $\sum_\alpha \theta_\alpha$ will couple to the gauge field, and is identified as the single charged mode, while all other combinations $\theta_\alpha - \theta_\beta$ do not couple, and are neutral. Note that for $N = 1$ only the charged mode remains. Two important points need to be emphasized. Firstly, the composite variables are not compact in the same sense that the individual phases are. This means that the composite variables do not support topological defects by themselves, only composite topological defects. Secondly, the last term in the action of Eq. (7) has $N(N-1)/2$ terms. Therefore, one may not interpret the phase differences $\theta_\alpha - \theta_\beta$ as independent degrees of freedom. This is because of the multiple connectedness of the physical space, fluctuations in a single individual phase induce fluctuations in $N-1$ composite neutral modes, as well as in the charged mode.

In the present form, with $\lambda = 0$ and e sufficiently large, this model is known to have one phase transition in the inverted $3dXY$-universality class, and $N-1$ transitions in the $3dXY$-universality class at a higher temperature[17,19]. These transitions correspond to proliferations of the composite charged mode and the composite neutral modes, respectively. If the charge is lowered, the charged and neutral transitions will approach each other in temperature. When they merge, the proliferation of neutral vortices will trigger proliferation of the charged mode. Consequently, the N phase transitions collapse into a single first-order transition. This interplay between the charged and neutral sector has been coined a *preemptive* phase transition[25], and has been verified numerically in two-component systems in the absence of inter-component Josephson-coupling in several detailed large-scale Monte Carlo simulations[18,19,25].

In the following Section, we reformulate the model in terms of integer-valued current fields, considering first the case with zero Josephson-coupling and then move on to include Josephson coupling. The first case is useful to consider in connecting the results of previous works mentioned above to the current-formulation.

III. CURRENT REPRESENTATION OF THE MODEL

A. Zero intercomponent Josephson coupling

The basis of the expansion used is a character expansion[23,24].

$$e^{\beta\cos\gamma} = \sum_{b=-\infty}^{\infty} I_b(\beta)e^{ib\gamma}, \tag{8}$$

where $I_b(\beta)$ are the modified Bessel functions of integer order. We apply this to the terms $\exp\beta\cos(\Delta_\mu\theta_{\boldsymbol{r},\alpha} - e\boldsymbol{A}_{\boldsymbol{r}})$ for each value of $\boldsymbol{r}$, μ, and α. This introduces integer vector fields $\boldsymbol{b}_{\boldsymbol{r},\alpha}$, representing supercurrents. The low-temperature phase is characterized by a state with proliferated current-loops on all length scales, while the high-temperature phase only features small current-loops.

By applying Eq. (8) to the partition function with Eq. (4) as the action, and integrating out the phases and the gauge field, details of which may be found in Appendix A, we arrive at the partition function

$$\mathcal{Z} = \sum_{\{\boldsymbol{b},m\}} \prod_{\boldsymbol{r},\alpha} \delta_{\boldsymbol{\Delta}\cdot\boldsymbol{b}_{\boldsymbol{r},\alpha},0} \prod_{\boldsymbol{r},\mu,\alpha} I_{b_{\boldsymbol{r},\alpha,\mu}}(\beta) \prod_{\boldsymbol{r},\boldsymbol{r}'} e^{-\frac{e^2}{2\beta}\sum_{\alpha,\beta}\boldsymbol{b}_{\boldsymbol{r},\alpha}\cdot\boldsymbol{b}_{\boldsymbol{r}',\beta}D(\boldsymbol{r}-\boldsymbol{r}')}. \tag{9}$$

This is a model of N current fields, with contact intracomponent interactions parametrized via the Bessel functions, and long-range intra- and inter-component interactions originating with the gauge-field fluctuations, $D(\boldsymbol{r}-\boldsymbol{r}')$. The constraint $\boldsymbol{\Delta}\cdot\boldsymbol{b}_{\boldsymbol{r},\alpha} = 0$ forces the currents, $\boldsymbol{b}_{\boldsymbol{r},\alpha}$ to form closed loops, and implies a non-analytical behavior of each individual component, and an associated phase transition.

In the current language, the interpretation of the phase transitions explained in the previous Section is as follows. Consider first a single component model. In the high temperature state, only the lowest term in the Bessel-function expansion will contribute, and only small loops of supercurrents will be present in the system. As the temperature is *lowered* all orders of the expansion contribute, and the integer currents will proliferate, filling the system with loops of supercurrent. In the low temperature state all b-fields have proliferated. As temperature is increased, the proliferated current loops in the charged sector will collapse. Only the neutral superfluid currents fill the system, and the state is therefore a metallic superfluid[15]. As temperature is lowered further the superfluid currents collapse as well, and the system is in the normal metallic state.

B. Non-zero intercomponent Josephson couplings

The expansion of Eq. (8) may also be applied to the Josephson term. This introduces an additional $N(N-1)/2$ integer fields $m_{\boldsymbol{r},\alpha,\beta}$. After expanding both the kinetic terms and the Josephson terms, the partition function reads

$$\begin{aligned}\mathcal{Z} = &\int \mathcal{D}\boldsymbol{A}\left(\prod_\alpha \int \mathcal{D}\theta_\alpha\right) \\ &\times \prod_{\boldsymbol{r},\mu,\alpha}\sum_{b_{\boldsymbol{r},\mu,\alpha}=-\infty}^{\infty} I_{b_{\boldsymbol{r},\mu,\alpha}}(\beta)e^{ib_{\boldsymbol{r},\mu,\alpha}(\Delta_\mu\theta_{\boldsymbol{r},\alpha} - eA_{\boldsymbol{r},\boldsymbol{\mu}})} \\ &\times \prod_{\boldsymbol{r},\alpha<\beta}\sum_{m_{\boldsymbol{r},\alpha,\beta}=-\infty}^{\infty} I_{\boldsymbol{m}_{\boldsymbol{r},\alpha,\beta}}(\beta\lambda)e^{im_{\boldsymbol{r},\alpha,\beta}(\theta_{\boldsymbol{r},\alpha}-\theta_{\boldsymbol{r},\beta})} \\ &\times \prod_{\boldsymbol{r}} e^{-\frac{\beta}{2}(\Delta\times\boldsymbol{A}_{\boldsymbol{r}})^2}\end{aligned} \tag{10}$$

The effect of the Josephson coupling becomes apparent when we integrate out the phase fields. The divergences of the $\boldsymbol{b}$-fields will no longer be constrained to zero, but may take any finite integer value, determined by the value of the m-fields. The new constraints read

$$\boldsymbol{\Delta}\cdot\boldsymbol{b}_{\boldsymbol{r},\alpha} = \sum_{\beta\neq\alpha} m_{\boldsymbol{r},\alpha,\beta}\ \forall\ \alpha,\boldsymbol{r}, \tag{11}$$

where we have defined $m_{\boldsymbol{r},\alpha,\beta} = -m_{\boldsymbol{r},\beta,\alpha}$. The gauge-term is not coupled directly to the m-fields, and we may integrate it out in the same fashion as before. The resulting partition function is

$$\begin{aligned}\mathcal{Z} = \sum_{\{\boldsymbol{b},m\}} &\prod_{\boldsymbol{r},\alpha}\delta_{\boldsymbol{\Delta}\cdot\boldsymbol{b}_{\boldsymbol{r},\alpha},\sum_{\beta\neq\alpha}m_{\boldsymbol{r},\alpha,\beta}} \\ &\prod_{\boldsymbol{r},\mu,\alpha} I_{b_{\boldsymbol{r},\alpha,\mu}}(\beta)\prod_{\boldsymbol{r},\alpha<\beta} I_{m_{\boldsymbol{r},\alpha,\beta}}(\beta\lambda) \\ &\prod_{\boldsymbol{r},\boldsymbol{r}'} e^{-\frac{e^2}{2\beta}\sum_{\alpha,\beta}\boldsymbol{b}_{\boldsymbol{r},\alpha}\cdot\boldsymbol{b}_{\boldsymbol{r}',\beta}D(\boldsymbol{r}-\boldsymbol{r}')}\end{aligned} \tag{12}$$

C. Instantons and phase transitions

The effect of the m-fields is to introduce instantons into the closed loops of $\boldsymbol{b}$-currents. A current of a particular component (color) may now terminate at any site. However, this termination must always be accompanied by a current of another color originating at the same site. Termination of a current of one component, and the appearance of a current of another component at the same site represents an excitation of ±1 in m. An important observation is that if one adds the constraints, we have

$$\sum_\alpha \boldsymbol{\Delta}\cdot\boldsymbol{b}_{\boldsymbol{r},\alpha} = 0\ \forall\ \boldsymbol{r}. \tag{13}$$

This reflects the color changing event stated above, the total current when summing over all colors is conserved at all sites. It also shows that there is a particular combination of currents, the sum of all components, which will be divergence-free. The net effect of the Josephson coupling, pictorially, is to chop up the closed currents of the individual components and glue them together into closed loops that may change color on any site.

We may expand the partition function first in terms of m-fields, and then in terms of λ, by using the Bessel-function representation

$$I_\nu(z) = \left(\frac{z}{2}\right)^\nu \sum_{k=0}^{\infty} \frac{\left(\frac{z}{2}\right)^{2k}}{k!(\nu+k)!} \tag{14}$$

This demonstrates that the partition function consists of a single term with zero divergence on all sites, which we know has one or more phase transitions from a superconducting superfluid state into a non-superconducting normal fluid, and many terms where the divergence of $\boldsymbol{b}_{\boldsymbol{r},\alpha}$ is finite on any number of sites.

Let us now consider two limits, and assume e is large, so that there is no preemptive effect for $\lambda = 0$. For $\lambda = 0$, it is evident that only $m = 0$ will contribute, and we are left with only divergenceless terms, and hence the behaviour described previously. The other limit is $\lambda \to \infty$. In this case we must examine the asymptotic form of the Bessel functions, which to leading order in the argument is

$$I_m(z) \sim \frac{e^z}{\sqrt{2\pi z}}, \tag{15}$$

i.e. independent of m, and the instanton field will fluctuate strongly, causing the zero-divergence constraint on each component to be removed. The only remaining constraint on the current fields pertains to the composite current $\sum_\alpha \boldsymbol{b}_\alpha$, which is divergence-free. The interpretation of this is that the phase transitions in the $N-1$ superfluid modes are converted to crossovers by the Josephson coupling, while the single superconducting mode still undergoes a genuine phase transition. The neutral crossover will be far removed from the charged phase transition in this limit, and the remaining fluctuations in the neutral sector will be almost completely suppressed. There is no possibility of any interference between the sectors, and therefore no preemptive phase transition. The phase transition in the charged sector will therefore be in the universality class of the inverted $3DXY$ phase transition.

For intermediate and small values of λ, the effect of the Josephson coupling on the interplay between the charged and neutral sectors is quite subtle in the present formulation. We therefore choose to recast the individual currents into composite charged and neutral currents in the following.

D. Charged and neutral currents

The partition function presented in Eq. (12) is not particularly well suited for illuminating the interplay between the neutral superfluid and charged superconducting modes. A more direct approach is to start with the action where the phase sum and phase differences have been separated, Eq. (7), with a Josephson coupling included. To simplify the notation, we introduce composite fields $\Theta \equiv \sum_\alpha \theta_\alpha$ and $\vartheta_{\alpha\beta} \equiv \theta_\alpha - \theta_\beta$. Then we have the lattice action

$$\begin{aligned} S = \beta \sum_{\boldsymbol{r}} \Bigg\{ &- \sum_\mu \cos\left(\Delta_\mu \Theta_{\boldsymbol{r}} - N e A_{\boldsymbol{r},\mu}\right) \\ &- \sum_{\mu,\alpha<\beta} \cos\left(\Delta_\mu \vartheta_{\boldsymbol{r},\alpha\beta}\right) - \lambda \sum_{\alpha<\beta} \cos\left(\vartheta_{\boldsymbol{r},\alpha\beta}\right) \\ &+ \frac{1}{2}(\boldsymbol{\Delta} \times \boldsymbol{A}_{\boldsymbol{r}})^2 \Bigg\}. \end{aligned} \tag{16}$$

One may arrive at this form by defining the composite fields in Eq. (7), then use the Villain approximation on the original action of Eq. (4), rewrite the resulting action into one with the composite fields, then reverse the Villain approximation.

Note that in Eq. (16), there is one charged mode and $N(N-1)/2$ neutral modes, while the original theory has N degrees of freedom. There are therefore $(N-1)(N-2)/2$ variables too many. (Note that there are no redundant modes for $N = 1$ and $N = 2$). Therefore, not all of the phase differences are independent when $N > 2$. Consider the case $N = 3$, where one may form the phase differences $\theta_1 - \theta_2$, $\theta_2 - \theta_3$ and $\theta_1 - \theta_3$, but $\theta_1 - \theta_3 = (\theta_1 - \theta_2) + (\theta_2 - \theta_3)$. It suffices to include the phase differences ϑ_{12} and ϑ_{23}.

This may be generalized to arbitrary N. Identify all $\theta_{\alpha\beta}$ where

$$\{(\alpha,\beta) | \alpha \in (1,\ldots,N-1) \wedge \beta = \alpha + 1\}. \tag{17}$$

Then, all $\theta_{\alpha\beta}$ where

$$\{(\alpha,\beta) | \alpha \in (1,\ldots,N-2) \wedge \beta \in (\alpha+2,\ldots,N)\} \tag{18}$$

may be constructed by adding up the intermediate phase differences, that is $\vartheta_{\alpha\beta} = \vartheta_{\alpha,\alpha+1} + \vartheta_{\alpha+1,\alpha+2} + \cdots \vartheta_{\beta-1,\beta}$. With this in mind, we may write out the partition function in terms of the charged and neutral modes

$$\begin{aligned} \mathcal{Z} = \int \mathcal{D}\Theta \left(\prod_{\alpha<\beta} \int \mathcal{D}\vartheta_{\alpha\beta} \right) \\ \times \left(\prod_{\alpha=1}^{N-1} \prod_{\beta=\alpha+2}^{N} \delta\left(\vartheta_{\alpha\beta} - \sum_{\eta=\alpha}^{\beta-1} \vartheta_{\eta,\eta+1} \right) \right) e^S \end{aligned} \tag{19}$$

where S is the action of Eq. (16).

As an illustration, we perform the character expansion on the model where the charged and neutral sectors have been separated, for the special cases $N = 2$ and $N = 3$.

For $N = 2$ there are no redundant variables, and we have the two composite variables $\Theta \equiv \theta_1 + \theta_2$ and $\vartheta \equiv \theta_1 - \theta_2$. Using the identity Eq. (8), and integrating out the phases and gauge field, we obtain

$$\begin{aligned} \mathcal{Z} = \sum_{\{\boldsymbol{B},\boldsymbol{\mathcal{B}},m\}} \prod_{\boldsymbol{r}} \delta_{\boldsymbol{\Delta}\cdot\boldsymbol{B}_{\boldsymbol{r}},0} \delta_{\boldsymbol{\Delta}\cdot\boldsymbol{\mathcal{B}}_{\boldsymbol{r}},m_{\boldsymbol{r}}} \\ \prod_{\boldsymbol{r},\mu} I_{B_{\boldsymbol{r},\mu}}(\beta) I_{\mathcal{B}_{\boldsymbol{r},\mu}}(\beta) \prod_{\boldsymbol{r}} I_{m_{\boldsymbol{r}}}(\beta\lambda) \\ \prod_{\boldsymbol{r},\boldsymbol{r}'} \exp\left\{ -\frac{(Ne)^2}{2\beta} \boldsymbol{B}_{\boldsymbol{r}} \cdot \boldsymbol{B}_{\boldsymbol{r}'} D(\boldsymbol{r}-\boldsymbol{r}') \right\}. \end{aligned} \tag{20}$$

Here, $\boldsymbol{B}$ is the charged current field associated with Θ, while $\boldsymbol{\mathcal{B}}$ is the neutral current field associated with ϑ.

In this formulation, it is immediately clear that the model features two integer vector-field degrees of freedom, one which has long-range interactions mediated by the gauge field, and one with contact interactions. The neutral current field has its constraint removed by the m-field, while the charged field is still constrained to be divergenceless. Hence, the model will feature a single phase transition in the charged sector driven by the collapse of closed loops of charged currents, while the transition of the neutral sector is converted to a crossover by the complete removal of constraints on $\boldsymbol{\mathcal{B}}$.

Let us consider this in a bit more detail. In Eq. (20), we may perform the summation over the fields $m \in \mathbb{Z}$. Since we have that $\boldsymbol{\Delta}\cdot\boldsymbol{\mathcal{B}}_{\boldsymbol{r}} \in \mathbb{Z}$ as well, the summation over the m's will guarantee that the constraint is satisfied for some value of m, such that the summation over m effectively removes the constraints on $\boldsymbol{\Delta}\cdot\boldsymbol{\mathcal{B}}_{\boldsymbol{r}}$. Hence, we have $\sum_{\{m\}}\delta_{\boldsymbol{\Delta}\cdot\boldsymbol{\mathcal{B}}_{\boldsymbol{r}},m_{\boldsymbol{r}}}\prod_{\boldsymbol{r}} I_{m_{\boldsymbol{r}}}(\beta\lambda) = \prod_{\boldsymbol{r}} I_{\boldsymbol{\Delta}\cdot\boldsymbol{\mathcal{B}}_{\boldsymbol{r}}}(\beta\lambda)$, with no constraints on $\boldsymbol{\Delta}\cdot\boldsymbol{\mathcal{B}}_{\boldsymbol{r}}$. We may thus perform the now unconstrained summation of the field $\boldsymbol{\mathcal{B}}_{\boldsymbol{r}}$, namely

$$\sum_{\{\boldsymbol{\mathcal{B}}\}}\left(\prod_{\boldsymbol{r},\mu} I_{\mathcal{B}_{\boldsymbol{r},\mu}}(\beta)\right)\left(\prod_{\boldsymbol{r}} I_{\boldsymbol{\Delta}\cdot\boldsymbol{\mathcal{B}}_{\boldsymbol{r}}}(\beta\lambda)\right) = F(\beta,\lambda), \quad (21)$$

where F is an analytic function of its arguments. This may be seen by mapping the left hand side of Eq. (21) to a Villain model, using the approximation[23]

$$\frac{I_b(x)}{I_0(x)} \approx \frac{1}{|b|!}e^{\log(\beta/2)|b|}. \quad (22)$$

This may be rewritten as a gaussian provided β is sufficiently small so that contributions $|b| > 1$ are small,

$$\frac{I_b(x)}{I_0(x)} \approx e^{\frac{-b^2}{2\beta'}}, \quad (23)$$

where β' is a renormalized coupling constant, and we find

$$F(\beta,\lambda) = \sum_{\{\boldsymbol{\mathcal{B}}\}}\left(\prod_{\boldsymbol{r},\mu}\exp\frac{-\mathcal{B}^2_{\boldsymbol{r},\mu}}{2\beta'}\right)\left(\prod_{\boldsymbol{r}}\exp\frac{-\left(\boldsymbol{\Delta}\cdot\boldsymbol{\mathcal{B}}_{\boldsymbol{r}}\right)^2}{2\lambda\beta'}\right),. \quad (24)$$

Since ther are no constraints $\boldsymbol{\mathcal{B}}$, this demonstrates that Eq. (21) essentially is a discrete Gaussian theory, and the neutral sector therefore does not suffer any phase transition. This point may be further corroborated by going back to the formulation of Eq. 16. The neutral sector of the action is seen to be identical to that of an XY spin-model in an external magnetic field, with field strength λ. Any $\lambda \neq 0$ converts the phase transition, from a low-temperature ferromagnetic state to a high-temperature paramagnetic state, into to a crossover from an ordered to a disordered system. Note also that in the limit $\lambda = 0$, the Bessel function will revert to $I_{\boldsymbol{\Delta}\cdot\boldsymbol{\mathcal{B}}}(0) = \delta_{\boldsymbol{\Delta}\cdot\boldsymbol{\mathcal{B}},0}$, and the non-analytical constraint is re-introduced.

The total partition function for the entire system is thus given by

$$\mathcal{Z} = F(\beta,\lambda)\sum_{\{\boldsymbol{B}\}}\prod_{\boldsymbol{r}}\delta_{\boldsymbol{\Delta}\cdot\boldsymbol{B}_{\boldsymbol{r}},0}\prod_{\boldsymbol{r},\mu} I_{B_{\boldsymbol{r},\mu}}(\beta) \prod_{\boldsymbol{r},\boldsymbol{r}'}\exp\left\{-\frac{(Ne)^2}{2\beta}\boldsymbol{B}_{\boldsymbol{r}}\cdot\boldsymbol{B}_{\boldsymbol{r}'}D(\boldsymbol{r}-\boldsymbol{r}')\right\}. \quad (25)$$

The phase-transition in the neutral sector is converted to a crossover, and there are no longer any *critical* fluctuations associated with disordering the neutral sector, unlike the case $\lambda = 0$. This occurs as soon as λ is finite, however small. However, even without a phase transition and associated critical fluctuations, there will still be a crossover with associated fluctuations in its vicinity. Hence, the preemptive first-order phase transition in the charged sector, which occurs for $\lambda = 0$, may still take place provided λ sufficiently small.

The argument is as follows. In the preemptive scenario for $\lambda = 0$, fluctuations in the neutral and charged sectors increase as T is increased from below in the fully ordered state. The charged sector influences the fluctuations in the neutral sector and vice versa, such that the putative continuous transitions in these sectors are preempted by a common first order phase transition[17,19]. The important point to realize is that neither of the sectors actually reach criticality, since there are no critical fluctuations at the preemptive first-order phase transition.

We may have the same scenario occurring with finite but small λ. A necessary requirement is that the gauge-charge e is not too large, such that gauge-field fluctuations are not so large as to separate the phase-transitions in the charged and the neutral sector too much[17,19]. The key point is that the inclusion of Josephson-couplings converts the phase transition in the neutral sector to a crossover in exactly the same way that the ferromagnetic-paramagnetic phase transition in the $3DXY$ model is converted to a crossover by the inclusion of a magnetic field coupling linearly to the XY-spins, cf. Eq 16. This leaves only a phase-transition in the charged sector, but it does not completely suppress fluctuations in the neutral sector. It merely cuts the fluctuations off on a length-scale given by the Josephson-length $1/\lambda$, thereby preventing them from becoming critical. As temperature is increased, the neutral sector approaches its crossover region, with increasingly large fluctuations. At the same time, the charged sector approaches its putative inverted-$3dXY$ fixed point. Provided that the crossover region of the neutral sector and the fixed point of the charged sector are sufficiently close, the fluctuations in both sectors may still strongly influence each other, and a first-order preemptive phase transition may still occur in the charged sector. This is consistent with recent numerical work[20], which observed a first order phase transition in multi-band superconductors with weak Josephson-coupling in Monte-Carlo simulations using the original $\mathrm{U}(1)$ phases.

For $N = 3$ we must consider carefully the redundant variable, $\vartheta_{13} = \vartheta_{12} + \vartheta_{23}$. The partition function, prior to inte-

gration of the phases and the gauge field reads

$$\begin{aligned}\mathcal{Z} = &\int \mathcal{D}\Theta \left(\prod_{\alpha<\beta} \int \mathcal{D}\vartheta_{\alpha\beta} \right) \delta(\vartheta_{13} - \vartheta_{12} - \vartheta_{23}) \\ &\times \prod_{\boldsymbol{r},\mu} \sum_{B_{\boldsymbol{r},\mu}=-\infty}^{\infty} I_{B_{\boldsymbol{r},\mu}}(\beta) e^{iB_{\boldsymbol{r},\mu}(\Delta_\mu \Theta_{\boldsymbol{r}} - NeA_{\boldsymbol{r},\boldsymbol{\mu}})} \\ &\times \prod_{\substack{\boldsymbol{r},\mu \\ \alpha<\beta}} \sum_{\mathcal{B}_{\boldsymbol{r},\mu,\alpha\beta}=-\infty}^{\infty} I_{\mathcal{B}_{\boldsymbol{r},\mu,\alpha\beta}}(\beta) e^{i\mathcal{B}_{\boldsymbol{r},\mu,\alpha\beta}\Delta_\mu \vartheta_{\boldsymbol{r},\alpha\beta}} \\ &\times \prod_{\boldsymbol{r},\alpha<\beta} \sum_{m_{\boldsymbol{r},\alpha\beta}=-\infty}^{\infty} I_{\boldsymbol{m}_{\boldsymbol{r},\alpha,\beta}}(\beta\lambda) e^{im_{\boldsymbol{r},\alpha,\beta}\vartheta_{\alpha\beta}} \\ &\times \prod_{\boldsymbol{r}} e^{-\frac{\beta}{2}(\Delta\times \boldsymbol{A}_{\boldsymbol{r}})^2}. \end{aligned} \tag{26}$$

Again, $\boldsymbol{B}$ is the charged current associated with Θ, while $\boldsymbol{\mathcal{B}}_{\alpha\beta}$ are the neutral currents associated with $\vartheta_{\alpha\beta}$. The δ-function is included to account for the redundancy of the composite phase representation.

We now proceed with the integration of phases and gauge field, taking care to integrate out the redundant phase first. The partition function may then be written as

$$\begin{aligned}\mathcal{Z} = \sum_{\{\boldsymbol{B},\boldsymbol{\mathcal{B}},m\}} &\prod_{\boldsymbol{r}} \delta_{\boldsymbol{\Delta}\cdot\boldsymbol{B}_{\boldsymbol{r}},0} \prod_{\boldsymbol{r},\mu} I_{B_{\boldsymbol{r},\mu}}(\beta) \\ &\prod_{\boldsymbol{r}} \delta_{\boldsymbol{\Delta}\cdot\boldsymbol{\mathcal{B}}_{\boldsymbol{r},12}+\boldsymbol{\Delta}\cdot\boldsymbol{\mathcal{B}}_{\boldsymbol{r},13},m_{\boldsymbol{r},12}+m_{\boldsymbol{r},13}} \\ &\prod_{\boldsymbol{r}} \delta_{\boldsymbol{\Delta}\cdot\boldsymbol{\mathcal{B}}_{\boldsymbol{r},23}+\boldsymbol{\Delta}\cdot\boldsymbol{\mathcal{B}}_{\boldsymbol{r},13},m_{\boldsymbol{r},23}+m_{\boldsymbol{r},13}} \\ &\prod_{\substack{\boldsymbol{r},\mu \\ \alpha<\beta}} I_{\boldsymbol{\mathcal{B}}_{\boldsymbol{r},\mu,\alpha\beta}}(\beta) \prod_{\substack{\boldsymbol{r} \\ \alpha<\beta}} I_{m_{\boldsymbol{r},\alpha\beta}}(\beta\lambda) \\ \prod_{\boldsymbol{r},\boldsymbol{r}'} \exp&\left\{ -\frac{(Ne)^2}{2\beta} \boldsymbol{B}_{\boldsymbol{r}} \cdot \boldsymbol{B}_{\boldsymbol{r}'} D(\boldsymbol{r}-\boldsymbol{r}') \right\}. \end{aligned} \tag{27}$$

This is a model of a single gauge coupled supercurrent $\boldsymbol{B}$ which are constrained to form closed loops, and three superfluid currents $\boldsymbol{\mathcal{B}}_{12}$, $\boldsymbol{\mathcal{B}}_{23}$ and $\boldsymbol{\mathcal{B}}_{13}$ which are not constrained to form closed loops. The three superfluid currents are not independent, as is seen from the two constraints on them. As in the case $N = 2$, the summation over the m-fields may be performed, eliminating the constraints on the fields $\boldsymbol{\mathcal{B}}_{\boldsymbol{r},\mu,\alpha\beta}$, after which the *unconstrained* summation over these fields may be performed. As for $N = 2$, this yields multiplicative analytic factors in the partition function, and the phase transitions in the neutral sectors will be converted to crossovers. Given that the crossovers in the neutral sectors and the charged fixed point have sufficient overlap, the system may still feature a single preemptive first-order phase transition arising from the interplay between the charged and neutral modes. Furthermore, the inclusion of the additional degree of freedom enhances the combined fluctuations of the neutral mode at a given Josephson coupling, λ, and therefore strengthens the preemptive first-order transition. This is consistent with the results of recent numerical work[20].

IV. CURRENT CORRELATIONS AND THE HIGGS MECHANISM

The defining characteristic of the inverted 3DXY-transition in the charged sector is a spontaneous $U(1)$ gauge-symmetry breaking associated with the gauge field $\boldsymbol{A}$ becoming massive as the system crosses the transition point of the metallic state into the superconducting state. In this section, we investigate how the onset of the mass $m_{\boldsymbol{A}}$ of the photon (the Higgs mass), which is equivalent to the Meissner effect of the superconductor, comes about as result of a non-analytic change in the infrared properties of the current-correlations of the system. $m_{\boldsymbol{A}}$ is found from the limiting form of the gauge-field correlation function

$$\langle A^{\mu}_{\boldsymbol{q}} A^{\nu}_{-\boldsymbol{q}} \rangle \sim \frac{1}{q^2 + m^2_{\boldsymbol{A}}}. \tag{28}$$

To calculate $\langle A^{\mu}_{\boldsymbol{q}} A^{\nu}_{-\boldsymbol{q}} \rangle$, we consider the action of the charged sector given on the form Eq. (A7) before integrating out the gauge field, and insert source terms source $\boldsymbol{J}_{\boldsymbol{q}}$,

$$\begin{aligned} S_J = \sum_{\boldsymbol{q}} \Bigg[&\frac{ie}{2} \sum_{\alpha} \boldsymbol{b}_{\boldsymbol{q},\alpha} \cdot \boldsymbol{A}_{-q} + \frac{ie}{2} \sum_{\alpha} \boldsymbol{b}_{-q,\alpha} \cdot \boldsymbol{A}_{\boldsymbol{q}} \\ &+ \frac{\beta}{2} |\boldsymbol{Q}_{\boldsymbol{q}}|^2 \boldsymbol{A}_{\boldsymbol{q}} \cdot \boldsymbol{A}_{-\boldsymbol{q}} \\ &+ \frac{1}{2} \left(\boldsymbol{J}_{\boldsymbol{q}} \cdot \boldsymbol{A}_{-\boldsymbol{q}} + \boldsymbol{J}_{-\boldsymbol{q}} \cdot \boldsymbol{A}_{\boldsymbol{q}} \right) \Bigg]. \end{aligned} \tag{29}$$

which in turn may be written on form

$$\begin{aligned} S_J = \sum_{\boldsymbol{q}} \Bigg[&\left(\boldsymbol{A}_{\boldsymbol{q}} + \frac{1}{2} \left(\boldsymbol{J}_{\boldsymbol{q}} + ie \sum_{\alpha} \boldsymbol{b}_{\boldsymbol{q},\alpha} \right) D^{-1}_{\boldsymbol{q}} \right) D_{\boldsymbol{q}} \\ &\times \left(\boldsymbol{A}_{-\boldsymbol{q}} + \frac{1}{2} \left(\boldsymbol{J}_{-\boldsymbol{q}} + ie \sum_{\alpha} \boldsymbol{b}_{-\boldsymbol{q},\alpha} \right) D^{-1}_{\boldsymbol{q}} \right) \\ &+ -\frac{1}{4} \left(\boldsymbol{J}_{\boldsymbol{q}} + ie \sum_{\alpha} \boldsymbol{b}_{\boldsymbol{q},\alpha} \right) D^{-1}_{\boldsymbol{q}} \\ &\times \left(\boldsymbol{J}_{-\boldsymbol{q}} + ie \sum_{\beta} \boldsymbol{b}_{-\boldsymbol{q},\beta} \right) \Bigg]. \end{aligned} \tag{30}$$

Here, $D_{\boldsymbol{q}} = \beta |\boldsymbol{Q}_{\boldsymbol{q}}|^2 / 2$ as before. After shifting and integrating the gauge field, we have

$$\begin{aligned} S_J = -\sum_{\boldsymbol{q}} \Bigg[&\frac{1}{2\beta |\boldsymbol{Q}_{\boldsymbol{q}}|^2} \Big(J^{\mu}_{\boldsymbol{q}} P^{\mu\nu}_T J^{\nu}_{-\boldsymbol{q}} - e^2 \sum_{\alpha\beta} b^{\mu}_{\boldsymbol{q},\alpha} b^{\mu}_{-\boldsymbol{q}} \\ &+ ie \sum_{\alpha} \left(J^{\mu}_{-\boldsymbol{q}} b^{\mu}_{\boldsymbol{q},\alpha} + J^{\mu}_{\boldsymbol{q}} b^{\mu}_{-\boldsymbol{q},\alpha} \right) \Big) \Bigg], \end{aligned} \tag{31}$$

where repeated indices are summed over, and $P^{\mu\nu}_T$ is the transverse projection operator

$$P^{\mu\nu}_T = \delta^{\mu\nu} - \frac{Q^{\mu}_{\boldsymbol{q}} Q^{\nu}_{-\boldsymbol{q}}}{|\boldsymbol{Q}_{\boldsymbol{q}}|^2} \tag{32}$$

The gauge-field correlator is then given by

$$\begin{aligned}\langle A^{\mu}_{\boldsymbol{q}} A^{\nu}_{-\boldsymbol{q}}\rangle &= \frac{1}{\mathcal{Z}_0}\frac{\delta^2 \mathcal{Z}_J}{\delta J_{-\boldsymbol{q},\mu}\delta J_{\boldsymbol{q},\nu}}\bigg|_{\boldsymbol{J}=0} \\ &= \frac{1}{\mathcal{Z}_0}\sum_{\{\boldsymbol{b},m\}}\prod_{\boldsymbol{r},\alpha}\delta_{\boldsymbol{\Delta}\cdot\boldsymbol{b}_{\boldsymbol{r},\alpha},\sum_{\beta\neq\alpha}\epsilon_{\alpha\beta}m_{\boldsymbol{r},\alpha,\beta}}\prod_{\boldsymbol{r},\mu,\alpha} I_{b_{\boldsymbol{r},\alpha,\mu}}(\beta)\prod_{\boldsymbol{r},\alpha<\beta} I_{m_{\boldsymbol{r},\alpha,\beta}}(\beta\lambda) \\ &\quad\times\left(-\frac{\delta^2 S_J}{\delta \boldsymbol{J}^{\mu}_{-\boldsymbol{q}}\delta \boldsymbol{J}^{\nu}_{\boldsymbol{q}}} - \frac{\delta S_J}{\delta \boldsymbol{J}^{\mu}_{-\boldsymbol{q}}}\frac{\delta S_J}{\delta \boldsymbol{J}^{\nu}_{\boldsymbol{q}}}\right)e^{-S_J}\bigg|_{\boldsymbol{J}=0}\end{aligned} \tag{33}$$

Here, $\mathcal{Z}_0$ is the partition function with the sources set to zero. The functional derivatives of the action is given by

$$-\frac{\delta S_J}{\delta \boldsymbol{J}^{\nu}_{\boldsymbol{q}}} = \frac{1}{\beta\left|\boldsymbol{Q}_{\boldsymbol{q}}\right|^2}(J^{\nu}_{-\boldsymbol{q}}P^{\mu\nu}_T + ie\sum_{\alpha} b^{\nu}_{-\boldsymbol{q},\alpha}) \tag{34}$$

and

$$-\frac{\delta^2 S_J}{\delta \boldsymbol{J}^{\mu}_{-\boldsymbol{q}}\delta \boldsymbol{J}^{\nu}_{\boldsymbol{q}}} = \frac{1}{\beta\left|\boldsymbol{Q}_{\boldsymbol{q}}\right|^2}P^{\mu\nu}_T. \tag{35}$$

Inserting this into Eq. (33) and setting the currents to zero, we have

$$\langle A^{\mu}_{\boldsymbol{q}} A^{\nu}_{-\boldsymbol{q}}\rangle = \frac{P^{\mu\nu}_T}{\beta\left|\boldsymbol{Q}_{\boldsymbol{q}}\right|^2} - \frac{e^2}{\beta^2\left|\boldsymbol{Q}_{\boldsymbol{q}}\right|^4}\langle\sum_{\alpha\beta} b^{\mu}_{\boldsymbol{q},\alpha}b^{\nu}_{-\boldsymbol{q},\beta}\rangle \tag{36}$$

Setting $\nu=\mu$ and summing over μ yields the relevant correlator

$$\langle \boldsymbol{A}_{\boldsymbol{q}}\cdot\boldsymbol{A}_{-\boldsymbol{q}}\rangle = \frac{1}{\beta\left|\boldsymbol{Q}_{\boldsymbol{q}}\right|^2}\left(2 - \frac{e^2}{\beta\left|\boldsymbol{Q}_{\boldsymbol{q}}\right|^2}\langle \boldsymbol{B}_{\boldsymbol{q}}\cdot\boldsymbol{B}_{-\boldsymbol{q}}\rangle\right), \tag{37}$$

where we have defined $\langle \boldsymbol{B}_{\boldsymbol{q}}\cdot\boldsymbol{B}_{-\boldsymbol{q}}\rangle = \langle\sum_{\alpha\beta}\boldsymbol{b}_{\boldsymbol{q},\alpha}\cdot\boldsymbol{b}_{-\boldsymbol{q},\beta}\rangle$

The effective gauge field mass is given by the zero momentum limit of the inverse propagator,

$$m^2_{\boldsymbol{A}} = \lim_{\boldsymbol{q}\to 0}\frac{2}{\beta\langle \boldsymbol{A}_{\boldsymbol{q}}\boldsymbol{A}_{-\boldsymbol{q}}\rangle} \tag{38}$$

As is seen from Eq. (37), the relevant combination of current-field correlators is the superconducting current, while charge-neutral currents do not appear in the expression. The current-correlator may be interpreted as the helicity modulus, which at a charged fixed point has a non-analytic behavior of the term proportional to q^2. We expect the leading behavior to be[26]

$$\lim_{\boldsymbol{q}\to 0}\frac{e^2}{2\beta}\langle \boldsymbol{B}_{\boldsymbol{q}}\cdot\boldsymbol{B}_{-\boldsymbol{q}}\rangle \sim \begin{cases}(1-C_2(T))q^2, & T>T_C.\\ q^2 - C_3(T)q^{2+\eta_{\boldsymbol{A}}}, & T=T_C.\\ q^2 - C_4(T)q^4, & T<T_C.\end{cases} \tag{39}$$

The result given above is dual to an expression for the gauge-mass in terms of correlation function of topological defects of the superconducting order, i.e. vortices[17,26,27], since vortices are dual objects to the currents $\boldsymbol{b}$. In $3D$, it is known that the dual of a superfluid is a superconductor, and vice versa[17,24,26,27]. Therefore, the above result for the current-correlator of a superconductor features the same behavior as the vortex-vortex correlator at a *neutral* fixed point, since a neutral fixed point in the original theory is a charged fixed point in the dual theory. Here, C_2 is the helicity modulus of the system, C_3 is a critical amplitude, and C_4 is essentially the inverse mass of the gauge-field. The physical interpretation of $\lim_{\boldsymbol{q}\to 0}\frac{e^2}{2\beta}\langle \boldsymbol{B}_{\boldsymbol{q}}\cdot\boldsymbol{B}_{-\boldsymbol{q}}\rangle$ is that when this quantity is zero, there are no long-range correlations of current-loops in the system, i.e. there are no supercurrents threading the entire system which is therefore normal metallic. Conversely, when $T<T_c$ this correlator is non-zero. There are supercurrents threading the entire system, which is therefore superconducting. When $T>T_C$, the gauge mass will be zero in the long wavelength limit. When $T<T_C$, however, the factors of q^2 will cancel, and the gauge correlator obtains a finite expectation value, and hence a mass. The Higgs-mechanism (Meissner effect) in an N-component superconductor is therefore a result of a blowout of closed loops of charged currents as the temperature is lowered through the phase transition. Conversely, the transition to the normal state is driven by a collapse of closed current loops, which is dual to a blowout of closed vortex loops. In either way of looking at the problem, the Higgs-mechanism is fluctuation driven.

Note that the above result is valid for any number of components $N\geq 1$, and any value of the Josephson coupling $\lambda\geq 0$.

The preemptive scenario described in the previous section impacts the temperature-dependence of the Higgs-mass at the transition from the superconducting to the normal metallic state. The mass vanishes continuously in an inverted $3DXY$ phase transition if the value of the gauge-charge is large enough for the preemptive scenario to be ruled out for any λ, including $\lambda=0$. For small enough gauge-charge, such that fluctuations in the neutral sector strongly affect fluctuations in the charged sector, and vice versa, the preemptive effect comes into play. In that case, the Higgs-mass vanishes discontinuously at the phase transition.

A schematic phase-diagram for the case $N=2$ is shown in Fig. 1.

V. CONCLUSION

We have formulated an N-component London superconductor with intercomponent Josephson couplings as a model

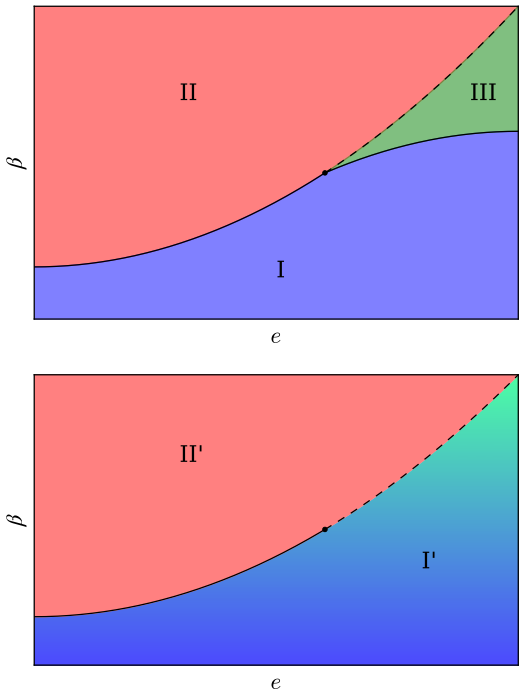

FIG. 1: A schematic phase diagram for the model with $N = 2$. The top panel shows the case $\lambda = 0$, while the lower panel shows the case with $\lambda > 0$. Top panel, $\lambda = 0$: Phase I is the fully symmetric normal phase with no superfluidity and no superconductivity. Phase III is the phase with no superconductivity, but non-zero superfluid stiffness in the neutral mode (metallic superfluid). Phase II is the low-temperature fully ordered state with finite Higgs mass in the charged sector and finite superfluid density in the neutral sector, a superconducting superfluid. The solid line separating phase I from phase II is a first-order phase transition line. The dotted line separating phase II from phase III is a critical line in the inverted $3DXY$ universality class. The solid line separating phase I from phase III is a critical line in the $3DXY$ universality class. Bottom panel, $\lambda > 0$: Phase I' is the high-temperature phase with no superconductivity. The entire phase is analytically connected with only a crossover regime separating the high-temperature phase from the lower-temperature phase. There is no spontaneous symmetry breaking in the neutral sector, since the Josephson coupling effectively acts as an explicit symmetry-breaking term in this sector, analogous to a magnetic field coupling linearly to XY spins. Phase II' is the low-temperature superconducting state. The solid part of the line separating phase I' from phase II' is a first-order phase transition line. The dotted part is a critical line in the inverted $3DXY$ universality class. Both for $\lambda = 0$ and $\lambda > 0$, the line separating the superconducting states (II and II') from the non-superconducting state changes character from a first-order phase transition (solid line) to a second-order phase-transition (dotted line) as via a tricritical point. The $3DXY$ critical line separating phase I from phase III for $\lambda = 0$, is converted to a crossover line in phase I' for $\lambda > 0$.

of N integer-current fields $\boldsymbol{b}_\alpha$ and $N(N-1)/2$ instanton fields, $m_{\alpha,\beta}$. These instantons allow supercurrents of a particular condensate component to be converted to a supercurrent of a different component, i.e. currents may change "color" at any site. For zero Josephson coupling, λ, only configurations where all the instanton fields are zero contribute, and the model reverts to an N-component gauge-coupled 3dXY-model. This model is known to have either i) $N-1$ transitions in the XY-universality class and a single phase transition in the inverted XY-universality class, or ii) a single preemptive first-order phase transition for intermediate values of the charge. For any $\lambda > 0$, the $N-1$ phase transitions in the neutral sector are converted to crossovers. In the limit $\lambda \to \infty$, all orders of instanton excitations will contribute. This effectively removes the constraints $\boldsymbol{\Delta} \cdot \boldsymbol{b}_\alpha = 0$ on each individual component. There is only one particular composite mode, $\sum_\alpha \boldsymbol{b}_\alpha$ which is still divergenceless, and which thus features a phase transition. This transition is known to be in the inverted 3dXY-universality class for $\lambda = 0$. For small, but finite λ, fluctuations in the neutral sector are still substantial although the phase transitions are all converted to crossovers. These charge-neutral non-critical fluctuations nonetheless substantially influence the putative critical fluctuations in the charged sector, particularly at temperatures close to the $\lambda = 0$ $3DXY$ critical point. This converts the inverted $3DXY$ critical point into a first-order phase-transition via a preemptive effect. The degree to which the charge-neutral fluctuations influence the fluctuations in the charged sector for small λ, increases with the number of composite charge-neutral fluctuating modes. In the parameter regime (e, λ) where one may have a preemptive effect, the first-order character of the superconductor-normal metal phase transition will therefore be more pronounced with increasing N.

As a byproduct of our analysis, we have recast the onset of the photon Higgs-mass in the superconductor (Meissner effect) in terms of a blowout of current loops associated with the onset of superconductivity. This analysis goes beyond mean-field theory and takes all critical fluctuations of the theory into account. The description giving the onset of the Higgs-mass of the photon in terms of a current-loop blowout going into the superconducting state as temperature is lowered, is dual to the description of the vanishing of the Higgs-mass of the photon in terms of vortex-loop blowout going into the normal metallic state as the temperature is increased.

Acknowledgments

P. N. G. was supported by NTNU and the Research Council of Norway. A. S. was supported by the Research Council of Norway, through Grants 205591/V20 and 216700/F20, as well as European Science Foundation COST Action MPI1201. We tank E. Babaev and J. Garaud for useful discussions.

Appendix A: The character expansion

We apply the expansion

$$e^{\beta\cos\gamma} = \sum_{b=-\infty}^{\infty} I_b(\beta) e^{ib\gamma}, \tag{A1}$$

to the cosine terms of Eq. (4), with $\lambda = 0$. This gives the action

$$\begin{aligned}\mathcal{Z} = &\int \mathcal{D}\boldsymbol{A}\left(\prod_{\alpha}\int\mathcal{D}\theta_{\alpha}\right)\\ &\times\prod_{\boldsymbol{r},\mu,\alpha}\sum_{b_{\boldsymbol{r},\mu,\alpha}=-\infty}^{\infty} I_{b_{\boldsymbol{r},\mu,\alpha}}(\beta)e^{ib_{\boldsymbol{r},\mu,\alpha}(\Delta_\mu\theta_{\boldsymbol{r},\alpha}-eA_{\boldsymbol{r},\mu})}\\ &\times\prod_{\boldsymbol{r}} e^{-\frac{\beta}{2}(\Delta\times\boldsymbol{A}_{\boldsymbol{r}})^2}\end{aligned} \tag{A2}$$

By performing a partial integration of each phase component, $\theta_{\boldsymbol{r},\alpha}$, we move the lattice derivative from the phase to the integer field $\boldsymbol{b}$ in the first term. Then we factorize the terms dependent on the phases on each lattice site, which may then be integrated separately.

$$\mathcal{Z}_\theta = \prod_{\boldsymbol{r},\alpha}\int_0^{2\pi} \mathrm{d}\theta_{\boldsymbol{r},\alpha} e^{-i\theta_{\boldsymbol{r},\alpha}(\sum_\mu \Delta_\mu b_{\boldsymbol{r},\mu,\alpha})}. \tag{A3}$$

This constrains the $\boldsymbol{b}$-fields to have zero divergence,

$$\boldsymbol{\Delta}\cdot\boldsymbol{b}_{\boldsymbol{r},\alpha} = 0\;\forall\;\boldsymbol{r},\alpha. \tag{A4}$$

The partition function then reads

$$\begin{aligned}\mathcal{Z} = \int\mathcal{D}(\boldsymbol{A})\sum_{\{\boldsymbol{b}\}}\prod_{\boldsymbol{r},\alpha}\delta_{\boldsymbol{\Delta}\cdot\boldsymbol{b}_{\boldsymbol{r},\alpha},0}\prod_{\boldsymbol{r},\mu,\alpha} I_{b_{\boldsymbol{r},\mu,\alpha}}(\beta)\\ \prod_{\boldsymbol{r}} e^{-\left[ie\sum_\alpha \boldsymbol{b}_{\boldsymbol{r},\alpha}\cdot\boldsymbol{A}_{\boldsymbol{r}}+\frac{\beta}{2}(\boldsymbol{\Delta}\times\boldsymbol{A}_{\boldsymbol{r}})^2\right]}\end{aligned} \tag{A5}$$

This represents N integer-current fields which must form closed loops individually, coupled by a single gauge field, $\boldsymbol{A}$.

The next step is to integrate out the gauge degrees of freedom. To this end we Fourier transform the action

$$S = \sum_{\boldsymbol{r}}\left[ie\sum_\alpha \boldsymbol{b}_{\boldsymbol{r},\alpha}\cdot\boldsymbol{A}_{\boldsymbol{r}} + \frac{\beta}{2}(\boldsymbol{\Delta}\times\boldsymbol{A}_{\boldsymbol{r}})^2\right] \tag{A6}$$

into

$$\begin{aligned}S = \sum_{\boldsymbol{q}}\Bigg[&\frac{ie}{2}\sum_\alpha \boldsymbol{b}_{\boldsymbol{q},\alpha}\cdot\boldsymbol{A}_{-q} + \frac{ie}{2}\sum_\alpha \boldsymbol{b}_{-q,\alpha}\cdot\boldsymbol{A}_{\boldsymbol{q}}\\ &+\frac{\beta}{2}(\boldsymbol{Q}_{\boldsymbol{q}}\times\boldsymbol{A}_{\boldsymbol{q}})(\boldsymbol{Q}_{-\boldsymbol{q}}\times\boldsymbol{A}_{-\boldsymbol{q}})\Bigg].\end{aligned} \tag{A7}$$

Here, we have symmetrized the $\boldsymbol{b}\cdot\boldsymbol{A}$-term, and $\boldsymbol{Q}_{\boldsymbol{q}}$ is the Fourier representation of the lattice differential operator, $\boldsymbol{\Delta}$. We can further simplify the expression by choosing the gauge $\boldsymbol{\Delta}\cdot\boldsymbol{A}_{\boldsymbol{r}} = 0$, which translates to $\boldsymbol{Q}_{\boldsymbol{q}}\cdot\boldsymbol{A}_{\boldsymbol{q}} = 0$ in Fourier space. This reduces the last term to $\beta\left|\boldsymbol{Q}_{\boldsymbol{q}}\right|^2\boldsymbol{A}_{\boldsymbol{q}}\cdot\boldsymbol{A}_{-\boldsymbol{q}}/2$, where $\left|\boldsymbol{Q}_{\boldsymbol{q}}\right|^2 = \sum_\mu(2\sin q_\mu/2)^2$. Now we complete the squares in $\boldsymbol{A}_{\boldsymbol{q}}$, to facilitate the Gaussian integration

$$\begin{aligned}S = \sum_{\boldsymbol{q}}\Bigg[&\Big(\boldsymbol{A}_{\boldsymbol{q}} + \frac{ie}{2}\sum_\alpha \boldsymbol{b}_{\boldsymbol{q},\alpha}D_{\boldsymbol{q}}^{-1}\Big)D_{\boldsymbol{q}}\\ &\times\Big(\boldsymbol{A}_{-\boldsymbol{q}} + \frac{ie}{2}\sum_\alpha \boldsymbol{b}_{-\boldsymbol{q},\alpha}D_{\boldsymbol{q}}^{-1}\Big)\\ &+\frac{e^2}{4}\Big(\sum_\alpha \boldsymbol{b}_{\boldsymbol{q},\alpha}\Big)D_{\boldsymbol{q}}^{-1}\Big(\sum_\beta \boldsymbol{b}_{-\boldsymbol{q},\beta}\Big)\Bigg],\end{aligned} \tag{A8}$$

where $D_{\boldsymbol{q}} = \beta\left|\boldsymbol{Q}_{\boldsymbol{q}}\right|^2/2$. Now we can shift and integrate out the gauge field, $A_{\boldsymbol{q}}$, which leaves us with

$$S = \sum_{\boldsymbol{q}}\frac{e^2}{2\beta\left|\boldsymbol{Q}_{\boldsymbol{q}}\right|^2}\Big(\sum_\alpha \boldsymbol{b}_{\boldsymbol{q},\alpha}\Big)\cdot\Big(\sum_\beta \boldsymbol{b}_{-\boldsymbol{q},\beta}\Big), \tag{A9}$$

or in real space

$$S = \sum_{\boldsymbol{r},\boldsymbol{r}'}\frac{e^2}{2\beta}\Big(\sum_\alpha \boldsymbol{b}_{\boldsymbol{r},\alpha}\Big)\cdot\Big(\sum_\beta \boldsymbol{b}_{\boldsymbol{r}',\beta}\Big)D(\boldsymbol{r}-\boldsymbol{r}'). \tag{A10}$$

Here, $D(\boldsymbol{r}-\boldsymbol{r}')$ is the Fourier transform of $1/\left|\boldsymbol{Q}_{\boldsymbol{q}}\right|^2$. Inserting this into the action, we arrive at

$$\begin{aligned}\mathcal{Z} = \sum_{\{\boldsymbol{b},m\}}\prod_{\boldsymbol{r},\alpha}\delta_{\boldsymbol{\Delta}\cdot\boldsymbol{b}_{\boldsymbol{r},\alpha},0}\prod_{\boldsymbol{r},\mu,\alpha} I_{b_{\boldsymbol{r},\alpha,\mu}}(\beta)\\ \prod_{\boldsymbol{r},\boldsymbol{r}'} e^{-\frac{e^2}{2\beta}\sum_{\alpha,\beta}\boldsymbol{b}_{\boldsymbol{r},\alpha}\cdot\boldsymbol{b}_{\boldsymbol{r}',\beta}D(\boldsymbol{r}-\boldsymbol{r}')},\end{aligned} \tag{A11}$$

which is Eq. (9)

Appendix B: Two-dimensional multiband superconductors

In a thin-film superconductor, the effective magnetic penetration depth is inversely proportional to the film thickness. Hence, in a two-dimensional system, the magnetic penetration depth becomes infinite, and the effective charge of the charge carriers become zero. This effectively freezes out the gauge-field fluctuations of the interior of the film, in turn eliminating the long-range gauge-field mediated vortex-vortex interactions. In this case the relevant lattice action will be

$$\begin{aligned}S = &-\beta\sum_{\boldsymbol{r}}\sum_{\mu,\alpha}\cos\left(\Delta_\mu\theta_{\boldsymbol{r},\alpha}\right)\\ &-\beta\lambda\sum_{\boldsymbol{r}}\sum_{\alpha<\beta}\cos\left(\theta_{\boldsymbol{r},\alpha}-\theta_{\boldsymbol{r},\beta}\right).\end{aligned} \tag{B1}$$

That is, it is effectively a neutral condensate.

We may apply the character expansion of Eq. (8) to Eq. (B1), which results in the partition function

$$\mathcal{Z} = \sum_{\{\boldsymbol{b},m\}} \prod_{\boldsymbol{r},\alpha} \delta_{\boldsymbol{\Delta}\cdot\boldsymbol{b}_{\boldsymbol{r},\alpha},\sum_{\beta\neq\alpha} m_{\boldsymbol{r},\alpha,\beta}} \prod_{\boldsymbol{r},\mu,\alpha} I_{b_{\boldsymbol{r},\alpha,\mu}}(\beta) \prod_{\boldsymbol{r},\alpha<\beta} I_{m_{\boldsymbol{r},\alpha,\beta}}(\beta\lambda). \tag{B2}$$

This is of course very similar to Eq. (12), with the differences being as follows. The integer-current field, $\boldsymbol{b}_{\boldsymbol{r}}$ is now a two-component vector, as is naturally the position vector, $\boldsymbol{r}$, and the gauge-field mediated interaction has disappeared.

We may apply the same reasoning to Eq. (B2) as we did in the main text. There will be a single mode, $\sum_\alpha \boldsymbol{b}_{\boldsymbol{r}}$ which is divergenceless, and $N(N-1)/2$ modes with finite divergence. The only difference now in the two-dimensional case is the lack of gauge-field mediated interactions in the divergenceless mode. Hence, the single remaining phase transition is expected to be a Kosterlitz-Thouless transition from a two-dimensional superfluid to a normal fluid. This prediction could be verified in Monte-Carlo simulations, as the partition function of Eq. (B2) is particularly well suited for worm-type algorithms.

[1] J. E. Jaffe and N. W. Ashcroft, Phys. Rev. B **23**, 6176 (1981).
[2] J. Oliva and N. W. Ashcroft, Phys. Rev. B **30**, 1326 (1984).
[3] K. Moulopoulos and N. W. Ashcroft, Phys. Rev. Lett. **66**, 2915 (1991).
[4] K. Moulopoulos and N. W. Ashcroft, Phys. Rev. B **59**, 12309 (1999).
[5] N. W. Ashcroft, Journal of Physics A: Mathematical and General **36**, 6137 (2003).
[6] N. W. Ashcroft, Phys. Rev. Lett. **92**, 187002 (2004).
[7] T. Senthil, L. Balents, S. Sachdev, A. Vishwanath, and M. P. A. Fisher, Phys. Rev. B **70**, 144407 (2004).
[8] O. I. Motrunich and A. Vishwanath, Phys. Rev. B **70**, 075104 (2004).
[9] F. Bouquet, R. A. Fisher, N. E. Phillips, D. G. Hinks, and J. D. Jorgensen, Phys. Rev. Lett. **87**, 047001 (2001).
[10] A. Y. Liu, I. I. Mazin, and J. Kortus, Phys. Rev. Lett. **87**, 087005 (2001).
[11] P. Szabó, P. Samuely, J. Kačmarčík, T. Klein, J. Marcus, D. Fruchart, S. Miraglia, C. Marcenat, and A. G. M. Jansen, Phys. Rev. Lett. **87**, 137005 (2001).
[12] Y. Kamihara, T. Watanabe, M. Hirano, , and H. Hosono, Journal of the American Chemical Society **130**, 3296 (2008).
[13] E. Babaev, A. Sudbo, and N. W. Ashcroft, Nature **431**, 666 (2004), ISSN 0028-0836, URL http://dx.doi.org/10.1038/nature02910.
[14] E. Smørgrav, J. Smiseth, E. Babaev, and A. Sudbø, Phys. Rev. Lett. **94**, 096401 (2005), URL http://link.aps.org/doi/10.1103/PhysRevLett.94.096401.
[15] E. Smørgrav, E. Babaev, J. Smiseth, and A. Sudbø, Phys. Rev. Lett. **95**, 135301 (2005).
[16] A. Kuklov, N. Prokofev, B. Svistunov, and M. Troyer, Annals of Physics **321**, 1602 (2006), ISSN 0003-4916, july 2006 Special Issue.
[17] J. Smiseth, E. Smørgrav, E. Babaev, and A. Sudbø, Phys. Rev. B **71**, 214509 (2005).
[18] S. Kragset, E. Smørgrav, J. Hove, F. S. Nogueira, and A. Sudbø, Phys. Rev. Lett. **97**, 247201 (2006).
[19] E. V. Herland, E. Babaev, and A. Sudbø, Phys. Rev. B **82**, 134511 (2010).
[20] K. A. H. Sellin and E. Babaev, Phys. Rev. B **93**, 054524 (2016).
[21] T. A. Bojesen, E. Babaev, and A. Sudbø, Phys. Rev. B **89**, 104509 (2014).
[22] T. Bojesen and A. Sudb, Journal of Superconductivity and Novel Magnetism **28**, 3193 (2015), ISSN 1557-1939, URL http://dx.doi.org/10.1007/s10948-015-3155-x.
[23] W. Janke and H. Kleinert, Nuclear Physics B **270**, 135 (1986).
[24] H. Kleinert, *Gauge Fields in Condensed Matter* (World Scientific Publishing, Singapore, 1989).
[25] E. K. Dahl, E. Babaev, S. Kragset, and A. Sudbø, Phys. Rev. B **77**, 144519 (2008).
[26] J. Hove and A. Sudbø, Phys. Rev. Lett. **84**, 3426 (2000).
[27] J. Smiseth, E. Smørgrav, and A. Sudbø, Phys. Rev. Lett. **93**, 077002 (2004).